

Journal of Advanced Transportation

Smart Technologies for Vehicle Safety and Driver Assistance

Lead Guest Editor: Mihai Dimian

Guest Editors: Luc Chassagne, Petru Andrei, and Pu Li






Smart Technologies for Vehicle Safety and Driver Assistance

Journal of Advanced Transportation

Smart Technologies for Vehicle Safety and Driver Assistance

Lead Guest Editor: Mihai Dimian

Guest Editors: Luc Chassagne, Petru Andrei, and Pu Li



Copyright © 2019 Hindawi. All rights reserved.

This is a special issue published in "Journal of Advanced Transportation." All articles are open access articles distributed under the Creative Commons Attribution License, which permits unrestricted use, distribution, and reproduction in any medium, provided the original work is properly cited.

Editorial Board

Francesco Bella, Italy
Abdelaziz Bensrhair, France
Cesar Briso-Rodriguez, Spain
María Calderon, Spain
Juan C. Cano, Spain
Giulio E. Cantarella, Italy
Maria Castro, Spain
Oded Cats, Netherlands
Anthony Chen, USA
Nicolas Chiabaut, France
Steven I. Chien, USA
Antonio Comi, Italy
Luca D'Acierno, Italy
Andrea D'Ariano, Italy
Alexandre De Barros, Canada
Stefano de Luca, Italy
Rocío de Oña, Spain
Luigi Dell'Olio, Spain
Cédric Demonceaux, France
Sunder Lall Dhingra, India
Vinayak Dixit, Australia
Yuchuan Du, China

Nour-Eddin El-fauzi, France
Juan-Antonio Escareno, France
David F. Llorca, Spain
Peter Furth, USA
Francesco Galante, Italy
Md. Mazharul Haque, Australia
Jérôme Haëri, France
Samiul Hasan, USA
S. P. Hoogendoorn, Netherlands
Hocine Imine, France
Lina Kattan, Canada
Victor L. Knoop, Netherlands
Alain Lambert, France
Ludovic Leclercq, France
Jaeyoung Lee, USA
Seungjae Lee, Republic of Korea
Zhi-Chun Li, China
Yue Liu, USA
Jose R. Martinez-De-Dios, Spain
Filomena Mauriello, Italy
Monica Menendez, UAE
Rakesh Mishra, UK

Andrea Monteriù, Italy
Giuseppe Musolino, Italy
Jose E. Naranjo, Spain
Aboelmagd Noureldin, Canada
Eneko Osaba, Spain
Eleonora Papadimitriou, Netherlands
Dongjoo Park, Republic of Korea
Paola Pellegrini, France
Luca Pugi, Italy
Nandana Rajatheva, Finland
Hesham Rakha, USA
Prianka N. Seneviratne, Philippines
Fulvio Simonelli, Italy
Richard S. Tay, Australia
Pascal Vasseur, France
Antonino Vitetta, Italy
Francesco Viti, Luxembourg
S. Travis Waller, Australia
Shamsunnahar Yasmin, Australia
Jacek Zak, Poland
Guohui Zhang, USA
G. Homem de Almeida Correia, Netherlands

Contents

Smart Technologies for Vehicle Safety and Driver Assistance

Mihai Dimian , Luc Chassagne, Petru Andrei, and Pu Li
Editorial (2 pages), Article ID 2690498, Volume 2019 (2019)



Simulation-Based Framework for Estimating Crash Modification Factors (CMFs): A Case Study for ITS Countermeasures

Plaban Das , Seri Park , and Parth Bhavsar 
Research Article (13 pages), Article ID 1980363, Volume 2019 (2019)






Drivers' Perceptions of Smartphone Applications for Real-Time Route Planning and Distracted Driving Prevention

Khaled Shaaban 
Research Article (10 pages), Article ID 2867247, Volume 2019 (2019)



Active Warning System for Highway-Rail Grade Crossings Using Connected Vehicle Technologies

Xu Wang , Jiangchen Li , Can Zhang, and Tony Z. Qiu 
Research Article (11 pages), Article ID 3219387, Volume 2019 (2019)



Advanced Modeling and Simulation of Vehicle Active Aerodynamic Safety

Krzysztof Kurec , Michał Remer , Jakub Broniszewski , Przemysław Bibik , Sylwester Tudruj, and Janusz Piechna 
Research Article (17 pages), Article ID 7308590, Volume 2019 (2019)




Classification of Metro Facilities with Deep Neural Networks

Deqiang He , Zhou Jiang , Jiyong Chen, Jianren Liu, Jian Miao, and Abid Shah
Research Article (8 pages), Article ID 6782803, Volume 2019 (2019)

A Novel Prediction Model for Car Body Vibration Acceleration Based on Correlation Analysis and Neural Networks

Shubin Zheng , Qianwen Zhong , Xiaodong Chai, Xingjie Chen, and Lele Peng
Research Article (13 pages), Article ID 1752070, Volume 2018 (2019)

An Efficient Color Space for Deep-Learning Based Traffic Light Recognition

Hyun-Koo Kim , Ju H. Park , and Ho-Youl Jung 
Research Article (12 pages), Article ID 2365414, Volume 2018 (2019)




Video Analytic Based Health Monitoring for Driver in Moving Vehicle by Extracting Effective Heart Rate Inducing Features

Kanghyu Lee, David K. Han, and Hanseok Ko 
Research Article (9 pages), Article ID 8513487, Volume 2018 (2019)


A Comparison Analysis of Surrogate Safety Measures with Car-Following Perspectives for Advanced Driver Assistance System

Sehyun Tak, Sunghoon Kim , Donghoun Lee , and Hwasoo Yeo 
Research Article (14 pages), Article ID 8040815, Volume 2018 (2019)



An Earlier Predictive Rollover Index Designed for Bus Rollover Detection and Prevention

Shun Tian , Lang Wei , Chris Schwarz, WenCai Zhou , Yuan Jiao, and YanQin Chen
Research Article (10 pages), Article ID 2713868, Volume 2018 (2019)

Characterization of Road Condition with Data Mining Based on Measured Kinematic Vehicle Parameters

Johannes Masino , Jakob Thumm, Guillaume Levasseur, Michael Frey, Frank Gauterin, Ralf Mikut, and Markus Reischl
Research Article (10 pages), Article ID 8647607, Volume 2018 (2019)

Blind Corner Propagation Model for IEEE 802.11p Communication in Network Simulators

Sanchai Jaktheerangkoon , Kulit Na Nakorn, and Kultida Rojviboonchai 
Research Article (11 pages), Article ID 9482325, Volume 2018 (2019)

Editorial

Smart Technologies for Vehicle Safety and Driver Assistance

Mihai Dimian ¹, Luc Chassagne,^{2,3} Petru Andrei,⁴ and Pu Li⁵

¹Stefan cel Mare University of Suceava, Suceava 720229, Romania

²University of Paris-Saclay, Saint-Aubin, France

³University of Versailles Saint-Quentin-en-Yvelines, Vélizy-Villacoublay 78140, France

⁴Florida State University, Florida A&M University, Tallahassee, Florida 32310, USA

⁵Technical University of Ilmenau, Ilmenau 98693, Germany

Correspondence should be addressed to Mihai Dimian; dimian@usm.ro

Received 16 April 2019; Accepted 16 April 2019; Published 15 May 2019

Copyright © 2019 Mihai Dimian et al. This is an open access article distributed under the Creative Commons Attribution License, which permits unrestricted use, distribution, and reproduction in any medium, provided the original work is properly cited.

Transportation is currently facing significant challenges from a variety of factors including growing populations and number of vehicles, rising urbanization, negligent driving, and environmental issues. An interdisciplinary approach is needed to address these complex problems, and information and communications technologies (ICT) are emerging as leading contributors to the future of transport. With more than one million victims in road accidents annually, the improvement in safety and efficiency of the transportation system is of major interest for industrial and academic research. The use of ICT in development of intelligent safety systems, driver assistance systems, cooperative driving networks, and smart transport infrastructure is expected to contribute to significant reduction of road accident and traffic congestion. In this context, this special issue aims at providing a collection of innovative and high-quality research contributions focusing on smart technologies for vehicle safety and driver assistance. 28 papers were submitted for this issue; 12 of them were accepted for publication and were summarized below.

The paper by P. Das et al. demonstrates a proof of concept of simulation-based framework for evaluating safety performances of Intelligent Transportation System (ITS) countermeasures. The traffic microsimulation model and surrogate safety assessment model are used to estimate crash modification factors while a case study is used to calibrate the model to real-world scenario. This approach can investigate the combined effect of multiple proposed countermeasures and improve traffic safety management.

The paper by K. Shaaban explores drivers' perceptions on smartphone applications for driving assistance. The survey

was conducted on 421 participants from Qatar with respect to their interests and perceptions in the installation and use of two smartphone applications for real-time route planning and distracted driving prevention. The results can be used by companies and government agencies for development of road safety and efficiency applications, as well as for safety campaign and awareness programs.

The paper by X. Wang et al. addresses active warning systems for highway-rail grade crossings (HRGC) using connected vehicle technologies. To mitigate the risk of collisions at HRGC, a novel active warning system was designed, implemented, and tested based on readily available connected vehicle technologies and devices. The results from simulations and field tests show that the proposed system offers a better estimation of risk probability, which enhances the system effectiveness and reliability, while the warning messages decrease the collision risk compared to the predicted risk probability.

The paper by K. Kurec et al. presents models and simulations of various controlling aspects of car aerodynamic characteristics by actuating movable aerodynamic add-ons on the car body to increase the traction, braking, and lateral force in road conditions requiring such action. The purpose of this work was to extend the safety limits of fast moving cars by controlling the moving aerodynamic elements.

The paper by D. He et al. is on detecting obstacles quickly and accurately during metro operation by using Google's Inception v3 deep convolution neural networks to classify the common facility images from metro tunnels. The developed module provides better quality than other existing methods chosen for comparison while using fewer model parameters

and reducing computational costs. The use of this approach for metro intelligent monitoring systems could improve the safety of metro operation.

The paper by S. Zheng et al. aims to develop a prediction model for car body vibration acceleration by taking into account railway parameters collected by various sensors and the previous vibration acceleration. The model was based on several training algorithms and neural network structures and was successfully applied to predict the car body vibration acceleration of test datasets on different railway segments. This approach overcomes the complexity and uncertainty of the multiparameters coupling analysis used in traditional models and offers an important instrument to assist the driver in ensuring a smooth operation of the train.

The paper by H.-K. Kim et al. provides a guideline for designing a traffic light recognition system which is useful for advanced driving assistance systems, as well as for autonomous vehicles. The investigation is focused on two main components of the traffic light detection system: the color space of the input video and the network model of deep learning, by considering six color spaces and three types of network models and by comparing the results of all possible combinations on a traffic light dataset.

The paper by K. Lee et al. proposes a novel approach to remotely estimating the heart rate in actual driving environments by using facial images. The driver face region is first detected, and the components related to heart rate are then extracted by using ensemble empirical mode decomposition and analyzed in frequency domain. Based on public human-computer-interface dataset, the method was tested and compared to previous studies. In addition, the method was applied to data obtained from an actual driving situation. This work can be used to prevent accidents due to acute heart rate disease by remotely estimating the heart rate and judiciously controlling the vehicle.

The paper by S. Tak et al. investigates the correlation between collision risk and driver behavior by analyzing three surrogate safety measures (SSM) in two car-following scenarios. This study provides solutions to improve the current advanced driver assistance systems. Among three analyzed SSM, the one based on deceleration (DSSM) features similarities to human behavior shows a balanced performance to estimate the collision risks in both deceleration and acceleration phase, thus providing enhanced driver compliance to the ADAS.

The paper by S. Tian et al. proposes a novel algorithm for predicting bus rollover, providing a faster solution to this problem compared to existing estimation algorithms and thus offering additional time for response. The enhanced method predicts the lateral load transfer ratio (LTR), the most common rollover index, and proves its effectiveness in two standard handling tests ("sine with dwell" and "double lane change").

The paper by J. Masino et al. develops two classifiers of road condition by using mining techniques on data provided by acceleration sensors and gyroscopes installed in vehicles. Due to its modular design, the system can be extended and adapted to multiple and various sensors. A

detailed presentation of this system design and capabilities is presented in the article.

In the paper by S. Jaktheerangkoon et al., the authors proposed and tested a blind-corner propagation model for intervehicular communication in order to enhance the standard simulation models used in vehicular ad hoc network. The distance calculation for signals traveling through blind corner is properly adjusted by taking into account IEEE 802.11p blind-corner experiments, and an additional parameter that adjusts the standard model to the degree of the obstruction is introduced. Additional real-life experiments are performed to prove the better performance of the developed model when compared to existing obstacle ones. This result can be used to realistically test intervehicle communication protocols and applications for blind-corner scenario.

Taken together, these 12 papers provide key ICT solutions to various challenges faced by the developers of technologies used for vehicle safety and driver assistance.

Conflicts of Interest

The guest editors declare that there are no conflicts of interest regarding this special issue.

Acknowledgments

The guest editors would like to thank the reviewers for the time and efforts devoted to the analysis of the submitted manuscripts, as well as for the comments and suggestions used to improve the quality of the accepted articles.

*Mihai Dimian
Luc Chassagne
Petru Andrei
Pu Li*

Research Article

Simulation-Based Framework for Estimating Crash Modification Factors (CMFs): A Case Study for ITS Countermeasures

Plaban Das ¹, Seri Park ², and Parth Bhavsar ³

¹KMA Consulting Engineers, Inc., 1010 Berlin Road, Cherry Hill, NJ 08034, USA

²Civil and Environmental Engineering, Villanova University, 800 E. Lancaster Avenue, Villanova, PA 19085, USA

³Center for Research and Education in Advanced Transportation Engineering (CREATEs),
107 Gilbreth Pkwy, Mullica Hill, NJ 08062, USA

Correspondence should be addressed to Parth Bhavsar; parthpbhavsar@outlook.com

Received 28 September 2018; Accepted 18 February 2019; Published 3 April 2019

Guest Editor: Petru Andrei

Copyright © 2019 Plaban Das et al. This is an open access article distributed under the Creative Commons Attribution License, which permits unrestricted use, distribution, and reproduction in any medium, provided the original work is properly cited.

The efficient movement of users and goods is the primary purpose of the surface transportation system. Roadway traffic crashes have devastating impacts on quality of life of the users as well as health of the system. While researchers are utilizing advanced computing and communication tools to reduce number of crashes on the roadways, there is still an absence of appropriate method to evaluate the safety performances of these advanced technologies in the planning stage. Development of crash modification factors (CMFs) is a standard method to evaluate the safety effect of proposed countermeasures. Though, the current practices of developing CMFs are not efficient and cost-effective in case of addressing impacts of Intelligent Transportation System (ITS) countermeasures. This study demonstrated a proof of concept of simulation-based framework for determining CMFs for ITS countermeasures. The proposed framework includes the application of traffic microsimulation model and Surrogate Safety Assessment Model (SSAM) developed by Federal Highway Administration (FHWA). The integration of these two models is suggested to estimate CMFs efficiently. However, the calibration of traffic microsimulation model and SSAM model is essential to portray the real-world scenarios. A case study for estimating CMFs of ITS countermeasures was conducted to validate the proposed simulation-based approach. Four ITS countermeasures were considered: ramp metering, variable speed limit, junction control, and dynamic lane assignment. They were coded in traffic microsimulation environment and vehicle trajectory files were generated to import into SSAM model. After analyzing these trajectory files in SSAM tool, it was found that all proposed ITS countermeasures, except variable speed limit assignment, could reduce the number of crashes at crash prone locations.

1. Introduction

The traffic fatality rate on United States highways and free-ways presented a declining trend from 2006 to 2014 after deploying safety initiatives, such as mandatory seat belt use and strict law imposition against driving under influence of drugs. Furthermore, advance technologies installed on vehicles (e.g., air bags, lane departure warning, blind spot warning, and adaptive cruise control) had contributed to decreasing the traffic fatalities [1]. Fatality rate has increased 5.6 percentages to 37,461 people in 2016, after exhibiting the highest increase rate of last three decades in 2015 which was 8.4 percentages increase [2]. To date, several researchers are working on developing crash prediction models and finding countermeasures to eradicate the traffic crashes on

our roads [3, 4]. However, an appropriate scientific method is essential to evaluate these proposed countermeasures prior to the actual implementation that usually requires significant budget and time.

To introduce a science-based technical approach that can assess safety performance of proposed countermeasures in planning stage, the Highway Safety Manual (HSM) was published by the cooperative efforts of the American Association of State Highway and Transportation Officials (AASHTO), Federal Highway Administration (FHWA), and Transportation Research Board [5]. HSM allows users to prioritize the countermeasures based on the changes in crash frequency and severity. In HSM, a catalog of safety performance functions (SPFs) and crash modification functions (CMFs) for different geometric and operational countermeasure types is

included to predict safety performance of any facility [5]. In addition to planning, the HSM can provide quantitative safety performance and assistance to select countermeasures for design, and operational phases of the project. However, the successes in safety performance predictions depend on the methodological and statistical validation of CMF values and functions [6]. Many potential CMFs are excluded from first HSM edition due to the failure of implicating proper validations and justifications [7]. While researchers are focusing on parameters such as crash types and severity [8], roadway types [9], different socioeconomic conditions [10], and time changes [11] to investigate the variability of CMFs, variables such as vehicle types, driver ages and characteristics, and weather conditions have not been examined so far [12]. On the other hand, estimating combined safety impacts of multiple countermeasures remain an unresolved key issue in HSM and just multiplication of the CMFs may lead to an over- or underestimation of combined effects [13]. In addition, AASHTO has addressed the failure in considering the local impact of different factors in HSM [14]. The duration of study for developing CMFs is another drawback, in that the research process requires data of traffic crashes before and after implementation of countermeasures. The further discussion regarding study duration continues, as discussed in literature review. Finally and most importantly, the implementation of countermeasures could demand a huge amount of investment, and once it is built, additional money could be wasted to undo in case of errors that may increase the number of traffic crashes. For example, installation of ramp meter on multilane highway could cost approximately 1 million excluding right of way acquisition.

The objectives of this study are to (i) develop a step-by-step traffic microsimulation-based method for developing CMFs which could be used to predict potential crash reduction benefit of proposed countermeasures, and (ii) provide a proof of concept of proposed method. Additionally, this proposed simulation-based method could be utilized to improve the local representation of existing CMFs. The remaining of this study is organized as follows. Section 2 discusses the current practices and their shortcomings, and Section 3 presents proposed method for developing CMFs. A case study is presented in Section 4 to investigate the proposed method with Section 5 focuses on the results of the case study and statistical analysis, and Section 6 concentrates on validation of the method. Then concluding remarks and future research direction are presented in Section 7.

2. Literature Review

The before-after, cross-sectional, and case-control studies are widely used methods to estimate/develop CMS [15]. In observational before-after study, it is required to implement a countermeasure at crash prone region and then over a period of time, crash frequency at that location is recorded. The comparison between before and after implementation provides the observed CMF value of that countermeasure. There are many approaches to perform observational before-after evaluations including but not limited to

- (a) naïve before-after,
- (b) before-after with comparison group,
- (c) empirical Bayes,
- (d) full Bayes.

Among the above listed approaches, naïve before-after is the simplest method, although this method fails to contemplate “regression toward the mean” effects [16]. As a result, this method overestimates the effect of countermeasure. Before-after method with comparison group compares the after implementation crash frequency with similar untreated locations [17]. Empirical Bayes method to calculate CMFs has been the most common and rigorous approach in last ten years [18]. This method overcomes the regression toward the mean effect and also considers the effect of the change in traffic volume over the period of study. Recently, empirical Bayes has been applied using negative binomial regression models to overcome the challenge of heterogeneity in traffic crash data [19, 20]. The full Bayes is a statistical inference method which is similar to empirical Bayes. However, this method uses the expected value and its variance to generate a predictive distribution of crash frequency [21]. Another advantage of this method is that CMFs can be determined using small sample size.

One of the disadvantages of the carefully designed observational before-after study method is that it fails to identify confounding factors [18]. Furthermore, the collection of traffic crash data after implementation could be time consuming and expensive [16]. The cross-sectional method is an observational study which isolates the magnitude of implementing a selected countermeasure upon crash frequencies from the effect of other treatments applied at the specific study regions in a prescribed time period. Researchers applied this method to calculate CMFs for the effects of lane width, shoulder width, and presence of edge-line marking for frontage roads, and median width for freeways and rural multilane highways [22]. However, the cross-sectional method sometimes overestimates the effect of the countermeasure due to the presence of confounding variables, whereas case-control method estimates the casual-effects while controlling impacts of confounding variables [23]. Although this method can be used to investigate the effect of multiple countermeasures, the data collection and sample selection become very complex in case of multiple countermeasures [24]. However, all these observational studies require high quality crash data of before and after implementation of countermeasures. To prove statistical significance, this data collection sometimes continues over multiple years. Table 1 presents the study duration of previous studies for developing different countermeasures' CMFs.

Recently, Banihashemi used four years rural highway crash data including about 5000 miles road geometry data and annual average daily traffic (AADT) and then proposed a heuristic method to calculate CMFs [33]. Researchers investigated the safety effectiveness of the seatbelt and driver training using cohort method [34]. The change in probability of crash occurring after implementation of countermeasure is estimated through the steps of this method. Meta-analysis

TABLE 1: Previous studies' duration for developing CMFs.

Study Region (State)	Proposed Countermeasure(s)	Years of Data Used	Reference
California, Colorado, Delaware, Maryland, Minnesota, Oregon, Washington	Centerline Rumble strips on Rural Two-Lane Roads (Principal arterial)	5 years prior & 3 years after	[25]
Wisconsin	Conversion of intersection into high speed roundabout on Rural and Urban (3-leg and 4-leg)	3 years prior & 2 years after	[26]
Connecticut	Installation of fluorescent curve signs on Urban and Rural Two-lane Roads	More than 10 years data	[27]
Louisiana	Impact of Edge on Narrow Two-Lane Undivided Rural Highway	3 years prior & 1 year after	[28]
Michigan, Minnesota, Washington, California	(i) Increase vertical grade by 1% on Two-Lane Rural Highway (ii) Convert minor road stop control to all-way stop (rural) (iii) Provide passing lane or climbing lane: Two-lane rural roads (iv) Increase/ Reduce shoulder width on Two-Lane Rural Roads (v) Changing from permissive to protected/ permissive or permissive/ protected phasing on 4-leg Urban signalized intersection	5 years prior & 3 years after	[29]
Texas	Modify lane width on Rural frontage roads (one & two way)	Several years	[30]
Florida	Installation of bicycle lanes on multilane urban roads	3 prior years & 2 years after	[16]
New York	(i) Increase cycle length for pedestrian crossing (ii) Install high visibility crosswalk (iii) Install traffic signal and provide split phase on 3-leg, 4-leg and more-leg urban signalized	5 years prior & 2 years after	[31]
Florida, Kentucky, Missouri, Pennsylvania	Installation of lane narrowing through rumble strips and painted median on undivided Rural roads (3-leg and 4-leg stop controlled)	5 years prior & 2 years after	[32]
Virginia	Installation of channelized separator islands on side road approaches with supplemental STOP signs on undivided Rural (4-leg stop controlled)	5 years prior & 2 years after	[32]

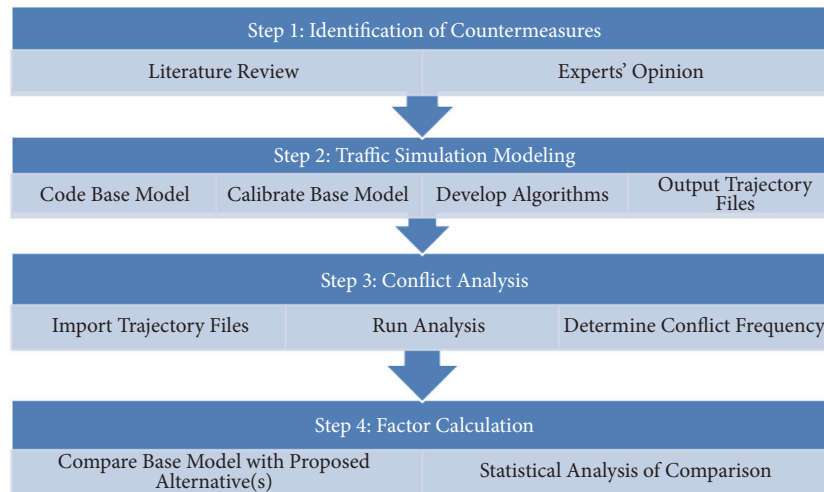


FIGURE 1: Proposed method for estimating CMFs.

method and expert panel survey were also proposed to estimate CMFs [35]. Furthermore, researchers have been exploring the global application of the HSM crash prediction algorithm, hence transferability of CMFs to different road networks in other countries, such as Italy, Canada, Denmark, Germany, and New Zealand [36]. However, Gettman and Head found that traffic simulation platforms could be potential resources for evaluating vehicle interactions regarding safety aspects [37]. Meanwhile, other researchers criticized this simulation-based approach arguing that built-in evasive algorithms in simulation platforms prevent modeling crash scenarios, and this can lead to the failure of developing the relation between risk behaviors and traffic crashes [38]. However, Sacchi et al. [39] utilized video based traffic conflict analysis and found similarity in results with previous observation study. Recently, Shahdah et al. [40] developed an integrated method by combining observational before-after method and simulation-based method and drew a conclusion that the estimated CMFs by using simulation could match with the outcomes of observational studies. However, this study failed to develop an independent system for estimating CMFs using simulation. Table 2 summarizes the methods used in previous studies and their limitations.

This paper aims to provide detailed step-by-step procedures for calculating CMFs of ITS countermeasures using simulation-based method and demonstrate the proof of concept in applying this method in real-world scenarios.

3. Proposed Method

A unique approach is proposed in this study, where estimation of CMFs could be conducted through four interconnected but distinct steps. The steps are (a) identification of countermeasures, (b) traffic simulation modeling, (c) conflict analysis, and (d) factor calculation. The overall method proposed in this research is illustrated in Figure 1.

To improve the safety aspects of a study location, the first step is to identify possible implementable countermeasures.

Previous studies on similar locations and experts' opinion can be used to identify countermeasures for the study location. Then the study site is modeled in traffic microsimulation software. It is important to note that several studies were conducted to evaluate the performances of traffic simulation modeling and study results showed that the simulation outputs were a statistically significant representation of the real-world [44]. However, the traffic simulation models need to be calibrated and validated using collected actual traffic data to mimic the real-world traffic operation [45]. In this study, the calibration is performed using real-world data and then the outputs from traffic microsimulation are considered as a satisfactory representation of the real-world. After developing base model, the necessary algorithms for simulation representation of proposed countermeasures are developed and coded. The simulations are run multiple times with different seed values to capture variability and initialize randomness in simulation traffic patterns [46]. The vehicle trajectory files, which is a binary file containing the course of vehicle positions in the simulation network, are generated while running the simulation model.

The next step is conflict analysis, where improvements in safety after implementing countermeasures can be inspected. Researchers defined conflict as an intersection of the trajectories of two or more vehicles and collision can happen if their movements remain unchanged [47]. After a thorough research on the relation between crash and conflicts, a conflict analysis tool called "Surrogate Safety Assessment Model (SSAM)" was developed by FHWA [48]. This conflict analysis tool uses the trajectory files imported from the runs of traffic microsimulation models. Five parameters are considered in SSAM tool to estimate the frequency of simulated conflicts; they are time-to-collision (TTC), postencroachment time (PET), deceleration rate (DR), maximum speed (MaxS), and speed difference (DeltaS). The threshold values of these parameters need to be adjusted with the driving behaviors of study locations. Then the number of conflicts is estimated by analyzing the trajectory files in SSAM tool. Figure 2 shows

TABLE 2: Summarization of methods used to estimate CMFs.

Strategies	Challenges	Proposed By
<i>Before-after Method</i>		
Naive before-after	(i) Simplest method, but fails to consider regression toward mean effect (ii) Overestimates results of countermeasure	Abdel-Aty et al., 2014 [16]
Before-after with comparison group	(i) Similar as Naïve before-after, it compares with untreated sites to reduce effects of external causal factors (ii) Fails to account naturally expected reduction in crashes, i.e. regression toward the mean effect (i) Captures a true effect of countermeasure by considering the regression to mean	Park & Abdel-Aty, 2016 [17]
Empirical Bayes	(ii) Lacks in considering uncertainty in data and model parameters (iii) Not flexible due to reliance on assumption of negative binomial distribution (iv) Affected significantly by site selection bias	Frank et al., 2010 [18], Park et al., 2016 [19], Zou et al., 2018 [20]
Full Bayes	(i) Application complexity and requires a high level of statistical training	El-Basyouny and Sayed, 2011 [21], Lord & Kuo, 2012 [41]
<i>Cross-sectional Method</i>	(ii) Fails to identify confounding factors and their impacts (i) Overestimates effect of countermeasure due to presence of confounding variables	Lord & Mannering, 2010 [22]
<i>Case-control Method</i>	(ii) Fails to omit unobserved heterogeneity (i.e. variable bias) (i) Control impacts of confounding variables	Fitzpatrick et al., 2008 [24], Gross & Donnell, 2011 [23]
<i>Cohort Method</i>	(ii) Data collection and sample selection are complex and time consuming (i) Requires a large distribution of samples data	Cummings et al., 2003 [34], Zhu et al., 2007 [42]
<i>Meta-analysis Method</i>	(ii) Changes in site parameters during study period impacts results of countermeasures (i) Recommended to perform sensitivity analysis to validate assumptions	Phillips et al., 2011 [35]
<i>Traffic Simulation</i>	(i) Built-in evasive algorithms in simulation platforms prevent modeling crash scenarios	Sacchi et al., 2013 [39], Shahdah et al., 2014 [40], Giuffrè et al., 2018 [43]

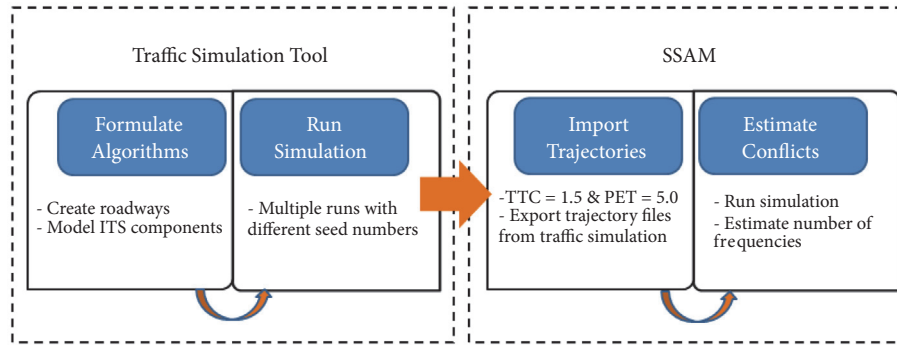


FIGURE 2: Integration platform of traffic simulation tool and SSAM.

the integration platform of traffic simulation software and the conflict analysis tool.

Finally, the numbers of conflicts calculated for base model (i.e., existing condition) and alternative models (i.e., proposed countermeasures) are compared to calculate the change in conflict frequency, i.e., CMFs after implementation of countermeasures. The following equation, proposed by [18], is utilized to estimate the CMFs of proposed countermeasures. A statistical analysis, Student's t-test, is performed to establish the statistical validation of calculated CMFs.

CMF

$$= \frac{\# \text{ of crashes after implementation of countermeasures}}{\# \text{ of crashes before implementation of countermeasures}} \quad (1)$$

4. Case Study for ITS Countermeasures

A case study was performed to validate the proposed simulation-based method and also to compute the values of CMFs when Intelligent Transportation Systems (ITS) countermeasures are being considered to lower crash severity and improve safety. Transportation professionals, automotive industry, and decision-makers throughout the world consider ITS measures as the viable solutions for traffic congestion reduction and safety improvement [49]. Researchers categorized different ITS measures into six major categories: advanced traffic management systems, advanced travelers information systems, commercial vehicles operation, advanced public transportation systems, advanced vehicles control systems, and advanced rural transports systems [49]. Examples of advanced traffic management systems include, but not limited to, ramp metering (RM), variable speed limit (VSL) assignments, junction controls (JC), dynamic lane assignment (DLA), automated warning system (AWS), arterial management (AM), traffic signal monitoring (TSM), road weather information system (RWIS), and incident monitoring (IM). In this research, RM, VSL, JC, and DLA were contemplated. The descriptions of these countermeasures are provided in Table 3.

There are multiple traffic simulation tools (e.g., VISSIM, Paramics, CORSIM, SimTraffic, and AIMSUN) currently available, which can be integrated with SSAM tool for safety evaluation. In this study, VISSIM was selected for modeling

ITS countermeasures as the corresponding software allows users to simulate user-defined driving behavior for modeling ITS equipment representations in simulation environment [50].

4.1. Traffic Simulation. In this study, a roadway segment of Interstate-76 (I-76), also known as Schuylkill Expressway, was modeled in microsimulation environment. This expressway has been experiencing significant traffic congestion since the traffic demand has almost doubled after the completion of this highway in 1960. A 15 mile long segment of I-76 (from the intersection of Schuylkill Expressway (I-76) and Pennsylvania Turnpike (I-276) to the intersection of Schuylkill Expressway (I-76) and U.S. Route-1) was coded in VISSIM simulation environment. In this network segment, 43% of total length had 2 lanes in both directions: 26% had 3 or more lanes and the rest had single lane roadway. Based on DVRPC's (Delaware Valley Regional Planning Commission) 2016 traffic counts dataset, the study site carried approximately 163,705 average annual daily traffic (AADT) in both directions [51]. In this study, morning rush hours (6:30 AM to 8:30 AM) traffic volumes were projected as simulation traffic volume over a period of two simulation hours. Researchers have utilized the peak hour volume(s) of study region for predicting crash frequency due to time consuming nature of the traffic simulation runs [52]. The results of simulation crash analysis using peak hour volume were utilized to develop statistically significant prediction models [53]. The traffic model was calibrated using observed speed distributions and travel time data collected from field visits. A map presenting the study area is shown in Figure 3.

After developing base model of the study area, ITS countermeasures were coded in simulation environment. As mentioned earlier, RM, VSL, JC, and DLA were contemplated in this study and programmed in four separate model files using VISSIM VAP (Vehicle Actuated Programming) platform. The authors proposed to replace 22 static speed limit signs in the study region by a variable speed limit system. Based on the downstream congestion level, the upstream speed limit will be adjusted to improve the safety of travelers. The speed limit values displayed in a variable speed limit system were assigned as speed distribution to grasp drivers' stochastic behaviors in simulation. For example, assume, due

TABLE 3: Description of proposed ITS countermeasures.

Countermeasures	Description	Equipment
Ramp Metering (RM)	Implementation of traffic control signals at freeway on-ramps that control the rate of vehicles entering the freeway	Detector, Ramp Signal
Variable Speed Limit (VSL) Assignments	Include implementation of communication platform to show the upstream drivers current advisory speed limit for certain time durations based on downstream congestion	Detector, VMS
Junction Controls (JC)	Regulate flow of traffic onto the mainline and facilitate ramp traffic to enter on freeway	Detector, VMS
Dynamic Lane Assignment (DLA)	Indicates downstream lane closures (due to congestion, accidents, work zones, or debris) and facilitates upstream drivers to change lane in advance	Detector, VMS

* VMS: variable message signs.

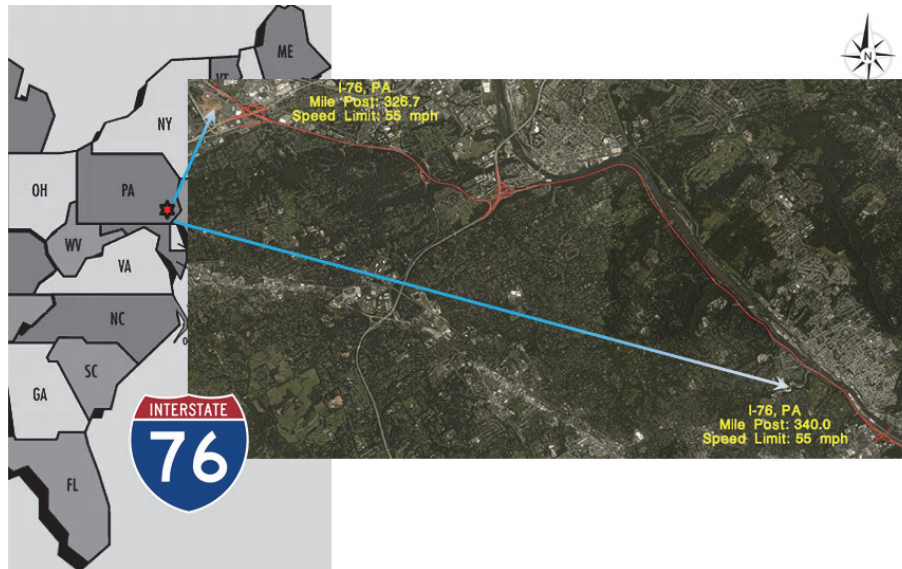


FIGURE 3: Study area, I-76 (source: Microsoft's Bing Maps).

to downstream congestions, the speed limit for upstream segment was estimated to 45 mph. Then 22% of all vehicles crossing the speed limit display will maintain a speed between 38 and 42.5 mph. Another 42% will drive at a speed between 42.5 and 47 mph, and the remaining will continue between 47 and 55 mph. Three ramp meters were recommended to implement on three entrance ramps along the study corridor. For each simulation model scenario (base model and four alternatives' models), 10 simulation runs were generated with linearly incremented random seed values starting from 5 and ending at 45. As a result, each simulation model yielded 10 trajectory files to be exported into SSAM tool.

4.2. Conflict Simulation. Calibration of SSAM model is essential for integration of the real-world time-space distributions for the safety evaluation. This calibration task is conducted by adjusting its five parameters (i.e., time-to-collision (TTC), postencroachment time (PET), deceleration rate (DR), maximum speed (MaxS), and speed difference (DeltaS)) based on field collected data. Researchers found that the threshold values of SSAM parameters could vary depending on many factors, i.e., time of day, highway geometry, driving behavior, and drivers' age [54]. For example, TTC threshold could be lower when significant numbers of the drivers in study area are more likely to drive aggressively, i.e., urban highways. However, due to data unavailability, SSAM model was not calibrated in this study. The default values of TTC and PET are 1.5 sec and 5.0 sec, respectively, which means when $TTC \leq 1.5$ sec and $PET \leq 5.0$ sec, this tool considers the events as the possibility of potential conflicts. These default values of TTC and PET are utilized by many other researchers [55] and thus applied in this study. Furthermore, there are three types of conflicts considered in SSAM tool. These types of conflicts are separated based on the conflict angles between the vehicles. They are (a) crossing collisions (when conflict angle between vehicles $> 85^\circ$), (b)

rear end collisions (when conflict angle $< 30^\circ$), and (c) lane-changing conflicts (when conflict angle $\geq 30^\circ$ and conflict angle $\leq 85^\circ$).

The trajectory files imported from five VISSIM simulation models were analyzed in SSAM tool. The estimated total conflicts for each model were distinguished into three conflicts types, i.e., crossing collisions, rear end collisions, and lane-changing conflicts. Each type of conflicts was averaged over 10 runs for base model and four alternatives. The comparisons of the estimated conflicts between base model and different ITS alternatives are shown in Figure 4.

5. Results and Discussion

There were 40,332 total conflicts (i.e., traffic crashes) identified after analyzing base model. Each conflict was then categorized based on its conflict angle between vehicles. It was found that among the total of 40,332 conflicts there were 7,304 crossing conflicts, 12,914 lane change conflicts, and 20,114 rear end conflicts. However, after implementing Ramp Metering, the crossing conflicts increased by about 1,300, while other two conflict types were decreased from base scenario. Total 39,045 conflicts were found after implementing RM. The deployment of JC reduced the total number of conflicts from base condition by around 250 conflicts. Other ITS countermeasure, DLA reduced all types of conflicts from the existing conditions. However, the number of identified conflicts after implementation of VSL was found higher than base model, since lane change and rear end conflicts were increased by around 3,300 conflicts. Dynamic changes of speeds, i.e., speed limit of road segment, within a short time interval (each 15-minute interval) could be the reason of increasing conflict frequencies in simulation models. This sudden change provoked the drivers in simulation to perform lane change more frequently than before. As a result, the

TABLE 4: Conflict reduction percentage after implementation of ITS countermeasures.

Countermeasures	Total Conflicts	% Conflicts Reduction*
Base Model	40,332	--
Alt 1: Ramp Metering	39,045	3.2%
Alt 2: Variable Speed Limit Assignments	43,543	- 7.9%
Alt 3: Junction Controls	40,083	0.6%
Alt 4: Dynamic Lane Assignment	38,267	5.1%

* Negative percentage of conflict represents the increase of conflicts after countermeasure implementation.

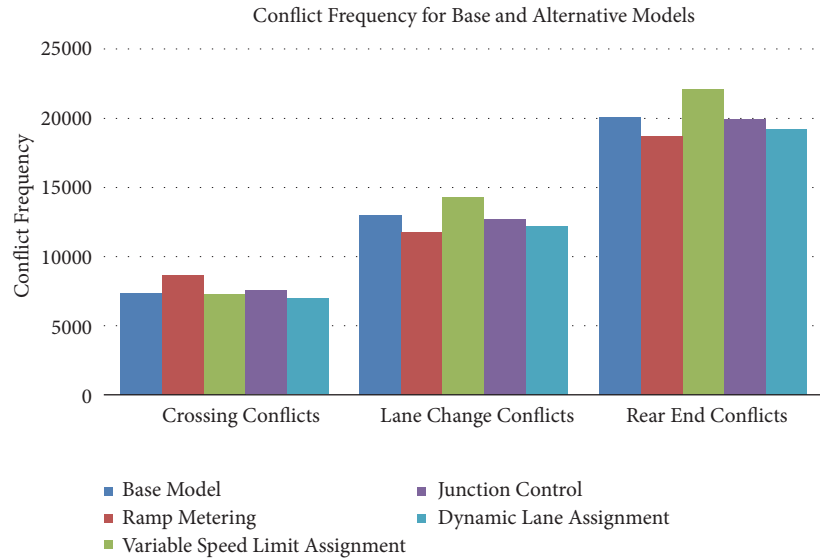


FIGURE 4: Conflict frequency for base model and proposed ITS countermeasures.

number of lanes change and rear end conflicts were increased after DLS implementation. The total conflicts after implementation of these four ITS countermeasures were compared with base model. The percentage changes of conflicts from base model are tabulated in Table 4.

It is found that the number of injurious crashes could be reduced by 3.20%, 0.60%, and 5.10% from the base scenario after implementing RM, JC, and DLA, respectively. However, conflict frequencies were increased by 7.90% after implementing VSL. Finally the CMF values for these proposed ITS countermeasures were calculated. The calculated CMFs would be 0.97, 0.99, 0.95, and 1.08 after accomplishing RM, JC, DLA, and VSL on the roadways in selected study region, respectively.

6. Validation of Proposed Method

It is recommended that the proposed method needs to be validated either qualitatively or quantitatively. Qualitative validation examines the relationship between output(s) and variables, where quantitative validation compares the predicted values of output(s) against the values of similar output(s) calculated using a well-established method. In this study, a quantitative approach was applied during the validation process by comparing the calculated CMFs with the values estimated in previous research studies. Though,

the technological feasibility of DLA and JC is under thorough investigations till today and they are not installed in different areas. So, there is limitation of crash data availability to validate the calculated CMFs of these two countermeasures. But the validation of other two countermeasures, i.e., RM and VSL, was performed in this study.

Researchers evaluated the safety effects of ramp meter implementation on a 9.2 miles segment of I-880 in Hayward, California [56]. They utilized a crash prediction model developed by Lee et al. (2002) [57] where the crash frequency was estimated using traffic flow characteristics of the study region. It was found that 5% of total crashes could be eliminated after implementation of ramp metering on the segment of I-880. Kansas Department of Transportation (KDOT) conducted a safety evaluation of its ramp meters in 2010, and it was found that the crash rate dropped by 24% on roads where ramp meter was implemented earlier on I-435 [58]. While they performed an observational before-after study to evaluate the ramp meters, there was no statistical evidence to validate the result of the study. Recently Chen et al. (2016) utilized a hypothetical traffic network to inspect the influence of ramp metering on safety improvement and observed 1.65% of the total crashes reduced after application of ramp metering [59]. Another research [60] was conducted to investigate the application of variable speed limits using the same crash prediction model developed by Lee et al. (2002). After analysis,

TABLE 5: Validation of proposed simulation-based method for estimating CMFs.

Countermeasures		Using	Using crash	Percentage error
		simulation-based method proposed in this paper	prediction model	
Ramp Metering: Study 1 [56]	% Reduction	3.2%	5%	--
	CMF	0.97	0.95	2.1%
Ramp Metering: Study 2 [59]	% Reduction	3.2%	1.65%	--
	CMF	0.97	0.98	1.0%
Variable Speed Limit Assignment: Study 3 [60]	% Reduction	7.9%	3.14~4.94%	--
	CMF	1.08	1.04	3.8%
Variable Speed Limit Assignment: Study 4 [61]	% Reduction	7.9%	24.0%	--
	CMF	1.08	0.76	42.0%

the researchers concluded that the variable speed limit could increase the crash potential when duration of intervention is low; i.e., frequency of speed limit changes. They found that variable speed limit could increase traffic crash by 3.14 to 4.94% depending on variations in road geometry. Saha et al. (2015) examined variable speed limits implemented in Wyoming and suggested that these variable speed limits could reduce crashes by minimum 24% [61]. However the scope of this study was limited, and researchers only considered crashes that occurred during adverse weathers. These results were compared with the estimated CMFs using proposed simulation-based method. For this purpose, the percentage error was calculated using the equation given below:

$$\text{Percentage error (\%)} = \left| \frac{\text{estimated value} - \text{theoretical value}}{\text{theoretical value}} \right| \times 100 \quad (2)$$

Table 5 represents the comparison between proposed method and crash prediction model. For calculating percentage error, the CMFs estimated using proposed simulation-based method were considered as “estimated value”. On the other hand, the similar values calculated using crash prediction model, i.e., developed by Lee et al. (2002), were tagged as “theoretical value”, since the authors utilized these values as references for validation. In Table 5, it is shown that CMFs calculated using proposed simulation-based method were slightly different than the same values calculated using crash prediction model, except study 4 cited for variable speed limit implementation. The percentage error for ramp meter was found to be 2.1% and 1.0% based on the data collected from study 1 and study 2, respectively. On the other hand, this percentage error for variable speed limit was 3.8% based on study 3. However, an error value of 42% was estimated in case of study 4. This significant difference between CMF values estimated using simulation-based method and crash prediction model could happen due to the limited number of crashes examined in study 4, since that study considered only crashes that occurred in adverse weathers.

7. Conclusion

Development of CMFs could be useful for the practitioners to perform safety evaluation, since significant statistical knowledge is required for utilizing HSM practically. The proposed simulation-based approach for estimating CMFs will provide a vital tool to them and assist them in traffic safety management. The application of this method could reduce the time dependency of developing CMFs over conventional observational method. Another benefit of using the proposed method is to achieve the ability of investigating the combined effect of multiple countermeasures. At present, the expected combined effects, i.e., combined CMF, are calculated by combining (for example: multiplication) the individual CMFs of proposed multiple countermeasures. Though, the validity of this method has not rigorously investigated. The simulation-based method proposed in this study can be used to model multiple countermeasures in simulation environment and evaluate their combined safety effect. Furthermore, traditional method of safety evaluation requires installation of countermeasures at crash prone locations, and the installation of ITS countermeasures could demand a “significant” investment. But the proposed simulation-based method could be used for evaluating ITS countermeasures before implementation at crash prone locations. As a result, potential errors in design could be avoided during planning stage. Additionally the impacts of geometric changes, for example, implementation of bus priority lanes [62], could be evaluated using proposed microsimulation method. Also, the proposed method could be utilized to validate existing CMFs for local representation, a validation process recommended by AASHTO [36]. As a result, the practitioners can comfortably transfer the prior developed CMFs and apply those at different problematic regions.

In this study, the proposed simulation-based approach was used to calculate CMFs for four ITS countermeasures: ramp metering, variable speed limit assignment, junction control, and dynamic lane assignment. These countermeasures were coded in traffic simulation environment. The simulation models were run to generate the trajectory files including binary information of the course of vehicles in simulation. Then these trajectory files were imported to

SSAM tool. In SSAM tool, the default values of TTC (= 1.5 sec) and PET (= 5.0 sec) were utilized to analyze the trajectory files. After analyzing, it is found that except variable speed limit assignment the proposed ITS countermeasures could reduce the number of crashes at crash prone location. Finally the CMFs for ramp metering, variable speed limit assignment, junction control, and dynamic lane assignment were estimated as 0.97, 1.08, 0.99, and 0.95, respectively.

7.1. Limitations of This Research. Even though the proposed approach could be performed in less time duration than current practices, the success of estimating CMFs using this method depends on the calibration of both traffic simulation and SSAM models. Another limitation of this method was lack of crash severity prediction. SSAM tool cannot draw a relation between trajectory information and severity of crashes due to evasive measures of traffic simulation. In this study, the traffic simulation model was calibrated, though SSAM model was not calibrated due to data unavailability. Furthermore, default thresholds of parameters were utilized. It is recommended to evaluate the change in conflict frequency with respect to change in these parameter values. The outcomes of the proposed method were compared with the CMF values developed for the proposed ITS countermeasures implemented in different study sites. However, the proposed method could not be validated with real-world traffic crash data of the study location, since the proposed countermeasures were in concept development stage at the time of this paper publication. As a result, the spatial dependency could not be evaluated in this study, and furthermore different time frames, i.e., midday rush hours, afternoon rush hours, and weekends traffic, were not modeled other than morning rush hours.

In future, the crash frequencies estimated using SSAM will be compared with available real-world crash records to validate the implementation of selected ITS countermeasures in the study region. Furthermore, a methodology will be developed to determine crash severity based on TTC, DR, and DeltaS thresholds.

Data Availability

The data used in this study were provided by Delaware Valley Regional Planning Commission (DVRPC). The traffic simulation models and codes developed by authors to support the findings of this study are available from the corresponding author upon request.

Disclosure

All opinions, findings, and conclusions or recommendations presented in this paper are those of the authors and do not necessarily reflect the views of the U.S. Department of Transportation Region 2 University Transportation Research Center (UTRC2), or Delaware Valley Regional Planning Commission (DVRPC).

Conflicts of Interest

The authors declare that they have no conflicts of interest.

Acknowledgments

The research was partially supported by U.S. Department of Transportation Region 2 University Transportation Research Center (UTRC2). The authors want to thank Delaware Valley Regional Planning Commission (DVRPC) for providing data required for traffic simulation modeling.

References

- [1] J. M. Owens, J. F. Antin, Z. Doerzaph, and S. Willis, "Cross-generational acceptance of and interest in advanced vehicle technologies: A nationwide survey," *Transportation Research Part F: Traffic Psychology and Behaviour*, vol. 35, pp. 139–151, 2015.
- [2] NHTSA, "2016 motor vehicle crashes: overview (traffic safety facts)," Publication DOT HS 812 246, 2017.
- [3] X. Pei, S. C. Wong, and N. N. Sze, "A joint-probability approach to crash prediction models," *Accident Analysis & Prevention*, vol. 43, no. 3, pp. 1160–1166, 2011.
- [4] F. Basso, L. J. Basso, F. Bravo, and R. Pezoa, "Real-time crash prediction in an urban expressway using disaggregated data," *Transportation Research Part C: Emerging Technologies*, vol. 86, pp. 202–219, 2018.
- [5] AASHTO, *Highway Safety Manual*, American Association of State Highway and Transportation Officials, 2010.
- [6] Y. Chen and B. Persaud, "Methodology to develop crash modification functions for road safety treatments with fully specified and hierarchical models," *Accident Analysis & Prevention*, vol. 70, pp. 131–139, 2014.
- [7] FHWA, "Crash modification factors clearinghouse," 2014.
- [8] J. Ma, K. M. Kockelman, and P. Damien, "A multivariate Poisson-lognormal regression model for prediction of crash counts by severity, using Bayesian methods," *Accident Analysis & Prevention*, vol. 40, no. 3, pp. 964–975, 2008.
- [9] J. Park, M. Abdel-Aty, J.-H. Wang, and C. Lee, "Assessment of safety effects for widening urban roadways in developing crash modification functions using nonlinearizing link functions," *Accident Analysis & Prevention*, vol. 79, article no. 3753, pp. 80–87, 2015.
- [10] J. Park, M. Abdel-Aty, J. Lee, and C. Lee, "Developing crash modification functions to assess safety effects of adding bike lanes for urban arterials with different roadway and socio-economic characteristics," *Accident Analysis & Prevention*, vol. 74, pp. 179–191, 2015.
- [11] J.-H. Wang, M. A. Abdel-Aty, J. Park, C. Lee, and P.-F. Kuo, "Estimating safety performance trends over time for treatments at intersections in Florida," *Accident Analysis & Prevention*, vol. 80, pp. 37–47, 2015.
- [12] J. Park, M. Abdel-Aty, and J. Lee, "Use of empirical and full Bayes before–after approaches to estimate the safety effects of roadside barriers with different crash conditions," *Journal of Safety Research*, vol. 58, pp. 31–40, 2016.
- [13] J. Park and M. Abdel-Aty, "Development of adjustment functions to assess combined safety effects of multiple treatments on rural two-lane roadways," *Accident Analysis & Prevention*, vol. 75, pp. 310–319, 2015.

- [14] B. Brimley, M. Saito, and G. Schultz, "Calibration of highway safety manual safety performance function," *Transportation Research Record*, no. 2279, pp. 82–89, 2012.
- [15] J. Fink, V. Kwizile, and J.-S. Oh, "Quantifying the impact of adaptive traffic control systems on crash frequency and severity: Evidence from Oakland County, Michigan," *Journal of Safety Research*, vol. 57, pp. 1–7, 2016.
- [16] M. A. Abdel-Aty, J. Park, J.-H. Wang, and M. Abuzwidah, *Validation and Application of Highway Safety Manual (Part D) and Developing Florida CMF Manual, Phase 2*, 2014.
- [17] J. Park and M. Abdel-Aty, "Evaluation of safety effectiveness of multiple cross sectional features on urban arterials," *Accident Analysis & Prevention*, vol. 92, pp. 245–255, 2016.
- [18] F. Gross, P. Bhagwant, and C. Lyon, *A Guide to Developing Quality Crash Modification Factors*, Federal Highway Administration, Washington, DC, USA, 2010.
- [19] B.-J. Park, D. Lord, and L. Wu, "Finite mixture modeling approach for developing crash modification factors in highway safety analysis," *Accident Analysis & Prevention*, vol. 97, pp. 274–287, 2016.
- [20] Y. Zou, J. E. Ash, B.-J. Park, D. Lord, and L. Wu, "Empirical Bayes estimates of finite mixture of negative binomial regression models and its application to highway safety," *Journal of Applied Statistics*, vol. 45, no. 9, pp. 1652–1669, 2018.
- [21] K. El-Basyouny and T. Sayed, "A full Bayes multivariate intervention model with random parameters among matched pairs for before-after safety evaluation," *Accident Analysis & Prevention*, vol. 43, no. 1, pp. 87–94, 2011.
- [22] D. Lord and F. Mannering, "The statistical analysis of crash-frequency data: a review and assessment of methodological alternatives," *Transportation Research Part A: Policy and Practice*, vol. 44, no. 5, pp. 291–305, 2010.
- [23] F. Gross and E. T. Donnell, "Case-control and cross-sectional methods for estimating crash modification factors: Comparisons from roadway lighting and lane and shoulder width safety effect studies," *Journal of Safety Research*, vol. 42, no. 2, pp. 117–129, 2011.
- [24] K. Fitzpatrick, D. Lord, and B.-J. Park, "Accident modification factors for medians on freeways and multilane rural highways in Texas," *Transportation Research Record*, vol. 2083, pp. 62–71, 2008.
- [25] B. N. Persaud, R. A. Retting, and C. A. Lyon, "Crash reduction following installation of centerline rumble strips on rural two-lane roads," *Accident Analysis & Prevention*, vol. 36, no. 6, pp. 1073–1079, 2004.
- [26] D. Zheng, X. Qin, R. Tillman, and D. A. Noyce, "Measuring modern roundabout traffic conflict exposure," *Journal of Transportation Safety & Security*, vol. 5, no. 3, pp. 208–223, 2013.
- [27] J. B. R. Srinivasan, D. Carter, P. Bhagwant et al., "Safety evaluation of improved curve delineation," Publication FHWA-HRT-09-045, 2009.
- [28] X. Sun and S. Das, "Safety improvement from edge lines on rural two-lane highways," Publication FHWA/LA.11/487, 2012.
- [29] D. W. Harwood, F. M. Council, E. Hauer, W. E. Hughes, and A. Vogt, *Prediction of The Expected Safety Performance of Rural Two-Lane Highways*, Midwest Research Institute, Kansas City, Miss, USA, 2000.
- [30] D. Lord and J. A. Bonneson, "Development of accident modification factors for rural frontage road segments in Texas," *Transportation Research Record*, no. 2023, pp. 20–27, 2007.
- [31] L. Chen, C. Chen, and R. Ewing, "The relative effectiveness of signal related pedestrian countermeasures at urban intersections—Lessons from a New York City case study," *Transport Policy*, vol. 32, pp. 69–78, 2014.
- [32] FHWA, "Two low-cost safety concepts for two-way stop-controlled, rural intersections on high-speed two-lane, two-way roadways," 2008.
- [33] M. Banihashemi, "Highway safety manual, new model parameters vs. calibration of crash prediction models," in *Proceedings of the Moving Toward Zero: 2011 ITE Technical Conference and Exhibit*, Lake Buena Vista, FL, USA, 2011.
- [34] P. Cummings, B. McKnight, and N. S. Weiss, "Matched-pair cohort methods in traffic crash research," *Accident Analysis & Prevention*, vol. 35, no. 1, pp. 131–141, 2003.
- [35] R. O. Phillips, P. Ulleberg, and T. Vaa, "Meta-analysis of the effect of road safety campaigns on accidents," *Accident Analysis & Prevention*, vol. 43, no. 3, pp. 1204–1218, 2011.
- [36] E. Sacchi, B. Persaud, and M. Bassani, "Assessing international transferability of highway safety manual crash prediction algorithm and its components," *Transportation Research Record*, no. 2279, pp. 90–98, 2012.
- [37] D. Gettman and L. Head, "Surrogate safety measures from traffic simulation models," *Transportation Research Record*, no. 1840, pp. 104–115, 2003.
- [38] A. P. Tarko, "Use of crash surrogates and exceedance statistics to estimate road safety," *Accident Analysis & Prevention*, vol. 45, pp. 230–240, 2012.
- [39] E. Sacchi, T. Sayed, and P. Deleur, "A comparison of collision-based and conflict-based safety evaluations: The case of right-turn smart channels," *Accident Analysis & Prevention*, vol. 59, pp. 260–266, 2013.
- [40] U. Shahdah, F. Saccomanno, and B. Persaud, "Integrated traffic conflict model for estimating crash modification factors," *Accident Analysis & Prevention*, vol. 71, pp. 228–235, 2014.
- [41] D. Lord and P.-F. Kuo, "Examining the effects of site selection criteria for evaluating the effectiveness of traffic safety countermeasures," *Accident Analysis & Prevention*, vol. 47, pp. 52–63, 2012.
- [42] M. Zhu, P. Cummings, H. Chu, and L. J. Cook, "Association of rear seat safety belt use with death in a traffic crash: A matched cohort study," *Injury Prevention*, vol. 13, no. 3, pp. 183–185, 2007.
- [43] O. Giuffrè, A. Granà, M. L. Tumminello et al., "Evaluation of roundabout safety performance through surrogate safety measures from microsimulation," *Journal of Advanced Transportation*, vol. 2018, pp. 1–14, 2018.
- [44] G. Gomes, A. May, and R. Horowitz, "Calibration of VISSIM for a congested freeway," in *California PATH Program*, p. 46, Institute of Transportation Studies, California, CA, USA, 2004.
- [45] H. Mahmassani, T. Hou, and J. Dong, "Characterizing travel time variability in vehicular traffic networks: deriving a robust relation for reliability analysis," *Transportation Research Record: Journal of Transportation Research Board*, no. 2315, pp. 141–152, 2012.
- [46] P. Das, *Risk analysis of autonomous vehicle and its safety impact on mixed traffic stream [Msc. thesis]*, Civil and Environmental Engineering, No. Master of Science, Rowan University, 2018.
- [47] F. Amundsen and C. Hyden, *Proceedings of the First Workshop on Traffic Conflicts: Oslo 77*, Norwegian Council for Scientific and Industrial Research, 1977.
- [48] L. Pu and R. Joshi, *Surrogate Safety Assessment Model (SSAM): Software User Manual*, Federal Highway Administration, McLean, Va, USA, 2008.

- [49] T. G. Crainic, M. Gendreau, and J.-Y. Potvin, "Intelligent freight-transportation systems: Assessment and the contribution of operations research," *Transportation Research Part C: Emerging Technologies*, vol. 17, no. 6, pp. 541–557, 2009.
- [50] PTVGroup, *PTV Vissim Version 8*, PTV Group, 2015.
- [51] DVRPC, "Traffic volume counts," 2017.
- [52] T. Saleem, B. Persaud, A. Shalaby, and A. Ariza, "Can microsimulation be used to estimate intersection safety?" *Transportation Research Record: Journal of the Transportation Research Board*, vol. 2432, no. 1, pp. 142–148, 2018.
- [53] L. Li, B. Persaud, and A. Shalaby, "Using micro-simulation to investigate the safety impacts of transit design alternatives at signalized intersections," *Accident Analysis & Prevention*, vol. 100, pp. 123–132, 2017.
- [54] R. J. Kiefer, C. A. Flannagan, and C. J. Jerome, "Time-to-collision judgments under realistic driving conditions," *Human Factors: The Journal of the Human Factors and Ergonomics Society*, vol. 48, no. 2, pp. 334–345, 2006.
- [55] F. Huang, P. Liu, H. Yu, and W. Wang, "Identifying if VISSIM simulation model and SSAM provide reasonable estimates for field measured traffic conflicts at signalized intersections," *Accident Analysis & Prevention*, vol. 50, pp. 1014–1024, 2013.
- [56] C. Lee, B. Hellinga, and K. Ozbay, "Quantifying effects of ramp metering on freeway safety," *Accident Analysis & Prevention*, vol. 38, no. 2, pp. 279–288, 2006.
- [57] C. Lee, F. Saccomanno, and B. Hellinga, "Analysis of crash precursors on instrumented freeways," *Transportation Research Record*, no. 1784, pp. 1–8, 2002.
- [58] KDOT, "Ramp metering 2010 evaluation report: maximizing the flow," 2011.
- [59] X. Chen, O. Salem, and B. Salman, "Life-cycle benefit-cost analysis framework for ramp-metering deployments," *Transportation Research Record: Journal of the Transportation Research Board*, vol. 2554, pp. 69–76, 2016.
- [60] C. Lee, B. Hellinga, and F. Saccomanno, "Assessing safety benefits of variable speed limits," *Transportation Research Record*, no. 1897, pp. 183–190, 2004.
- [61] P. Saha, M. M. Ahmed, and R. K. Young, "Safety effectiveness of variable speed limit system in adverse weather conditions on challenging roadway geometry," *Transportation Research Record*, vol. 2521, pp. 45–53, 2015.
- [62] K. Goh, G. Currie, M. Sarvi, and D. Logan, "Experimental microsimulation modeling of road safety impacts of bus priority," *Transportation Research Record*, no. 2402, pp. 9–18, 2014.

Research Article

Drivers' Perceptions of Smartphone Applications for Real-Time Route Planning and Distracted Driving Prevention

Khaled Shaaban 

Associate Professor, Department of Civil Engineering/Qatar Transportation and Traffic Safety Center, Qatar University, P.O. Box 2713, Doha, Qatar

Correspondence should be addressed to Khaled Shaaban; kshaaban@qu.edu.qa

Received 25 May 2018; Revised 30 November 2018; Accepted 12 February 2019; Published 11 March 2019

Guest Editor: Mihai Dimian

Copyright © 2019 Khaled Shaaban. This is an open access article distributed under the Creative Commons Attribution License, which permits unrestricted use, distribution, and reproduction in any medium, provided the original work is properly cited.

Given the increasing importance and availability of traffic-related smartphone applications, understanding their potential use is vital, especially in developing countries. This research explores motorist perceptions of the installation and use of two smartphone applications—a distraction-prevention application and a real-time traffic information and navigation application—in Qatar, a rapidly developing country in the Arabian Gulf region. This study represents the first attempt to investigate the potential market for these types of applications in a region with a unique social and cultural environment. A questionnaire-based survey was conducted to examine the drivers' interest in using both applications, their willingness to buy the applications, and their data privacy concerns. The results indicated that the potential market for these types of smartphone applications in Qatar is high. The potential for the real-time route planning application was found to be much higher than that of the antidistracted application, especially among female drivers. A high percentage of the drivers, especially younger and local drivers, were less enthusiastic about installing and using the distracted driving prevention application. Most of the participants willing to use both smartphone applications did not have data privacy concerns, but in return for allowing the applications to access their data, they expected some reduction in travel time and a safer trip. These findings provide a direction for the development of future policies and smart solutions in this region.

1. Introduction

With the high increase in the use of smartphones and mobile applications, more drivers are taking more risks by utilizing their mobile phones while driving [1, 2]. Qatar, a wealthy and rapidly developing country, is first among Arab countries and second in the world (behind only South Korea) in terms of engagement with mobile services and applications [3]. The continuous growth in mobile phone usage in Qatar is due to its consumers' high purchasing power. This high level of mobile phone ownership contributes to the high rate of mobile phone use while driving in Qatar [4]. Over the past few decades, Qatar has had a huge increase in the number of vehicles, traffic violations, and collisions; many of these are fatal, and they aggravate congestion problems on road networks [5].

Therefore, it is necessary to find new solutions to improve driver safety and network efficiency in Qatar. Throughout the

last decade, there has been an increase in the use of traffic-related smartphone applications. These types of applications have made an astonishing difference in the way information is transmitted to people, making them better informed about traffic conditions and helping them make safer, faster, and smarter use of transportation networks. Given the increasing availability of smartphone applications and the potential for this technology to improve traffic safety and efficiency in Qatar, this study aims to examine public perception of different types of smartphone traffic applications, which is timely and much-needed information.

Two types of smartphone applications were investigated. The first application aims at assisting drivers by providing a navigation system and real-time information about traffic conditions to improve motorway efficiency, and the second aims to restrict mobile phone usage while driving to improve drivers' behavior and provide a safe trip. The investigation of two applications that serve different functions was important

to investigate the drivers' interest in and perspective towards two different issues: traffic safety and time-saving. This study represents the first attempt to investigate the public perception of these types of applications in this region.

2. Related Work

Smartphone applications have increasingly been utilized for different applications in transportation. In the area of navigation, different smartphone applications are available in the market to help the drivers by displaying their existing locations and directing them to their target locations using voice information in different languages, graphics, and text. Drivers can save time and fuel by using these navigation systems, especially when in an unknown area. Lee and Cheng [7] examined the navigation performance of drivers using smartphone applications and those using printed directions. They found better driving performance and increased efficiency when drivers used a smartphone application for navigation. The benefits are even more significant if the applications can provide real-time information about impending traffic conditions, which also has clear links to reducing congestion.

A study investigated route choice behavior in the case of a traffic information system using revealed-preference data. The study revealed that different factors affected the decisions of the drivers, including the characteristics of the trip; the perceptions of the traffic reports reliability [8]. Another study shows that providing high-quality information has a high impact on the compliance behavior of the drivers [9]. A study investigated the impact of real-time traffic information on traveler behavior by using repeated day-to-day revealed-preference observations. It was found that the drivers who received access to real-time traffic information through their smartphone reacted to the daily variations in travel times stronger than the way they reacted in the before case (without traffic information). The results indicated that providing real-time traffic information affects driver behavior [10].

Despite the abovementioned advantages of mobile phones in the area of navigation and real-time traffic information, some activities associated with the mobile phone use can distract a driver or a pedestrian. These activities include talking, dialing, browsing, texting, hanging up a call, reaching for the phone, picking up a dropped phone, dialing, or answering the phone. These types of activities cause drivers to take their hands off the steering wheel and both drivers and pedestrians to take their eyes off of the road. These types of inattention are the primary causes of crashes. An estimated 20% to 30% of all road crashes occurred because of driver distraction [11]. Furthermore, the risk of being involved in a traffic collision is four times higher in the case of using a mobile phone while driving [12]. Even receiving a mobile phone notification without interacting with the phone was found to significantly disrupt the performance of the driver [13].

Many applications are available to restrict the mobile phone use while driving. Some applications work automatically by detecting the movement of the car, then different actions can be taken after that. For example, calls can

be automatically sent to voicemail, access to the keyboard and screen can be blocked, or all notifications including alerts, texts, emails, and incoming calls can be blocked. Other applications are less sophisticated and require the driver input. In this case, the driver has to enable it every time before driving. Some applications restrict the use of mobile phones in addition to other equipment in the car. Other applications promote hands-free usage as a solution [14–20].

There are also other applications related to road safety. For speed detection, a smartphone application collects speed and location data. If the driver increases the speed near a school zone, a sound alarm will be triggered [21]. For drunk driving, a smartphone application calculates the different accelerations of the vehicle and then compares them with a typical drunk driving pattern stored on the application. If a match is confirmed, the phone will automatically alert the driver or call the police to seek help before being involved in a crash [22]. For pedestrians, a smartphone application is able to detect the approaching vehicles when pedestrians use their phones while walking using the back camera of the phone. The application alerts the pedestrian in case of anticipated conflict with an approaching vehicle [23].

In summary, no studies in the literature have investigated the willingness of drivers to install these types of applications. Furthermore, no studies were conducted throughout the Arabian Gulf region where the drivers have different culture, language, and habits. Given the increasing availability of smartphone applications and the potential for technology to improve traffic safety and efficiency in Qatar, the present study aims to examine the public perception of two different smartphone applications. The first application aims to assist drivers by improving motorway efficiency by providing real-time information on the traffic conditions, and the latter aims at restricting smartphone usage to improve the driver behavior.

3. Smartphone Traffic Applications in Transportation

3.1. Smartphone Applications for Navigation and Real-Time Route Planning. Smartphone applications have increasingly been utilized for navigation purposes. This type of applications helps drivers by displaying their existing locations and directing them to their target locations using voice information in different languages, graphics, and text. Many drivers receive driving directions using their mobile phones. Many free services currently exist to provide drivers with navigation directions, including Google Maps, Waze, and MapQuest. Paid applications include Navigon, Sygic, and MapsWithMe Pro. Drivers can also save time and fuel by using these navigation systems when in an unknown area. These systems have additional benefits, including improving driving performance. This is true even for those with small display screens. The benefits are even more significant if the applications can provide real-time information about impending traffic conditions, which also has clear links to reducing congestion. Different applications currently offer

this service. For example, INRIX Traffic provides a color-coded signal of existing traffic conditions versus the typical traffic and an indication to recommend the best time to travel. It depends on users to improve its data and to provide updates to fellow users on topics such as police presence, accidents, and incorrect traffic assessments. The application is free, but users have to pay if they want to use the route planning features [24].

3.2. Smartphone Application for Distracted Driving Prevention. Many applications are available to reduce the mobile phone use while driving. Some applications work automatically by detecting the movement of the car. For example, Spring's Driver First application is a monthly paid smartphone application that locks phones when a car is moving faster than 10 mph, using the phone's accelerometer but not GPS to prevent battery drain. This application is targeted at parents who want to enable restrictions on their driving-age children. When using the application, calls are automatically sent to voicemail. Audio tones for email and text messages are silenced. The application also triggers autoreply messages. When the application detects that the vehicle has stopped moving for a few minutes (i.e., not at stop signs or traffic lights), all phone functions return to normal automatically. The device can be unlocked by using the exit and 911 buttons, which can override the application, but parents can choose to be notified when this occurs [25]. Another application with similar capabilities is bSafeMobile. This application identifies the driving condition and then automatically switches the device to safe mode. During this stage, access to the keyboard and screen is blocked. Furthermore, all notifications and alerts, texts, emails, and incoming calls are blocked [26].

Other applications are less sophisticated and require driver input. For example, DriveMode is a free application that helps to keep drivers' attention on the road, but the driver has to enable it every time before driving. It automatically replies to any incoming text messages; silences audio tones for texts, emails, and phone calls; and blocks web browsing and outgoing phone calls [27]. Some applications restrict the use of mobile phones in addition to other equipment in the car. For example, Cellcontrol uses Bluetooth-enabled technology in the vehicle instead of using GPS to detect vehicle movements and then apply the policy. Cellcontrol prevents distracted driving by disabling mobile phones and also mobile devices such as tablets and laptops [28]. Other applications promote hands-free usage as a solution. For example, the DriveSafely application reads to the driver the received emails and text messages and then responds automatically without the user having to touch the phone [29].

4. Methods

The present study aims to examine the public perception of two smartphone applications: iTraffic and Salamtek. The first application aims to assist drivers by real-time traffic information for route planning, and the latter aims at restricting mobile phone usage to limit distraction and improve driver behavior. Two applications were selected for the study based

on their local availability, free cost, and availability in the Arabic language to ensure that users can easily understand and use them. Both applications were developed by the Qatar Mobility Innovations Center, which is a local research center that was initiated to develop and deploy different smart applications and intelligent solutions in different areas, including road safety, transportation, smart city platforms, and environment [6]. Figure 1 shows screenshots of the two smartphone applications.

4.1. iTraffic Smartphone Application. iTraffic is a real-time traffic information and navigation smartphone application. It is the first smartphone application developed in Qatar with a comprehensive traveler information system. It is available in both Arabic and English languages for free. It enables the user to monitor traffic conditions and receive real-time traffic information on Qatar's streets. A pictorial representation of the congestion rate on various streets of Qatar is included. This makes it easier to identify the fastest and/or shortest routes, depending on traffic conditions. Voice alerts for roadblocks and congested roads are also available.

4.2. Salamtek Smartphone Application. Salamtek is a smartphone application that limits the use of mobile phones while driving to reduce driver distraction. This application is available in English and Arabic languages for downloading from any country. It manages all distracting smartphone functions by eliminating all of them except the ability to receive calls from up to three contacts. The driver can also set the minimum driving speed upon which the safety measures will be activated. The application also keeps a log of all calls that have been automatically blocked, and callers are automatically notified via an autoreply message once a message is blocked.

4.3. Data Collection. The data for this study was collected using a questionnaire survey conducted at several locations such as shopping malls, universities, libraries, colleges, high schools, and sports clubs. The main questions of the questionnaire form addressed (1) whether the participants were willing to install these free smartphone applications and why, (2) would they purchase the applications if they were not free, (3) would they install the applications if these collected private data from their mobile, (4) whether the driver antidistracted application should be enforced by the government, (5) any comments, recommendations, and suggestions for the enhancement of these applications, and (6) demographic questions, including gender, age, and nationality.

The data collection process involved three phases. The first phase included selecting the participants. The participation in this study was voluntary and anonymous and was limited to people who were at or above 18 years old, had a valid driving license, and owned a smartphone at the time of the interview. To ensure randomization, the trained interviewers approached every 10th person entering, explained the importance of the questionnaire, and asked them if they met the criteria and if they were willing to do the survey. In the second phase, the participants who agreed to participate were

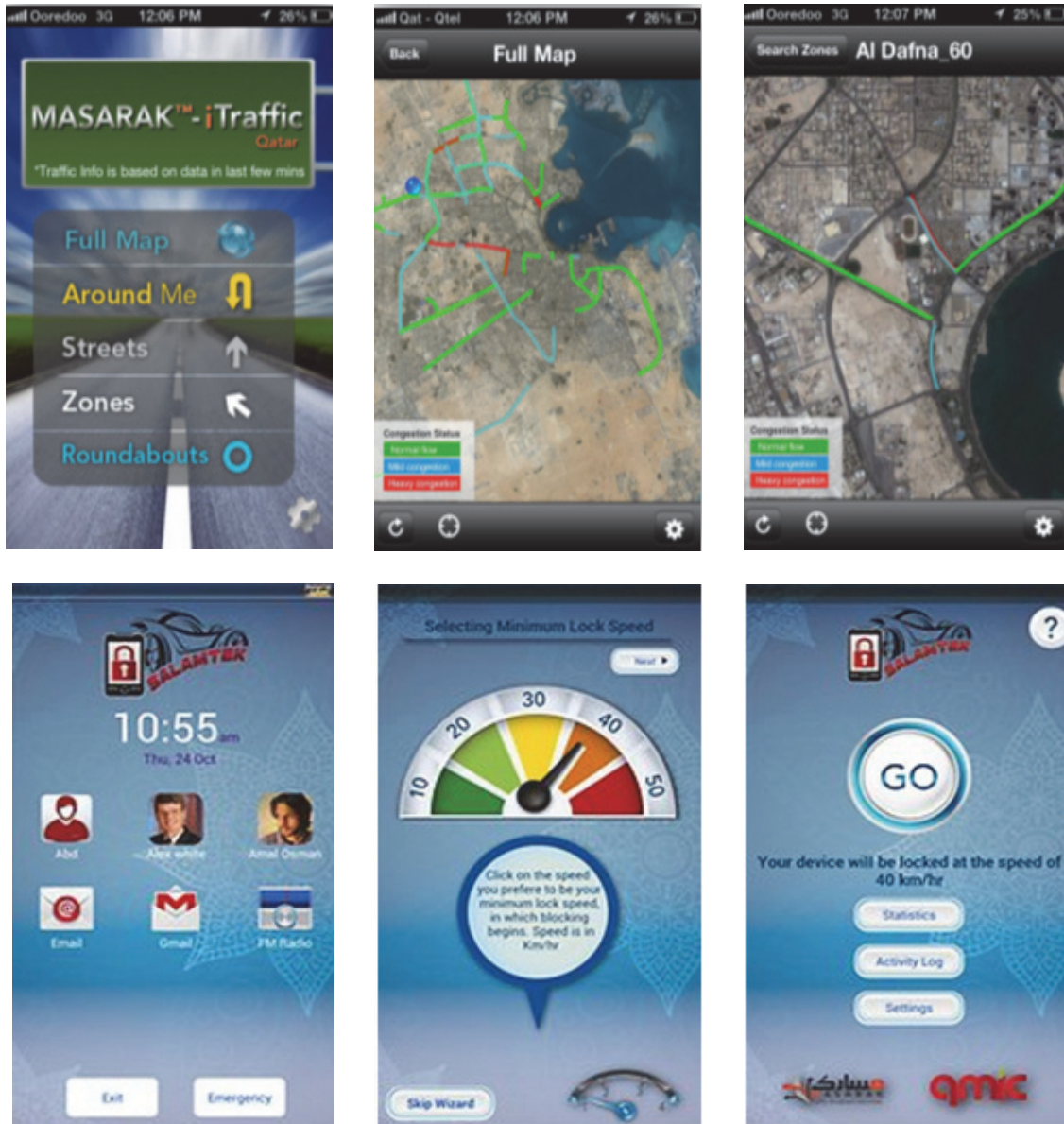


FIGURE 1: Screenshots of iTraffic (top) and Salamtek (bottom) [6].

shown (via a demonstration) how to operate the applications. A group of interviewers was trained to present a demo of the two applications. The interviewers showed the demo of the first smartphone application, explained its advantages, and answered any questions the participants had. These steps were repeated for the second application. In the third phase, the participants were provided with the questionnaire form. The interviewers explained the form to each participant in person. The participants were asked to complete the form by hand and return them then and there. The participants were allowed to ask any questions during the process if any parts of the form were not clear. The minimum sample size required for the study was calculated as follows:

$$SS = Z^2 * \frac{p(1-p)}{C^2} \tag{1}$$

where

SS = sample size,

Z = Z-value,

p = percentage of population picking a choice expressed as a decimal,

C = confidence interval expressed as decimal.

Assuming a 95% confidence level (Z=1.96) and 5% confidence interval (C=0.05), the minimum sample size was found to be 385. In this study, 450 survey forms were handed out to the participants. All 450 forms were returned. Only 421 forms were considered complete and used for the analysis. The other forms had a high percentage of missing responses and were not used during the analysis.

TABLE 1: Characteristics of the participants.

Gender	Frequency	Percentage
Male	266	63.2%
Female	155	36.8%
Age		
18-25	197	46.8%
26-50	178	42.3%
51 or more	46	10.9%
Nationality		
Qatari	128	30.4%
Non-Qatari Arab	247	58.7%
Other	46	10.9%
Total	421	100.0%

The distribution of data collected is given in Table 1. The characteristics of the participants were generally representative of the characteristics of the population in Qatar; however, there were some differences. Male respondents were the majority with 63.2%, (females 36.8%). This ratio reflects the imbalanced gender population in Qatar (which is 75.5% male and 24.5% female) [30]. As the sample selected were for drivers who own and use smartphones; the percentage of participants older than 50 was low (10.9%). The rest of the respondents were less than 25, 46.8%, and 26-50, 42.3%. The sample consisted of Qatari nationals (30.4%) and non-Qatari Arabs (58.7%) and other nationalities (10.9%). It should be noted that only 14.3% of the general population are Qataris [31]. Consideration of driver nationality was important due to the cultural diversity across the country. The oversampling of the female and Qatari participants in this study was necessary to ensure that there are enough members of these two subgroups within the population so that more reliable estimates can be reported for both groups.

4.4. Logistic Regression. Logistic regression was utilized for the analysis throughout this study. This type of analysis is one of the most useful assessment methods to determine which factors influence the outcome response of participants, given that it intrinsically adjusts each factor considered for the presence of the other factors. As shown in Table 2, the response variable (install application) is binary with two levels: 0 for not installing and 1 for installing. Three independent variables were used in the analysis. These variables include the driver age (18–25=1, 26–50=2, and 51 or older=3), driver nationality (1=Qatari, 2=non-Qatari Arab, 3=other), and driver gender (1=male and 2=female). In the used model, the probability (P_1) of installing application Y_1 [32] is as follows:

$$Y_1 = \text{logit}(P_1) = \ln\left(\frac{P_1}{1 - P_1}\right) \quad (2)$$

$$= \beta_0 + \beta_1 x_1 + \beta_2 x_2 + \dots + \beta_j x_j$$

where

Y_1 : latent variable for install application,

x_j : value of j^{th} independent variable,

β_j : corresponding coefficient for the j^{th} independent variable.

The comparison between the referred group can be indicated by the odds ratio, which is given by

$$OR = \exp(\beta_j) \quad (3)$$

An odds ratio that is greater than 1 indicates that the condition to install the application is more likely to occur in the first group, and vice versa.

5. Results

5.1. Installing versus Not Installing. A central question was asked to the participants to explore their willingness to install the two studied smartphone applications. As shown in Figure 2, 321 (76.2%) participants liked the iTraffic application, and they were willing to install it. The remaining 100 participants mentioned that they are not willing to install the application. Most of this group (46%) mentioned that it is not needed because they know the streets well in the city in terms of traffic conditions during the day. The rest of the participants mentioned that they would not install it to avoid distraction (28%), due to data privacy concerns (22%), or other reasons such as difficulties to position the phone inside the vehicle (4%). Non-Qatari Arabs and others showed more willingness to install the applications than Qataris. Also, female participants were more willing to install the application than male participants. Table 3 lists the model estimation and the odds ratio for the independent variables. Based on the effect model, the binary logistic regression model identified significant factors directly associated with installing the two applications. In order to take the Bonferroni correction into consideration, a critical value was calculated by dividing the familywise error rate by the number of tests. For iTraffic, the model showed that the odds of the non-Qatari Arab drivers to install iTraffic were 2.41 times of the odds for Qatari drivers. The model also showed that the odds of the female drivers to install iTraffic were 1.88 times of the odds for male drivers.

5.2. Installation of Salamtek. Two-hundred and forty-one (221) participants (52.5%) were willing to install the Salamtek application as indicated in Figure 2. The remaining 200 participants indicated that they are not willing to install the application because it is not needed (73.5%). This group of participants mentioned they want to keep using their phone while driving, and they do not see a problem with it. The rest of the participants mentioned that they would not install it due to privacy concerns (23%) or other reasons such as must use my phone for work purposes (3.5%). Some participants mentioned that the application was not important, or necessary as most of them were aware of the danger of mobile use while driving. Also, blocking the incoming calls except for three VIP numbers, made a few participants concerned they might miss an emergency call from an unknown person or situation.

Elder participants (participants with an age greater than 50) were more willing to install this application. Fewer

TABLE 2: Variable coding and definitions.

Variable	Description
<i>Dependent Variable</i>	
Install Application	Not Installing:0, Installing:1
<i>Independent Variable</i>	
Gender	Male*:1, Female:2
Age Group	18-25*:0, 26-50:1, 51 or more:2
Nationality	Qatari*:1, Non-Qatari Arab:2, Others:3

*Reference group for binary logistic analysis.

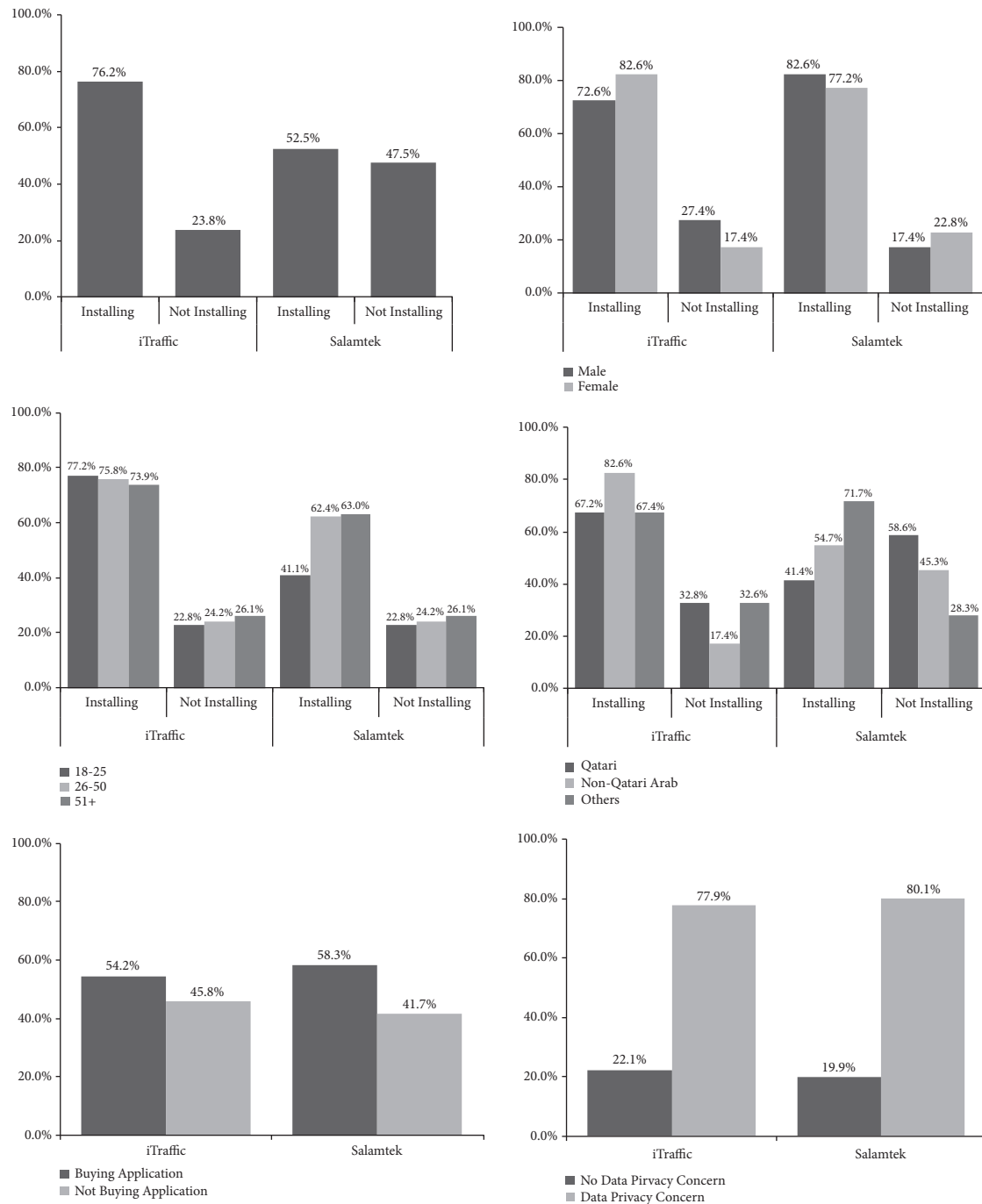


FIGURE 2

TABLE 3: Drivers' choice of installing/not installing iTraffic and logistic model results.

iTraffic	Total	Gender		Age			Nationality		
		Male	Female	18-25	26-50	51+	Qatari	Non-Qatari Arab	Others
Installing	321	193	128	152	135	34	86	204	31
Not Installing	100	73	27	45	43	12	42	43	15
% Installing	76.2%	72.6%	82.6%	77.2%	75.8%	73.9%	67.2%	82.6%	67.4%
Variable	B	S.E.	Wald	df	Sig.	Odds Ratio Exp(B)	95% C.I. for EXP(B)		
							Lower	Upper	
Gender [Female vs Male]*	0.631	0.257	6.014	1	0.014	1.880	1.135	3.113	
Age [26-50] vs [18-25]	0.027	0.259	0.011	1	0.918	1.027	.618	1.707	
Age [51 or more] vs [18-25]	-0.171	0.389	0.193	1	0.660	.843	0.393	1.806	
Nationality [Non-Qatari Arab vs Qatari]*	0.878	0.255	11.835	1	0.001	2.406	1.459	3.967	
Nationality [Others vs Non-Qatari Arab]	0.016	0.383	0.002	1	0.967	1.016	0.479	2.153	
Constant	0.494	0.241	4.212	1	0.040	1.639			

* refers to significance at 5 percent level.

TABLE 4: Drivers' choice of installing/not installing Salamtek and logistic model results.

Salamtek	Total	Gender		Age			Nationality		
		Male	Female	18-25	26-50	51+	Qatari	Non-Qatari Arab	Others
Installing	221	137	84	81	111	29	53	135	33
Not Installing	200	129	71	116	67	17	75	112	13
% Installing	52.5%	51.5%	54.2%	41.1%	62.4%	63.0%	41.4%	54.7%	71.7%
Variable	B	S.E.	Wald	df	Sig.	Odds Ratio Exp(B)	95% C.I. for EXP(B)		
							Lower	Upper	
Gender [Female vs Male]	0.167	0.210	0.628	1	0.428	1.181	0.782	1.784	
Age [26-50] vs [18-25]*	0.779	0.219	12.614	1	0.000	2.180	1.418	3.351	
Age [51 or more] vs [18-25]*	0.836	0.342	5.966	1	0.015	2.308	1.180	4.515	
Nationality [Non-Qatari Arab vs Qatari]*	0.530	0.225	5.555	1	0.018	1.699	1.093	2.640	
Nationality [Others vs Non-Qatari Arab]*	1.013	0.384	6.975	1	0.008	2.755	1.299	5.844	
Constant	-0.796	0.228	12.165	1	0.000	0.451			

* refers to significance at 5 percent level.

younger participants (41.1%) were willing to install the application. A possible explanation is that young drivers are more attached to the new social media culture and not as prepared to get disconnected from their mobile phone. The other nationality participants who included drivers other than Qataris and non-Qataris Arab were more willing to install the application than other nationalities. Qataris were the least willing to install Salamtek.

Table 4 lists the model estimation and the odds ratio for the independent variables. Based on the effect model, the binary logistic regression model identified significant factors directly associated with installing Salamtek. The model showed that the odds of the non-Qatari Arab drivers to install Salamtek were 1.7 times of the odds for the Qatari driver. For other than Qataris and non-Qataris Arab drivers, the odds to install Salamtek were 2.8 times of the odds of the Qatari drivers. The model also showed that the odds of the middle-aged drivers to install Salamtek were 2.2 times of the odds for young drivers. The odds of older drivers were 2.3 times the odds of young drivers.

5.3. Buying versus Not Buying. A second central question was to examine participants' willingness to purchase the applications. Additionally, participants were also asked how much they were willing to pay for the purchase of the applications. This information can provide an indication of the importance of the applications to the participant and can also provide guidance to the developers of these types of applications. Three options were given: (i) less than 5 US dollars, (ii) 6-10 US dollars, and (iii) US 11 to 20 dollars. Approximately 54% (174 participants out of 321) were willing to buy the iTraffic application if it was not free (Figure 2). Male, middle-aged, and Qatari drivers showed more willingness to buy the iTraffic application. The results showed that 122 participants were willing to pay \$5 or less, 32 participants were willing to spend \$6 to \$10, and 8 of them were willing to buy the application for the higher cost of 11-20 dollars. One hundred and twenty-six (126) participants (58.3%) were willing to buy the Salamtek application out of the 221 that are going to install even if it was not free (Figure 2). Female, young and middle-aged, and Qatari drivers showed more willingness to buy the

Salamtek application. Ninety-five (95) participants (86.4%) were willing to pay \$5 or less, 13 participants were willing to spend \$6 to \$10, and 2 of them were willing to buy the application for the higher cost of 11-20 dollars.

5.4. Data Privacy Concerns. Another question of interest was related to examining the level of concern regarding data privacy. Only participants who reported a willingness to install the application answered this question. The question highlighted that data collected would be used to improve the applications, which would reflect on providing better service for the users. Out of the 345 participants who were willing to install the iTraffic application, 250 participants (77.9%) were willing to install the application even if it collected the data such as the location and phone ID as shown in Figure 2. For Salamtek, out of the 241 of the participants who were willing to install the Salamtek application, 173 participants (80.1%) were willing to install the application even if it collected the same sort of data. The remaining participants were concerned about privacy and were against the collection of data.

5.5. Enforcement versus Motivation. A high percentage of the participants who were willing to install the Salamtek application (52%) responded that the government should enforce these types of traffic safety applications to enhance road safety when asked about their preference. The rest mentioned that there was no need for compulsory enforcement for these types of applications. One of the reasons provided was that enforcement hinders personal freedom and that using a mobile phone is an individual choice. Another reason was that enforcing the use of the application would result in buying smartphones by all drivers; that might not be a cost-effective or realistic solution.

6. Discussion and Conclusions

A questionnaire-based survey was conducted with 421 participants to understand their perceptions towards two different types of traffic-related smartphone applications: a driver antidistraction application and a real-time traffic information and navigation application. The results indicated that 321 (76.2%) participants were willing to install the real-time traffic application; female drivers (82.6%) were especially interested in this application. Furthermore, 188 (54.2%) participants were willing to buy the application in the future. Most of the participants willing to install the application (77.9%) were open to sharing their personal data to improve the performance of the application. The remaining participants willing to install the application (22.1%) were concerned about the security and privacy of their personal details.

On the other hand, 221 (52.5%) participants were willing to install the driver antidistraction application. This application was not popular among young and Qatari drivers. More than half this group (58.3%) were willing to buy the application, and 80.1% of this group were willing to use the application even if it collected personal data. In summary, the potential market for the real-time traffic application was higher than that of the antidistraction application. In general, the participants willing to use the applications did not have

privacy concerns, but in return for sharing their personal data, they expected some reduction in travel time and a safer trip.

These results can provide guidance for safety campaigns and awareness programs that focus on motivating drivers to make smart travel choices. Changing drivers' methods of selecting specific routes to be based on real-time information can substantially improve the performance of the transportation network and reduce costs and vehicle emissions. Similarly, promoting the use of distraction-prevention smartphone applications through awareness programs, especially among young drivers, can have significant safety benefits for all road users; solutions such as driver education and stricter punishments or fines for mobile phone use while driving are not enough.

These results are useful for policymakers and government agencies and can be used to appropriately promote these types of smartphone applications in Qatar. Although this study was conducted in Qatar, the findings can be applied throughout the Arabian Gulf region, which includes Kuwait, the United Arab Emirates, Oman, and Saudi Arabia. These countries share similar social and cultural environments.

6.1. Applications of the Findings. In conclusion, there is a potential market for these types of smartphone applications in Qatar. Once they become popular, these applications could provide important benefits for drivers and transportation networks. Drivers can benefit from efficient route planning and travel information, which can reduce their travel time and fuel consumption costs. This, in turn, can reduce travel times, costs, and vehicle emissions for the entire road transportation network. In addition, distraction-prevention applications can improve driver safety by preventing mobile phone distractions, which could significantly reduce the incidences of distracted driving and consequently the number of road collisions.

There are also many other possibilities for public agencies to effectively benefit from these applications. These applications could be used to collect traffic data and information, such as vehicle speeds and counts. However, before utilizing these applications for data collection, their accuracy must be evaluated, and data obtained from these applications must be compared with real-life data obtained from trusted sources. Such comparisons will also assist developers in calibrating and validating their applications. These applications can also be used to conduct before and after studies to evaluate the impact of different traffic-related policies.

There is also potential for these applications to provide real-time traffic information for incidents and congestion. This information can be used by public agencies to make rapid decisions and to provide information to drivers via dynamic message signs, for example. It can also be used by public transportation agencies to provide real-time arrival and departure information.

6.2. Limitations and Future Studies. Although the objectives of the study were achieved, there were a few limitations. The participants did not actually experience the applications under real driving conditions; therefore, they had limited

experience to guide their responses. In addition, the study only investigated the potential market for these types of applications without investigating how the applications may influence driver behavior in the future. Therefore, follow-up studies are necessary to find the actual number of installations. In addition, postinstallation preference studies are needed to measure user perceptions and preferences, as well as gaps between the number of installations and frequency of use. Several studies have shown that only a limited number of installed applications are being frequently used. Finally, there is a need to measure the impact of these types of applications on driver behavior to discover whether drivers make changes to their commutes based on the information provided by these applications and to reveal the degree to which they rely on the applications.

Data Availability

The survey data used to support the findings of this study are available from the corresponding author upon request.

Disclosure

The statements made herein are solely the responsibility of the author.

Conflicts of Interest

The author declares that there are no conflicts of interest regarding the publication of this paper. The survey data used to support the findings of this study are available from the corresponding author upon request.

Acknowledgments

This publication was made possible by a UREP Award [UREP 22-062-2-022] from the Qatar Research Fund (a member of Qatar Foundation).

References




- [1] J. Tison, N. Chaudhary, and L. Cosgrove, "National phone survey on distracted driving attitudes and behaviors," 2011.
- [2] K. Shaaban, S. Gaweesh, and M. M. Ahmed, "Characteristics and mitigation strategies for cell phone use while driving among young drivers in Qatar," *Journal of Transport & Health*, vol. 8, pp. 6–14, 2018.
- [3] Peninsula, *Qatar ranked second in Global Mobile Engagement Index*, The Peninsula, 2018, <https://www.thepeninsulaqatar.com/article/10/05/2018/Qatar-ranked-second-in-Global-Mobile-Engagement-Index>.
- [4] K. Shaaban and K. Abdelwarith, "Understanding the association between cell phone use while driving and seat belt noncompliance in Qatar using logit models," *Journal of Transportation Safety & Security*, pp. 1–17, 2018.
- [5] K. Shaaban and A. Pande, "Evaluation of red-light camera enforcement using traffic violations," *Journal of Traffic and Transportation Engineering (English Edition)*, vol. 5, no. 1, pp. 66–72, 2018.
- [6] qmicqatar, *Qatar Mobility Innovations Center (QMIC)*, 2017, <http://www.qmic.com/>.
- [7] W.-C. Lee and B.-W. Cheng, "Effects of using a portable navigation system and paper map in real driving," *Accident Analysis & Prevention*, vol. 40, no. 1, pp. 303–308, 2008.
- [8] A. Polydoropoulou, M. Ben-Akiva, and I. Kaysi, "Influence of traffic information on drivers' route choice behavior," *Transportation Research Record*, no. 1453, 1994.
- [9] P. S.-T. Chen, K. K. Srinivasan, and H. S. Mahmassani, "Effect of information quality on compliance behavior of commuters under real-time traffic information," *Transportation Research Record: Journal of the Transportation Research Board*, no. 1676, pp. 53–60, 1999.
- [10] Y.-Y. Tseng, J. Knockaert, and E. T. Verhoef, "A revealed-preference study of behavioural impacts of real-time traffic information," *Transportation Research Part C: Emerging Technologies*, vol. 30, pp. 196–209, 2013.
- [11] N. Dragutinovic and D. Twisk, *Use of Mobile Phones While Driving—Effects on Road Safety*, SWOV Institute, Leidschendam, Netherlands, 2005.
- [12] D. A. Redelmeier and R. J. Tibshirani, "Association between cellular-telephone calls and motor vehicle collisions," *The New England Journal of Medicine*, vol. 336, no. 7, pp. 453–458, 1997.
- [13] C. Stothart, A. Mitchum, and C. Yehner, "The attentional cost of receiving a cell phone notification," *Journal of Experimental Psychology: Human Perception and Performance*, vol. 41, no. 4, pp. 893–897, 2015.
- [14] K. Kinoshita, "Mobile telephone system configured to confirm receiver speed conditions," 2005, Google Patents.
- [15] M. J. Smith and D. R. Stephens, "Detecting use of a mobile device by a driver of a vehicle, such as an automobile," 2011, Google Patents.
- [16] R. Bose, J. Brakensiek, K.-Y. Park, and J. Lester, "Morphing smartphones into automotive application platforms," *The Computer Journal*, vol. 44, no. 5, pp. 53–61, 2011.
- [17] M. Böhmer, C. Lander, S. Gehring, D. Brumby, and A. Krüger, "Interrupted by a phone call: Exploring designs for lowering the impact of call notifications for smartphone users," in *Proceedings of the 32nd Annual ACM Conference on Human Factors in Computing Systems, CHI 2014*, pp. 3045–3054, ACM, Canada, May 2014.
- [18] G. J. J. Lipovski, "System for inhibiting texting and similar distractions while driving moving vehicles," 2010, Google Patents.
- [19] D. Ahl, F. Farrell, J. M. Fernandez, J. Mangione, and S. Vowell, "Mobile phone based system for disabling a cell phone while traveling," 2008, Google Patents.
- [20] C. Irani, "Preventing cellphone usage when driving," 2007, Google Patents.
- [21] J. Whipple, W. Arensman, and M. S. Boler, "A public safety application of GPS-enabled smartphones and the android operating system," in *Proceedings of the 2009 IEEE International Conference on Systems, Man and Cybernetics, SMC 2009*, pp. 2059–2061, USA, October 2009.
- [22] J. Dai, J. Teng, X. Bai, Z. Shen, and D. Xuan, "Mobile phone based drunk driving detection," in *Proceedings of the 2010 4th International Conference on Pervasive Computing Technologies for Healthcare, Pervasive Health 2010*, IEEE, Germany, March 2010.
- [23] T. Wang, G. Cardone, A. Corradi, L. Torresani, and A. T. Campbell, "WalkSafe: a pedestrian safety app for mobile phone users who walk and talk while crossing roads," in *Proceedings of*

the 12th Workshop on Mobile Computing Systems & Applications (HotMobile '12), p. 5, ACM, February 2012.

- [24] INRIX, *Discover The Best Route, With The Least Delay*, 2017, <http://www.inrixtraffic.com/features/>.
- [25] Sprint, *Commit to distraction-free driving with Sprint Drive First*, 2017, <http://www.sprint.com/landings/focusondriving/index.html?ECID=vanity:drive>.
- [26] Cogosense, *bSafeMobile by Cogosense*, 2017, <http://bsafemobile.com/>.
- [27] Drivemode, *Drivemode: No-look Freedom for Driving*, 2017, <https://drivemode.com/>.
- [28] Cellcontrol, *Stop Texting While Driving — Texting While Driving Solution*, 2017, <https://www.cellcontrol.com>.
- [29] iSpeech, *Free Mobile App Stops Texting While Driving - DriveSafe.ly*, 2017, <http://www.drivesafe.ly/>.
- [30] MDPS, *Qatar Population and Social Statistics*, 2015, Q.M.o.D.P.a. Statistics, Editor.
- [31] F. De Bel-Air, *Demography, Migration, and Labour Market in Qatar*, Gulf Research Center, 2014.
- [32] P. McCullagh and J. A. Nelder, *Generalized Linear Models*, vol. 37, CRC Press, 2nd edition, 1989.

Research Article

Active Warning System for Highway-Rail Grade Crossings Using Connected Vehicle Technologies

Xu Wang ^{1,2}, Jiangchen Li ², Can Zhang,² and Tony Z. Qiu ²

¹School of Qilu Transportation, Shandong University, Jinan 250061, China

²Department of Civil and Environmental Engineering, University of Alberta, Edmonton T6G2W2, Canada

Correspondence should be addressed to Tony Z. Qiu; zhijunqiu@ualberta.ca

Received 14 September 2018; Revised 14 January 2019; Accepted 27 January 2019; Published 11 February 2019

Guest Editor: Luc Chassagne

Copyright © 2019 Xu Wang et al. This is an open access article distributed under the Creative Commons Attribution License, which permits unrestricted use, distribution, and reproduction in any medium, provided the original work is properly cited.

Highway-rail grade crossing (HRGC) collisions are a significant safety concern around the world. HRGC collisions have a high risk of injuries and fatalities. To mitigate that risk, safety countermeasures for both active and passive HRGCs have been implemented. Leveraging the latest developments in connected vehicle (CV) technologies, CV-based warning systems perform well in safety applications for roadway networks. However, few have been developed to focus on safety improvements specifically for HRGCs. To bridge this gap, this paper proposes a novel active warning system that was created with readily available CV technologies and devices. A crossing risk assessment model was developed and evaluated in simulation and field applications. The proposed model predicts the crossing risk probabilities in the near future. When road users are in great risk of a collision, the warning system sends out auditory and visual alerts and displays the estimated waiting time. The test results reveal that the proposed warning system is promising for field implementation to improve safety at grade crossings.

1. Introduction

Highway-rail grade crossing (HRGC) collisions are a primary concern for railway authorities and the public at large. The Canadian Transportation Safety Board [1] reported that more than 240 fatalities and 260 serious injuries took place in Canada as a result of grade-crossing collisions over the past decade. Grade crossings can be classified as active HRGCs or passive HRGCs. Usually, more incidents, injuries, and fatalities occur at active HRGCs than in passive HRGCs. Active HRGC incidents are mainly caused by drivers violating or ignoring the control devices meant to keep them safe as trains arrive at the crossing [2]. Thus, safety measures at active HRGCs, such as signals and automatic gates, have been meticulously investigated [3–12] from which safety risk countermeasures have been implemented to provide dynamic train information to drivers and pedestrians.

In recent years, the emergence of connected vehicle (CV) technologies has enabled vehicle-to-infrastructure (V2I), vehicle-to-vehicle (V2V), and vehicle-to-pedestrian (V2P) communication applications. In mitigating the risk of grade-crossing collisions, CV-based active warning systems have

shown great promise because they incorporate the latest advances in CV technologies. CV-based active warning systems apply CV technologies to remind crossing road users of the right-of-way on railroads. It warns road users to stop for crossing or approaching trains regardless of whether the safety devices installed at the crossing are passive or active.

Previous research has validated the use of CV technologies in various safety applications [2, 9, 10, 12–16]; however, few studies have focused on CV-based applications in rail safety management. There is a significant need to design and evaluate CV-based warning systems at grade crossings in a multimodal user environment. Therefore, the primary focus of this study was to develop and evaluate an active warning system for grade crossings. The proposed active warning system is promising in real-world applications to reduce grade crossing incidents.

The remainder of this paper is organized into sections: the next section reviews the existing conventional and advanced warning applications to improve grade crossing safety; the Methodology section describes the system framework, probabilistic kinematic model, and crossing risk assessment method; the Case Study section presents the simulation and

field test results of the proposed active warning system; and the last section discusses the concluding remarks and suggests future work.

2. Literature Review

Signs are the first line of defense but also the most marginal measure in terms of warning devices that prevent HRGC violations and collisions. Regulated by Transport Canada [17], the installation of grade crossing signs is mandatory in Canada. A STOP AHEAD sign or a YIELD sign must be installed along with a warning sign to enhance safety. However, these signs provide no information on the actual presence of a train to vehicle drivers and pedestrians.

Additional devices, such as obstacle detectors, signals, law enforcement cameras, and horn systems, have been implemented to provide real-time warning of the presence of trains. Existing studies [3–8] have confirmed that these devices improve safety performance at HRGCs. Unfortunately, a communication failure between control devices and road users often causes collisions at passive grade crossings. Thus, many studies have been devoted to enhancing communication by updating control devices. Noyce and Fambro [3] installed a vehicle-activated strobe light and a supplemental sign. The sign tells drivers the desired action at grade crossings. The before-and-after tests showed that the enhanced sign system increased drivers' caution at grade crossings. Similarly, Gent et al. [4] implemented an automated-horn system to alert road users at crossings. Two horns were mounted at a crossing and activated using the track-signal circuitry for the gate arms and bells. The system proved to be less annoying for nearby residents and slightly safer from the locomotive drivers' perspective than the previously installed measures. Moreover, Gilleran [5] discussed the use of presignals at grade crossings. The author found that proper implementation of presignals effectively prevents vehicles from crossing the track area when trains are approaching. To compare the effectiveness of different warning control devices, Hu and Lin [6] conducted a before-and-after study using 15-year data. They found that both the LED approaching train indicator and the law enforcement camera are more effective than obstacle detectors in reducing collisions and improving safety. In addition, other studies attempted to enhance the operational policy of control devices. For example, Moon and Coleman [7] presented an operating policy for a four-quadrant gate, which determines a dynamic dilemma zone and gate operation parameters to reduce grade crossing collisions. Likewise, Siques [8] defined the four phases of pedestrian behaviours at crossings: Pedestrians must (1) be aware of the crossing; (2) take the appropriate path; (3) be aware of an approaching train; and (4) understand potential hazards. Siques then proposed amelioration measures, including passive signs, pedestrian channelization and gates, audio warnings, and public education.

Advanced driver or pedestrian assistance systems improve traffic safety from the road users' perspective. Alerting drivers through in-vehicle systems was proposed as early as 1975 [18]. Since then, several tests have been conducted for in-vehicle warning systems, in which trains

send signals to alert vehicles within the radio range [19, 20]. However, these systems lacked vehicle-to-train communication, and they were not in control of drivers' dangerous crossing behaviours. Thus, Hartong et al. [9] integrated positive train control systems with vehicular ad-hoc networks to fulfill their communication. To avoid HRGC incidents, they provided integration architectures and identified protocols. Following this, several studies focused on different aspects of grade crossing warning based on wireless communication. To evaluate the feasibility of wireless communication, Ku [10] established a detecting and warning system. The system shows grade crossings in real-time video to the train drivers through an onboard unit and alerts road users about the train's distance through a roadside unit. These components are linked by wireless communication. Ku's subsequent field tests prove that the system is feasible, and live videos help train drivers react fast. As for auditory alerts, Landry et al. [11] conducted driving simulator experiments to investigate the effectiveness of in-vehicle auditory alert systems at grade crossings. Their experiment results show that human voices, especially female voices, are more effective than text-to-speech voices. In-vehicle auditory alerts improve driver compliance. In terms of stopping distance, Hsu and Jones [2] conducted a sensitivity analysis on stopping distance at grade crossings. Field data from two sites was used for the non-CV case while data from a driving simulator was used for the CV case. The sensitivity analysis shows that the initial speed and perception-reaction time are the most sensitive safety factors at grade crossings. Earlier onboard warning in CVs reduces the initial speed and thus improves safety at grade crossings. In addition, for signal propagation, Tedesso et al. [12] investigated the dedicated short range communications (DSRC) signal propagation conditions encountered in a railroad environment. The train-to-infrastructure communication in both clear and cluttered environments was set up. They proved that DSRC signals can handle relatively long-distance communication.

Existing studies have examined the feasibility of CV-based warning at grade crossings. When the warning system is properly designed, it addresses the non-line-of-sight problem and improves safety at grade crossings. However, throughout the related literature, few studies have been devoted to developing a risk assessment method for grade crossings and evaluating its safety performance in simulation or in the field. To bridge this research gap, this study included the development of a novel probabilistic kinematic model that replicates the motion of road users and rail trains and applies a crossing risk assessment model to evaluate crossing risk in real time. There were three objectives of this study: (1) developing an active warning system for road users at grade crossings; (2) validating the developed warning system in simulation and field tests; and (3) assessing the sensitivity of the model parameters. This paper presents the proposed system's design. The system was evaluated through simulation and field tests conducted in Edmonton, Alberta, Canada. The developed warning system is promising for field implementation to reduce collisions and improve safety at grade crossings.

3. Methodology

3.1. System Framework. Enhancing communication between railway warning systems and road users can reduce collision probability and improve overall safety at HRGCs. The main function of the proposed active warning system is to alert road users of crash-imminent situations at a grade crossing through CV technologies. The system includes a wireless connection via DSRC between roadside equipment (RSE) and onboard equipment (OBE) to activate crucial warning messages about an approaching train. The warning messages can be either visual or auditory. While the system may not prevent all crashes, it is expected that, with an effective warning system, the number of violations will decrease, which will in turn reduce the number and severity of crashes at railroad crossings.

Figure 1 illustrates the basic components, conceptual communication framework, and system framework of the proposed active warning system. On one end of the communication pathway, RSE is installed at the grade crossing and OBE is placed on trains. The basic parameters of the grade crossing and the train need to be written into the RSE and OBE in advance, respectively. On the other end of the communication pathway, road users (i.e., vehicles and pedestrians) equipped with OBE can receive grade crossing and train information in real time when they are in proximity to the grade crossing. The system evaluates the collision risk and sends out warning messages by smart devices when required.

Specifically, the RSE archives basic static information of the grade crossing and receives real-time information from any control devices. The static information includes geometric characteristics and positioning accuracy parameters for collision risk assessment. Additional information, such as real-time control device status and communication latency, can be customized in the RSE. In the meantime, the OBE obtains location information from its Global Position System (GPS) module and thus derives the approach speed and travel direction. Together with the information archived in the RSE, the system first estimates actual locations considering communication latency and user reaction behaviours. Then, the actual locations are formulated as probabilistic kinematic models to account for positioning inaccuracy. The system then assesses the collision probability through a crossing risk assessment model. Once the collision probability between a road user and a train is larger than a predetermined threshold, the warning is activated and sent to road users immediately. At the same time, the road user can also receive the estimated waiting time for the train to pass.

3.2. Probabilistic Kinematic Model of Highway-Rail Crossing System. This study included the development of a probabilistic kinematic model to assess the actual locations of trains and road users with positioning accuracy. The model was extended and modified from the one proposed by He et al. [21] and adapted to reduce grade crossing collisions. The model proposed by He et al. [21] is for vehicle-to-pedestrian system so the following extensions and modifications have been made to adapt the characteristics of

highway-rail crossing system. First, the vehicle-to-pedestrian system involves the locations of pedestrians in order to prevent vehicle-pedestrian collisions. However, the highway-rail crossing warning system needs to prevent not only collisions between vehicles and rail trains but also those between vehicles and gates at grade crossings. Thus, the extended probabilistic kinematic model also involves gate operation when gates are present. Second, the walking behaviours of pedestrians are highly dynamic and hard to predict, leading to the uncertainty of pedestrian location estimation, whereas rail trains travel along rail tracks so that the location estimation of trains is more certain compared with that of pedestrians. The modified model excludes the uncertainty of behaviors, which was done in the model of the vehicle-to-pedestrian system. Third, as the motions of trains are more certain than pedestrians, the time when trains leave grade crossings is predictable. The highway-rail crossing system provides remaining waiting time for road users.

The extended model quantifies collision risk in real time in consideration of the road user's reaction behaviours, communication latency, uncertainty of positioning accuracy, and grade crossing control system. Figure 2 demonstrates the relative motion between trains and other road users. It is important to note that road users include vehicles and pedestrians. Figure 2 uses a vehicle to represent all road users. In addition, the arrows in Figure 2 only indicate the travel directions of trains and road users but their real trajectories do not have to be always straight.

A probabilistic model describes the motions shown in Figure 2. As shown in Figure 2, the train is approaching the origin $O(0, 0)$. First, at time instant t_0 , the initial locations of the rail train and road users are measured as $p_{r,0}(x_{r,0}, y_{r,0})$ and $p_{u,0}(x_{u,0}, y_{u,0})$. However, the delay caused by the road user's behaviours influences the positioning measurements. Additionally, data is transmitted by vehicle-to-everything (V2X) communication, which may experience communication latency thereby affecting position measurements. Hence, the actual locations of the train and road users $\bar{p}_{r,0}$ and $\bar{p}_{u,0}$ in consideration of user behaviours and communication latency are given in the equations below:

$$\bar{x}_{r,0} = x_{r,0} - v_{r,x,0} (t_{prt} + t_{cl}) \quad (1)$$

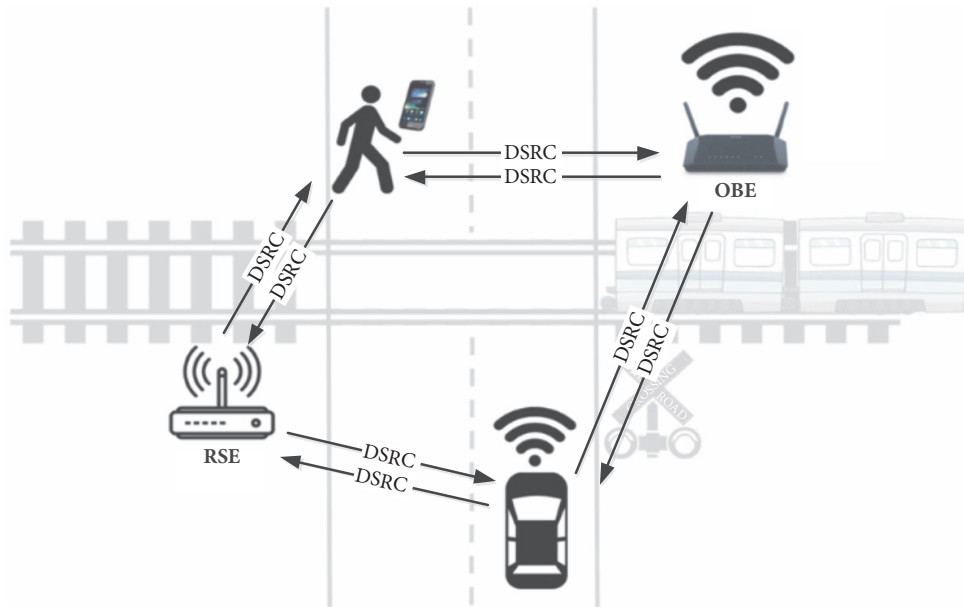
$$\bar{y}_{r,0} = y_{r,0} - v_{r,y,0} (t_{prt} + t_{cl}) \quad (2)$$

$$\bar{x}_{u,0} = x_{u,0} + v_{u,x,0} (t_{prt} + t_{cl}) \quad (3)$$

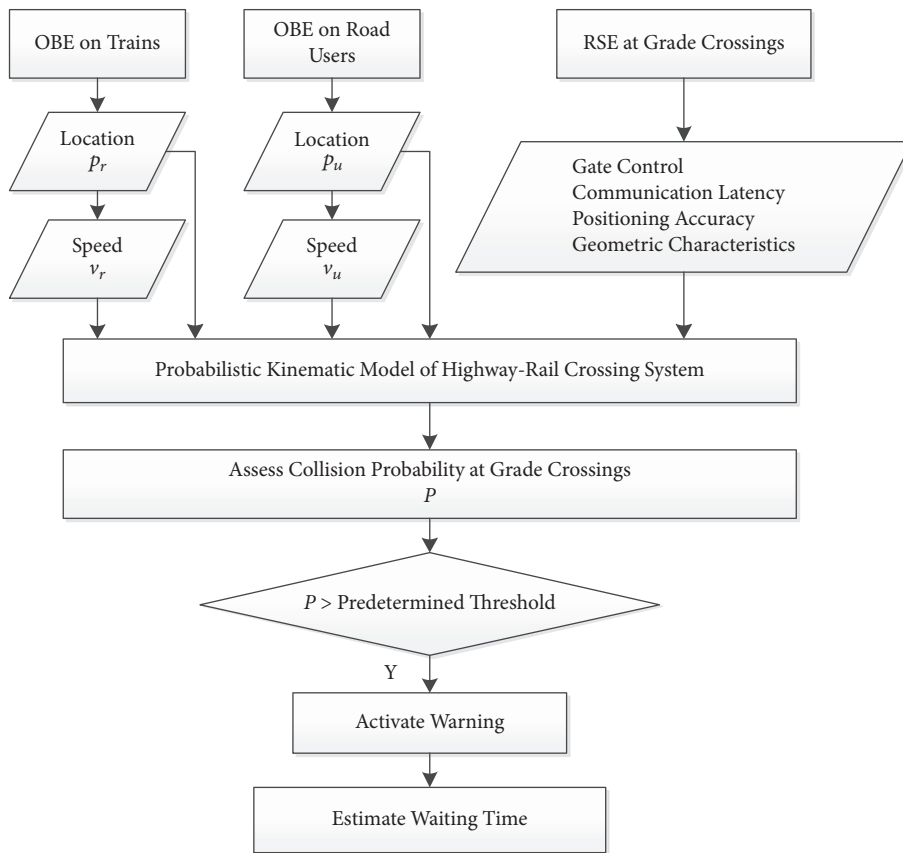
$$\bar{y}_{u,0} = y_{u,0} + v_{u,y,0} (t_{prt} + t_{cl}) \quad (4)$$

where $\bar{x}_{r,0}$, $\bar{y}_{r,0}$, $\bar{x}_{u,0}$, and $\bar{y}_{u,0}$ are the actual location coordinates of the train and road user in meters (m); $x_{r,0}$, $y_{r,0}$, $x_{u,0}$, and $y_{u,0}$ are the measured location coordinates of the train and road user in m; $v_{r,x,0}$, $v_{r,y,0}$, $v_{u,x,0}$, and $v_{u,y,0}$ are the measured velocity components on x and y axes in meters per second (m/s); and t_{prt} and t_{cl} are the road user's perception-reaction time and communication latency in seconds (s), respectively.

Then, the locations of the train and road users after time period t ($p_{r,t}$ and $p_{u,t}$) can be predicted. Assuming that



(a)



(b)

FIGURE 1: System framework. (a) Conceptual communication framework. (b) System flowchart.

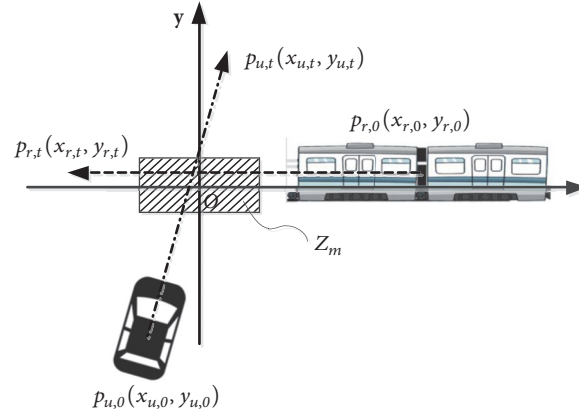


FIGURE 2: Kinematic model.

both the road segment and the rail track are straight, the corresponding coordinates of the train and road user at time instance t are as shown in the following equations:

$$\bar{x}_{r,t} = \bar{x}_{r,0} - v_{r,x,0}t \quad (5)$$

$$\bar{y}_{r,t} = \bar{y}_{r,0} - v_{r,y,0}t \quad (6)$$

$$\bar{x}_{u,t} = \bar{x}_{u,0} + v_{u,x,0}t \quad (7)$$

$$\bar{y}_{u,t} = \bar{y}_{u,0} + v_{u,y,0}t \quad (8)$$

However, the positioning accuracy is limited by the efficiency or inefficiency of the GPS service. Inaccuracy may result from device problems and environmental factors. Therefore, positioning uncertainty was considered in this research because the positioning accuracy plays a critical role in the active warning application. This study assumed that the actual locations of trains and road users were normally distributed: $p \sim N(\bar{p}, \delta^2)$. By this means, their probability density functions were formulated as follows:

$$f(p_{r,t}) = \frac{1}{2\pi\delta_{r,x}\delta_{r,y}} \exp \left\{ -\frac{1}{2} \left[\frac{(x_r - \bar{x}_{r,t})^2}{\delta_{r,x}^2} + \frac{(y_r - \bar{y}_{r,t})^2}{\delta_{r,y}^2} \right] \right\} \quad (9)$$

$$f(p_{u,t}) = \frac{1}{2\pi\delta_{u,x}\delta_{u,y}} \exp \left\{ -\frac{1}{2} \left[\frac{(x_u - \bar{x}_{u,t})^2}{\delta_{u,x}^2} + \frac{(y_u - \bar{y}_{u,t})^2}{\delta_{u,y}^2} \right] \right\} \quad (10)$$

where $f(p_{r,t})$ and $f(p_{u,t})$ are the probability density functions for the actual locations of the train and road user at time instant t , respectively; $p_r(x_r, y_r)$ and $p_u(x_u, y_u)$ are coordinates of any location along the railway track and the roadway; and $\delta_{r,x}$, $\delta_{r,y}$, $\delta_{u,x}$, and $\delta_{u,y}$ are the standard deviations of position measurements on x and y axes (in m).

3.3. Probabilistic Kinematic Model Considering Gate Operation. Transport Canada regulates that grade crossings that meet certain criteria must be equipped with a warning system

with gates. The detailed criteria are listed in [17, 22]. For grade crossings with gates, the active warning system works to prevent the collision through gate operation. Thus, gate operation was also considered in the proposed model. First, road users who enter the grade crossing during the gate operation time t_g are regarded as collisions. As such, (1)–(4) were modified as follows. The locations after time period t ($p_{r,t}$ and $p_{u,t}$) are still predicted by (5)–(8):

$$\bar{x}_{r,0} = x_{r,0} - v_{r,x,0}(t_{prt} + t_{cl} + t_g) \quad (11)$$

$$\bar{y}_{r,0} = y_{r,0} - v_{r,y,0}(t_{prt} + t_{cl} + t_g) \quad (12)$$

$$\bar{x}_{u,0} = x_{u,0} + v_{u,x,0}(t_{prt} + t_{cl} + t_g) \quad (13)$$

$$\bar{y}_{u,0} = y_{u,0} + v_{u,y,0}(t_{prt} + t_{cl} + t_g) \quad (14)$$

where t_g is gate operation time ($t_g = t_d + t_i$, in s); t_d is gate delay time, which is the time between the initiation of flashing lights and entry gate descent (in s); and t_i is gate interval time, which is the time between entry and exit gate descent (in s) [7]. t_d is the necessary stopping time for vehicles to stop safely in front of the stop bar [23] and t_i is the necessary time for vehicles to completely pass the grade crossing. t_d and t_i can be determined by the following equations. For grade crossings without gate control, t_d and t_i are set zeros:

$$t_d = t_{prt} + \frac{v}{2(a + G \cdot g)} + \frac{D_{s2g}}{v} \quad (15)$$

$$t_i = \frac{D_{g2g}}{v_{cr}} \quad (16)$$

where a is the deceleration rate in meters per second² (m/s^2); g is the acceleration of gravity in m/s^2 ; G is the grade in percent/100; v is the road user's approach speed (in m/s); D_{s2g} is the distance between the stop bar and gate (in m); D_{g2g} is the distance between the entry and exit gates (in m); and v_{cr} is the critical minimum speed of a road user in the track zone (in m/s). These parameters are predetermined, while t_d and t_i can be measured from the field.

Likewise, the warning system calculates the relative distance of road users from the gates instead of the trains. Hence, in addition to the probabilities of the train and road user locations calculated in (9)-(10), the probability of the gate status is also taken into account. The gate status can be derived from the real-time train locations because the relationship between the gate operation and train arrival is fixed. As regulated by Transport Canada, gate arms must be horizontal at least five seconds before the train's arrival where trains travel faster than 25 kilometers per hour (km/h) [22]. Considering this relationship, the probability of the gate status $f(p_{g,t})$ is given as the following conditional probability:

$$f(p_{g,t}) = f(p_{g,t} | Y < 0) \cdot F(Y < 0) \quad (17)$$

where $Y = d_{r2g,t} - v_{r,t} \cdot T_{threshold}$; $d_{r2g,t}$ is the distance between the train and the centre of the gate zone; ($d_{r2g,t} = \|p_{r,t} - p_g\|_2$, p_g was assumed to be $O(0,0)$ in this study); $v_{r,t}$ is the approaching speed of the train at time instant t ; and $T_{threshold}$ is the time gap from gate descent and train arrival, which is a fixed value from standards and guidelines.

Equation (17) can be degenerated to an equation for a no-gate grade crossing. In this case, the model assumes that a virtual gate exists. The virtual gate is equivalently open all the time and thus $f(p_{g,t}) = 1$. Consequently, the probability of the gate status in (17) in the no-gate scenario is degenerated as below:

$$f(p_{g,t}) = f(p_{g,t}) \cdot F(Y) = F(Y) \quad (18)$$

3.4. Crossing Risk Assessment. To assess the collision risk, the target roadway Z was divided into M subsegments. The width of the railroad track was W_r and road length was L , so M equaled L/W_r . Also, the width of the road user (e.g., vehicles and pedestrians) was W_u . Thus, the m^{th} subsegment Z_m was defined as a region with $x_m^0 = -(1/2)W_u$ to $x_m^1 = (1/2)W_u$ for its x coordinates, and $y_m^0 = (m-1)W_r$ to $y_m^1 = mW_r$ for its y coordinates. The collision risk was defined as the collision probability $P_{Z_m}^{t_k}$ over Z_m at the time instant t_k ($t_k = t_0 + kt$ and k is the prediction time step) as follows:

$$P_{Z_m}^{t_k} = \int_{y_m^0}^{y_m^1} \int_{x_m^0}^{x_m^1} f(p_{g,t}) \cdot f(p_{v,t})|_{t=t_k} dx dy \quad (19)$$

where the double integral indicates the generic description of Z_m in the approaching rail track. The information of coordinates can be obtained from MAP data.

As mentioned in the System Framework subsection, when collision risk $P_{Z_m}^{t_k}$ at time instant t_k was larger than a predetermined threshold, a warning to road users was activated. In this study, the scenario that caused the most devastating collision was selected to calculate the collision probability P_{Z_m} in the collision moment. The threshold was determined as a certain percentage (e.g., 50%) of P_{Z_m} .

3.5. Waiting Time Estimation. When a crossing warning is activated, the active warning system also provides estimated waiting time at grade crossings. The gate arm starts to ascend

after the train leaves by a safe distance, which was assumed to be $v_{r,0} \cdot T_{threshold}$. The safe point p_s is $(-v_{r,0} \cdot T_{threshold}, 0)$. After then, the time for the gate arm to ascend to vertical (T_{ascend}) must be 6 to 12 seconds, as regulated in [22]. Thus, the waiting time (T_w) was estimated as follows. Once the waiting time is estimated, the waiting time will be counted down:

$$T_w = \frac{\|p_{r,0} - p_s\|_2}{v_{r,0}} + T_{ascend} \quad (20)$$

4. Case Study

4.1. Study Site. The grade crossing at 82 Avenue and 114 Street in Edmonton, Alberta, Canada (as shown in Figure 3) was selected as the test site. This intersection is located at the south side of Health Sciences Jubilee Station. There are two light rail transit (LRT) lines running across. This location already had treatments to improve the grade crossing. Passive railway warning signs visually alert vehicle drivers and pedestrians of an imminent LRT crossing. Pedestrian paths across the tracks guide pedestrians to pass through the crossing in a safe manner. Horizontal entry gates and flashing lights prevent road users from entering the crossing when a train is in hazardous proximity. Moreover, LRT trains have the priority of the signal control to ensure safety. The tested grade crossing is close to the University of Alberta and experiences heavy traffic during AM and PM peaks. Although the treatments were well designed and well implemented, alerts for road users can still be improved in terms of the communication between the railway warning and road users to improve safety. Therefore, the proposed active warning system was applied to this grade crossing.

4.2. Simulation Results. Prior to the field tests, simulation tests were conducted by coding the collision risk assessment model in MATLAB to evaluate the model effectiveness and parameter sensitivity. It was assumed that there was no other road user in front of the target user. To simplify the computation of crossing risk, a random location, which obeyed the normal distribution of the location measurement, was assumed to be the actual location of a train or a road user. In this study, at each time instant t_0 , 20 random locations were selected for each train and each vehicle, separately. The crossing risk was calculated as the average collision frequency based on the 20×20 random location combinations.

Two scenarios were tested: no-control and control. The signal and gate control were operated for the control scenario, while no controls were operated for the no-control scenario. The two scenarios were designed to show the safety performance difference resulting from traditional control treatments. Three specific cases were simulated for one-parameter sensitivity analysis: Case 1 varied the road user's initial speed and fixed the other parameters; Case 2 varied the vehicle's initial locations and fixed the other parameters; Case 3 changed the communication latency only but fixed the other parameters; and Case 4 changed the standard deviations of GPS position measurements while other parameters were fixed. Table 1 lists the model parameter values used in the

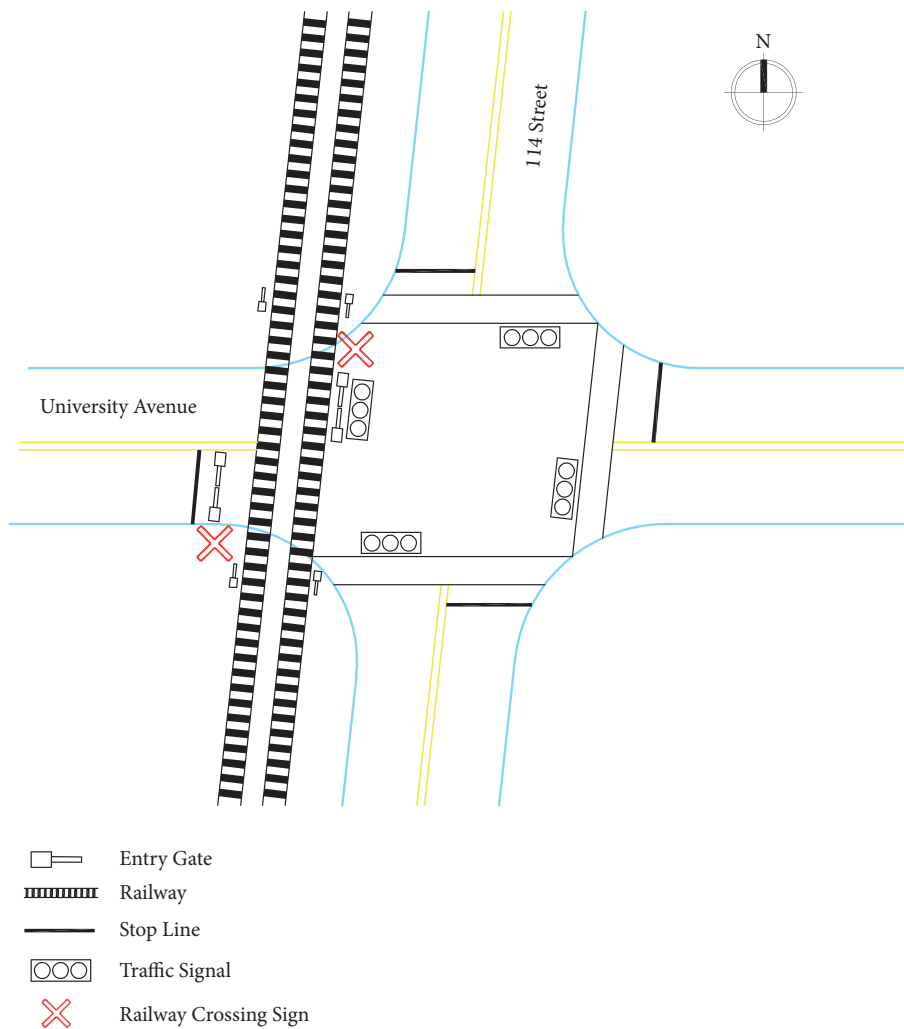


FIGURE 3: Study site.

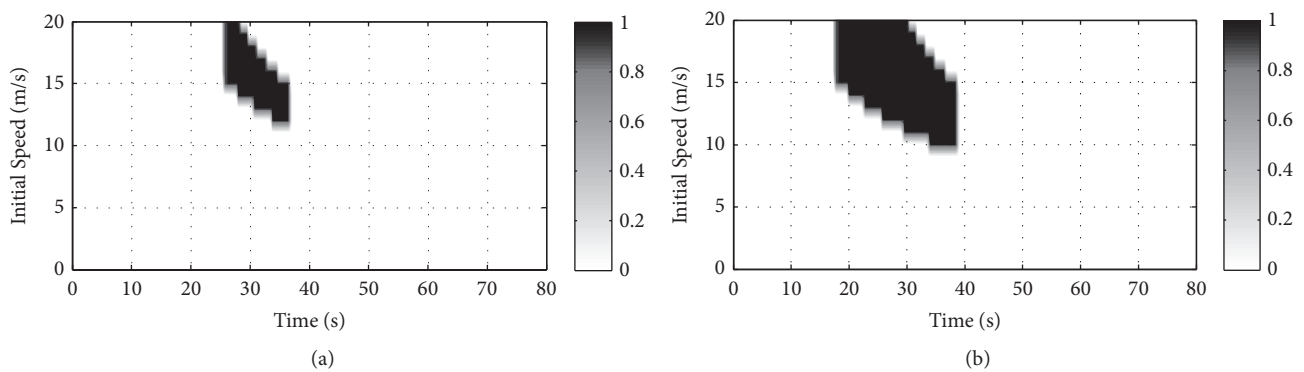


FIGURE 4: Crossing risk probability for different initial road user speeds. (a) No-control scenario. (b) Control scenario.

simulation. The three cases show how the crossing risk varies for road users in different conditions.

Figures 4–7 show the simulation results for the three cases, respectively. Throughout the contour maps, the high-risk areas in parts (a) in all figures are the collisions with the train, while those in parts (b) are the collisions with

the gate. Obviously, the high-risk areas in parts (a) are all larger than those in parts (b). These results show that the traditional control equipment at the grade crossing can keep road users away from trains. In this way, the traditional control equipment effectively reduces collision frequency and severity.

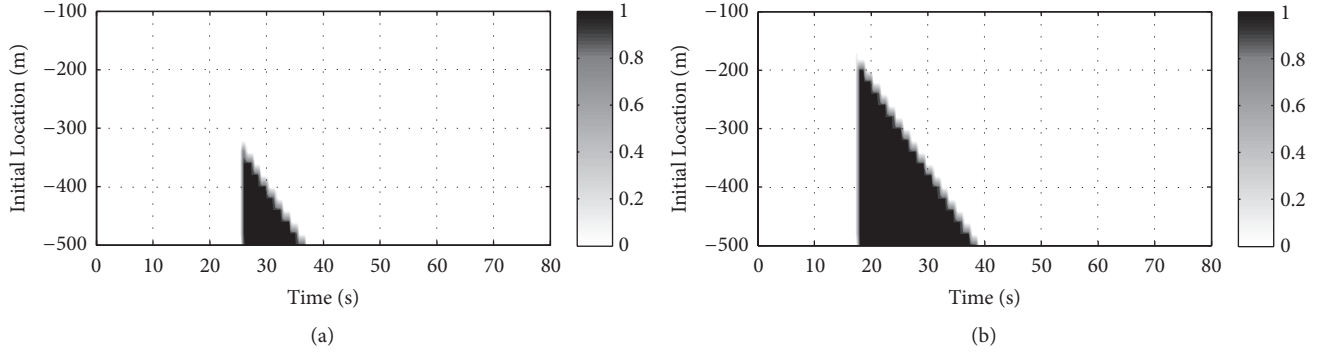


FIGURE 5: Crossing risk probability for different initial locations. (a) No-control scenario. (b) Control scenario.

TABLE 1: Model parameter values in simulation. (a) Location parameters. (b) Speed parameters. (c) Communication latency parameter. (d) Other parameters.

(a)	
Parameter	$p_{r,0}(x_{r,0}, y_{r,0})$ [m]
Value	(500, 0)
	Case 1: (0, -500)
	Case 2: (0, -500 ~ -100)
	Case 3: (0, -500)
	Case 4: (0, -500)

(b)				
Parameter	$v_{r,x,0}$ [m/s]	$v_{r,y,0}$ [m/s]	$v_{u,x,0}$ [m/s]	$v_{u,y,0}$ [m/s]
Value	-15	0	0	Case 1: 0 ~ 20
				Case 2: 15
				Case 3: 15
				Case 4: 15

(c)	
Parameter	t_{cl} [s]
Value	Case 1: 0.1
	Case 2: 0.1
	Case 3: 0~1
	Case 4: 0.1

(d)					
Parameter	t_{prt} [s]	t_g [s]	$T_{threshold}$ [s]	$\delta_{r,x}, \delta_{r,y}, \delta_{u,x}, \delta_{u,y}$ [m]	t [s]
Value	2	3	10	Case 1: 3	0.2
				Case 2: 3	
				Case 3: 3	
				Case 4: 0~10	

In addition to the high-risk conditions, there are other conditions that will not cause a collision. For example, if a pedestrian walks at 1 m/s in the control scenario of Case 1 (see Figure 4(b)), the pedestrian has no collision risk as predicted by the model. As a result, the model can predict the collision risk at grade crossings. Road users and trains have collision risks only under certain conditions, which are combinations of real-time road user and train travel speeds, locations, and other environmental factors. Only the road users who are in risk of collision will be alerted to the impending collision. In contrast, road users who do not have a collision risk will not

receive a warning. Additionally, the model estimates waiting time so that road users can plan their travel behaviours. By these means, the model improves the warning system reliability and user compliance.

Moreover, as shown in Figure 4, the collision risk decreased with a decrease in speed. This means that early speed reduction can remarkably reduce collision probability and severity. As for communication latency, as shown in Figure 6, considering communication latency in the model provides earlier warning. Thus, the consideration of communication latency in the model has a positive impact on the risk

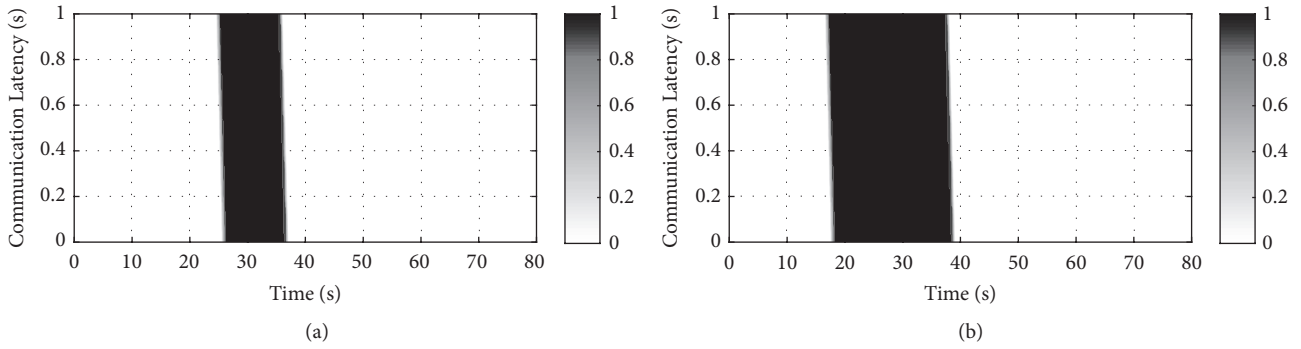


FIGURE 6: Crossing risk probability for different communication latencies. (a) No-control scenario. (b) Control scenario.

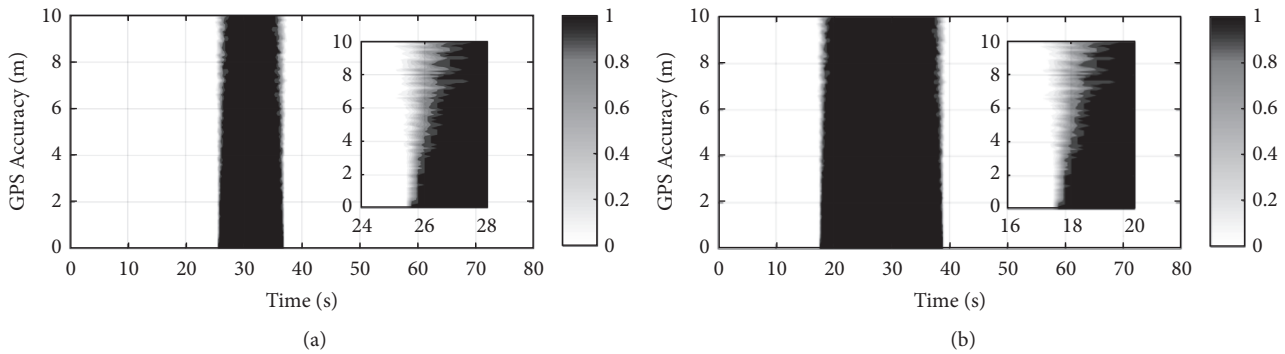


FIGURE 7: Crossing risk probability for different GPS accuracy. (a) No-control scenario. (b) Control scenario.

assessment and system effectiveness. For GPS accuracy, when crossing risk probability is about to increase, compared with a smaller standard deviation of GPS position measurements, a larger one generates a lower risk probability. As the system predetermines a warning threshold, the warning delay is minor even when the standard deviation is 10 m, which is the positioning accuracy obtained from nearly the least accurate GPS devices in practice.

4.3. Field Test Results. After the model performance was confirmed in simulation, the active warning system was tested in the field. During the field tests, the OBE devices, which are self-contained portable units, were placed on LRT trains and in the test vehicle. The OBE devices transmitted messages between one another via DSRC. The active warning system described in the last section was coded in C++ for the field test. The location-specific parameters of the grade crossing were input into the model beforehand. The field tests were conducted from 1 PM to 2 PM on July 13, 2018. During the tests, the test vehicle with OBE and smart devices travelled across the intersection. Using the real-time information from the test vehicle and trains collected every 1 s, the risk assessment model in the system predicted the collision risk 30 s in advance. The communication latency value in the model was 0.1 s and the standard deviation of GPS position measurements was 3 m. Once the model obtained a high-risk probability, the system sent out the warning to the vehicle driver. Along with auditory alerts, the smart devices displayed warning messages and waiting times when an LRT



FIGURE 8: User interface on smart devices.

approached or crossed (as displayed in the interface shown in Figure 8). Real-time location and speed data from both the LRT and the vehicle was collected to evaluate the CV technologies and improve the safety of grade crossings.

Figure 9 shows the results from the two field tests. In the first test (Figure 9(a)), the test vehicle travelled from the west to the east along University Avenue, while an LRT train travelled from the north to the south. At the time of 13:17:20, the warning system predicted that the vehicle and train would have a high collision risk at 13:17:31 under their current speed and location combination. The system alerted the vehicle driver by auditory and visual warnings. After the warning, the vehicle driver decelerated and stopped behind the stop

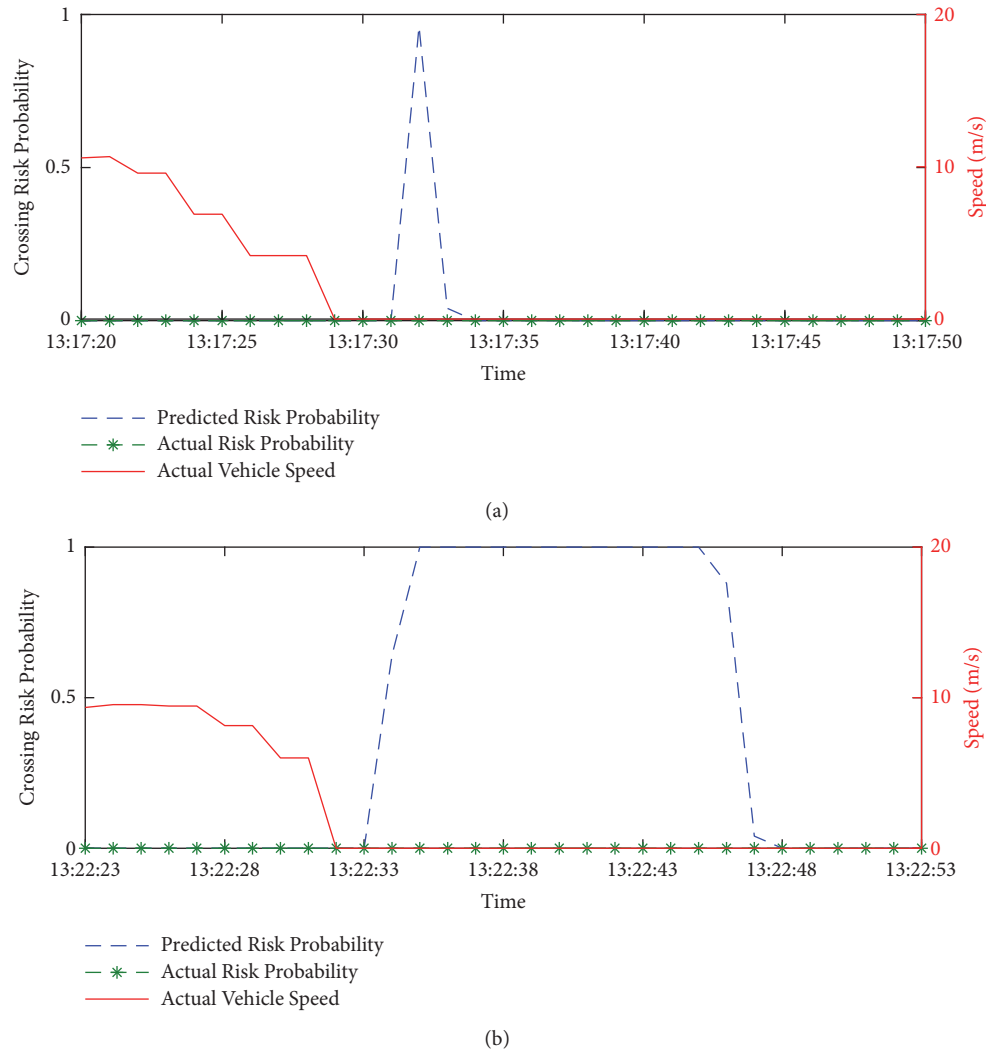


FIGURE 9: Field test results. (a) Test 1. (b) Test 2.

line. With the help of the warning system, the crossing risk remained at zero during the test. Likewise, in the second test (Figure 9(b)), another train travelled from the north to the south while the test vehicle travelled from the east to the west. At the time of 13:22:23, the warning system sent out a warning message to alert the driver of the potential collision risk. After the driver decelerated gradually, the predicted risk decreased. Based on the observations from the two tests, it can be concluded that the proposed grade crossing warning system forecasts collision risk, alerts road users to take proactive driving behaviours, and decreases collision risk.

5. Conclusions and Future Work

Traffic safety at highway-rail grade crossings is a major concern for transportation authorities and the public at large. CV technologies have performed well in active driver assistance systems. This paper presented an active warning system, which aims at eliminating collisions at grade crossings. The proposed model and system were evaluated in simulation and

field tests. The simulation and field tests revealed several key findings.

(a) The proposed model predicts the crossing risk in near future based on real-time information from road users and trains. The developed system sends auditory and visual alerts to road users who are at risk of a collision. Results from the simulation and field tests show that the accurate estimation of risk probability enhances the system effectiveness and reliability.

(b) When road users have collision probabilities with trains, the collision risk decreases with a decreased speed. The early deceleration alert given by the proposed active warning system effectively mitigates collision risk.

(c) The proposed active warning system performed well in field tests. After the drivers responded to the warning messages, the collision risk decreased remarkably compared with the predicted risk probability.

Based on the findings, future work will make effort to evaluate the warning system in various grade crossing locations and traffic scenarios. In the present study, only communication latency was considered in the proposed

model, future work will also analyse the system performance based on other important communication parameters, for example, packet loss rate. In addition, more field tests are required to assess the model parameter relationships, system performance, and reliability.

Data Availability

The GPS data used to support the findings of this study are available from the corresponding author upon request.

Conflicts of Interest

The authors declare that there are no conflicts of interest regarding the publication of this paper.

Acknowledgments

The authors would like to thank the anonymous reviewers for their valuable comments and suggestions that have contributed tremendously to improving the quality of our manuscript. This research work was jointly supported by Transport Canada, the National Natural Science Foundation of China (61703236), Shandong Provincial Natural Science Foundation, China (ZR2017QF014), and China Postdoctoral Science Foundation Funded Project (2017M612275).

References

- [1] "Transportation Safety Board of Canada, "Railway occurrences 2016,"" <http://www.tsb.gc.ca/eng/stats/rail/2016/sser-ssro-2016.asp>, 2017.
- [2] C.-J. Hsu and E. G. Jones, "Sensitivity analyses of stopping distance for connected vehicles at active highway-rail grade crossings," *Accident Analysis & Prevention*, vol. 99, pp. 210–217, 2017.
- [3] D. Noyce, H. U. Bahia, J. M. Yambó, and G. Kim, *Incorporating road safety into pavement management: maximizing asphalt pavement surface friction for road safety improvements*, Midwest Regional University Transportation Center Traffic Operations and Safety (TOPS) Laboratory, University of Wisconsin–Madison, 2005.
- [4] S. J. Gent, S. Logan, and D. Evans, "Automated-horn warning system for highway-railroad grade crossings: Evaluation at three crossings in Ames, Iowa," *Transportation Research Record: Journal of the Transportation Research Board*, vol. 1708, pp. 77–82, 2000.
- [5] B. F. Gilleran, "Use of pre-signals in advance of a highway-rail grade crossing: A specialized tool with specific applications," *ITE Journal (Institute of Transportation Engineers)*, vol. 76, no. 5, pp. 22–25, 2006.
- [6] S.-R. Hu and J.-P. Lin, "Effects of three advanced devices on preventing crashes and gate-breaking incidents at highway-rail grade crossings," *Transportation Research Record: Journal of the Transportation Research Board*, vol. 2384, pp. 109–117, 2013.
- [7] Y. J. Moon and F. Coleman III, "Highway-rail quad gate operation time by system simulation of dynamic dilemma zone," *Journal of Transportation Engineering*, vol. 129, no. 3, pp. 253–261, 2003.
- [8] J. T. Siques, "Pedestrian warning and control devices, guidelines, and case studies," *Transit Rail, Commuter Rail, Major Activity Center Circulation Systems, Light Rail, and Ferry Service*, vol. 1762, no. 1, pp. 18–24, 2018.
- [9] M. Hartong, R. Goe, C. Farkas, and D. Wijesekera, "PTC-VANET interactions to prevent highway rail intersection crossing accidents," in *Proceedings of the IEEE 65th Vehicular Technology Conference - VTC2007-Spring '07*, pp. 2550–2554, Dublin, Ireland, 2007.
- [10] B. Ku, "Grade-Crossing Safety," *IEEE Vehicular Technology Magazine*, vol. 5, no. 3, pp. 75–81, 2010.
- [11] S. Landry, M. Jeon, P. Lautala, and D. Nelson, "Getting active with passive crossings: Investigating the use of in-vehicle auditory alerts for highway-rail grade crossings," in *Proceedings of the Joint Rail Conference, JRC '16*, Columbia, SC, USA, 2016.
- [12] T. W. Tedesso, C. Rowe, C. R. Anderson, and C. B. Dietrich, "Propagation measurements at 5.8 GHz for railroad intelligent transportation systems," in *Proceedings of the IEEE Wireless Communications and Networking Conference, WCNC '17*, San Francisco, Calif, USA, March 2017.
- [13] K. David and A. Flach, "CAR-2-X and pedestrian safety," *IEEE Vehicular Technology Magazine*, vol. 5, no. 1, pp. 70–76, 2010.
- [14] A. Tahmasbi-Sarvestani, H. Kazemi, Y. P. Fallah, M. Naserian, and A. Lewis, "System Architecture for Cooperative Vehicle-Pedestrian Safety Applications Using DSRC Communication," in *Proceedings of the World Congress and Exhibition SAE '15*, vol. 2015, Detroit, Mich, USA.
- [15] S. E. Shladover and S.-K. Tan, "Analysis of vehicle positioning accuracy requirements for communication-based cooperative collision warning," *Journal of Intelligent Transportation Systems: Technology, Planning, and Operations*, vol. 10, no. 3, pp. 131–140, 2006.
- [16] M. Wang, W. Daamen, S. P. Hoogendoorn, and B. van Arem, "Connected variable speed limits control and car-following control with vehicle-infrastructure communication to resolve stop-and-go waves," *Journal of Intelligent Transportation Systems: Technology, Planning, and Operations*, vol. 20, no. 6, pp. 559–572, 2016.
- [17] "Transport Canada, Grade crossings standards," 2014, <https://www.tc.gc.ca/eng/railsafety/grade-crossings-standards.htm>.
- [18] D. D. Peterson and D. S. Boyer, *Feasibility Study of In-Vehicle Warning Systems*, U.S. Department of Transportation, Wash, D.C., USA, 1975.
- [19] M. F. Aycin and R. F. Benekohal, *Performance Evaluation of The Pilot Study of Advisory On-Board Vehicle Warning Systems at Railroad Grade Crossings*, The Illinois Department of Transportation, 2002.
- [20] A. Carroll, A. Passera, and I. Tingos, *Vehicle proximity alert system for highway-railroad grade crossings prototype research*, U.S. Department of Transportation, Wash, D. C., USA, 2001.
- [21] S. He, J. Li, and T. Z. Qiu, "Vehicle-to-pedestrian communication modeling and collision avoiding method in connected vehicle environment," *Transportation Research Record: Journal of the Transportation Research Board*, vol. 2621, pp. 21–30, 2017.
- [22] Transport Canada, *Grade Crossing – Handbook*, 2016, https://www.tc.gc.ca/media/documents/railsafety/RDIMS-12526323-v50-OD-EN-HQ-GCR_HANDBOOK_WEB_VERSION.PDF.
- [23] American Association of State Highway and Transportation Officials (AASHTO), *A policy on geometric design of highways and streets, 2011*, Wash, D.C., USA, 2011.

Research Article

Advanced Modeling and Simulation of Vehicle Active Aerodynamic Safety

Krzysztof Kurec ¹, Michał Remer ¹, Jakub Broniszewski ¹, Przemysław Bibik ¹,
Sylwester Tudruj² and Janusz Piechna ¹

¹Warsaw University of Technology, Institute of Aeronautics and Applied Mechanics, Warsaw 00-665, Poland

²Warsaw University of Technology, Institute of Micromechanics and Photonics, Warsaw 02-525, Poland

Correspondence should be addressed to Janusz Piechna; jpie@meil.pw.edu.pl

Received 3 August 2018; Accepted 6 January 2019; Published 3 February 2019

Guest Editor: Mihai Dimian

Copyright © 2019 Krzysztof Kurec et al. This is an open access article distributed under the Creative Commons Attribution License, which permits unrestricted use, distribution, and reproduction in any medium, provided the original work is properly cited.

The aim of this study was to extend the safety limits of fast moving cars by the application, in a controlled way, of aerodynamic forces which increase as the square of a car's velocity and, if left uncontrolled, dramatically reduce car safety. This paper presents the methods, assumptions, and results of numerical and experimental investigations by modeling and simulation of the aerodynamic characteristics and dynamics of a small sports car equipped with movable aerodynamic elements operated by an electronic subsystem for data acquisition and aerodynamics active automatic control.

1. Introduction

Currently, the trend to minimize emissions by limiting fossil fuel consumption leads to lighter cars with a low drag coefficient. This situation introduces new challenges for car designers. They need to ensure that stability will be good enough to allow safe driving in all road conditions (wind gusts, moving obstacles, etc.). Studies found in the literature mainly focus on sensitivity to lateral wind. These methods attempt to reproduce the test procedure according to the ISO 12021:2010 standard [1]. However, it is rather rare to take into account the coupling of car dynamics and aerodynamics. Very often, it is assumed that car movement will not affect aerodynamic forces. The study presented in [2] is in contrast to this assumption. The authors have shown that the inclusion of a bidirectional fluid structure interaction can lead to a significant change in the aerodynamics forces.

The development of the quality of highways together with the increase in the potential maximum speed of cars has turned the attention of car designers towards the dynamic features of cars at high speeds. The external shapes of cars are typically optimized for low aerodynamic drag. Unfortunately,

such action has drawbacks in the form of car bodies generating aerodynamic lift forces at high speed, together with a decrease in a car's directional stability and reduction of safety limits during fast cornering. The frailty of the car body shape is typically compensated by fixed or movable aerodynamic elements activated at high speed. Typically, such aerodynamic elements have the form of a wing, generating downforce which compensates the lift force generated by the car body. The additional aerodynamic elements generate additional drag, so it is desirable to activate the movable elements only when necessary. Some sports cars such as, for example, the Porsche 918 Spyder [3], have predefined aerodynamic settings for a specific range of speeds which make it possible to either minimize drag or maximize downforce, while the active aerodynamics of the McLaren Senna additionally enables it to shift the aerodynamics balance towards the rear of the car to enhance braking. These two examples relate to a case when the active aerodynamics is used to support the maneuvers performed by the driver. However, with the increased number of different types of sensors [4] that can be mounted on a car, it is possible to design a driver assistance system that is able to evaluate the current road conditions [5] and automatically modify the aerodynamic properties. One example where

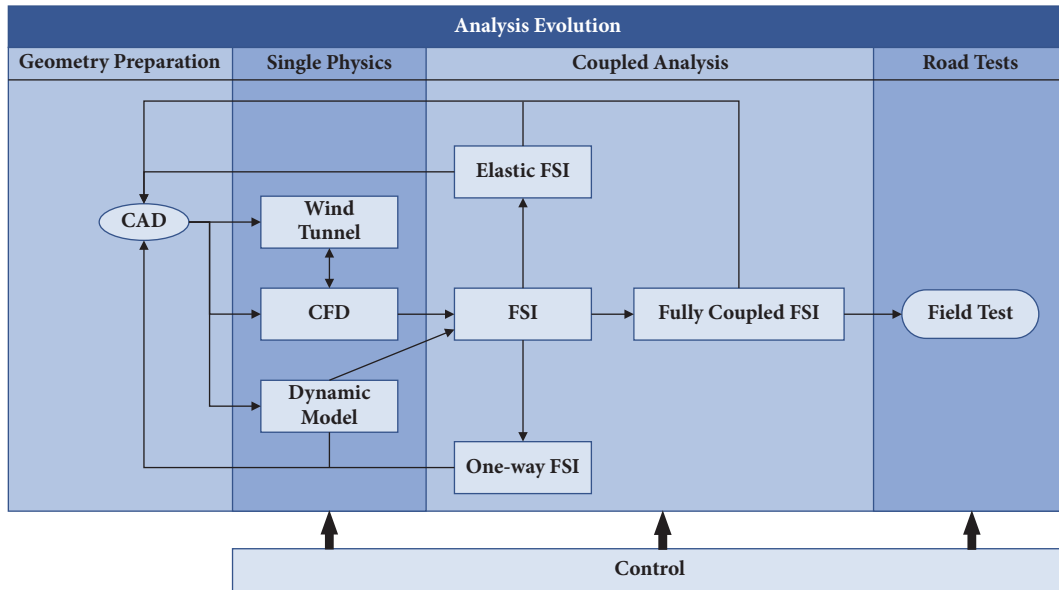


FIGURE 1: Scheme of the data flow in the project of vehicle active aerodynamic safety, where CAD is computer aided design, CFD is computer fluid dynamics, and FSI is fluid structure interaction.

a driver can be assisted during a rapid maneuver could be the use of machine vision technology to estimate the road curvature [6] and utilize the driving assistance system to assess not only whether the speed is within the safety margin but also whether the vehicle's aerodynamic setup is the most appropriate for the car's safety. This could also give the time essential to perform more significant movements of the active aerodynamic surfaces so that a higher value of the aerodynamic forces can be utilized, even before the driver realizes that some kind of action needs to be taken. The introduction of autonomous driving itself can make it possible to increase safety limits during rapid maneuvers [7]. The development of such systems needs to rely on model based validation due to the costs and complexity, which was emphasized by researchers developing a highway pilot assisting the driver [8].

An aerodynamic active control system requires information about the actual state of the car, the position of the movable aerodynamic elements located on the car body and the steering algorithms. This paper presents information about the methods used for modeling and simulation to develop an active system extending the safety limits of a fast moving car. The electronic control system is the key to the integration of many aspects of scientific and technical activity.

It was considered that information can be collected from sensors located inside the car and that a set of movable aerodynamic elements would be attached to the car body to form a control loop. The control part of the system was assumed to be open for programming taking into account information about the characteristics of the sensors, the actuators and the aerodynamic characteristics of the added aerodynamic elements. The general scheme of data flow in the project is presented in Figure 1.

2. System of Data Acquisition and Active Control of Movable Aerodynamic Elements

A measurement and control system was developed to achieve the project goals. It was decided that, for research purposes, the system should be flexible and easy to modify. The other requirement for the hardware was immunity to vibrations and an ability to work in a broad range of environmental conditions. For those reasons, an industrial real-time controller was selected as the core of the system. The controller was fitted with a set of different types of communication interfaces, which enabled the connection of different sensors and devices. The general architecture of the developed system is presented in Figure 2. The whole system is divided into three subsystems: the measurement subsystem, the actuation (control) subsystem, and the user interface.

The measurement subsystem consists of several sensors together with their interfaces. In the current configuration, all the sensors were connected to the system controller via RS-232C interfaces. The main sensor is an integrated GPS (Global Positioning System) and AHRS (Attitude and Heading Reference System) sensor. This sensor provides navigation and vehicle state data: linear acceleration, linear velocity components, inertial position, angular rates, and attitude angles in three perpendicular axes. All the data was collected at a frequency of 200 Hz. The next sensor is the vehicle control measurement sensor. This sensor provides data of the vehicle steering wheel angle and the throttle and brake pedal positions at a frequency of 100 Hz. These two sensors are sufficient for the control of the vehicle aerodynamic surfaces. For some parts of this research, the system may also use suspension deflection sensors which use linear potentiometer sensors in each of the vehicle shock absorbers.

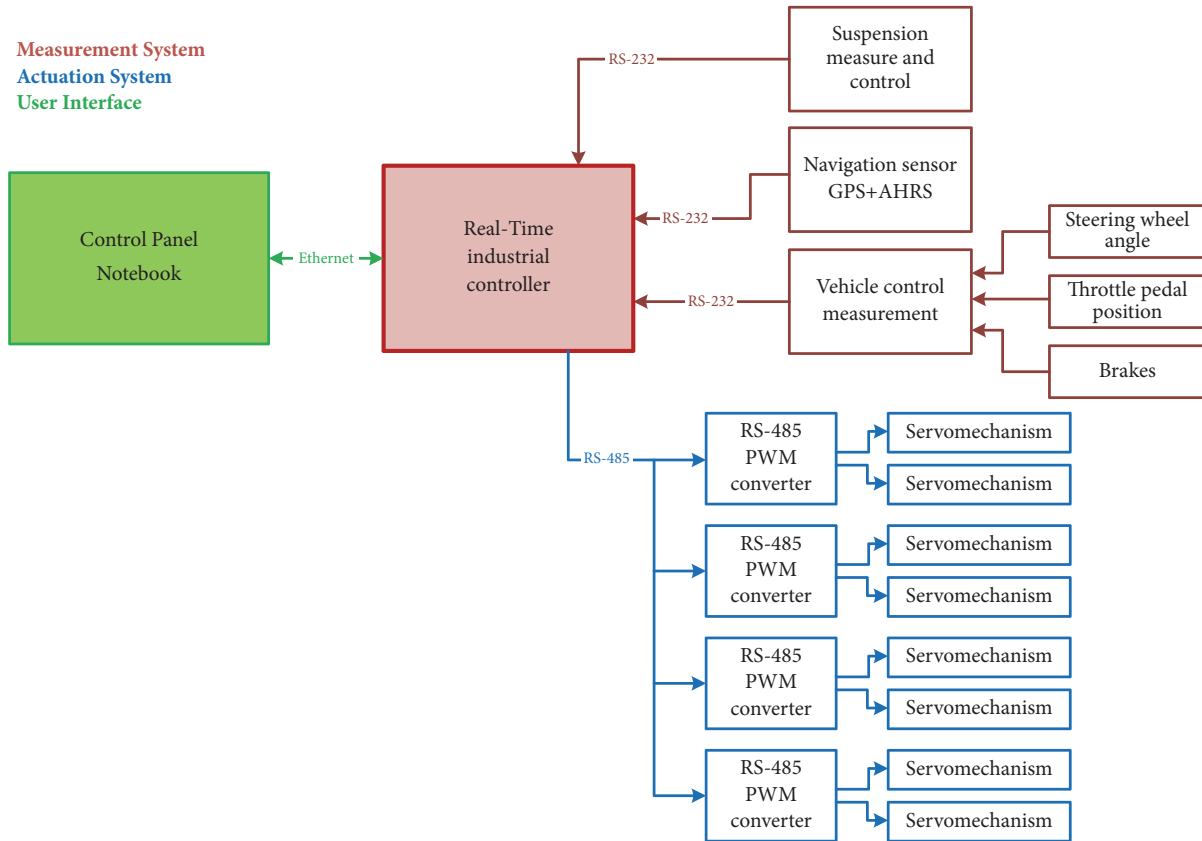


FIGURE 2: Hardware architecture of the measurement and control system.

The actuation subsystem consists of two parts, actuation of aerodynamic elements and suspension control. The aerodynamic surfaces are fitted with PWM (Pulse Width Modulation) signal controlled servomechanisms. An RS-485 interface is used to control those servomechanisms and all servomechanisms are connected to the RS-485 control line via signals converters. All servomechanisms are controlled at a frequency of 20 Hz.

The third subsystem is the user interface. The GUI is installed on the notebook connected to the system controller via an Ethernet interface. The GUI allows the operator to observe the measurement data, configure the controller (different modes of operation are possible), and manually control the aerodynamic surfaces. The RT controller may also be configured to operate in a fully automatic way without the user control interface panel connected.

The system software was developed using National Instruments LabVIEW software. The main objective of the application was to ensure real-time operation of the system. Several parallel modules are defined in the architecture of the software (see Figure 3). The system processes module is responsible for governing the operation of the system. The user interface communication module exchanges data with the user control panel by sending sensor readings and receiving commands and instructions from the user. The data acquisition module ensures communication with the sensors and is responsible for the synchronous reading of

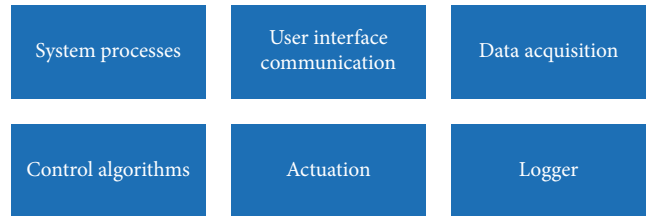


FIGURE 3: System software modules.

data from all sensors. The control algorithms module receives data from the data acquisition module and processes the data according to defined control laws and sends commands to the actuation module which then sends the commands to all control elements. The logger module records both data from all sensors and all control commands during operation of the system.

3. Models and Simulations

The aim of the presented study was to extend the safety limit of a fast moving vehicle in conditions of strong changes to the atmospheric and physical environment and the rapid reactions of the driver. Widely used ESP systems for vehicle stabilization use forces generated during braking of selected

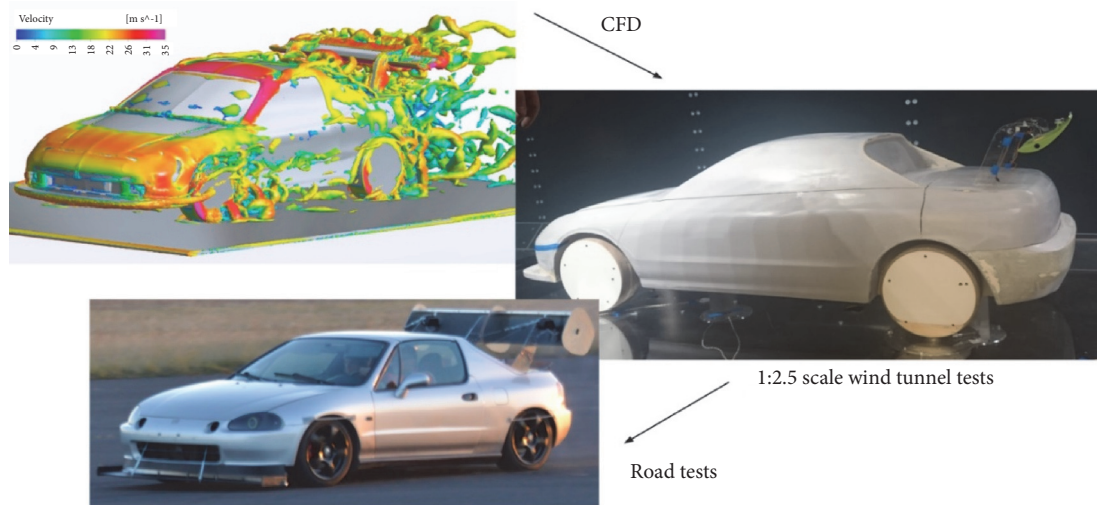


FIGURE 4: The three different types of aerodynamic study.

vehicle wheels. In this analysis, it is proposed to use aerodynamic forces for this purpose. The results of the active actions of moving aerodynamic elements aimed at stabilizing vehicle motion are discussed below. During the development of a new aerodynamic solution, it is necessary to identify the problems to be solved and the tools needed to achieve the goal. The final solution should be tested in real life on a test car; however, a wide range of modeling techniques can be utilized to aid development.

3.1. The Use of a Variety of Different Modeling Techniques.

In the analyzed case, the objective is to actively control the aerodynamic properties of a light sports car such as the Honda CRX del Sol. It was recognized that the conclusions resulting from the flow analysis of this car could be extended to many other high-speed designs. The geometry of this car is presented in Figure 4 which shows the car used during track tests together with its wind tunnel model and CAD model incorporated into the CFD calculations.

The most important data was recorded during the test rides and gave the answer to the question of which aerodynamic setups were the most efficient to control the car's dynamics, while the results from the CFD calculations were used to complement the data acquired during wind tunnel tests and were used to gain additional knowledge of the nature of the flow around the car body. Each of the described actions is shown in Figure 4 to emphasize the fact that a very wide range of data can be obtained by employing them all together. The use of modeling techniques makes it possible to study many different scenarios, including scenarios that could be dangerous to test on a real car.

Below, a brief review of the modeling techniques used is presented, starting with the wind tunnel tests through to the different kinds of modeling based on CFD calculations. In each consecutive case, the CFD calculations were expanded by additional elements. In most cases of traditional automotive aerodynamics, stationary and solid bodies are being

investigated. This paper describes more advanced techniques that are essential to accurately predict the behavior of a car subjected to active control by moving aerodynamic surfaces. This includes studies of such cases as the movement of the rear wing, the behavior and influence of deformable surfaces attached to the car body, as well as a complete simulation of a moving car. Apart from the simulations, the development of an algorithm enabling the control of moving aerodynamic elements is presented as well.

To carry out the proposed activities, the following software was selected:

- (1) to construct the 3D geometry of a vehicle and moving aerodynamic elements installed on its body; it was assumed that SolidWorks, Unigraphics software, and software included in the ANSYS-Fluent package would be used;
- (2) for vehicle body flow analysis; it was assumed that CFD ANSYS-Fluent commercial software would be used together with the freely available OpenFOAM software;
- (3) for vehicle dynamics; it was assumed that MCS.Adams/Car would be used alongside Matlab/Simulink as an interface between MCS.Adams and ANSYS-Fluent;
- (4) in-house software for analyzing the motion of deformable elastic car body parts and simulating the dynamics of vehicle body motion.

Taking into account the multidisciplinary problems accompanied by the main and general problem, some new ideas of transferring expert knowledge to the engineering level can be applied. An example is the SORCER software [9] used by some team members for the solution of other problems. The idea of preparing software blocks by experts to solve separate detailed problems and integrating individual solutions into a bigger and wider problem consideration is the basis of the SORCER software. Due to the personal limitation of the team

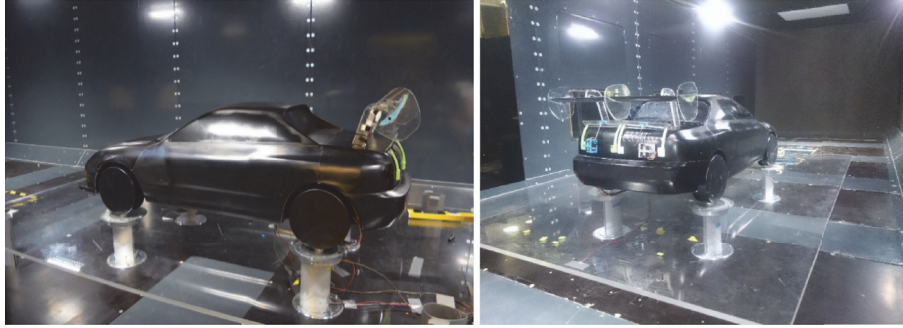
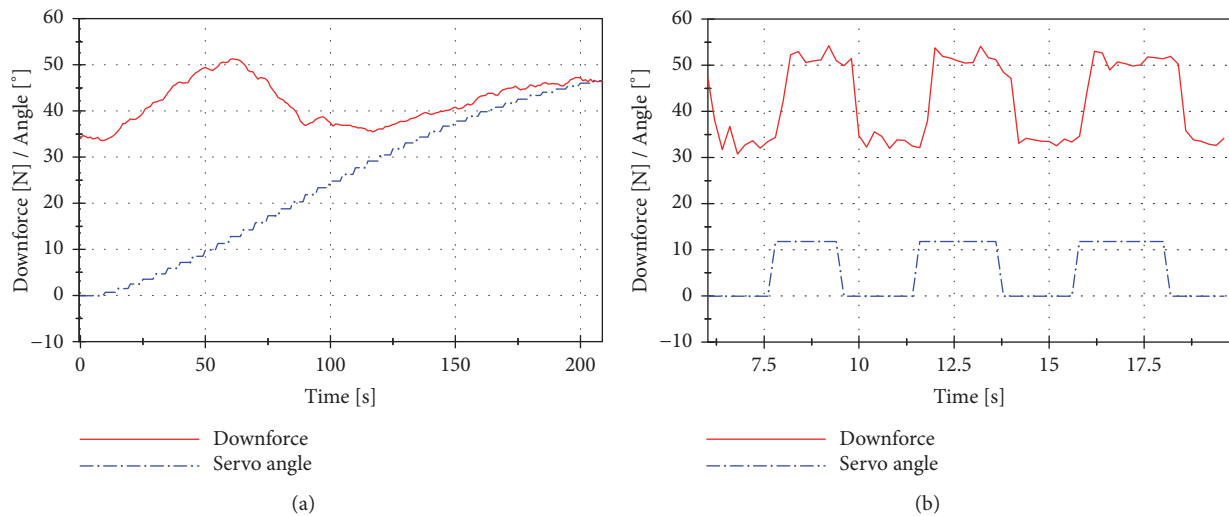


FIGURE 5: Model of the vehicle in the wind tunnel.

FIGURE 6: Characteristics of the downforce and the servo angle for (a) a slow movement of the wing and (b) quick changes of the wing's placement from -5° up to 50° .

engaged in problem development it was finally decided to use a more conventional approach.

3.2. Investigations of the Flow in the Wind Tunnel on a Scaled Down Model. As the flow around a vehicle equipped with additional aerodynamic surfaces has a sophisticated nature, experimental fluid mechanics is the best way to acquire knowledge about the aerodynamic forces acting on a car body. In the presented study, the experimental measurements of the aerodynamic forces were collected during the wind tunnel tests performed on a model of the Honda CRX del Sol. The model of the car body was prepared at a 1:2.5 scale and was thoroughly tested in the wind tunnel at an inflow velocity of 23 m/s and at a turbulence intensity equal to 3.5%, whereas the Reynolds number exceeded two million. The experimental set-up was equipped with four load cells, each installed below a wheel of the vehicle, measuring appropriate forces and momentums. The model was laid on a separation plate to reduce the influence of the boundary layer generated on the wind tunnel's walls [10], as can be seen in Figure 5. The model was tested for various configurations, starting with a clean body, without any additional aerodynamics surfaces, and finishing with over six surfaces provided with

servomechanisms. Additionally, the flow was visualized with the use of a Ti_2O oil mixture and minitufts. The results obtained for the clean configuration (see Figure 7) were the reference for further more complicated geometrical configurations, also calculated by means of numerical fluid mechanics. Such a configuration makes it possible to receive both time dependent results for force values and typical static measurements, which were recalculated to nondimensional coefficients of downforce (see Figure 8) and drag force (Figure 8).

The other feature of the wind tunnel results, apart from the ability to study the characteristics of a stationary rigid geometry, is the ability to perform tests of fast and time dependent changes of the airfoil and spoiler attached to the model of the car. Moreover, the typical characteristic of downforce coefficient as a function of the angle of attack is presented (see Figure 8(a)), and information about the forces as a function of time are also provided. The flow response to the vehicle aerodynamic configuration changes is presented in Figures 6(a) and 6(b). The maximum increase of the downforce is generated in less than two seconds for the wing movement from about 20° to the value of maximum angle of attack. Several configurations were tested achieving a

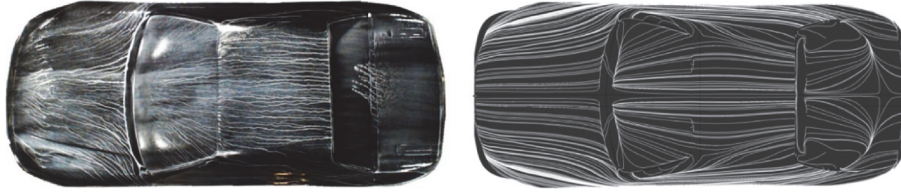


FIGURE 7: Comparison of the experimental visualization of the oil flow over a clean configuration of the car body (left) and from the CFD calculations (right).

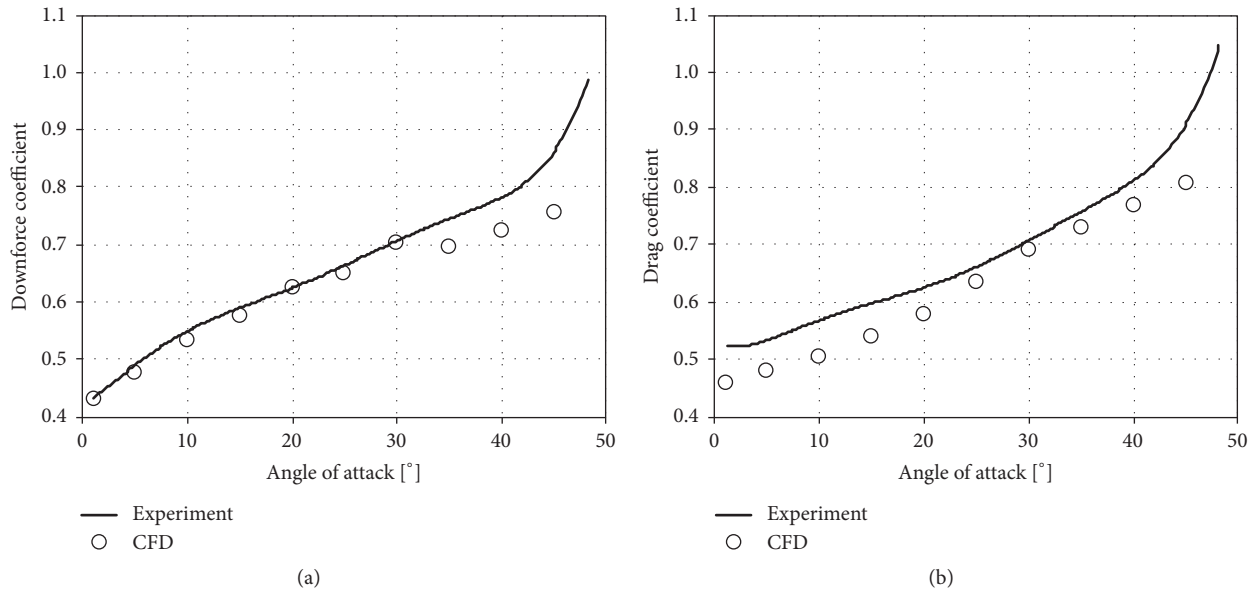


FIGURE 8: Characteristics of (a) the downforce coefficient and (b) the drag coefficient obtained during the wind tunnel measurements of a car with a mounted rear wing and a spoiler, compared with the CFD results acquired for a wide range of angles of attack.

minimum time to reach maximum increase of the downforce is around 0.6 seconds by the movement of a special spoiler.

3.3. Validation of the CFD Calculations. The values of the aerodynamic forces, as well as some of the flow features recorded during wind tunnel testing, were used to perform validation of the CFD methods. A comparison of the flow features on the surface of the car body is presented in Figure 7, whereas in Figure 8 the values of the downforce coefficient together with the drag coefficient obtained during the experiments and the CFD calculations are presented together. It was established that, for a wide range of studied cases, the SST $k-\omega$ turbulence model [11] makes it possible to achieve CFD results close to the experimental data. As can be observed in Figures 7 and 8, a good agreement with the wind tunnel tests was achieved. The SST $k-\omega$ turbulence model is one of the most commonly used turbulence models in the field of automotive aerodynamics [12], however, it is best practice to check it for every specific case being studied.

3.4. The Unsteady Aerodynamics: The Search for the Flow Response Time to the Movement of the Active Aerodynamic

Elements. One of the most commonly used active aerodynamic elements in the field of the automotive design is a rear wing [13]. The main advantage of such a device is its high efficiency, which makes it possible to achieve a high downforce in a trade-off for a relatively low increase of drag. The rear wing is mounted near the trunk at such a distance from the rest of the car body so that it should not create any negative aerodynamic interferences with the car's silhouette. The area of the wing is proportional to the forces that it can generate, so the larger the wing the higher the values of downforce that can be achieved. Unfortunately, the addition of the rear wing can be seen as a disturbance of a car's aesthetics which leads designers to reduce its size, or to create a mechanism to enable the wing to hide within the car's silhouette or even to completely remove it. Currently, most sports cars have some sort of rear wing, which is used to enhance the car's handling at high speeds. In the case of some cars, for example, the Bugatti Veyron, the rear wing also works in braking mode, by rotating to a high angle of attack, creating additional drag that slows the car down.

If the rear wing is designed to be an active aerodynamic element, apart from its aerodynamic characteristics, it is very important to know how it will be controlled and adjusted to

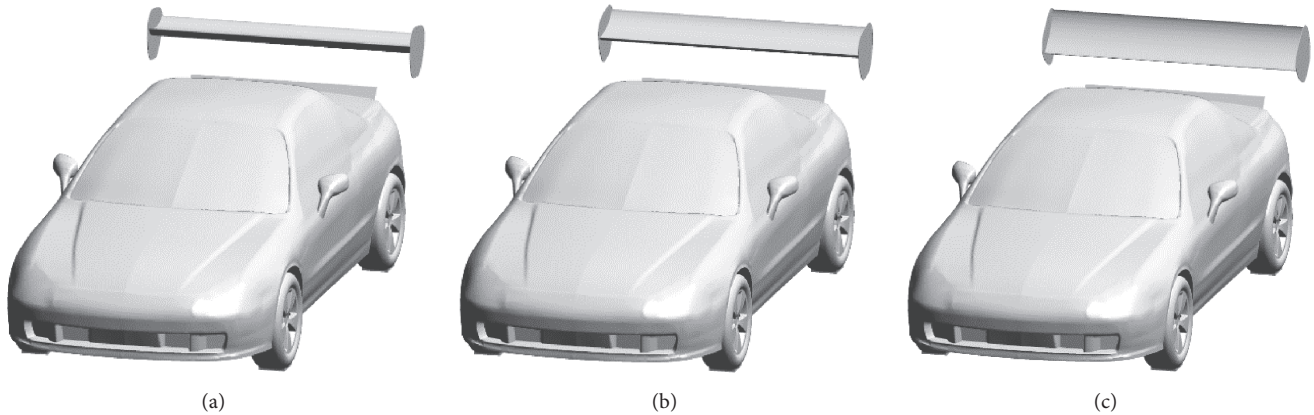


FIGURE 9: The car body with the rear wing set to the three different angles of attack: (a) 0° , (b) 20° , and (c) 50° .

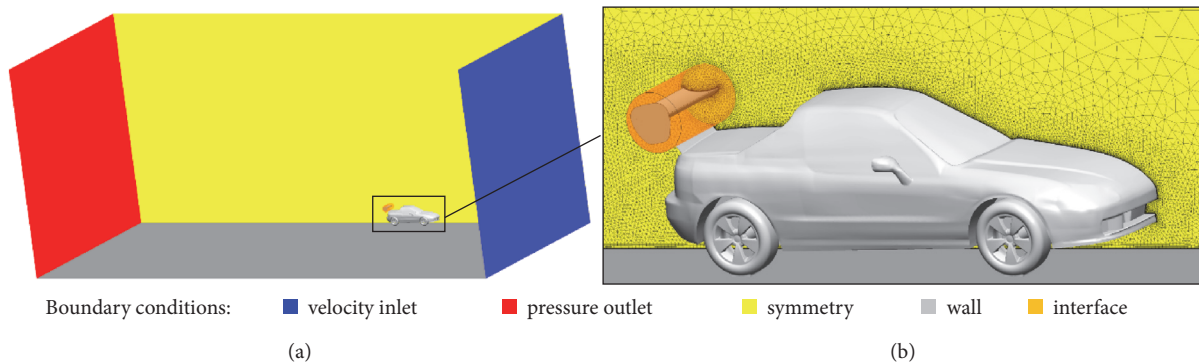


FIGURE 10: (a) Geometry of the computational domain. (b) Close-up on the car body with mesh on the symmetry plane.

the desired angle of attack or moved to a specific location relative to the car's silhouette. For this purpose, in this research, it was decided to use electric servomechanisms due to their ability to perform fast movements that allow adjustments of the car's aerodynamic properties in a short time.

The aim of the study presented in this section was to show the unsteady flow features developing over time due to a change of the rear wing's angle of attack (see Figure 9). This research was performed by means of CFD calculations in ANSYS Fluent. Due to the analysis of the unsteady phenomena, a transient solver was utilized together with the SST $k-\omega$ turbulence model. Two cases were studied. The first case was for the change of the rear wing's angle of attack from 0° to 20° , which corresponds to a scenario in which an additional downforce needs to be generated by the car body to improve the car's handling. The second case was for the change of the angle of attack from 0° to 50° , which significantly increases not only the downforce but also the drag force by raising the frontal area of the car by 14%, which is beneficial during braking maneuvers. The most important difference between those two cases is that for the change of the angle of attack to 20° , the flow only slightly adjusts to the new orientation of the rear wing, whereas for the case in which the angle of attack is changed to 50° , the flow separates from the

wing right at its tip, which creates a separation zone behind it.

The 1:1 scale model of the Honda del Sol was studied within the flow field of the velocity equal to 40 m/s. The domain used in the CFD calculations is presented in Figure 10(a), whereas a close-up of the car itself can be seen in Figure 10(b). The mesh consisted of 11 million tetrahedral elements. The use of the symmetry boundary condition made it possible to perform the calculations only on half of the geometry and thus reduce the total number of elements. To make it possible to change the rear wing's angle of attack, the whole wing together with the side plate was placed inside a cylinder. The cylinder was connected with the rest of the computational domain via a sliding interface. To enable the use of this kind of interface, the rear wing could not include any elements directly connected with the car body. For this reason, the rear wing's mounting was not included in the model. However, the mountings designed for the test car had a "swan shape", which minimized their influence on the downforce generated on the wing, and their omission from the CFD model should not lead to significant discrepancies.

The change of the rear wing's angle of attack over time is depicted in Figures 11(a) and 11(b), the angular velocity of the wing's rotation is the same for both studied cases, which results in the wing reaching an angle equal to 20° in 0.1 s

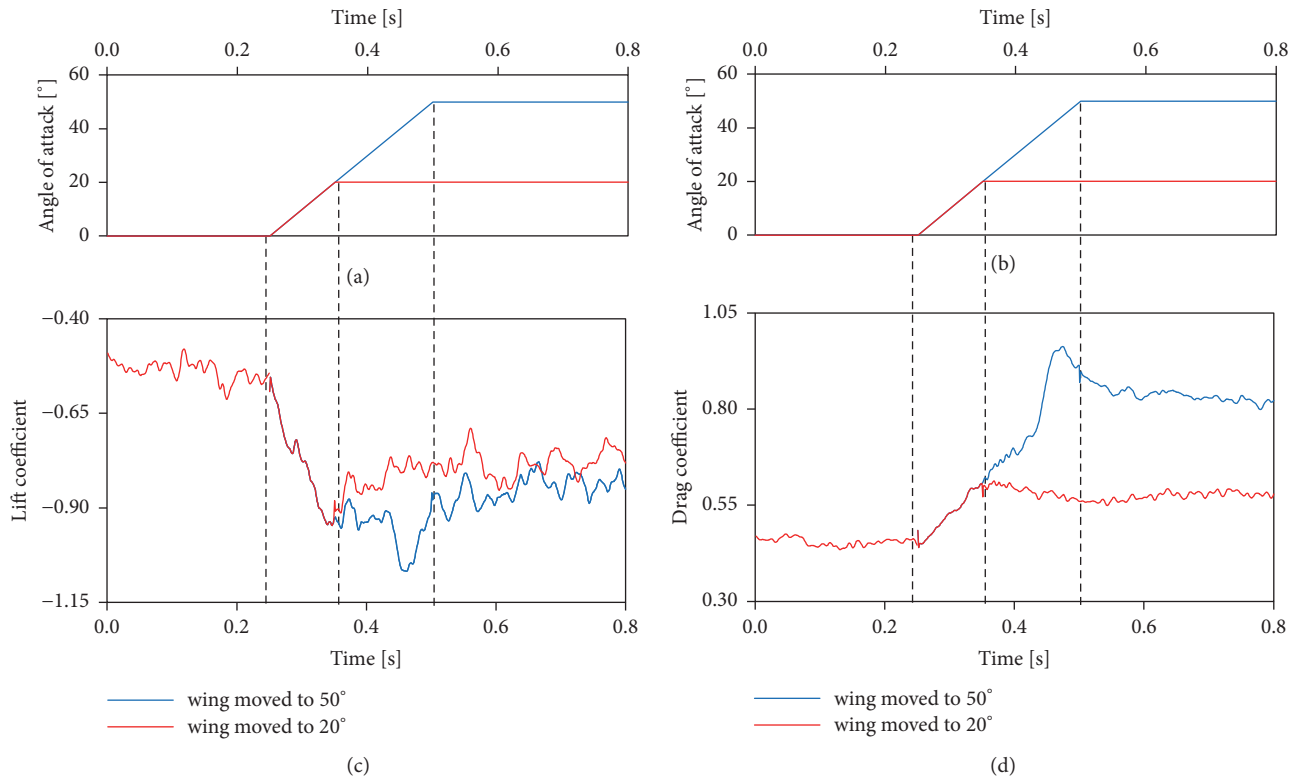


FIGURE 11: (a), (b) Plots of the rear wing's angle of attack. (c) The characteristics of the lift coefficient over time. (d) The characteristics of the drag coefficient over time.

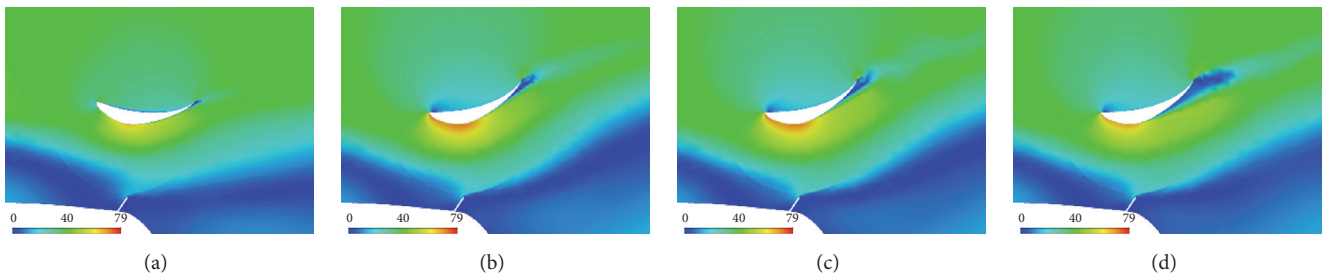


FIGURE 12: Contours of the velocity in the symmetry plane while the wing is moved to 20° at the following time frames: (a) 0.25 s, (b) 0.35 s, (c) 0.40 s, and (d) 0.45 s.

whereas it takes another 0.15 s for it to rotate up to 50°. The characteristics of the lift coefficient and the drag coefficient (see Figures 11(c) and 11(d)) are the same until 0.35 s, which is the time frame when the wing which was rotated to 20° stops moving and the flow conditions for this case stops changing, whereas for the other case, the wing stops rotating at 0.50 s. In both cases, it takes approximately 0.5 s after the wing stops moving for the flow to fully adapt. It should be noted that, due to the unsteady phenomena, the peak of the absolute values of the lift coefficient as well as the drag coefficient are higher than when the flow settles down, which means that with the fast movement of the active aerodynamic elements it is possible to generate an additional aerodynamic force, although only for a very short duration.

The flow features during the different time frames for both of the studied cases are presented in Figures 12 and 13, where it can be seen that the flow only needs to slightly adapt when the wing is set to 20°, whereas after rotation to 50° a recirculation zone is formed behind it and the flow features change significantly. It should also be noticed that there is a spoiler underneath the wing which is redirecting the flow towards it and makes it possible for the air to “stick” to it at higher angles of attack reaching up to 20°.

The data presented above proves that the unsteady phenomena must be taken into account in the control mechanism of the active aerodynamic elements to accurately predict the aerodynamic load that the car body is subjected to.

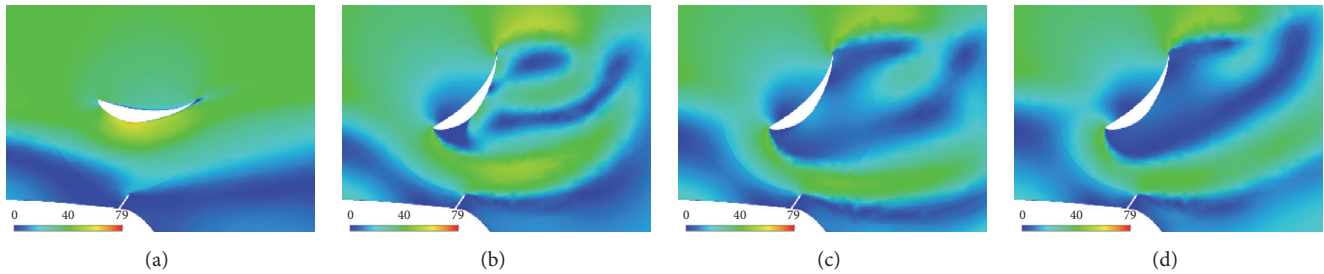


FIGURE 13: Contours of the velocity in the symmetry plane while the wing is moved to 50° at the following time frames: (a) 0.25 s, (b) 0.50 s, (c) 0.55 s, and (d) 0.60 s.

TABLE 1: A comparison of the aerodynamic coefficient values for different variants of the tested car model.

	Drag coefficient	Lift coefficient
Base model	0.506	-0.101
Model with an active airbag	0.557	-0.212
Model with an active airbag and side curtains	0.572	-0.312

3.5. Untypical Movable Add-Ons: Elastic Type of the Active Aerodynamic Elements. Typically, rigid elements are used as movable elements. The motion of such an element is achieved by electric servomechanisms with complicated mechanical elements. A pneumatic system of actuation of flexible movable aerodynamic elements was considered. One such solution is presented below.

As described in previous sections of this paper, a rear wing can be used to generate aerodynamic forces, whereas the value of the force is dependent on the wing's angle of attack. A different kind of solution is also proposed in this study, which incorporates the use of flexible deformable surfaces placed in various locations on the vehicle. These deformable surfaces can have the form of airbags, which in an inactive state adhere closely to the body of the vehicle, whereas in an active state (inflated) change their shape and at the same time modify the shape of the vehicle. Such a change in shape would change the value of the aerodynamic forces acting on the car while driving. Controlling the shape of such surfaces consists of supplying compressed air to their interior, and so the material of the airbag stretches and bulges. Once the air is released the elastic resilient material returns to its original shape, adhering to the car's body. The vehicle model tested was equipped with a splitter partially blocking the inflow of air under the car. The main deformable element used was an airbag placed under the splitter. Additionally, to increase its efficiency, deformable side curtains were used [14], whose task was to block the inflow of air under the car from the outside, i.e., from the external environment (see Figure 14(a)).

It was assumed that compressed air would be used to control the shape of the flexible aerodynamic elements with a much higher pressure when compared with the ambient pressure. Thanks to this, these elements would have a fixed shape, regardless of the speed at which the car moves. To determine the shape that the inflated pneumatic side curtains and the airbag under the splitter would take, FEM numeric simulation was performed using the ANSYS software. The surface of the deformable elements was loaded with air at

constant pressure, under which they assumed the target shape (see Figure 14(b)). It was assumed that the shape changes associated with the dynamic pressure acting on these elements are negligibly small. The values of the forces and aerodynamic coefficients acting on the car were obtained by means of CFD based numerical simulation using the OpenFOAM software (see Figure 14(c)). The results obtained (see Table 1) confirm the possibility of using flexible deformable elements attached to the car to control the value of the downforce acting on it.

To prepare an appropriate algorithm to control the position of aerodynamic movable elements, it is necessary to predict the way these elements change the motion of a car equipped with such elements. To perform such tests, separate software modeling the dynamics of the car influenced by additional aerodynamic elements was designed.

3.6. Numerical Simulation of Car Dynamics Influenced by the Active Aerodynamic Elements. On the one hand, road test data are the deciding data but, on the other hand, the car dynamics are influenced by a lot of unpredictable factors such as tire pressure and temperature, mistakes in suspension geometry, side wind, road inclination, predisposition of the driver, etc. Therefore, independent software for car dynamic analysis was developed and validated by comparison with known solutions [15–17].

Information about the aerodynamic characteristics of the car body had to be transferred to the car dynamic analysis software to check the influence of the proposed modifications. The intention was to have the model with all mechanical coefficients precisely defined and check the car's reaction only for the chosen parameters.

The 6DOF (six degrees of freedom) car dynamic model that was developed employed the Segel model of lateral forces generated by the tire [17, 18]. This model is relatively old (it was developed in the early 1970s). However, the Segel model is fairly easy to use and useful for the planned tests.

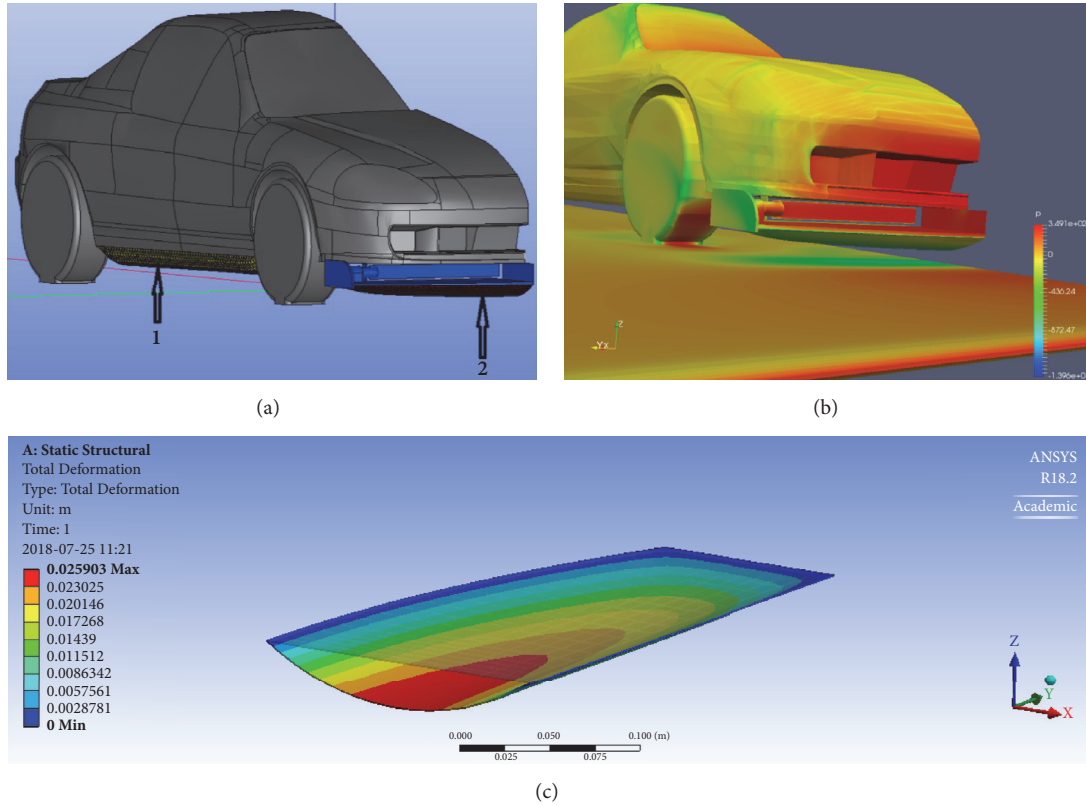


FIGURE 14: (a) Car with additional aerodynamic elements. The splitter is marked blue. Number 1 is a pneumatic side curtain. Number 2 is the airbag under the splitter. (b) An example of simulation results obtained using the OpenFOAM program. (c) Deformation of the airbag under the splitter. Numerical simulation carried out using the ANSYS program.

It is a function of the slip angle, cornering stiffness, tire vertical load, friction coefficient, and longitudinal force. A 6DOF model takes into account the possible rotation of the car body along the main 3 axes as well as vertical and horizontal body motion. This takes into account the lateral forces generated during acceleration and braking, defines the tire road contact forces, lateral forces and slip angles influenced by additional aerodynamic forces generated by movable aerodynamic elements. The action of suspension stabilizers is also taken into account. The scheme of forces and body movement definition is shown in Figure 15. The algorithm was coded in Fortran 95.

The software delivers information about the temporal car body position (rolling; pitching), tire slip angles, and forces. It can help develop algorithms for the electronic control system to steer the movable aerodynamic elements. Figure 16(a) depicts the variation of the longitudinal and lateral acceleration during cornering with an initial speed of 50 m/s, the “low aero” corresponds to a drag coefficient equal to 0.40 and the lift coefficient equal to -0.45 , whereas the “high aero” corresponds to a drag coefficient equal to 0.75 and the lift coefficient equal to -0.75 . The steering wheel changes the angle of the front wheels sinusoidally in 2 seconds from 0° to 15° .

Figure 16(b) presents some results showing differences in car motion with and without the action of the aerodynamic

elements. The observed car motion is characteristic for a case with high slip angles on the rear tires which cause oversteer when the aerodynamic downforce is not sufficient (“low aero”), when the aerodynamic load is high enough the balance of the car changes to neutral (“high aero”). This proves that relatively small changes in car dynamics can generate large changes in car position.

Each of the models and solutions presented so far were created separately without a direct two-way interaction between the fluid flow and the car body dynamics. Knowing the results of the investigation of coupled FSI problems [19], the simultaneous simulation of flow problems connection with car body motion caused by aerodynamic forces was also undertaken.

3.7. Coupled FSI Simulation of the Car Braking Process Assisted and Strengthened by Movable Aerodynamic Elements: Fully Coupled Analysis of the Braking Process. Designing lighter cars with lower drag coefficients requires an assurance of car stability in all road conditions. In simulations, it is rather rare to take into account coupling between car dynamics and aerodynamics. Very often, it is assumed that car movement will not affect aerodynamic forces. As shown in [2], this assumption is not correct. The authors showed that including bidirectional fluid structure interaction can lead to significant changes in aerodynamic forces.

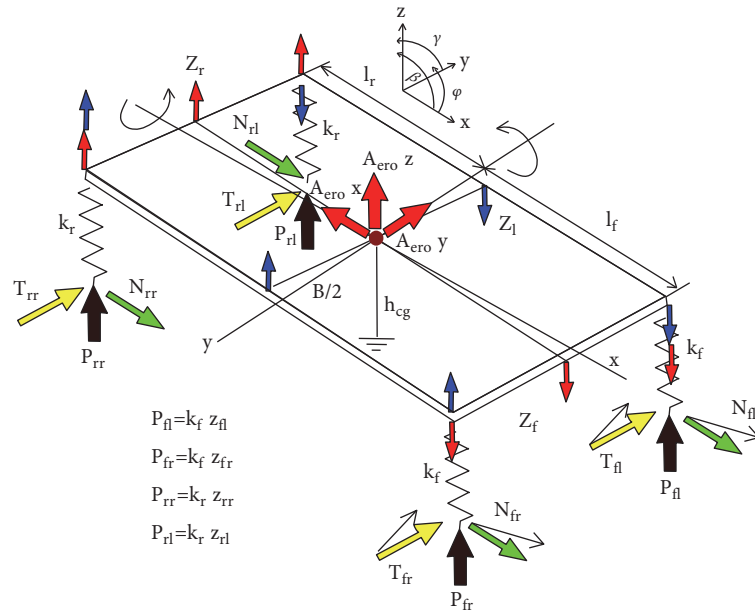


FIGURE 15: Scheme of forces and body movement definition.

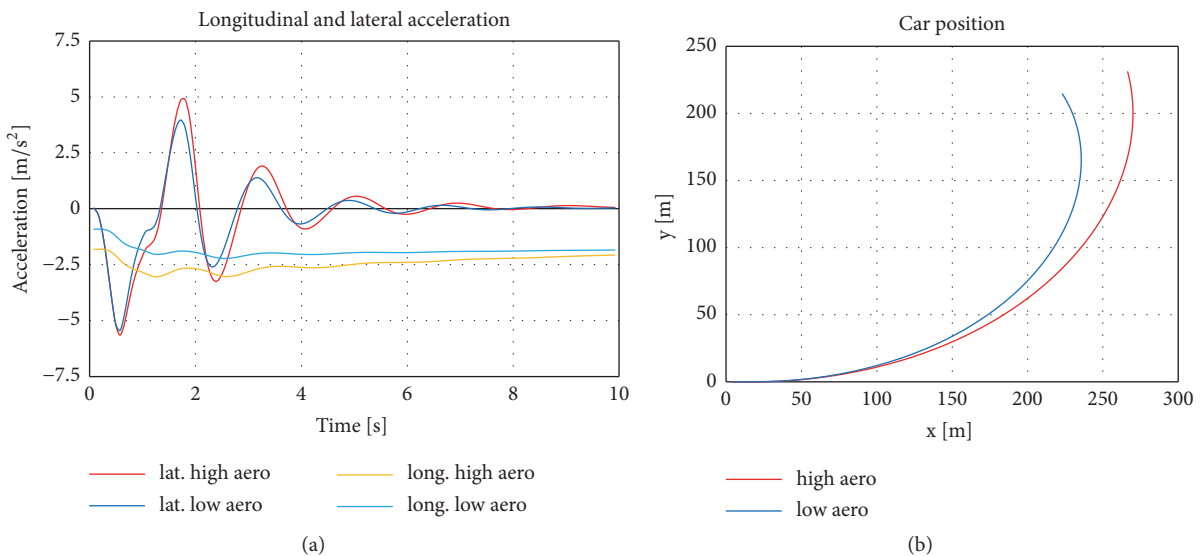


FIGURE 16: (a) Variation of the longitudinal and lateral acceleration during cornering. (b) Car position influenced by the aerodynamic forces.

The physics is complicated during the car braking process. A braking car generates a transfer of load to the front axis (see Figure 17), pressing the suspension springs and changing the inclination of the body resulting in a change of aerodynamic forces. During braking, the car slows down and this reduces the aerodynamic forces again thus changing the car body position. This is a fully coupled FSI process which had to be modeled and simulated.

In the case of braking (or accelerating), the car body pitches due to the elastic suspension system and the acting inertia forces. The pitch angle can be treated as an angle of attack for the car body. At the same time, the clearance

between the car and the ground also changes. Figure 17 illustrates the possible configurations. This situation causes a change in the pressure distribution over the entire body. Furthermore, a change in pressure distribution affects the pitch angle and clearance. In other words, there is a strong coupling between the car behavior and the aerodynamic forces.

In this research, fully coupled analyses were performed to check if it is possible to predict car dynamic behavior during braking. The obtained results were validated against a full car experiment as described in Section 3.3. Currently, very few of the published papers refer to a fully coupled

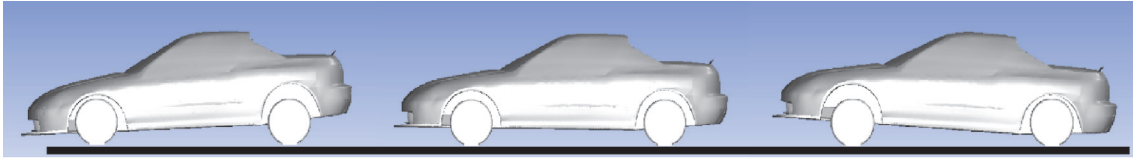


FIGURE 17: Pitching of the car body due to the elastic suspension system during braking or acceleration.

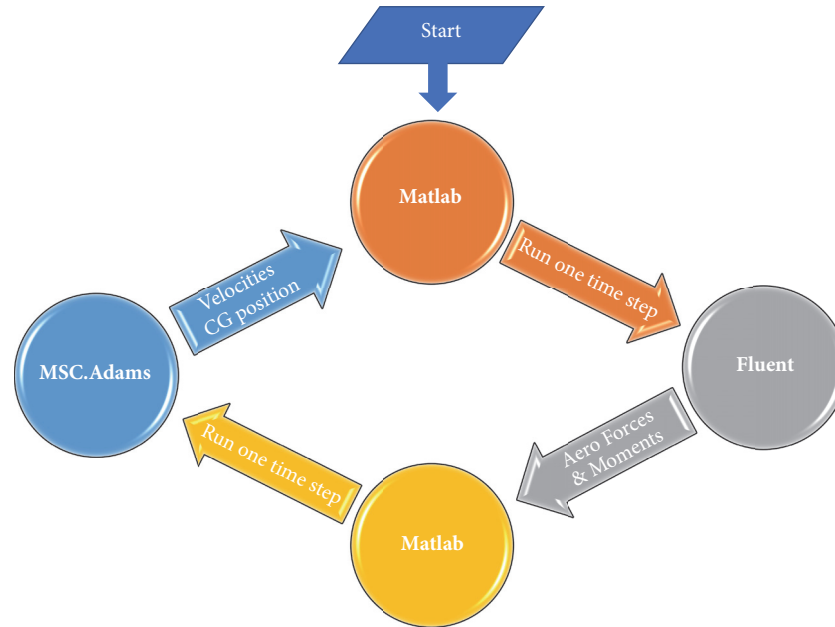


FIGURE 18: Scheme of the connections of the programs and exchange of data.

car analysis in which the vehicle speed significantly varies over time (such as during the acceleration/braking process). The method presented in this study to simulate the braking process utilizes a combination of high-end software for CFD modeling (Ansys® FLUENT®), vehicle dynamics (MSC.ADAMS/Car®), and a block diagram environment for multidomain simulation (MATLAB/Simulink®) which acts as an interface to exchange data between the first two tools. To allow communication with FLUENT®, it is launched in “as-a-server” mode. This option creates a COM port which enables remote connection to and control of FLUENT® sessions from an external application. Connection to MSC.ADAMS® is achieved via the “Adams Plant” option. On the Matlab side, dedicated Level 2 S-Functions were created. These functions are responsible for driving the CFD and dynamics analyses. The data workflow is presented in Figure 18.

The coupling procedure was validated against the wind tunnel experimental data. In this case self-excited vibration of square beam in crossflow was used. The set-up of the test stand is presented in Figure 11(a). Corresponding models were built for CFD and dynamic analyses (Figure 11(b)). The obtained results show that frequency and amplitude were captured with a high level of accuracy. With a validated coupling mechanism and the selected turbulence model – $k-\omega$ SST – which assures a good correlation to the wind tunnel

(see Section 3.3), a coupled analysis of the full car dynamics was performed.

During the research, it was concluded that the reference frame needed to be changed to simulate velocity change in the CFD analysis. Instead of a classical reference frame with an observer at rest, the reference frame with a moving observer was used. In this case, the whole computational domain was moved during the analysis with velocity which varies over time. The car instantaneous speed is calculated using MSC.Adams/Car®. The overset mesh was used to allow the movement of the car body and additional aerodynamics surfaces. The split into subdomains was performed according to elements which can be moved independently (car body, wheels, and rear airfoil). Based on the grid convergence study, for the steady state case, the hybrid hexa/polyhedra mesh used contained 7.7 million elements. Flow symmetry was assumed and a half car model was used. The analysis was performed in double precision, and the second-order spatial discretization schemes were used. The full car MSC.Adams® dynamic model (Figure 19) was fed with the measured data: suspension stiffness and damping nonlinear characteristics.

Mass properties were estimated based on “Measured vehicle inertial parameters” by NHTSA [20]. Friction coefficient between the tires and the road was set to 0.71 which corresponds to dry road conditions and is in line with the

TABLE 2: A comparison of the numerical and experimental data.

Value	Unit	Experiment	Analysis	Difference	%
Traveled Distance	m	111	112	1	0.90
Time to Stop	s	5.34	5.29	0.05	-0.94
Max Deceleration	g	1.0	0.95	0.05	-5

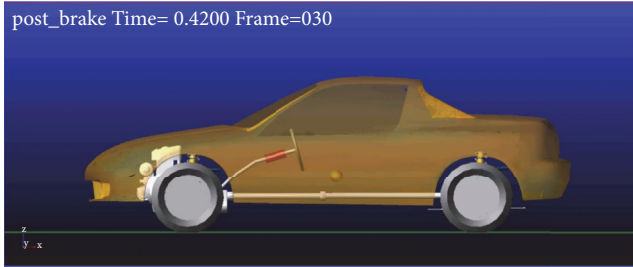


FIGURE 19: MSC.Adams/Car model used in the analysis.

Jones and Childers report [21]. The initial velocity for braking was 40.31 m/s (145 km/h). Based on [15], it was assumed that 0.5 s is needed to achieve full braking torque after the decision for emergency braking. The rear airfoil in the investigated configuration was in position “zero”. Figure 20(a) shows the pressure distribution on the car body and the isosurface of Q-Criterion colored with velocity magnitude at the starting point for braking.

The obtained braking characteristics presented in Figure 21 show a good agreement between the numerical prediction and the experimental data. The discrepancy in the traveled distance and time to stop is less than 1%. The mismatch in maximum deceleration is 5%. However, this value can be affected by the irregular shape of the experimental characteristic. A summary of the results is presented in Table 2.

The current research activities also focused on cornering analysis. The aim of this part of the study was to check the impact of aerodynamic configuration on cornering critical speed. It was necessary to switch the reference frame to a moving observer. With such an approach it was possible to simulate cornering and take into account all car movements associated with this maneuver. Figure 20(b) presents the initial CFD solution for quasi steady condition. It is clearly visible that flow symmetry is broken, especially on the rear part of the car body.

4. Road Tests

The final part of the presented study includes real vehicle road tests performed on a Honda CRX del Sol with some custom modifications. The test took place on a training track which was suitable for evaluating how the designed active control system can enhance emergency car maneuvers that sometimes need to be performed while driving on city roads. The radius of the curves and the length of the longest straight were insufficient to test the scenarios of emergency maneuvers during a very high-speed drive which could occur

on a highway. It should be noted that the aerodynamic forces aiding the drive were limited by the fact that lower ranges of speed were achieved during the tests. The test car was driven by an experienced rally driver, Arkadiusz Nowikow, whose driving technique made it possible to complete all test scenarios in a highly repetitive manner. He also gave invaluable insight about the car’s handling and its change with different aerodynamics and suspension settings. The passenger of the car who was also the operator of the control system when it was tested in semiautomatic mode was a source of information about the driving comfort. In this way, the data acquired by the sensors was enriched by subjective human experiences.

The active aerodynamic elements mounted on the rear side of the test car can be seen in Figure 22. They include a pair of moving wings and spoilers which can work independently and enable an asymmetrical configuration to be set. The active suspension and the aerodynamics play an important role in the distribution of force while the vehicle is moving. The system described in Section 2 was developed and thoroughly tested. Part of the data acquired is presented below.

With known values of the aerodynamic forces, which depend on the flow around the vehicle and knowledge of the vehicle dynamics, a set of track tests was conducted. The control and acquisition system was tested by means of active aerodynamic and suspension control for predefined scenarios, as well as being controlled, in a dynamic way, by software algorithms. Several different scenarios were executed during the track tests which included rapid braking, slalom and tight turns. For a braking scenario, detection of the braking pedal being pushed was the onset value of the aerodynamic brake activation, the rear wing and spoilers were set to the maximum angle of attack to maximize drag produced by the car body. Slalom involved slight adjustments of the rear wings that could be undertaken in split seconds before the turning direction was changed to the other side. For the scenario of driving into a tight curve, the system was activated when the values of the side (Y component) acceleration (see Figure 23) as well as the angular position of the steering wheel exceeded predetermined values. In this case, the active aerodynamic elements were configured to maximize the downforce on the car’s side closer to the inside of the curve, whereas the aerodynamic properties of the other side of the car remained neutral. Additionally, the suspension on the outer side was stiffened to limit the negative effects caused by body roll.

A comparison of two configurations is presented in Figure 24 and Figure S1. The red color is data for the configuration with active aerodynamics and active suspension turned on, whereas the blue data is for static positions of the

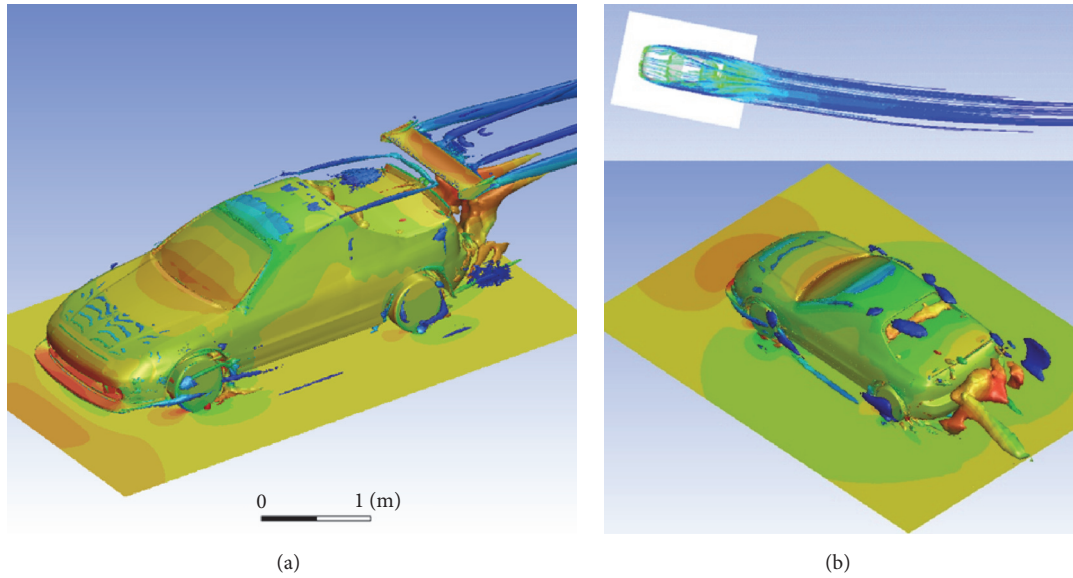


FIGURE 20: (a) Starting point for braking analysis. Car body colored with static pressure and iso-surface of Q-Criterion colored with velocity magnitude. (b) Initial CFD results for cornering analysis. Streamlines colored with velocity magnitude (upper) and static.

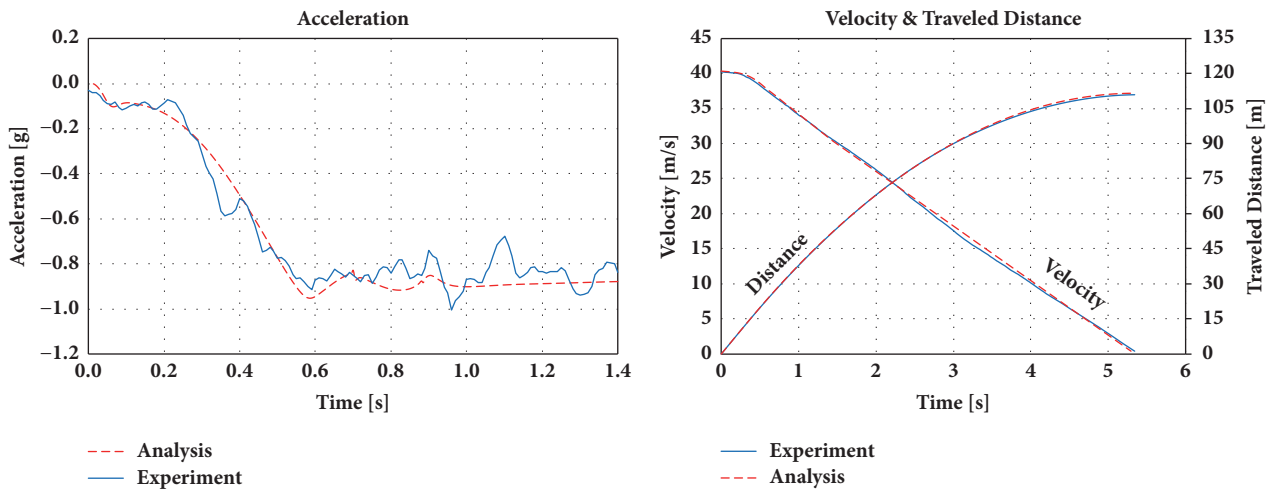


FIGURE 21: A comparison of the data from the simulations and the road tests.



FIGURE 22: Snapshot from a test drive with the active aerodynamics deployed, where Lw/Rw – active left/right wing, Ls/Rs – active left/right spoiler.

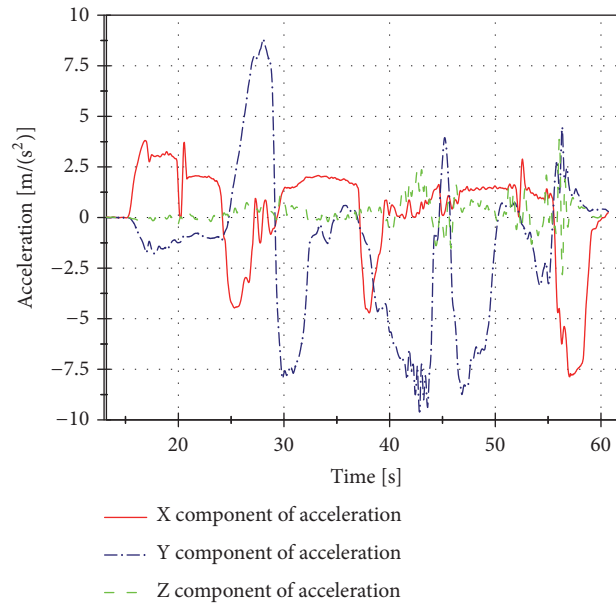


FIGURE 23: Set of data obtained from acquisition system, vehicle acceleration plot.

aerodynamic surfaces. Selected data, such as speed, lateral acceleration, steering wheel position and suspension deflection is presented in Figure 24, whereas the data presented in Figure S1 is supplemented by the GPS position noted on the map. Moreover, the gathered data also included information about throttle, braking, pitch, yaw and roll angles, as well as settings of the suspension stiffness and the aerodynamic surfaces configurations.

The data obtained from the tests made it possible to verify all of the preceding stages of the work. The track test can specify those points where, for example, the theoretical assumptions, the road conditions (roughness) and wind tunnel results were not enough to maintain a steady equilibrium and the assumed conditions. In Figure 24(b), it can be seen that, for the red line, the Y component of acceleration have an oscillatory character, which means that the car's suspension is at its limit. In other words, the car is moving in the manner of small jumps in a direction perpendicular to the driving direction. Moreover, it is clearly noticeable that there is a difference in the velocity reached at the fastest corner, with the configuration using active aerodynamics having the highest velocity.

5. Conclusions

The realization of the optimal design of the geometry and control system of movable aerodynamic devices increasing the safety of fast moving cars requires multidisciplinary synchronized action correlating the weak and strong points of the considered solutions.

This paper presented a range of methods of modeling and simulating different aspects of controlling car aerodynamic characteristics by actuating movable aerodynamic adds-on on the car body to increase the traction, braking and lateral force in road conditions requiring such action. The reaction

time required by the flow structure to change after a change of the car body geometry is an important factor. On the one hand, mechanical elements require fast movement but on the other hand the flow around the car body needs time to accommodate the new flow conditions. Different physical processes exist simultaneously in the considered problem and, especially, FSI problems required the use of different software for modeling and simulation.

The synchronized action of specialists in unsteady flow simulations, flexible material FSI simulations, car dynamic simulations, coupled FSI car aerodynamics and car dynamics, experimental tests in wind tunnel, and road tests can lead to a solution of electronically controlled movable aerodynamic elements activated and controlled in a manner to extend the driving limits of fast cars.

Data Availability

Data in the form of figures and tables that support the findings of the numerical calculations presented in this study are included within the article. Data acquired during the track tests are included within the article as well as within the supplementary information files.

Conflicts of Interest

The authors declare that they have no conflicts of interest.

Acknowledgments

The project was financed by the National Center for Research and Development (Narodowe Centrum Badań i Rozwoju) as part of the project entitled "The Active System of Car Body Oscillation Damping", Grant no. PBS3/B6/34/2015.

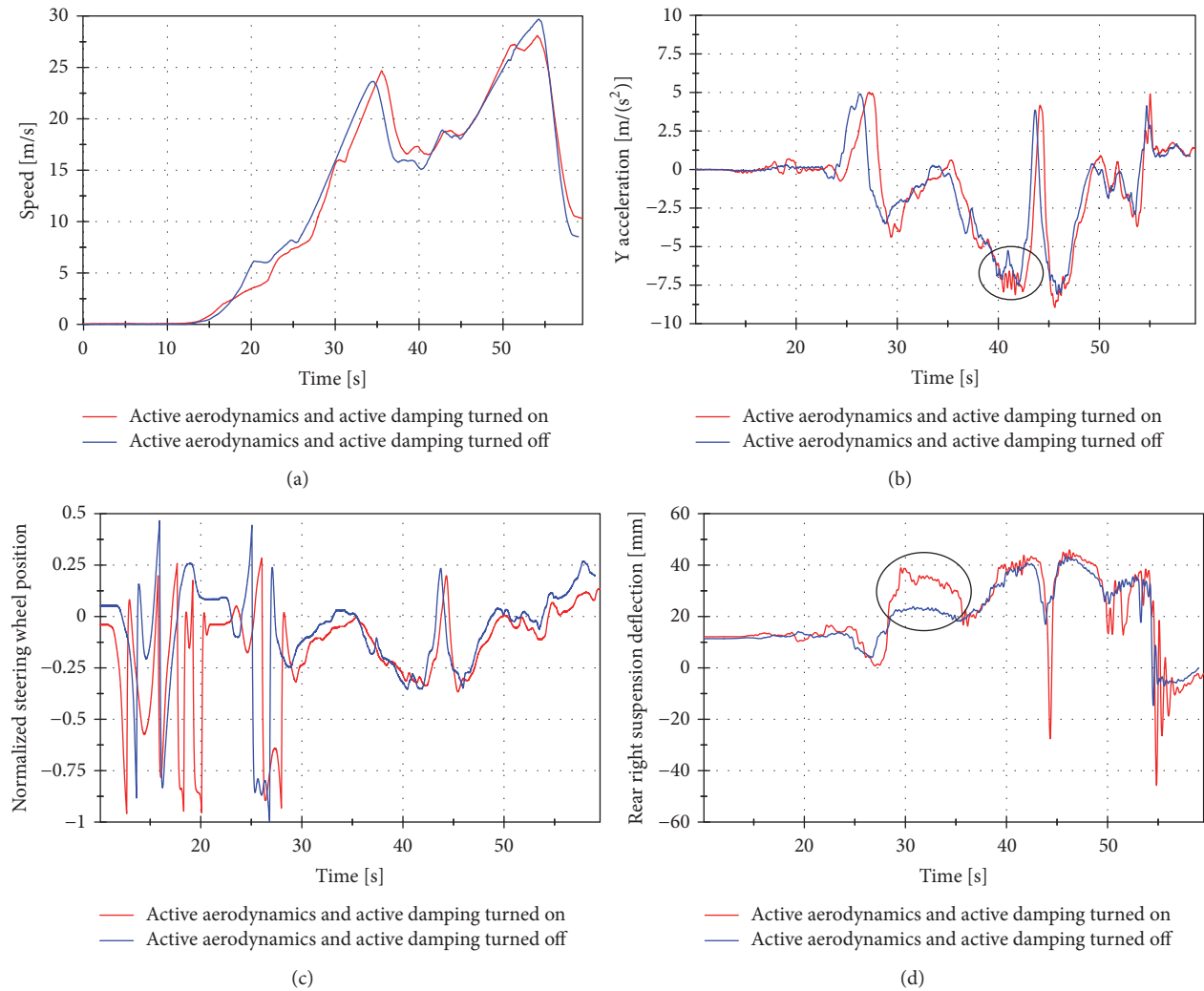


FIGURE 24: (a) Speed. (b) Lateral acceleration. The suspension instability is marked with a circled area. (c) Steering wheel position. (d) Rear right suspension deflection. The differences in the deflections are marked with a circled area.

Supplementary Materials

The supplementary material consists of a movie called “track_test_data.mp4” which is sample data acquired during the track test drive; one time frame from this movie is presented in Figure S1. The movie contains plots of such data as speed, lateral acceleration, steering wheel position, and suspension deflection, matched with the car’s position on the test track. (*Supplementary Materials*)

References

- [1] ISO 12021:2010, *Road Vehicles – Sensitivity to Lateral Wind – Open-Loop Test Method Using Wind Generator Input*, 2010, <https://www.iso.org/standard/53602.html>.
- [2] D. C. Forbes, G. J. Page, M. A. Passmore, and A. P. Gaylard, “A Fully Coupled, 6 Degree-of-Freedom, Aerodynamic and Vehicle Handling Crosswind Simulation using the DrivAer Model,” *SAE International Journal of Passenger Cars—Mechanical Systems*, vol. 9, no. 2, 2016.
- [3] G. Wahl, “918 Spyder – the impulse source for future sports car concepts,” in *Proceedings of the 5th International Munich Chassis Symposium 2014*, pp. 35–56, Springer Fachmedien, Wiesbaden, Germany, 2014.
- [4] A. Eskandarian, *Handbook of Intelligent Vehicles*, Springer, 2012, https://scholar.google.pl/scholar?hl=pl&as_sdt=0%2C5&q=%22Handbook+of+Intelligent+Vehicles%22+Azim+Eskandarian&btnG=.
- [5] W. Jarisa, “FUTURE TECHNOLOGY – Road condition classification using information fusion,” in *Proceedings of the 7th International Munich Chassis Symposium 2016*, pp. 939–957, Springer Fachmedien, Wiesbaden, Germany, 2017.
- [6] X. Qu, F. Yu, and S. Zhao, “Research on Curve Safety Speed Warning for Vehicle with Risk Prediction,” in *Proceedings of SAE-China Congress 2016: Selected Papers*, vol. 418 of *Lecture Notes in Electrical Engineering*, pp. 431–445, Springer, Singapore, 2017.
- [7] M. Fainello, “Optimizing passive vehicle dynamics for active safety and autonomous driving,” in *Proceedings of the 8th International Munich Chassis Symposium 2017*, pp. 243–251, Springer Fachmedien, Wiesbaden, Germany, 2017.

- [8] H. Beglerovic, A. Ravi, N. Wikström, H. Koegeler, A. Leitner, and J. Holzinger, "Model-based safety validation of the automated driving function highway pilot," in *Proceedings of the 8th International Munich Chassis Symposium 2017*, pp. 309–329, Springer Fachmedien, Wiesbaden, 2017.
- [9] M. Abramowicz, K. Kamieniecki, A. Piechna, and P. Rubach, "Using ANSYS and SORCER Modeling Framework for the Optimization of the Design of a Flapping Wing Bionic Object," *Mach. Dyn. Res.*, vol. 39, pp. 21–36, 2015.
- [10] J. Katz, *Race Car Aerodynamics: Designing for Speed*, Bentley (Robert) Inc, Cambridge, UK, 2nd edition, 1996.
- [11] F. R. Menter, "Two-equation eddy-viscosity turbulence models for engineering applications," *AIAA Journal*, vol. 32, no. 8, pp. 1598–1605, 1994.
- [12] C. Fu, M. Uddin, and A. C. Robinson, "Turbulence modeling effects on the CFD predictions of flow over a NASCAR Gen 6 racecar," *Journal of Wind Engineering & Industrial Aerodynamics*, vol. 176, pp. 98–111, 2018.
- [13] J. Katz, *Automotive Aerodynamics*, Wiley, 2016.
- [14] J. Piechna, T. Janson, P. Sadowski, S. Tudruj, A. Piechna, and L. Rudniak, "Numerical study of aerodynamic characteristics of sports car with movable flaps and deformable airbags," in *Proceedings of the Automotive Simulation World Congress*, 2013.
- [15] M. Mitschke, *Car Dynamics*, Transport and Communication Publishers, 1st edition, 1977.
- [16] M. Guiggiani, *The Science of Vehicle Dynamics: Handling, Braking, and Ride of Road and Race Cars*, Springer, the Netherlands, 2014.
- [17] G. Genta, *Motor vehicle dynamics: modeling and simulation*, World Scientific, 1997.
- [18] R. Rajamani, *Vehicle Dynamics and Control*, Springer US, Boston, Mass, USA, 2012.
- [19] T. Janson and J. Piechna, "Numerical Analysis of Aerodynamic Characteristics of a of High-Speed Car With Movable Bodywork Elements," *Archive of Mechanical Engineering*, vol. 62, no. 4, pp. 451–476, 2015.
- [20] G. J. Heydinger, R. A. Bixel, W. R. Garrott, M. Pyne, J. G. Howe, and D. A. Guenther, "Measured Vehicle Inertial Parameters-NHTSA's Data Through November 1998," in *Proceedings of the International Congress & Exposition*, pp. 10–4271, 1999.
- [21] E. R. Jones and R. L. Childers, *Contemporary College Physics*, McGraw Hill, 2001.

Research Article

Classification of Metro Facilities with Deep Neural Networks

Deqiang He , Zhou Jiang , Jiyong Chen, Jianren Liu, Jian Miao, and Abid Shah

*Guangxi Key Laboratory of Manufacturing System & Advanced Manufacturing Technology,
College of Mechanical Engineering, Guangxi University, 530004, Nanning, China*

Correspondence should be addressed to Zhou Jiang; xyq031256@163.com

Received 1 May 2018; Revised 15 December 2018; Accepted 10 January 2019; Published 3 February 2019

Guest Editor: Mihai Dimian

Copyright © 2019 Deqiang He et al. This is an open access article distributed under the Creative Commons Attribution License, which permits unrestricted use, distribution, and reproduction in any medium, provided the original work is properly cited.

Metro barrier-detection has been one of the most popular research fields. How to detect obstacles quickly and accurately during metro operation is the key issue in the study of automatic train operation. Intelligent monitoring systems based on computer vision not only complete safeguarding tasks efficiently but also save a great deal of human labor. Deep convolutional neural networks (DCNNs) are the most state-of-the-art technology in computer vision tasks. In this paper, we evaluated the effectiveness in classifying the common facility images in metro tunnels based on Google's Inception V3 DCNN. The model requires fewer computational resources. The number of parameters and the computational complexity are much smaller than similar DCNNs. We changed its architecture (the last softmax layer and the auxiliary classifier) and used transfer learning technology to retrain the common facility images in the metro tunnel. We use mean average precision (mAP) as the metric for performance evaluation. The results indicate that our recognition model achieved 90.81% mAP. Compared with the existing method, this method is a considerable improvement.

1. Introduction

With the rapid development of urban public transport in recent years, urban rail transport has become the preferred choice for many people because of its various advantages, such as high speed, punctuality, and environmental friendliness. Urban rail transit in China is developing at an amazing pace. The metro is an important part of urban rail transit. On pace with the improvement of metro train design, communication technology, and automation technology, the metro has seen immediate development. Its advanced technology with high safety makes it effective for solving saturated line conditions and enhances transport capacity. However, the main problem that influences driverless metro operation is obstacles. A collision with an obstacle will cause train impulses, derailments, vehicle equipment damage, and other problems. Thus, how to detect obstacles on the track quickly and accurately during operation has become a key issue in the study of safe metro operation. Currently, the detection of obstacles in metro tunnels is performed through manual observation. Detection that is dependent on manual labor has many drawbacks, including a high rate of missed detection, low efficiency, and low reliability. An improvement is

automatic detection based on object detection and recognition. However, there are too many metro tunnel images, and this detection method has very high requirements for the efficiency and accuracy of the algorithm. The current research status of object detection and recognition technology can be classified into two categories. One is based on traditional methods [1] in image processing. The other uses DCNNs [2]. Traditional methods have three steps: target feature extraction, target recognition, and target location. The features used in this method can be categorized into two groups: global features including a color histogram [3] or circular shapes [4] and local features such as pixel color [5] or SIFT [6] features, which are all designed manually. Reference [7] proposed a method for visualizing pedestrian traffic flow using SIFT feature point tracking. Reference [8] used the strongly supervised deformable part models for object detection. Due to the diversity of features, it is difficult to extract features standardly and find the best way to represent them [9]. However, this problem could be solved if there were a general method to learn how to extract features automatically. Thus, the advantages of DCNNs have received more attention. A DCNN has recently developed a new kind of method for classification and recognition. It is a multilayer

cascade consisting of linear and nonlinear processing units that are able to extract features automatically and integrate with the process of classification and recognition and then learn by themselves. Reference [10] proposed a DCNN for the detection of arcs in pantograph-catenary systems. Reference [11] used a DCNN for car detection. Although the DCNN has shown impressive results, limited data and high computational resources are barriers to its use [2]. Therefore, this is a barrier in metro obstacle detection. In this paper, we studied the detection of obstacles in metro tunnels using a modified DCNN. In view of a few appropriate examples, we used a common facility image in a metro tunnel to replace the obstacles.

2. Methodology

To achieve high performance with the DCNN, an extremely common practice increases the size of layers or widths [12]. In theory, with a higher width and depth of the DCNN, it has a stronger learning capacity and higher forecasting precision. However, this method may have several drawbacks. The first is that a large DCNN has more convolutions and more layers, which means that the network requires training more parameters. It requires tremendous computational resources and makes the whole network more prone to overfitting the training set, especially if the training data are limited [13]. The second is that changes in feature distributions lead to model failure. In most cases where the DCNN achieved good performance, both the training set and the testing set were obtained from the same feature space and the same distribution. This easily causes the model to fail where feature distributions have large changes. Thus, before the application, the above issues must be settled. Based on massive experimentation with various convolutional network structures, GoogLeNet designers provided several general guiding principles [14]:

(1) Avoid representational bottlenecks, especially early in the network. The representation size should gently decrease from the inputs to the outputs rather than being extremely compressed before reaching the final representation used for the current task

(2) Higher dimensional representations are easier to process locally within a network

In the CNN, increasing the activations per tile can obtain more disentangled features. This allows resulting networks to be trained faster.

(3) Spatial aggregation can be performed over lower dimensional embedding without much or any loss in representational power

(4) When designing the network structure, one must consider the balance of the width and depth of the network. A reasonable network structure should distribute computational resources on its structure, which contributes to higher quality networks

2.1. GoogLeNet. GoogLeNet first appeared in the ILSVRC 2014 competition and won first place by a wide margin. The first version is often called Inception V1 [15]. The main feature of Inception V1 is that it showed good results while

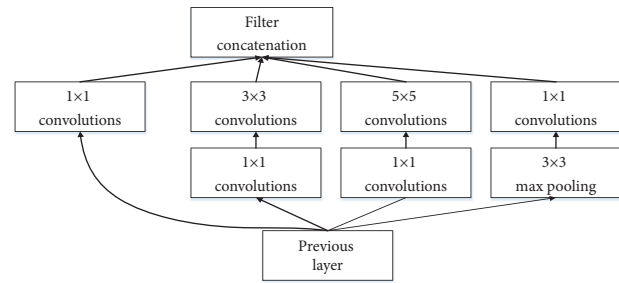


FIGURE 1: Inception module.

limiting the number of computations and parameters—by 93.33% as top 5, which is less than half of AlexNet. Inception V1 proposed a module named Inception. This module contains four branches (the architecture is given in Figure 1): the first branch makes convolution with inputs by a 1*1 size convolution kernel that is also an important structure proposed in the NIN (network in network) [16]. The 1*1 convolution kernel, an excellent structure, adds a layer for feature transformation and nonlinear changes with few computational resources, which enhances the ability of the expression of the whole network and increases or decreases the dimension of the outputs. As Figure 1 shows, all branches use a 1*1 size convolution kernel for low-cost cross-channel feature transformation. The second branch first uses a convolution of 1*1 and then connects to a convolution of 3*3, which is equivalent to twice the feature transformations. The third one is similar to the second, but it connects to a 5*5 size convolution kernel, and the last one has a 3*3 max pooling and 1*1 size convolution. The Inception module allows the depth and width of the network to be extended efficiently, improving the accuracy and avoiding overfitting.

Inception V2 [17], the second version of GoogLeNet, replaces the 5*5 size convolution kernels with two 3*3 convolution kernels to reduce the number of parameters and overfitting. It proposed a very effective regularization method called batch normalization (BN). BN speeds up the training rate of large-scale convolutional networks by many times, and the classification accuracy after convergence is also greatly improved. When used in the network layers, BN normalizes the interior of the mini-batch data to output the normally distributed data and decreases internal covariate shift. In traditional deep neural networks, the input distribution of each layer varies during training, making it difficult to train. Therefore, only by setting a small learning rate can the training process continue. However, using batch normalization in each layer of the network could solve this problem because the training allows a high learning rate to run, in which the number of iterations is considerably reduced. After this measure was employed, the training time of Inception V2 was fourteen times faster compared to Inception V1 and had higher convergence accuracy.

The third version, Inception V3 [14], had two major improvements. One was the introduction of the thought of factorization into small convolutions. The other was that the

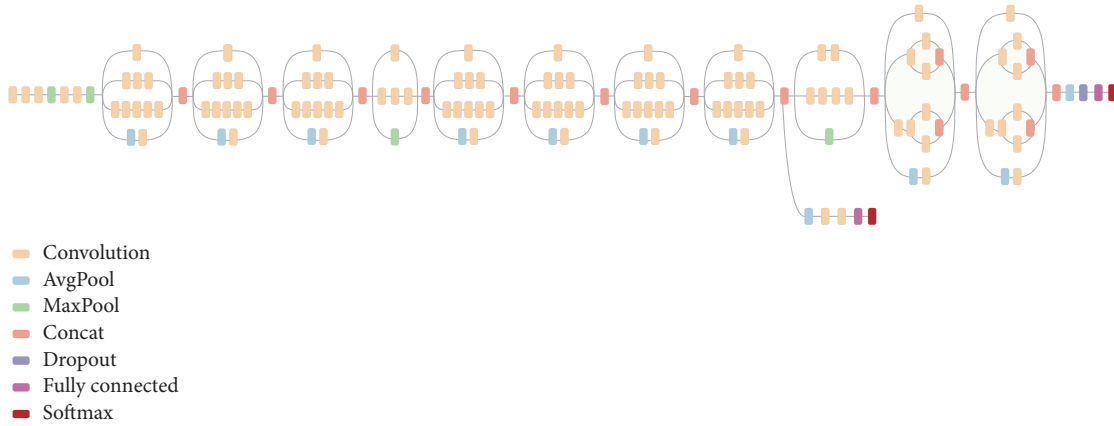


FIGURE 2: Model architecture.

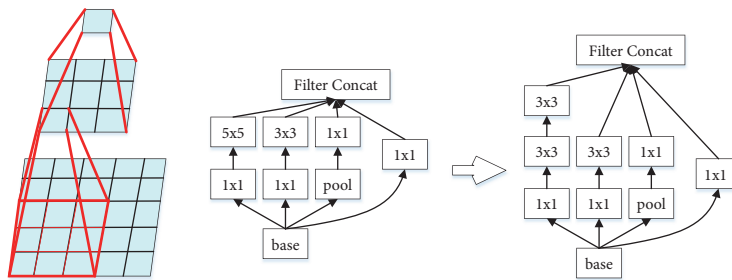


FIGURE 3: Mini-network replacing the 5×5 convolutions.

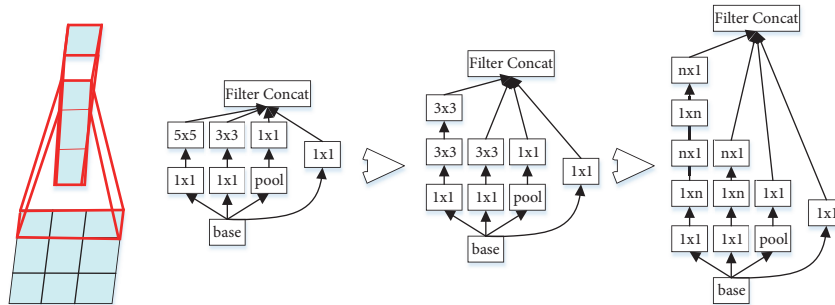


FIGURE 4: Mini-network replacing the 3×3 convolutions. The lower layer of this network consists of a 3×1 convolution with 3 output units.

Inception module was optimized. The visualization of the model architecture is given in Figure 2.

The ideal of factorization into small convolutions is a large improvement of Inception V3. As shown in Figure 3, a large convolution layer can be replaced by a multilayer network with fewer parameters.

For example, a 5×5 convolution with n filters over a grid with m filters is $25/9 = 2.78$ times more computationally expensive than a 3×3 convolution with the same number of filters. Thus, two 3×3 convolutions replace one 5×5 convolution having $(9 + 9)/25 \times$ reduction with a relative gain of 28% [14]. Furthermore, spatial factorization into asymmetric convolutions can factorize a convolution into smaller convolutions. For instance, using a 3×1 convolution followed by a 1×3 convolution is equivalent to a two-layer network with the same 3×3 receptive field (Figure 4).

If the number of input and output filters is equal, the two-layer solution is 33% cheaper for the same number of output filters.

The Inception model helps to reduce computational complexity and increase the width and number of stages. It has 1×1 , 3×3 , and 5×5 convolution layers. The 1×1 convolution layers are used to increase the network depth and improve the network nonlinearity. It also reduces the number of 3×3 and 5×5 convolution layers, which is the main reason that the GoogLeNet network model is expanded in terms of depth and width, but the total number of parameters is smaller than that of the classical VGG network. The Inception module accepts the previous input and forms the output of the Inception module through the parallel processing of different scales and functional branches, thus achieving multiscale feature fusion in Inception V3 that was achieved by setting a top 5 error rate

TABLE 1: The outline of the proposed network architecture.

Type	Patch size/stride or remarks	Input size
conv	3×3 / 2	299×299×3
conv	3×3 / 1	149×149×32
conv padded	3×3 / 1	147×147×32
pool	3×3 / 2	147×147×64
conv	3×3 / 1	73×73×64
conv	3×3 / 2	71×71×80
conv	3×3 / 1	35×35×192
Inception module	3×Inception	35×35×288
Inception module	5×Inception	17×17×768
Inception module	2×Inception	8×8×1280
pool	8×8	8×8×2048
linear	logits	1×1×2048
softmax	classifier	1×1×1000

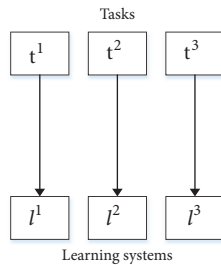


FIGURE 5: Traditional machine learning.

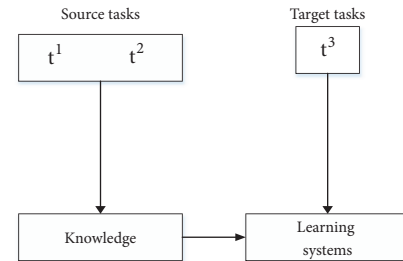


FIGURE 6: Transfer learning.

of 3.64% on the 2012 validation dataset. Our measure is based on Inception V3.

2.2. Transfer Learning. In network training procedures, there is an important hypothesis that the training and testing dataset must be in the same feature space and have the same distribution. However, it cannot be held in many applications. For example, we sometimes have a classification task in a domain of interest, but we have sufficient training data in another domain, and the latter data may be in different feature spaces or follow different data distributions. In this case, the successful transfer of knowledge will avoid a large amount of expensive data markup work and greatly improve the performance of learning. Transfer learning [18], as the name implies, simply transfers learned-trained model parameters to a new model to help train the model. Because most of the data or tasks are related, a trained model can share its parameters (also understood as knowledge learned by the model) to a new model in a way that expedites and optimizes the learning rate of the new model without starting over as is required in most other networks. Thus, transfer learning is a simple method to transfer knowledge between task domains. The following is the difference between traditional machine learning and transfer learning. Traditional machine learning needs to be retrained for different target tasks, while transfer learning is not necessary (see Figures 5 and 6).

In transfer learning, the network weights and biases are initialized with existing useful values, which can obviously reduce the training time to finish the final training task and significantly lower the required amount of training data. Deep convolutional networks with transfer learning are the best way to solve this detection problem and achieve the most advanced performance with the lowest computational requirements.

2.3. Model. The layout of the entire network is given in Table 1.

The output size of each module is the input size of the next module. To keep the size of the grid, the convolution is marked with zero padding, and the inside of the Inception modules also uses zero padding for the same purpose. The network uses softmax for classification. The original architecture has 1,000 object classes, so we adjusted its structure to fit our project. We changed the final classification layer (the last softmax layer and the auxiliary classifier) on a pretrained Inception V3 network and retrained it with our dataset, fine-tuning the parameters across all layers.

3. Experiments

3.1. Data Collection and Processing. Our dataset was collected during a metro inspection, authorized by Nanning Rail Transit Co. It contains 6000 original images that were



FIGURE 7: A few examples.

divided into 6 classes: distribution box (DB), jet fan (JF), wireless communication base station module (AP), passenger information system wireless terminal box (PIS), radio transmission equipment (TRE), and billboard (BI). Figure 7 shows a few examples.

We extended the dataset by applying a series of methods, as follows:

- (1) Randomly rotating each image; the number of images doubled
- (2) Resizing each image to 299×299
- (3) Adjusting the brightness of the image
- (4) Adjusting the image contrast
- (5) Adjusting the image saturation

To evaluate the results, each category was divided into a training set and a testing set: 75% for the training set and 25% for the testing set.

We use mean average precision (mAP) [19] as the metric for performance evaluation. The average precision (AP) is the area under the precision-recall curve. It is widely used for object detection and is calculated by averaging the precision over a group of spaced recall levels $[0, 0.1, \dots, 1]$, and the mAP is the AP calculated over all classes. The details are as follows:

$$AP = \frac{1}{11} \sum_{r \in \{0, 0.1, \dots, 1\}} p_{interp}(r). \quad (1)$$

The precision at each recall level r is interpolated by taking the maximum precision measured for a method for which the corresponding recall exceeds r :

$$p_{interp}(r) = \max_{\tilde{r}: \tilde{r} \geq r} p(\tilde{r}), \quad (2)$$

where $p(\tilde{r})$ is the measured precision at recall \tilde{r} .

3.2. Training Methodology. Our experiment was conducted on Google's TensorFlow [20]. TensorFlow is an open source software library for machine learning of various perception and language comprehension tasks. It aims to promote the study of machine learning and the rapid and simple transition from prototype research to production.

It is challenging to train deep neural networks on smaller datasets. However, by transfer learning, a large number of acquired feature parameters are extracted from one of the largest datasets—ImageNet—that can be transferred to our new model, which provided better results in detection. The whole network was trained using backpropagation and used a global learning rate of 0.001 using RMSProp with a decay of

0.9 and a momentum of 0.9. The training stopped when there were no more obvious improvements.

3.3. Experimental Results and Comparisons. The probability that a photo belongs to a category was given by the multinomial logistic regression. The category with the highest probability was taken as the predicted category. Parts of the results are shown in Figure 8, and category predictions are accompanied by probabilities.

This work aims at classifying the common facility images in metro tunnels. To the best of our knowledge, this is the first work for this task. There are limited approaches that we could compare in the literature. We resort to other image classification approaches for comparison. Since random forest has been widely used in image classification and object detection [21], we compare our model with random forest. This approach first appeared in [22] and was further developed in [23]. Random forest for this experiment is provided by [23]. We also compare the proposed method with deformable part models (DPM) [1], which have achieved state-of-the-art results on the PASCAL and INRIA person datasets. It is based on mixtures of multiscale deformable part models to represent highly variable object classes. The original implementation of DPM provided by [1] is used for this experiment. Since both random forest and DPM are traditional image recognition, we compare with another method based on a plain CNN. The architecture we used was introduced by [2], which won the 2012 ILSVRC competition.

The experimental data are the same as the data used by Inception V3 and are also divided into 75% for the training set and 25% for the testing set. Parts of the experimental examples are shown in Figures 9–11. Table 2 shows the experimental results.

In Table 2, the first two lines show the results obtained by the traditional method. The performance of the DPM-based method is poor; it only achieves 27.94% mAP. Although DPM has achieved state-of-the-art performance in general object detection, the performance of metro detection is not satisfactory. Random forest is better than DPM, but it only achieves 45.17%. The reason for the low mAP of these two methods is that both methods are based on traditional image processing. Such methods need to manually select the filters that require multiple experiments to determine satisfied filters in type and quantity. The variety of features, rich color changes, and complex environmental backgrounds make such traditional methods difficult to correctly identify. The mAP was better



FIGURE 8: A few results.

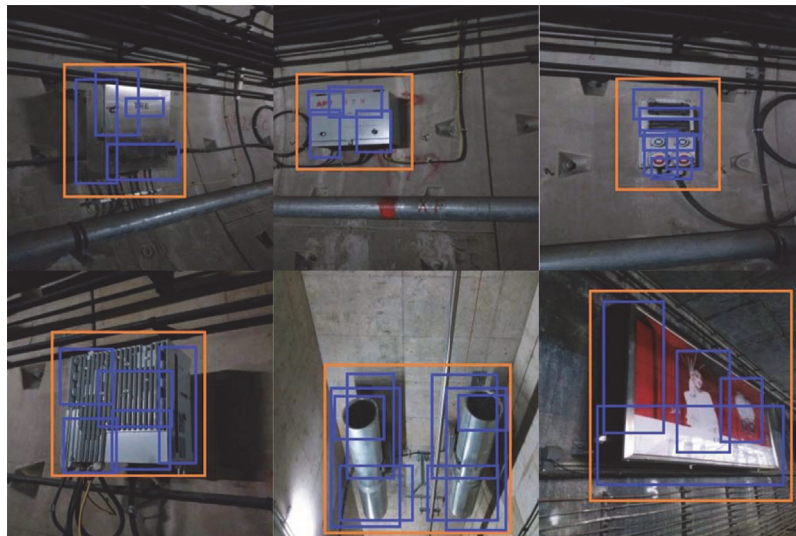


FIGURE 9: A few results by DPM.

TABLE 2: Experimental results.

Method	DB(%)	JF(%)	AP(%)	PIS(%)	TRE(%)	BI(%)	mAP(%)
DPM	28.56	27.62	29.53	21.27	29.41	31.24	27.94
Random forest	45.27	41.38	45.79	50.45	42.35	45.78	45.17
CNN	60.92	58.14	55.47	53.33	51.67	53.95	55.58
Inception V3	90.65	88.30	93.09	93.78	85.49	93.55	90.81



FIGURE 10: A few results by the CNN.

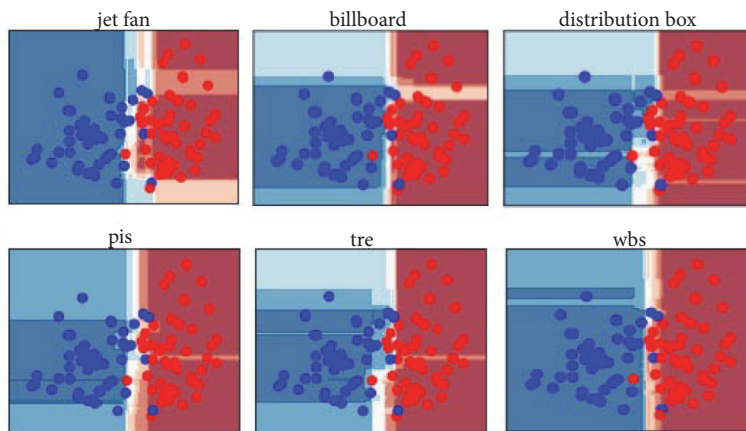


FIGURE 11: Results by random forest.

when the convolutional neural network was applied, especially using the deep convolution neural network. Instead of manual feature extraction, the feature extraction layer of the CNN learns features directly when training the data, which means that it can avoid the limitations of manual feature extraction. A plain CNN achieves an mAP of 55.58%, and Inception V3 achieves 90.81%. In contrast to the plain CNN, Inception V3 factorizes the convolution filter into a small filter. It reduces many parameters and accelerates the calculation and adds a nonlinear layer extending the whole

network expression ability. Such a feature made Inception V3 perform much better than the plain CNN.

4. Conclusion

In this paper, we used a deep convolutional neural network model, Inception V3, devised by Google. By this module, a very deep network can be built with fewer parameters, thus reducing computational resources. The final classification layer of the network was removed and retrained with our

dataset to construct a satisfactory structure. The application of transfer learning trained a very deep model rapidly from scratch and with a small dataset. Our modified Inception V3 achieved impressive results on the datasets, 90.81%, which were much better than published methods. Considering the number of parameters and the consequent computational cost, this approach could actually be a viable choice for metro intelligent monitoring systems.

Data Availability

The dataset used to support the findings of this study is related to the safety of subway operation and is copyrighted; it is partly available from the corresponding author upon request.

Conflicts of Interest

The authors declare that they have no conflicts of interest.

Acknowledgments

This work was financially supported by the National Natural Science Foundation of China (Grant No. 51765006), the Natural Science Foundation of Guangxi Province of China (Grant No. 2017GXNSFDA198012), the Key Project of Science and Technology of Guangxi (Grant No. 1598009-6, AB17195046), the Guangxi Manufacturing Systems and Advanced Manufacturing Technology Key Laboratory Director Fund (15-140-30S003), and the Innovation Project of Guangxi Graduate Education (YCSW2018033).

References

- [1] P. F. Felzenszwalb, R. B. Girshick, D. McAllester, and D. Ramanan, "Object detection with discriminatively trained part-based models," *IEEE Transactions on Pattern Analysis and Machine Intelligence*, vol. 32, no. 9, pp. 1627–1645, 2010.
- [2] A. Krizhevsky, I. Sutskever, and G. E. Hinton, "Imagenet classification with deep convolutional neural networks," in *Proceedings of the 26th Annual Conference on Neural Information Processing Systems (NIPS '12)*, pp. 1097–1105, Lake Tahoe, Nev, USA, December 2012.
- [3] Z. Zivkovic and B. Kröse, "An EM-like algorithm for color-histogram-based object tracking," in *Proceedings of the Computer Society Conference on Computer Vision and Pattern Recognition (CVPR '04)*, vol. 1, pp. 798–803, IEEE, July 2004.
- [4] T. Garlipp and C. H. Müller, "Detection of linear and circular shapes in image analysis," *Computational Statistics & Data Analysis*, vol. 51, no. 3, pp. 1479–1490, 2006.
- [5] Y. Deng, B. Manjunath S, and H. Shin, "Color image segmentation," in *Proceedings of the IEEE Conference on Computer Vision & Pattern Recognition*, pp. 1021–1036, 1999.
- [6] H. Zhou, Y. Yuan, and C. Shi, "Object tracking using SIFT features and mean shift," *Computer Vision and Image Understanding*, vol. 113, no. 3, pp. 345–352, 2009.
- [7] Y. Tsuduki and H. Fujiyoshi, "A method for visualizing pedestrian traffic flow using SIFT feature point tracking," *Pacific Rim Symposium on Advances in Image and Video Technology*, pp. 25–36, 2009.
- [8] H. Azizpour and I. Laptev, "Object detection using strongly-supervised deformable part models," *Lecture Notes in Computer Science*, vol. 7572, no. 1, pp. 836–849, 2012.
- [9] B. Zhou, A. Lapedriza, J. Xiao, A. Torralba, and A. Oliva, "Learning deep features for scene recognition using places database," in *Proceedings of the 28th Annual Conference on Neural Information Processing Systems (NIPS '14)*, pp. 487–495, December 2014.
- [10] G. Karaduman, M. Karakose, and E. Akin, "Deep learning based Arc detection in pantograph-catenary systems," in *Proceedings of the International Conference on Electrical and Electronics Engineering*, pp. 12–63, 2017.
- [11] Y. Xu, G. Yu, Y. Wang, X. Wu, and Y. Ma, "Car detection from low-altitude UAV imagery with the faster R-CNN," *Journal of Advanced Transportation*, vol. 2017, Article ID 2823617, 10 pages, 2017.
- [12] H. Hassannejad, G. Matrella, P. Ciampolini, I. De Munari, M. Mordonini, and S. Cagnoni, "Food image recognition using very deep convolutional networks," in *Proceedings of the 2nd International Workshop on Multimedia Assisted Dietary Management (MADiMa '16)*, pp. 41–49, 2016.
- [13] D. M. Hawkins, "The problem of over-fitting," *Journal of Chemical Information and Computer Sciences*, vol. 44, no. 1, pp. 1–12, 2004.
- [14] C. Szegedy, V. Vanhoucke, S. Ioffe, J. Shlens, and Z. Wojna, "Rethinking the inception architecture for computer vision," in *Proceedings of the IEEE Conference on Computer Vision and Pattern Recognition (CVPR '16)*, pp. 2818–2826, July 2016.
- [15] C. Szegedy, W. Liu, Y. Jia et al., "Going deeper with convolutions," in *Proceedings of the IEEE Conference on Computer Vision and Pattern Recognition (CVPR '15)*, pp. 1–9, IEEE, Boston, Mass, USA, June 2015.
- [16] M. Lin, Q. Chen, and S. Yan, "Network in network," in *Proceedings of the International Conference on Learning Representations*, vol. 1, pp. 56–63, 2014.
- [17] S. Ioffe and C. Szegedy, "Batch normalization: Accelerating deep network training by reducing internal covariate shift," in *Proceedings of the 32nd International Conference on Machine Learning (ICML '15)*, vol. 1, pp. 448–456, July 2015.
- [18] S. J. Pan and Q. Yang, "A survey on transfer learning," *IEEE Transactions on Knowledge and Data Engineering*, vol. 22, no. 10, pp. 1345–1359, 2010.
- [19] M. Everingham, L. van Gool, C. K. I. Williams, J. Winn, and A. Zisserman, "The pascal visual object classes (VOC) challenge," *International Journal of Computer Vision*, vol. 88, no. 2, pp. 303–338, 2010.
- [20] M. Abadi, P. Barham, J. Chen et al., "TensorFlow: a system for large-scale machine learning," *Operating Systems Design and Implementation*, vol. 1, pp. 265–283, 2016.
- [21] A. Bosch, A. Zisserman, and X. Muñoz, "Image classification using random forests and ferns," in *Proceedings of the IEEE 11th International Conference on Computer Vision (ICCV '07)*, vol. 2, pp. 1–8, IEEE, Rio de Janeiro, Brazil, October 2007.
- [22] Y. Amit and D. Geman, "Shape quantization and recognition with randomized trees," *Neural Computation*, vol. 9, no. 7, pp. 1545–1588, 1997.
- [23] L. Breiman, M. Last, and J. Rice, "Random forests: finding quasars[M]//Statistical challenges in astronomy," Springer, New York, NY, 243–254, 2003.

Research Article

A Novel Prediction Model for Car Body Vibration Acceleration Based on Correlation Analysis and Neural Networks

Shubin Zheng , Qianwen Zhong , Xiaodong Chai, Xingjie Chen, and Lele Peng

School of Urban Railway Transportation, Shanghai University of Engineering Science, Shanghai 201620, China

Correspondence should be addressed to Shubin Zheng; shubin.zheng@sues.edu.cn

Received 31 July 2018; Accepted 2 December 2018; Published 27 December 2018

Guest Editor: Luc Chassagne

Copyright © 2018 Shubin Zheng et al. This is an open access article distributed under the Creative Commons Attribution License, which permits unrestricted use, distribution, and reproduction in any medium, provided the original work is properly cited.

This paper aims to create a prediction model for car body vibration acceleration that is reliable, effective, and close to real-world conditions. Therefore, a huge amount of data on railway parameters were collected by multiple sensors, and different correlation coefficients were selected to screen out the parameters closely correlated to car body vibration acceleration. Taking the selected parameters and previous car body vibration acceleration as the inputs, a prediction model for car body vibration acceleration was established based on several training algorithms and neural network structures. Then, the model was successfully applied to predict the car body vibration acceleration of test datasets on different segments of the same railway. The results show that the proposed method overcomes the complexity and uncertainty of the multiparameter coupling analysis in traditional theoretical models. The research findings boast a great potential for application.

1. Introduction

Passenger comfort is an important indicator of the operation quality of passenger trains. Previous studies [1, 2] have shown that passenger comfort can be estimated indirectly by parameters like vibration acceleration of the car body. Based on the estimated passenger comfort, it is possible to identify the warning signals or system statuses needed to ensure the smooth operation of the train.

Much research has been done to forecast the vibration acceleration of trains. For instance, Shafullah et al. [3] predicted the forward and backward vertical acceleration conditions by popular regression algorithms. Zhai et al. [4] created a comprehensive train-track dynamics model to predict the ground vibrations of high-speed trains. Inspired by the dynamics model, Czop et al. [5] proposed a rail irregularity detection method based on the bearing box acceleration during train operation and successfully applied the method to recognize the rail regularities of a typical railway in Poland. Qian et al. [6] established a model to predict the vibration acceleration of high-speed trains based on nonlinear autoregressive neural network with exogenous inputs (NARX NN) and multibody dynamic model and

proved the prediction accuracy of the model through experimental analysis.

In addition, some scholars have attempted to infer important parameters of railways from vibration acceleration of the car body. For example, Connolly et al. [7] assessed the effects of vibration acceleration on passenger comfort and track performance. Koo et al. [8] put forward theoretical derailment coefficients for single wheel pairs, considering the impacts from lateral vibration acceleration and gyroscopic factors as well as flange angle, friction coefficient, wheel unloading, wheel radius, gauge, and bearing position. Navik et al. [9] developed a new sensor system that captures the dynamic behaviour of high-speed rail with several sensors placed at an interval of 150m and predicted the maximum vertical displacement, train speed, dynamic behaviour, and quantification modal parameters with vibration acceleration time series.

In general, the previous research into vibration acceleration had concentrated on the traditional multibody dynamics modelling, and the research results were mainly derived through simulation. In actual operation, the train is faced with a complex environment and uncertain track conditions. Thus, there is always some gap between the simulated state

and the actual state of railway track and train operation. This calls for a new theoretical model that can accurately reflect the actual conditions of the train and the track.

In light of the above, this paper aims to propose a prediction model for car body vibration acceleration that is reliable, effective, and close to real-world conditions. Therefore, a huge amount of data on railway parameters were collected by multiple sensors, and different correlation coefficients were selected to screen out the parameters closely correlated to car body vibration acceleration. Taking the selected parameters and previous car body vibration acceleration as the inputs, a prediction model for car body vibration acceleration was established based on several training algorithms and neural network structures. Then, the model was successfully applied to predict the car body vibration acceleration of test datasets on different segments of the same railway. The results show that the proposed method overcomes the complexity and uncertainty of the multiparameter coupling analysis in traditional theoretical models. The research findings boast a great potential for application.

The remainder of this paper is organized as follows: Section 2 introduces the data preprocessing and feature selection methods; Section 3 describes the structures of the neural networks and several popular training algorithms; Section 4 verifies the effect of the proposed model on different datasets, and the results under different structures are discussed and compared; Section 5 wraps up this paper with some meaningful conclusions.

2. Data Preprocessing and Feature Selection

2.1. Data Preprocessing. The research data are a collection of useful data from actual railways. The sensors were subjected to noise reduction and antijamming processing, aiming to enhance the readability and usability of the collected data. In addition, the data underwent a multistep preprocessing.

Firstly, time synchronization was performed on the huge amount of data captured by multiple sensors to remove time points with missing or abnormal values and eliminate the variables of constant values. In this way, the data containing useful information were screened out.

Secondly, the modelling variables were determined, excluding those rarely used, irrelevant to mechanics, or difficult to measure in actual conditions.

Thirdly, the influencing factors of the relevant variables in the transfer part were minimized, e.g., the angular acceleration at different positions of car body, as the prediction variables were expected to consider such parameters as train structure, track state, and operation state. Note that the minimization only treats the transfer process as a black box, rather than overlooking the impacts of the influencing factors. The treatment simplifies the modelling process.

Finally, the preprocessed data were normalized for further use.

2.2. Variable Selection

2.2.1. Linear Correlation. The linear correlation of two random variables can be measured by the Pearson's correlation

coefficient (P). If each variable has N scalar observations, then the Pearson's correlation coefficient ρ_P can be defined as [10–12]

$$\rho_P(M_1, M_2) = \frac{1}{N-1} \sum_{i=1}^N \left(\frac{M_{1i} - \mu_{M_1}}{\sigma_{M_1}} \right) \left(\frac{M_{2i} - \mu_{M_2}}{\sigma_{M_2}} \right) \quad (1)$$

where μ_{M_1} and σ_{M_1} are the mean and standard deviations of M_1 , respectively, and μ_{M_2} and σ_{M_2} are the mean and standard deviations of M_2 , respectively.

The Pearson's correlation coefficient can also be described based on the covariance of M_1 and M_2 as follows.

$$\rho_P(M_1, M_2) = \frac{\text{cov}(M_1, M_2)}{\sigma_{M_1} \sigma_{M_2}} \quad (2)$$

2.2.2. Nonlinear Correlation. The linear correlation coefficient cannot fully reflect the relationship between variables, owing to the possible existence of nonlinear correlations. Thus, the Spearman's rank correlation coefficient (S) [13] was employed to analyze the nonlinear correlations between variables. This coefficient ρ_S can be defined as follows.

$$\rho_S(M_1, M_2) = \frac{\sum_i (M_{1i} - \bar{M}_1) (M_{2i} - \bar{M}_2)}{\sqrt{\sum_i (M_{1i} - \bar{M}_1)^2 \sum_i (M_{2i} - \bar{M}_2)^2}} \quad (3)$$

By this definition, M_1 and M_2 are fully correlated as long as they share a monotonic functional relationship. This is different from Pearson's correlation, in which only linearly correlated variables are considered as relevant to each other.

Then, the correlation coefficient matrix C_f of n random variables is a matrix of correlation coefficients for each pair of variable combinations.

$$C_f = \begin{pmatrix} \rho(M_1, M_1) & \cdots & \rho(M_1, M_n) \\ \vdots & \ddots & \vdots \\ \rho(M_n, M_1) & \cdots & \rho(M_n, M_n) \end{pmatrix} \quad (4)$$

Since M_1 and M_2 are always directly correlated, the diagonal entries are 1, that is,

$$C_f = \begin{pmatrix} 1 & \cdots & \rho(M_1, M_n) \\ \vdots & \ddots & \vdots \\ \rho(M_n, M_1) & \cdots & 1 \end{pmatrix}. \quad (5)$$

Through the above calculation, the variables with the greater values under the two types of correlation coefficients, C_{f_P} and C_{f_S} , can be selected as predictor variables.

3. Method of Prediction Model

3.1. Training Algorithms. The training algorithms pursue the minimum gap between the predicted value and the measured

value. In most cases, the minimization is achieved by adjusting the weights of each layer in the neural networks. Below is a brief introduction to the training algorithms adopted for our research.

(1) *Broyden–Fletcher–Goldfarb–Shanno (BFGS) Quasi-Newton Backpropagation (BQ)*. The BQ is an alternative to the conjugate gradient methods for fast optimization. The basic formula [14] is as follows:

$$d_{k+1} = d_k - \mathbf{H}_k^{-1} g_k \quad (6)$$

where d_{k+1} is the step distance of $k + 1$; d_k is the step distance of k ; \mathbf{H}_k^{-1} is the Hessian matrix (second derivatives) of performance index at the current weights and biases; and g_k is the gradient of step k .

(2) *Conjugate Gradient Backpropagation with Powell-Beale Restarts (CGB)*. For all conjugate gradient algorithms, the search direction is periodically reset to the negative of the gradient. The reset happens whenever there is too little orthogonality left between the current and the previous gradients. This condition is tested with the following inequality [15].

$$|g_{k-1}^T g_k| \geq 0.2 \|g_k\|^2 \quad (7)$$

(3) *Conjugate Gradient Backpropagation with Fletcher-Reeves Updates (CGF)*. The optimal distances to move along the current search direction, the new search direction, and the conjugate weight adjustment coefficient are, respectively, computed by the following equations [16]:

$$d_{k+1} = d_k \alpha_k p_k \quad (8)$$

$$p_k = -g_k + \beta_k p_{k-1} \quad (9)$$

$$\beta_k = \frac{g_k^T g_k}{g_{k-1}^T g_{k-1}} \quad (10)$$

where α_k is a variable to minimize the performance along the current search direction; p_k is the next search direction, which is conjugate to the previous search direction; and β_k is a constant that adjusts the conjugate weights. Most conjugate gradient algorithms differ only in the calculation of the constant β_k .

(4) *Conjugate Gradient Backpropagation with Polak-Ribière Updates (CGP)*. For this algorithm, the search direction in each iteration is the same as the new search direction in the CGF algorithm [16]. The constant β_k can be obtained by

$$\beta_k = \frac{\Delta g_{k-1}^T g_k}{g_{k-1}^T g_{k-1}} \quad (11)$$

where $\Delta g_{k-1}^T = (g_k - g_{k-1})^T$ is the change transposing form in the gradient from the previous iteration.

(5) *One-Step Secant Backpropagation (OSS)*. The OSS algorithm is an approximate secant method with relatively small

storage and computing load [17]. By this method, the weights can be adjusted in the following manner:

$$p_{k+1} = -g_k + a_k s_k + b_k \Delta g_k \quad (12)$$

where a_k is the weight adjustment coefficient; s_k is the change in the weights of the previous iteration; and b_k is the gradient adjustment coefficient.

(6) *Resilient Backpropagation (RB)*. The RB is a local learning algorithm that is easy to implement and compute. In this algorithm, the weights are updated according to the behaviour of the sign sequence for the partial derivatives in each dimension of the weight space [18]:

$$\Delta \mathbf{w}_k = -\epsilon \frac{\partial E_k}{\partial \mathbf{w}_k} + \mu \Delta \mathbf{w}_{k-1} \quad (13)$$

$$\frac{\partial E_{k-1}}{\partial \mathbf{w}_{k-1}} \cdot \frac{\partial E_k}{\partial \mathbf{w}_k} = 0 \quad (14)$$

where μ is a parameter to scale the influence of the previous iteration and ϵ is the learning rate.

(7) *Scaled Conjugate Gradient Backpropagation (SCG)*. The SCG is a step-size scaling algorithm [19, 20] created to expand the applicable scope of conjugate gradient (CG) algorithm from the functions with positive definite Hessian matrices. The SCG works faster than other second-order algorithms, as it prevents the time-consuming search in each iteration.

(8) *Levenberg-Marquardt Backpropagation (LM)*. The LM algorithm uses the approximate Hessian matrix in the following Newton-like update [21, 22]:

$$\mathbf{H} = \mathbf{J}^T \mathbf{J} \quad (15)$$

$$d_{k+1} = d_k - [\mathbf{J}^T \mathbf{J} + \mu \mathbf{I}]^{-1} \mathbf{J}^T \mathbf{e} \quad (16)$$

where \mathbf{H} is the Hessian matrix; \mathbf{J} is the Jacobian matrix containing the first-order derivatives of network errors with respect to the weights and biases; and \mathbf{e} is a vector of network errors. When the scalar μ is zero, the LM algorithm is essentially a Newton's method using the approximate Hessian matrix.

(9) *Bayesian Regularization Backpropagation (BR)*. Besides reducing the sum of squared errors, E_D , the regularization adds an additional term. Thus, the objective function $E(\mathbf{w})$ can be expressed as

$$E(\mathbf{w}) = \beta E_D + \alpha E_W \quad (17)$$

where E_W is the sum of squares of network weights and α and β are two parameters of the objective function. Under the Bayesian framework [23, 24], this method can optimize the regularization parameters.

With different weight adjustment mechanisms, the above algorithms differ in training accuracy, storage, and running time. Their performance will be compared in the following

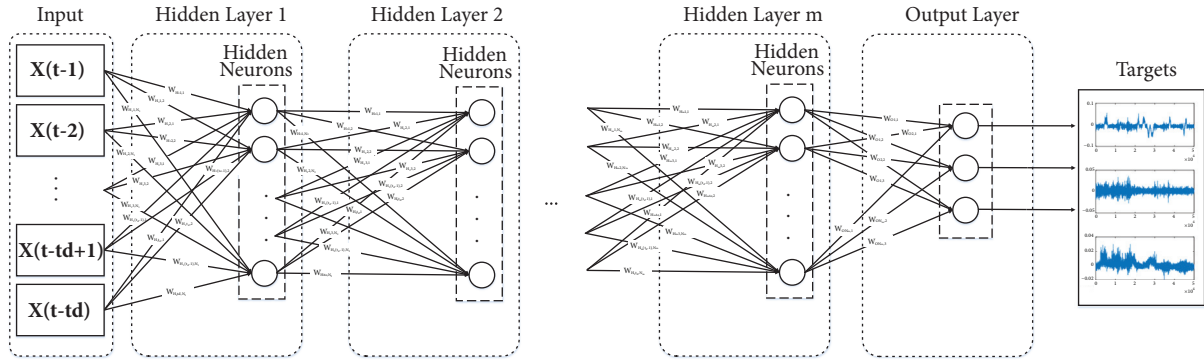


FIGURE 1: Structure of the TSNE.

section. In addition, the functions of the output layer and the hidden layer are as follows.

$$f_H(x) = \text{tansig}(x) = \frac{2}{1 + \exp(-2 * x)} - 1 \quad (18)$$

$$f_O(x) = \text{purelin}(x) = x \quad (19)$$

3.2. Structures of Neural Networks

3.2.1. Feedforward Neural Networks (FFNN). The FFNN is one of the most popular neural networks. The networks have multiple layers, including an input layer, several hidden layers, and an output layer. Layers are connected to each other by nodes or neurons. The input layer is connected to the inputs, while the output layer exports the predicted results. Each hidden layer treats the output of the previous layer as its input.

3.2.2. Time-Series Neural Network without Feedback Time Delays (TSNF). The parameters like vibration and body attitude are often affected by relevant factors and the existing states. This type of variable often uses more accurate time-series neural network prediction methods. A typical time-series neural network structure is as shown in Figure 1, where the input vectors are formed by the input variables and their delays.

Other than the input layer, the other parts of the TSNF are similar to those of the FFNN. In other words, the TSNF also has multiple hidden layers and one output layer. Each hidden layer contains a certain number of neurons.

3.2.3. Time-Series Neural Networks with Feedback Time Delays (TSF). TSF is another common time-series neural network (Figure 2). The structure of TSF originates from the NARX. Unlike the TSNF, the TSF contains both input delayed variables and feedback delays.

The introduction of delayed feedback is equivalent to taking the states of the target close to the next predicted moment as the input variables. According to the analysis in the previous section, the TSF structure is expected to further improve the prediction accuracy. Hence, the performance of the prediction model can be optimized by this structure. Of

course, the other two structures cannot be neglected in actual practice; it is sometimes necessary to make predictions based on predictors with or without feedback.

3.3. Model Construction Process. The optimal prediction model can be constructed in two phases, namely, data preprocessing and variable selection, and the model construction based on neural networks. Figure 3 is the flow chart of the model construction.

In the data preprocessing and variable selection block, firstly the dataset applied here is from GJ-5 track inspection car. To make the following process more effective, we screen the missing and singular values and delete the corresponding sampling points that may deteriorate the analysis results. Then the target variables are defined as the vibration acceleration of car body from three directions, i.e., horizontal, vertical, and lateral directions. The rest measured parameters (139 other parameters in our dataset) are all considered as the predictors at this step. However, under reasonable deduction, there must be a big amount of the predictors being redundant and almost having no impact on the vibration of car body. To solve this problem, next, the correlation analysis between the predictors and the response parameters is carried out. Specifically, the Pearson's correlation coefficient and Spearman's rank correlation coefficient were adopted to select the predictor variables. Since the accuracy of car body vibration forecast model is one of the common key indices, all the predictors with absolute correlation coefficient over 0.1 are taken into consideration as inputs in the following model building process. It should be noted that if the data is very large or selected predictors are still redundant, the chosen bound of the correlation coefficient could be changed to improve the efficiency.

Next, in the building the prediction model block, the selected variables were used to generate the models trained by different algorithms under three neural network structures. The algorithms chosen are widely verified effectively in neural network method and briefly introduced in Section 3.1, which contains LM, BR, BFG, RP, SCG, CGB, CGE, CGP, and OSS, respectively. The three neural networks structures are FF, TSNF, and TSF, respectively, which are illustrated in Section 3.2. The performance evaluation indices of these models were compared to determine the optimal prediction

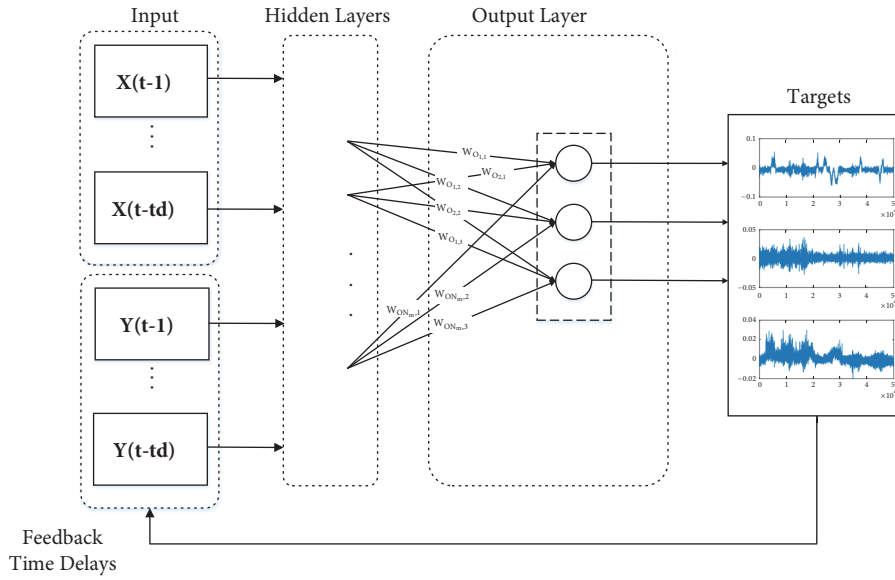


FIGURE 2: Structure of the TSE.

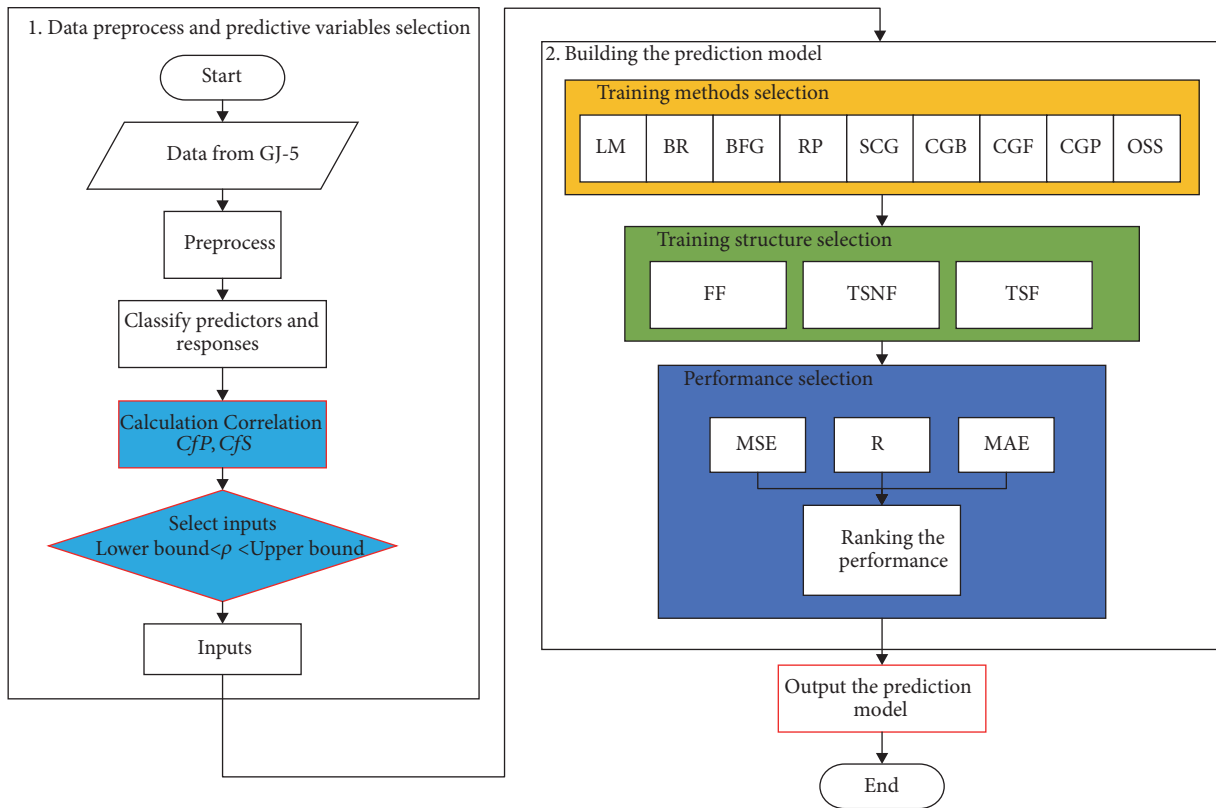


FIGURE 3: Flow chart of model construction.

model for car body vibration acceleration. In this work, the accuracy is defined as the priority pursuing goal of the ranking as we want to improve the suitability of the proposed forecast model, and the real measured values of car body vibration acceleration are very low, normally less than 0.1. Under such consideration, the MSE is set to be the main index of the comparison. If the MSE values are very close,

the R and MAE values are compared as the auxiliary indices. Once the data are large and the running times of algorithms are obviously different, a more comprehensive ranking equation should be designed containing both the three indices and the running time with reasonable corresponding weights. Finally, the forecast model of car body vibration is obtained.

TABLE 1: Main parameters of track inspection and test accuracy of the inspection vehicle.

Test items	Accuracy	Range
Gauge	±0.8 mm	1420~1480 mm
Rail direction (left & right, $\lambda \leq 30\text{m}$)	±1.0 mm	±100 mm
Rail direction (left & right, $\lambda \leq 50\text{m}$)	±2.0 mm	±100 mm
Height (left & right, $\lambda \leq 30\text{m}$)	±1.0 mm	±100 mm
Height (left & right, $\lambda \leq 50\text{m}$)	±2.0 mm	±100 mm
Horizon	±1.5 mm	±50 mm
Super elevation	±1.5 mm	±50 mm
Triangle pit	±1.5 mm	±220 mm
Curve	$1.2 \times 10^{-4} \text{ m}^{-1}$	--
Body acceleration	±0.01 g	±1 g
Rail bottom slope	±0.25 deg	--
Rail cross section (left & right)	±0.5 mm	--

TABLE 2: The prediction variables selected through correlation analysis.

Car body_HACCEL (g)			Car body_VACCEL (g)			Car body_LACCEL (g)		
	ρ_P	ρ_S		ρ_P	ρ_S		ρ_P	ρ_S
Superelev (mm)	-0.50	-0.25	L Surf 1 (mm)	-0.23	-0.20	Mileage (km)	-0.49	-0.49
Curve (rad/km)	-0.14	-0.18	R Surf 1 (mm)	-0.27	-0.22	Gauge (mm)	0.16	0.11
C_IRREG_LEFT (mm)	0.31	0.19	L Surf 2 (mm)	-0.29	-0.24	Superelev (mm)	0.26	0.24
C_IRREG_RIGHT (mm)	0.30	0.18	R Surf 2 (mm)	-0.32	-0.26	Curve (rad/km)	0.29	0.26
CURVE_RATE (rad/km/m)	-0.15	-0.11	L Surf 3 (mm)	-0.31	-0.25	Speed(kph)	-0.48	-0.60
LOFFSET (mm)	-0.22	0.05	R Surf 3 (mm)	-0.35	-0.29	CURVE_RATE (rad/km/m)	-0.11	-0.09
ROFFSET (mm)	-0.27	0.04	L Surf 4 (mm)	-0.17	-0.12	LOFFSET (mm)	0.25	0.20
LSURFACE (mm)	-0.43	-0.31	R Surf 4 (mm)	-0.21	-0.16	ROFFSET (mm)	0.23	0.20
RSURFACE (mm)	0.39	0.26	-	-	-	LSURFACE (mm)	-0.18	-0.15
YAW (deg/s)	0.12	0.14	-	-	-	YAW (deg/s)	-0.21	-0.19
-	-	-	-	-	-	BOGIE_FRAME_HACCEL (g)	0.43	0.44
-	-	-	-	-	-	BOGIE_FRAME_VACCEL (g)	0.41	0.42
Total number 10			Total number 8			Total number 12		

4. Results and Discussion

4.1. Measurement System. The training data were collected by a GJ-5 track inspection vehicle of ImageMap, Inc., between Shenzhen and Guangzhou, two first-tier cities in China. The verification data were acquired on the return section. The main test items include geometry inspection items, on-board dynamics test items, and ground dynamics test items. Specifically, the track geometry inspections include different wavelengths and gauge, track pitch variation rate, level, triangle pit twisting curvature, and curvature change rate; on-board dynamics test items mainly include wheel rail force and left and right wheel vertical forces, lateral force, derailment coefficient, deceleration rate, three-section acceleration reduction rate of wheel load, lateral stability index of the structure, stability and the vehicle body vertical and lateral acceleration of the left and right axle box, frame, and body of the vehicle left and right axle boxes, vertical and lateral acceleration of the frame, car body vertical and lateral acceleration of the left and right axle boxes, frames, and bodywork of the middle car; ground dynamics test items include derailment coefficient, load shedding rate, lateral

force, vertical force, and vertical rail displacement horizontal. The main parameters of track inspection and test accuracy of the inspection vehicle are listed in Table 1.

Through the correlation analysis, the predictor variables for car body vibration acceleration were selected by the absolute values of coefficients falling between 0.1 and 0.9. This interval was chosen to exclude parameters loosely correlated with or similar to the target variable, making it possible to obtain a practical analysis of the impact of each track factor on the target variable. The selected variables are listed in Table 2.

As shown in Table 2, it is clear that the vertical vibration acceleration of the car body directly hinges on the surface conditions of the track. The horizontal and lateral acceleration are affected by relatively more factors, owing to the track state and train operation. Moreover, there are some repeated variables, which is not out of expectation. Through the above processes, the main influencing factors of car body vibration acceleration were all identified, laying the basis for subsequent improvement of train structure and passenger comfort. Finally, the repeated variables were eliminated, leaving a total of 23 predictor variables.

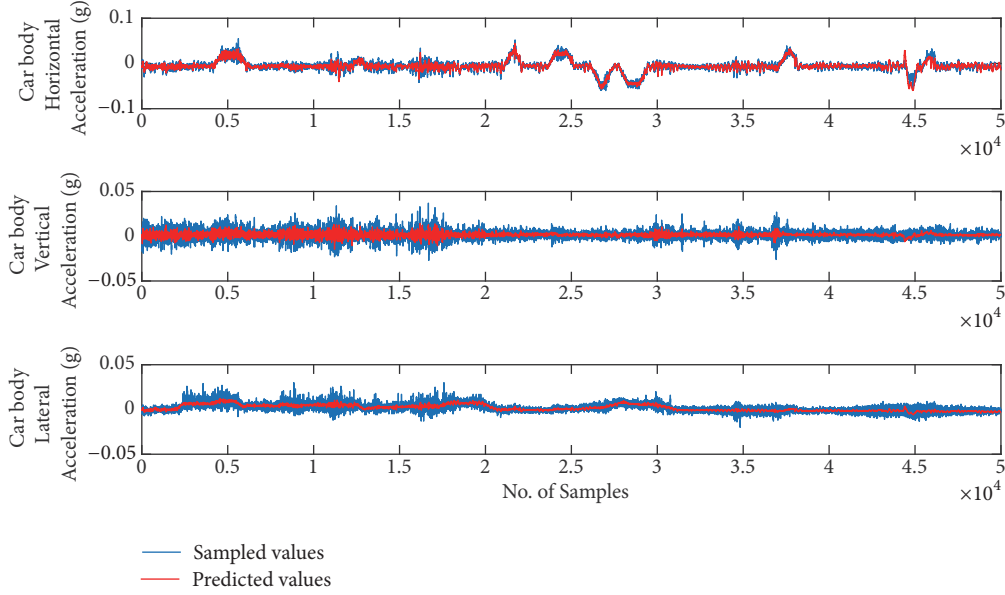


FIGURE 4: Comparison between the predicted values of the FFNN-structure prediction model trained by BR with the measured values.

4.2. Performance Evaluation Indices. Three indices were selected to evaluate the performance of our prediction model: the mean square error (MSE), mean absolute error (MAE), and regression coefficient (R). The MSE served as the main index and the other two as the auxiliary indices.

The MSE can be calculated by the equation below:

$$MSE = \frac{1}{N} \sum_{i=1}^N (e_i)^2 = \frac{1}{N} \sum_{i=1}^N (\hat{y}_i - y_i)^2 \quad (20)$$

where \hat{y}_i is a vector of N predictions; y_i is the vector of observed values corresponding to the inputs; and e_i is the square of the errors. When the MSE is close to zero, it means the model is suitable for prediction when it is not overfitted.

The MAE is a yardstick of the accuracy of evaluation and prediction [25, 26]. The definition of the MAE is as follows.

$$MAE = \frac{1}{N} \sum_{i=1}^N |y_i - \hat{y}_i| \quad (21)$$

The R indicates the amount of variance explained by the prediction model. This index can be expressed as

$$R = \frac{\sum_{i=1}^N (\hat{y}_i - \bar{\hat{y}}) (y_i - \bar{y})}{\sqrt{\sum_{i=1}^N (\hat{y}_i - \bar{\hat{y}})^2} \sqrt{\sum_{i=1}^N (y_i - \bar{y})^2}} \quad (22)$$

where \bar{y} is the mean value of the measured data; $\bar{\hat{y}}$ is the mean value of the predicted data; $\sum_{i=1}^N (y_i - \hat{y}_i)^2$ is the residual sum of squares; and $\sum_{i=1}^N (y_i - \bar{y})^2$ is the explained sum of squares. The value of R falls between 0 and 1. If the R is close to one, it means the model has explained the majority of the variance [27, 28].

4.3. Model Performance. Our prediction models were built on the Matlab software with some codes in the neural network toolbox. The program runs on a Lenovo workstation (CPU: Intel® Xeon® Processor E5-2623 v3; 3.00GHz; RMB: 64GB). To compare the models based on the said three neural network structures, the number of hidden layers and the number of hidden layer nodes were set to 1 and 15, respectively. The number of hidden layer nodes was determined because the FFNN structure can achieve the optimal performance with 15 hidden layer nodes through 10~20 traversal iterations.

4.3.1. Training Performance. As mentioned before, the modelling data were captured at the interval of 0.25m by a GJ-5 track inspection vehicle moving from Shenzhen to Guangzhou. In total, 50,000 sample points which are continuous in time series were selected for modelling. eX replaces 10^X . It can be seen that the models trained with LM and BR outperformed those trained by other algorithms, but the run times of the two models were relatively long.

For better understanding, the predicted values of the FFNN-structure model trained by BR were compared with the measured values in Figure 4, where the horizontal axis is the total number of samples and the vertical axis is the target variable (i.e., the car body vibration acceleration in three directions).

As shown in Figure 4, the predicted acceleration in all three directions basically conformed to the trend of the target variables. However, only the predicted acceleration in the horizontal direction was entirely consistent with the measured value, while that in the other two directions merely approximated the mean value of the target variables. The magnitude and range of the measured values were not well reflected.

TABLE 3: Performance of the FFNN-structure prediction model.

Method	Set	MSE	R	MAE	Running time (s)
BQ	Training	1.67e-04	0.21	0.0095	4.04
	Validation	1.88e-04	-0.10	0.0105	
	Test	5.43e-04	0.21	0.0191	
CGB	Training	5.29e-05	0.75	0.0053	2.21
	Validation	4.81e-05	0.58	0.0052	
	Test	1.15e-04	0.71	0.0085	
CGF	Training	1.42e-04	0.25	0.0089	1.52
	Validation	1.94e-04	0.24	0.0112	
	Test	3.71e-04	0.38	0.0163	
CGP	Training	1.01e-04	0.52	0.0077	1.81
	Validation	8.24e-05	0.34	0.0068	
	Test	3.38e-04	0.33	0.0136	
OSS	Training	5.79e-04	-0.22	0.0196	1.68
	Validation	4.04e-04	-0.44	0.0174	
	Test	5.77e-04	-0.43	0.0208	
RB	Training	2.91e-05	0.89	0.0040	1.77
	Validation	2.52e-05	0.80	0.0038	
	Test	7.86e-05	0.71	0.0057	
SCG	Training	1.32e-04	0.43	0.0088	1.09
	Validation	1.31e-04	0.53	0.0094	
	Test	7.86e-05	0.30	0.0213	
LM	Training	2.61e-05	0.92	0.0038	16.20
	Validation	4.91e-05	0.87	0.0053	
	Test	2.21e-04	0.86	0.0134	
BR	Training	1.77e-05	0.94	0.0031	289.73
	Test	2.38e-05	0.78	0.0033	

TABLE 4: Performances of the TSNF-structure prediction model.

Method	MSE	R	MAE	Running time (s)
BQ	1.51e-05	0.94	0.0029	2.01e+03
CGB	1.40e-05	0.95	0.0028	244.87
CGF	1.44e-05	0.94	0.0028	252.16
CGP	1.41e-05	0.95	0.0028	237.03
OSS	1.81e-05	0.92	0.0032	299.56
RB	2.03e-05	0.91	0.0034	27.15
SCG	1.41e-05	0.95	0.0028	119.79
LM	1.19e-05	0.96	0.0026	5.64e+04
BR	1.20e-05	0.96	0.0026	8.76e+03

The performance of the TSNF-structure prediction model is presented in Table 4. It can be seen that the three indices were all improved from the levels in Table 3, indicating that it is meaningful to consider the time delays. This is because the car body has some time delays in its response to the relevant factors, such as track surface and driver's operation. Nonetheless, it is also learned that the TSNF increased the run time from that of the FFNN.

The predicted values of the TSNF-structure model trained by BR were compared with the measured values in Figure 5. It is clear that the TSNF-structure model reflected

the magnitude and range of the measured values more accurately than the FFNN-structure model.

Finally, the performance of the TSF-structure model (Table 5) shows that the model performance changed little with the training algorithms. The order of magnitude of the MSE was always at 10^{-6} ; the R value remained near 0.99. Therefore, the TSF structure can bless the model with a good performance with a short run time.

The predicted values of the TSF-structure model trained by LM were compared with the measured values in Figure 6. It can be seen that the predicted values were highly consistent

TABLE 5: Performance of the TSF-structure prediction model.

Method	MSE	R	MAE	Running time (s)
CGB	2.27e-06	0.9898	0.0012	257.82
CGF	2.29e-06	0.9897	0.0012	263.01
CGP	2.29e-06	0.9897	0.0012	258.24
OSS	3.18e-06	0.9876	0.0014	321.94
BQ	2.54e-06	0.9890	0.0012	1.91e+03
RB	7.67e-06	0.9618	0.0021	36.37
SCG	2.39e-06	0.9895	0.0012	81.06
LM	2.02e-06	0.9910	0.0011	5.26e+04
BR	2.05e-06	0.9908	0.0011	1.14e+04

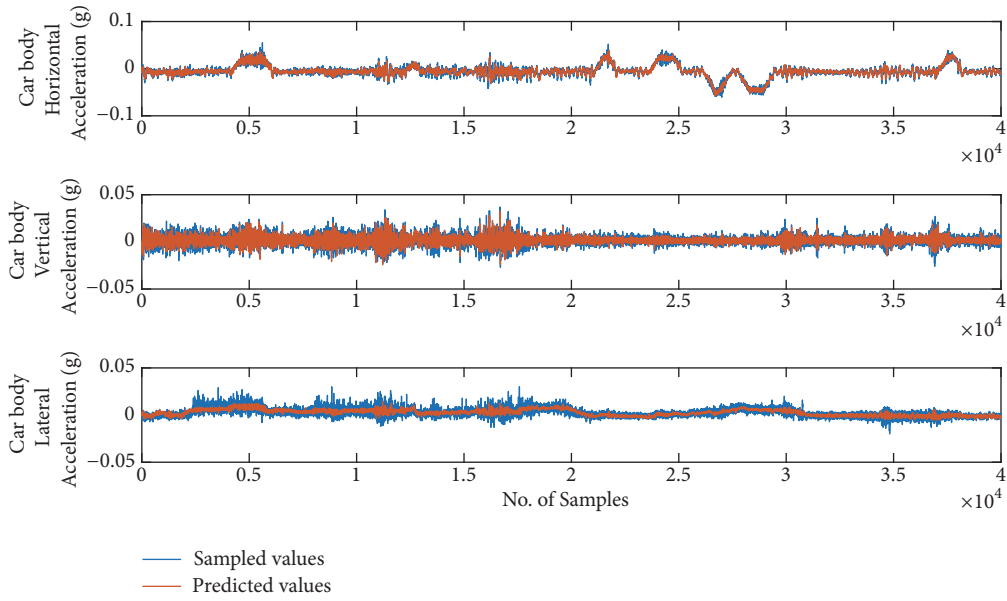


FIGURE 5: Comparison between the predicted values of the TSNF-structure prediction model trained by BR with the measured values.

with the measured values. Compared to the other two structures, the TSF managed to reflect the actual magnitude and range of the measured values.

4.3.2. Additional Dataset Verification. To verify the universality of the proposed model, another 40,000 sample points were selected from the data acquired by the GJ-5 track inspection vehicle on the return journey. Table 6 compares the performances of the FFNN-, TSNF-, and TSF-structure models on the additional dataset. Figures 7–10 display the best performing model of each structure on the test dataset.

As shown in Figures 7, 8, 9, and 10, the predicted values of FFNN- and TSNF-structure models deviated significantly from the measured results in some intervals. The possible reasons are as follows: First, the target variables may be affected by other implicit variables. Second, the correlation analysis fails to screen out all the representative predictor variables. Before applying the models of these two structures to actual projects, it is necessary to expand the dataset to include various situations and calculate correlation coefficients in a

proper manner. These are the necessary steps to acquire the typical influencing factors of the target variables.

Besides, the predicted values of the TSF-structure model trained by CGB and CGP were basically consistent with the measured values, which are obviously better than those of the other two structure models. In some stationary phases, however, there was a constant deviation between the predicted and measured values. A possible reason lies in the fact that the predicted values are less affected by other influencing factors in relatively stable phases and are only determined by the impacts from delayed feedback values. By contrast, the constant deviation did not appear in the FFNN-structure model. Thus, the FFNN structure might be helpful to eliminate the deviation in the TSF-structure model. This idea will be examined in future research.

Given the accurately predicted vibration acceleration of the car body, the passenger comfort can be derived according to international standards like ISO2631 or UIC513. Thus, the proposed prediction model lays the basis for early warning and fault detection in operation and maintenance processes.

TABLE 6: Performances of the FFNN-, TSNF-, and TSF-structure models on the new dataset.

Method	FF			TSNF			TSF		
	MSE	R	MAE	MSE	R	MAE	MSE	R	MAE
BQ	1.31e-03	-0.37	3.07	6.61e-04	0.2305	0.0213	4.83e-04	0.61	1.86
CGB	1.30e-03	-0.16	2.97	0.0020	0.3609	0.0413	1.06e-04	0.78	0.81
CGF	7.14e-03	-0.25	7.95	0.0029	0.4036	0.0376	9.35e-04	0.95	2.76
CGP	1.01e-03	0.39	2.84	0.0011	0.2284	0.0275	1.53e-04	0.91	1.03
OSS	4.28e-03	0.09	5.63	0.0011	-0.0584	0.0275	1.71e-03	0.80	3.79
RB	2.35e-03	-0.06	3.61	0.0021	0.2364	0.0351	4.50e-04	0.42	1.72
SCG	3.85e-03	0.69	4.36	3.05e-04	0.0131	0.0128	4.06e-04	0.79	1.64
LM	1.02e-03	0.66	2.76	0.0122	-0.3984	0.0864	5.50e-03	0.04	4.52
BR	3.74e-04	0.68	1.27	0.0111	-0.0890	0.0696	1.01e-03	0.84	2.93

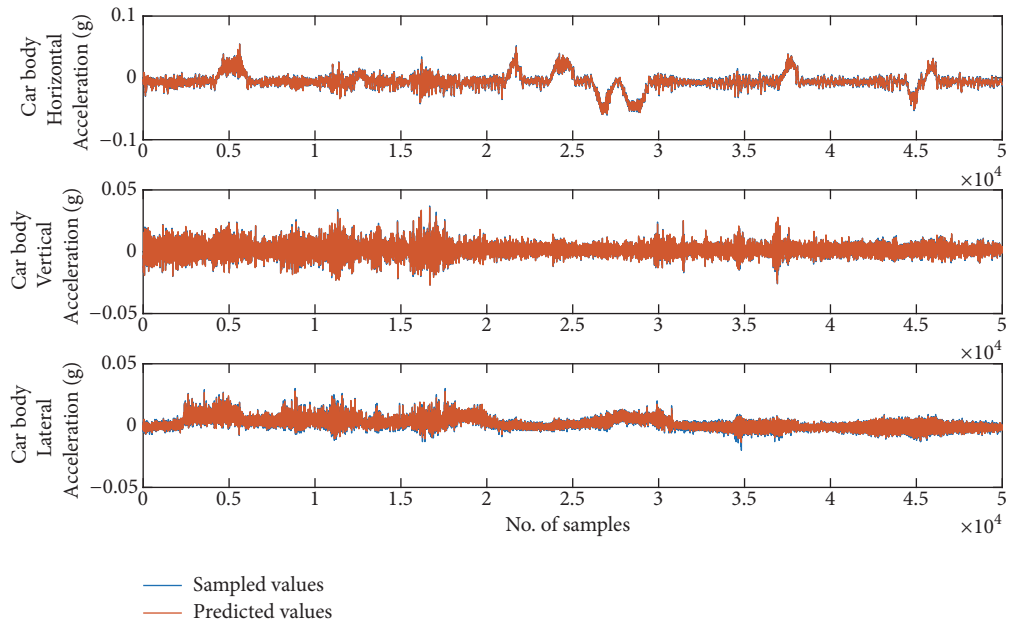


FIGURE 6: Comparison between the predicted values of the TSNF-structure prediction model trained by LM with the measured values.

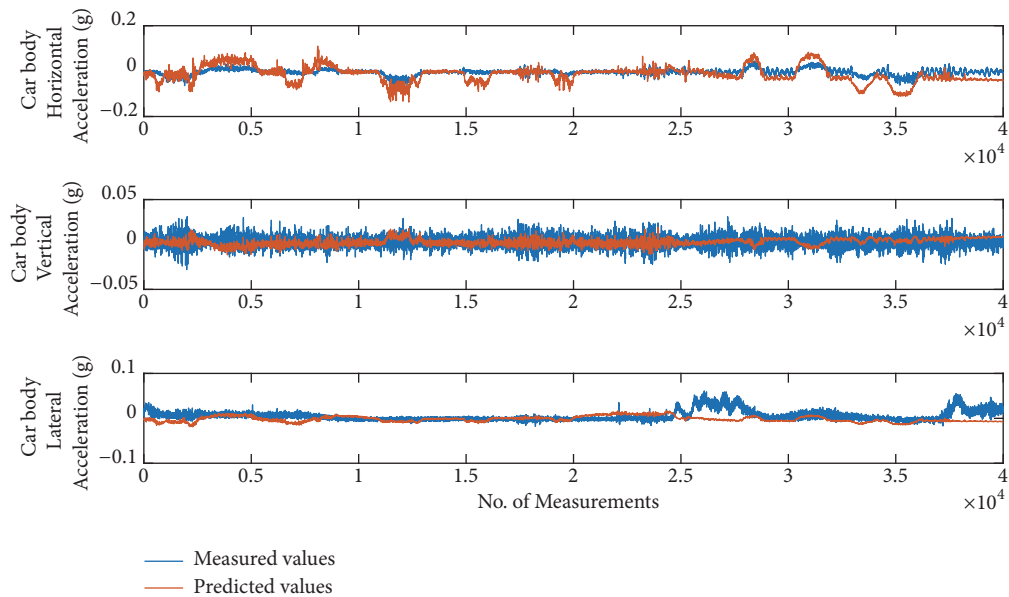


FIGURE 7: FFNN-structure model trained by BR.

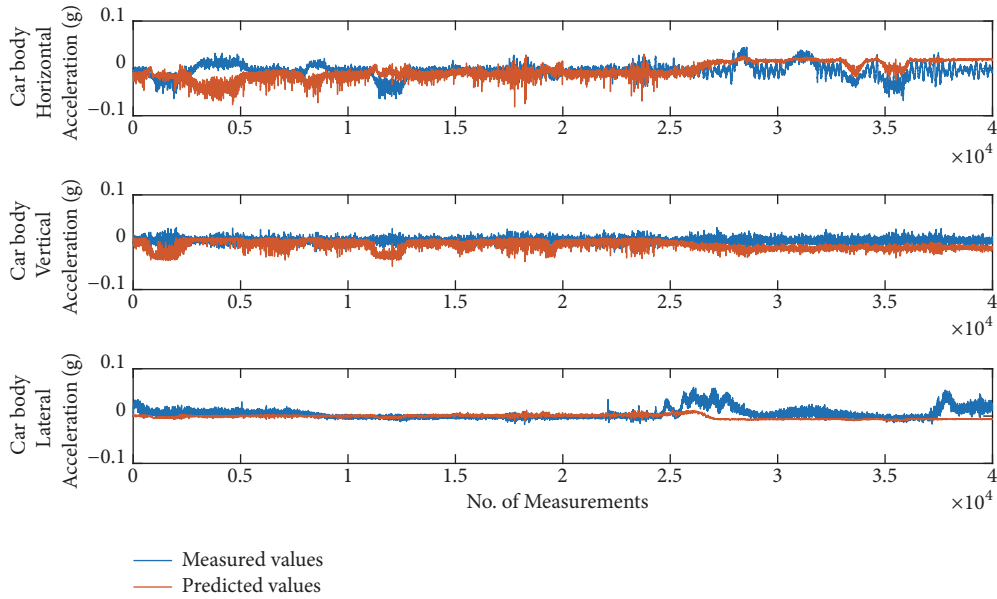


FIGURE 8: TSNF-structure model trained by SCG.

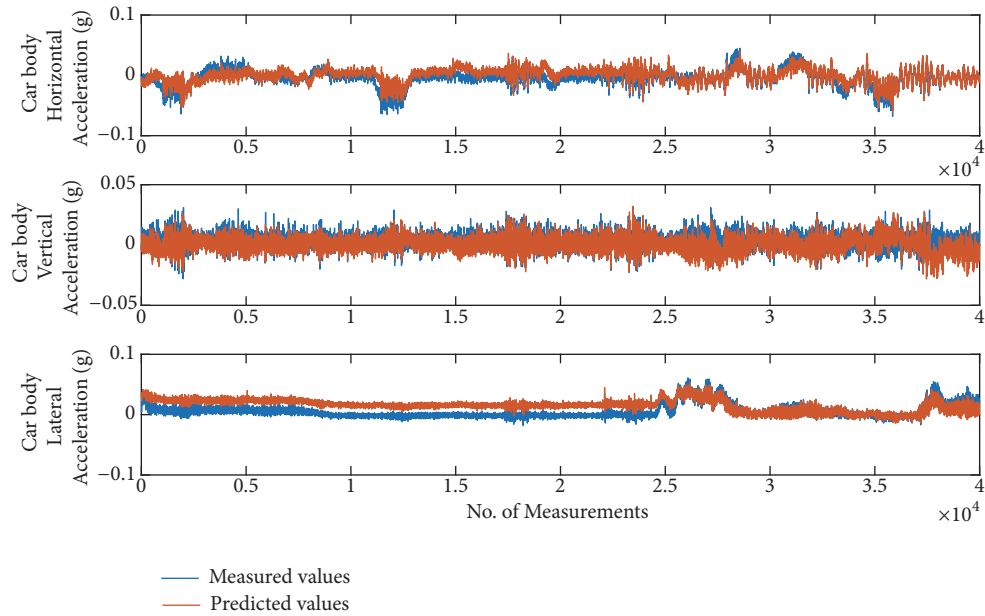


FIGURE 9: TSF-structure model trained by CGB.

5. Conclusions

This paper establishes a prediction model for car body vibration acceleration. In the beginning, the various parameters related to the track and the train were filtered by correlation analysis based on both Pearson' correlation coefficient and Spearman's rank correlation coefficient. The parameters closely correlated with the target variable were selected as predictor variables. Then, the selected variables were used to construct prediction models with three different neural network structures, namely, the FFNN, the TSNF, and the TSF. To verify the performance, the proposed models were applied

to predict the car body vibration acceleration with actual railway datasets. The following phenomena were observed from the predicted results.

During the training process and new prediction, according to the obtained values of indices, the BR training algorithm achieved very good performances both on the training dataset and the new dataset under FFNN and TSNF structures, but it consumed too much time. The LM boasted the best performance under the TSF structure but performed poorly on the new test dataset. The TSF-structure models trained by CGB and CGP achieved even more accurate prediction on the new dataset.

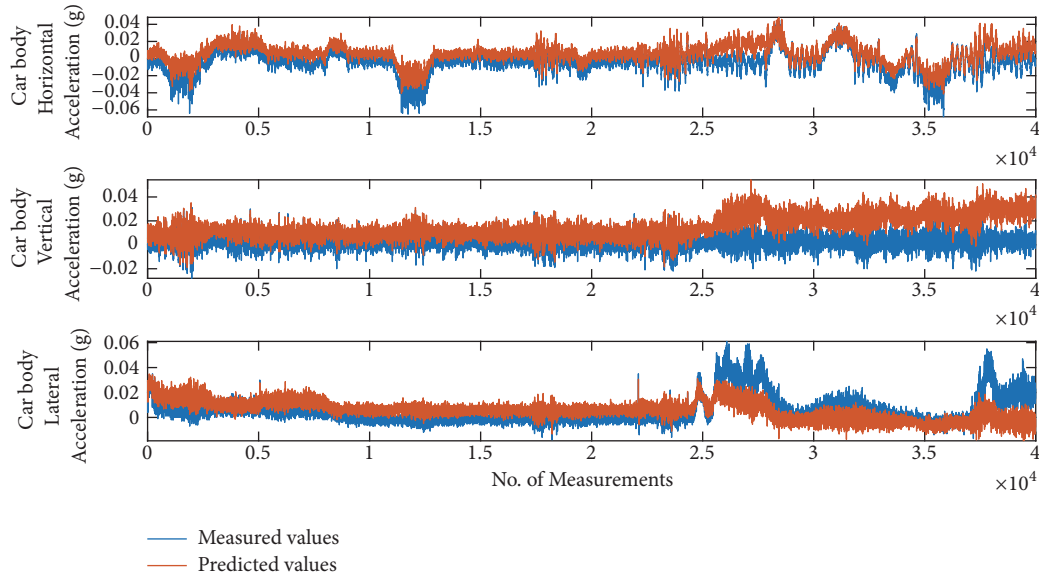


FIGURE 10: TSF-structure model trained by CGP.

The future research will further improve the adaptability of the proposed model and apply the predicted values to enhance passenger comfort.

Nomenclature

NN:	Neural networks	TS_NF:	Time-series neural networks without feedback time delays
P:	Pearson correlation coefficient	TS_F:	Time-series neural networks with feedback time delays
S:	Spearman correlation coefficient	Superelev:	Superelevation
BFGS:	Broyden–Fletcher–Goldfarb–Shanno	C_IRREG_LEFT:	Left complex irregularity
BQ:	BFGS Quasi-Newton backpropagation	C_IRREG_RIGHT:	Right complex irregularity
CGB:	Conjugate gradient backpropagation with Powell-Beale restarts	LOFFSET:	Left offset
CGF:	Conjugate gradient backpropagation with Fletcher-Reeves updates	ROFFSET:	Right offset
CGP:	Conjugate gradient backpropagation with Polak-Ribière updates	LSURFACE:	Left surface
OSS:	One-step secant backpropagation	RSURFACE:	Right surface
RB:	Resilient backpropagation	BOGIE_FRAME_HACCEL:	Horizontal acceleration of bogie framework
SCG:	Scaled conjugate gradient backpropagation	BOGIE_FRAME_VACCEL:	Vertical acceleration of bogie framework
LM:	Levenberg-Marquardt backpropagation	L Surf 1:	Left vertical irregularity of long wave
BR:	Bayesian regularization backpropagation	R Surf 1:	Right vertical irregularity of long wave
FF:	Feedforward net	L Surf 2:	Left vertical irregularity of medium wave
		R Surf 2:	Right vertical irregularity of medium wave
		L Surf 3:	Left vertical irregularity under 20 cm chord
		R Surf 3:	Right vertical irregularity under 20 cm chord
		L Surf 4:	Left vertical irregularity under 10 cm chord
		R Surf 4:	Right vertical irregularity under 10 cm chord
		CURVE_RATE:	Curvature change rate
		MSE:	Mean square error
		R:	Regression coefficient
		MAE:	Mean absolute error.

Data Availability

The data used to support the findings of this study are available from the corresponding author upon request.

Conflicts of Interest

The authors declare that the research was conducted in the absence of any commercial or financial relationships that could be construed as potential conflicts of interest.

Acknowledgments

This research was funded by National Natural Science Foundation of China [Grant No. 51478258 and 51405287] and Shanghai Committee of Science and Technology [Grant No. 18030501300].

References

- [1] L. L. Hoberock, "A survey of longitudinal acceleration comfort studies in ground transportation vehicles," *Journal of Dynamic Systems, Measurement, and Control*, vol. 99, no. 2, pp. 76–84, 1977.
- [2] P. E. Uys, P. S. Els, and M. Thoreson, "Suspension settings for optimal ride comfort of off-road vehicles travelling on roads with different roughness and speeds," *Journal of Terramechanics*, vol. 44, no. 2, pp. 163–175, 2007.
- [3] G. M. Shafiqullah, A. B. M. S. Ali, A. Thompson, and P. J. Wolfs, "Predicting vertical acceleration of railway wagons using regression algorithms," *IEEE Transactions on Intelligent Transportation Systems*, vol. 11, no. 2, pp. 290–299, 2010.
- [4] Z. Wanming, H. Zhenxing, and S. Xiaolin, "Prediction of high-speed train induced ground vibration based on train-track-ground system model," *Earthquake Engineering and Engineering Vibration*, vol. 9, no. 4, pp. 545–554, 2010.
- [5] P. Czop, K. Mendrok, and T. Uhl, "Application of inverse linear parametric models in the identification of rail track irregularities," *Archive of Applied Mechanics*, vol. 81, no. 11, pp. 1541–1554, 2011.
- [6] K. Qian, J. Liang, and Y. H. Gao, "The prediction of vibration and noise for the high-speed train based on neural network and boundary element method," *Journal of Vibroengineering*, vol. 17, no. 8, pp. 4445–4457, 2015.
- [7] D. P. Connolly, G. Kouroussis, O. Laghrouche, C. L. Ho, and M. C. Forde, "Benchmarking railway vibrations—track, vehicle, ground and building effects," *Construction and Building Materials*, vol. 92, pp. 64–81, 2014.
- [8] J. S. Koo and H. S. Oh, "A new derailment coefficient considering dynamic and geometrical effects of a single wheelset," *Journal of Mechanical Science and Technology*, vol. 28, no. 9, pp. 3483–3498, 2014.
- [9] P. Nàvik and A. Rønquist, "Uplift-Monitoring for Dynamic Assessment of Electrical Railway Contact Lines," *Dynamics of Civil Structures*, pp. 237–244, 2015.
- [10] R. A. Fisher, *Statistical Methods for Research Workers*, Hafner, 13th edition, 1958.
- [11] M. G. Kendall, *The Advanced Theory of Statistics*, Charles Griffin, 1976.
- [12] W. H. Press, S. A. Teukolsky, W. T. Vetterling, and B. P. Flannery, "Numerical Recipes in C," *Art of Scientific Computing*, vol. 10, no. 1, pp. 176–177, 1995.
- [13] D. J. Best and D. E. Roberts, "Algorithm AS 89: The Upper Tail Probabilities of Spearman's Rho," *Journal of Applied Statistics*, vol. 24, no. 3, pp. 377–379, 1975.
- [14] Murray and Walter, *Practical optimization*, Academic Press, 1981.
- [15] M. J. D. Powell, "Restart procedures for the conjugate gradient method," *Mathematical Programming*, vol. 12, no. 2, pp. 241–254, 1977.
- [16] L. E. Scales, *Introduction to Non-Linear Optimization*, Macmillan Education, London, UK, 1985.
- [17] R. Battiti, "First- and Second-Order Methods for Learning: Between Steepest Descent and Newton's Method," *Neural Computation*, vol. 4, no. 2, pp. 141–166, 1992.
- [18] M. Riedmiller and H. Braun, "A direct adaptive method for faster backpropagation learning: The RPROP algorithm," in *Proceedings of the IEEE International Conference on Neural Networks, ICNN 1993*, pp. 586–591, USA, April 1993.
- [19] M. F. Møller, "Efficient Training of Feed-Forward Neural Networks," *DAIMI Report Series*, vol. 22, no. 464, 1993.
- [20] M. F. Møller, "A scaled conjugate gradient algorithm for fast supervised learning," *Neural Networks*, vol. 6, no. 4, pp. 525–533, 1993.
- [21] D. W. Marquardt, "An Algorithm for Least-Squares Estimation of Nonlinear Parameters," *Journal of the Society for Industrial & Applied Mathematics*, vol. 11, no. 2, pp. 431–441, 1963.
- [22] M. Hagan and M. Menhaj, "Training feedforward networks with the Marquardt algorithm," *IEEE Transactions on Neural Networks and Learning Systems*, vol. 5, no. 6, pp. 989–993, 1994.
- [23] D. J. C. MacKay, *Bayesian Interpolation*, MIT Press, 1992.
- [24] F. D. Foresee and M. T. Hagan, "Gauss-Newton approximation to Bayesian learning," in *Proceedings of the IEEE International Conference on Neural Networks*, vol. 3, pp. 1930–1935, 1997.
- [25] C. J. Willmott and K. Matsuura, "Advantages of the mean absolute error (MAE) over the root mean square error (RMSE) in assessing average model performance," *Climate Research*, vol. 30, no. 1, pp. 79–82, 2005.
- [26] A. Borji, M.-M. Cheng, H. Jiang, and J. Li, "Salient object detection: a benchmark," *IEEE Transactions on Image Processing*, vol. 24, no. 12, pp. 5706–5722, 2015.
- [27] P. A. Bostan, G. B. M. Heuvelink, and S. Z. Akyurek, "Comparison of regression and kriging techniques for mapping the average annual precipitation of Turkey," *International Journal of Applied Earth Observation and Geoinformation*, vol. 19, no. 1, pp. 115–126, 2012.
- [28] X. Chai, S. Zheng, S. Geng, and L. Zhang, "The prediction of railway vehicle vibration based on neural network," *Journal of Information and Computational Science*, vol. 12, no. 16, pp. 5889–5899, 2015.

Research Article

An Efficient Color Space for Deep-Learning Based Traffic Light Recognition

Hyun-Koo Kim ¹, Ju H. Park ², and Ho-Youl Jung ¹

¹Multimedia Signal Processing Group, Department of Information and Communication Engineering, Yeungnam University, Gyeongsan 38544, Republic of Korea

²Nonlinear Dynamics Group, Department of Electrical Engineering, Yeungnam University, Gyeongsan 38544, Republic of Korea

Correspondence should be addressed to Ho-Youl Jung; hoyoul@yu.ac.kr

Received 21 May 2018; Accepted 19 November 2018; Published 6 December 2018

Guest Editor: Mihai Dimian

Copyright © 2018 Hyun-Koo Kim et al. This is an open access article distributed under the Creative Commons Attribution License, which permits unrestricted use, distribution, and reproduction in any medium, provided the original work is properly cited.

Traffic light recognition is an essential task for an advanced driving assistance system (ADAS) as well as for autonomous vehicles. Recently, deep-learning has become increasingly popular in vision-based object recognition owing to its high performance of classification. In this study, we investigate how to design a deep-learning based high-performance traffic light detection system. Two main components of the recognition system are investigated: the color space of the input video and the network model of deep learning. We apply six color spaces (RGB, normalized RGB, Ruita's RYG, YCbCr, HSV, and CIE Lab) and three types of network models (based on the Faster R-CNN and R-FCN models). All combinations of color spaces and network models are implemented and tested on a traffic light dataset with 1280×720 resolution. Our simulations show that the best performance is achieved with the combination of RGB color space and Faster R-CNN model. These results can provide a comprehensive guideline for designing a traffic light detection system.

1. Introduction

Over the past few years, various advanced driving assistance system (ADAS) have been developed and commercialized. In particular, most automotive companies are now doing their best to launch autonomous vehicles as soon as possible. According to the society of automotive engineers (SAE), the international standard defining the six levels of driving automation requires the autonomous driving to achieve level 3 and higher [1]. Obviously, the traffic light recognition is an essential task for ADAS as well as for autonomous vehicle.

For traffic light recognition, various methods have been proposed. These can be analyzed from three aspects such as color space, feature extraction, and verification/classification. Different color spaces, namely, gray scale [2, 3], RGB [4, 5], normalized RGB [6], Ruita's RGB [7], YCbCr [8, 9], HSI [10], HSV [11, 12], HSL [13], and CIE Lab [14], have been used. Moreover, some studies [15–18] have used more than one color spaces. For feature extraction, Haralick's circularity measure [19], Sobel edge detection [20], circle Hough transform [21], 2D Gabor wavelets [22], Haar-likes [23], histogram

of oriented gradients (HOG) [24], and geometric features [25] have been applied. For verification/classification, various conventional classifiers have been used, e.g., k-means clustering [26], template matching [27], 2D independent component analysis (ICA) [28], linear discriminant analysis (LDA) [29], decision-tree classifier, k-nearest neighbor (kNN) classifier [30], adaptive boosting algorithm (Adaboost) [31], and support vector machine (SVM) [32]. Recently, some basic deep-learning networks such as LeNet [33], AlexNet [34], and YOLO [35, 36] have been applied to traffic light recognition. Other approaches using visual light road-to-vehicle communication have been developed. LED-typed traffic lights broadcast the information, then photo-diode [37, 38] or high-frame-rate image sensor [39, 40] receives the optical signal. In this paper, we mainly focus on vision-based traffic light recognition using deep-learning.

In the last couple of years, deep-learning has achieved a remarkable success in various artificial intelligence research areas. In particular, deep-learning has become very popular in vision-based object recognition due to its high performances of classification. One of the first advances is OverFeat

that applies the convolutional neural network (CNN) [34] to multiscale sliding window algorithm [41]. Girshick et al. proposed a region with CNN (R-CNN), which achieves up to almost 50% improvement on the object detection performance [42]. In R-CNN, object candidate regions are detected and features are extracted using CNN, while objects are classified using SVM. Girshick proposed a Fast R-CNN, which uses selective search to generate object candidates and applies fully connected neural network to classify the objects [43]. However, the selective search algorithm slows down the object detection system performance. Redmon et al. proposed YOLO, which uses a simple CNN approach to achieve real-time processing by enhancing detection accuracy and reducing computational complexity attaining [35]. Ren et al. proposed a Faster R-CNN which replaces the selective search by region proposal network (RPN) [44]. The RPN is a fully convolutional network that simultaneously predicts the object bounds and object/objectless scores at each position. This method makes it possible to implement the end-to-end training. Recently, two notable deep-learning network models were proposed, single shot detector (SSD) and region-based fully convolutional networks (R-FCN). SSD uses multiple sized convolutional feature maps to achieve a better accuracy and higher speed than YOLO [45]. R-FCN is a modified version of Faster R-CNN, which consists of only convolutional networks [46]. It is to be noted that the feature extraction is included in deep-learning detection network in the cases of Fast R-CNN, YOLO, Faster R-CNN, SSD, and R-FCN frameworks. The above-mentioned deep-learning methods have been widely applied to detect objects such as vehicle and pedestrian [47–51]. However, only a few deep-learning based network models have been applied to traffic light detection system [52–55].

From the viewpoints of color representation, various color spaces of input video data have been used in conventional traffic light recognition methods. However, only a few color spaces have been applied in deep-learning based methods. Because color information plays an important role in the performance of traffic light detection, it is necessary to select the color space carefully in deep-learning based methods. In this study, we focus on how to design a high-performance deep-learning based traffic light recognition system. To find color space most suitable to deep-learning based traffic light recognition, six color spaces such as RGB, normalized RGB, Ruta's RYG, YCbCr, HSV, and CIE Lab are investigated. For deep-learning network models, three models based on the Faster R-CNN and R-FCN are applied. All combinations of color spaces and network models are implemented and compared.

The rest of this paper is organized as follows. Second section discusses the previous research works on traffic light detection system. In third section, we describe various color spaces and deep-learning network models. All combinations of color spaces and network models have been designed in this study. In fourth section, we explain the configurations such as parameter and data set for the performance evaluation. Fifth section presents the simulation results. Final section draws the conclusions.

2. Related Works

In this section, we briefly introduce the work done so far on traffic light detection. These works are categorized into two groups, namely, deep-learning based and conventional classification methods, depending on whether the deep-learning is used or not. They are investigated mainly from the viewpoints of color representation and verification/classification. The analysis is summarized in Table 1.

2.1. Conventional Classification Based Methods. In general, conventional traffic light recognition methods mainly consist of two steps, candidate detection, and classification. Various color representations have been used. Charette and Nashashibi did not use any color information [2, 3]. They proposed to use the gray-scale image as input data. After the top-hat morphological filtering, adaptive template matching with geometry and structure information was applied to detect the traffic lights. Park and Jeong used color extraction and k-means clustering for candidate detection [4]. The average and standard deviation of each component in RGB color space were then calculated and used. Here, Haralick's circularity was used for verification. Yu et al. used the difference of each pair of components in RGB space to extract the dominant color [5]. They applied region growing and segmentation for candidate detection. For verification, the information of shape and position was used. Omachi and Omachi used normalized RGB for color segmentation [6]. The edge detection and circle Hough transform were applied for verification of traffic light. Kim et al. used Ruta's RGB based color segmentation for the detection of traffic light candidates at night [7]. Some geometric and stochastic features were extracted and used in SVM classifier. Kim et al. used YCbCr color-based thresholding and shape filtering for candidate detection [8]. Here, Haar-like features and Adaboost were used for classification. Kim et al. used YCbCr color segmentation for candidate detection [9]. Here, candidate blobs with red and green lights were detected by thresholding Cb and Cr components. Various shape and modified Haar-like features were extracted and used in decision-tree classifier. Siogkas et al. used the CIE Lab color space [14], where the multiplications of L and a components (RG), and L and b components (YB) are used to enhance the discrimination of red and green regions. They used fast radial symmetry transform and persistency to identify the color of traffic lights. Cylindrical color spaces such as HSI, HSV, and HSL have also been used [10–13]. Hwang et al. used HSI color-based thresholding, morphological filtering, and blob labeling for candidate detection [10]. For verification, they used convolution of the candidate region with Gaussian mask using existence-weight map. HSV color space was also used, where the histograms of hue and saturation components are used for candidate extraction [11]. Probabilistic template matching was applied for classification. Recently, it has been reported that the detection performance of traffic lights can be improved by using the 3D geometry map that are prebuild from GPS, INS/IMU, and range sensors such as stereo camera or 2D/3D range lidar [12, 13]. Jang et al. used Haar-like feature based Adaboost with 3D map information for candidate

TABLE 1: Color space and verification/classification used in previous traffic light detection.

Ref. #	Color space	Verification / Classification
[2], [3]	Gray-scale	Template matching
[4]	RGB	K-means clustering, Circularity check
[5]	RGB	Region growing, Color segmentation
[6]	Normalized RGB	Color segmentation, Circle Hough transform
[7]	Ruta's RGB	SVM
[8]	YCbCr	Adaboost
[9]	YCbCr	Decision-tree classifier
[10]	HSI	Gaussian mask, Existence-Weight Map
[11]	HSV	Template matching
[14]	CIE Lab	Fast radial symmetry transform
[12]	HSV	SVM
[13]	HSL	SVM
[15]	Normalized RGB, RGB	Color clustering
[16]	Normalized RGB, RGB	Fuzzy logic clustering
[17]	RGB, YCbCr	Nearest neighbor classifier
[18]	RGB, HSV	LDA, kNN, SVM
[53]	CIE Lab	SVM, LeNet, AlexNet
[52]	HSV	SVM, Simple CNN
[54]	RGB	YOLO v1
[55]	RGB	YOLO 9000

detection [12]. HOG and HSV color histogram were applied to SVM classifier. Moreover, traffic light candidates are detected by using HOG features based linear SVM classifier with the uncertainty of 3D prior that constrains the search regions [13]. For classification, image color distribution in HSL color space is used.

Some researchers used two color spaces [15–18]. Omachi and Omachi used RGB and normalized RGB color spaces to find candidates, and circle Hough transform was applied for verification [15]. Combination of RGB and normalized RGB was also used for color segmentation based on fuzzy logic clustering, where some geometric and stochastic features were used as primary clues to discriminate traffic lights from others [16]. Cai et al. used RGB and YCbCr color spaces for candidate extraction and classification, respectively [17]. Gabor wavelet transform and ICA based features were extracted and applied to the nearest neighbor classifier. Furthermore, red, yellow and green traffic light regions are detected by thresholding based HSV color segmentation and geometrical features [18]. HOG features were extracted in RGB space and used to determine whether arrow sign is on the light or not. Three different classification algorithms such as LDA, kNN, and SVM were applied, respectively.

Since the selection of color space plays the most important role in traffic light detection performance, past studies have explored all the possible options. Clearly, it is important to identify the best among all these color spaces.

2.2. Deep-Learning Based Methods. Deep-learning has been also used for traffic light detection and classification [52–55]. At first, deep learning was applied only in the classification of traffic lights, where candidates were detected

by conventional method [52, 53]. Saini et al. used HSV color space-based color segmentation, aspect ratio, and area-based analysis and maximally stable extremal region (MSER) to localize the candidates [52]. HOG features and SVM were used for verification, whereas simple CNN was used for classification. Lee and Park used CIE Lab color space-based segmentation to find the candidate regions [53]. To reduce false regions, they use SVM with size, aspect ratio, filling ratio and position. The classification was performed by two cascaded CNN which consists successively of LeNet and AlexNet. LeNet quickly differentiates between traffic lights and background. AlexNet classifies traffic light types. Recently, deep-learning has been applied both to candidate detection and classification. Behrendt et al. [54] and Jensen et al. [55] applied YOLO-v1 [35] and YOLO-9000 [36] for traffic light detection/classification.

As discussed, only a few color spaces have been applied in deep-learning based traffic light detection. Because color information plays an important role in the performance of detection, it is necessary to select the color space carefully. It is also required to apply more sophisticated and efficient deep-learning network models to traffic light detection and classification.

3. Deep-Learning Based Traffic Light Detection

In this section, we present a deep-learning based traffic light detection system that consists of the preprocessing, deep-learning based detection, and postprocessing as shown in Figure 1. In preprocessing, the input video data is

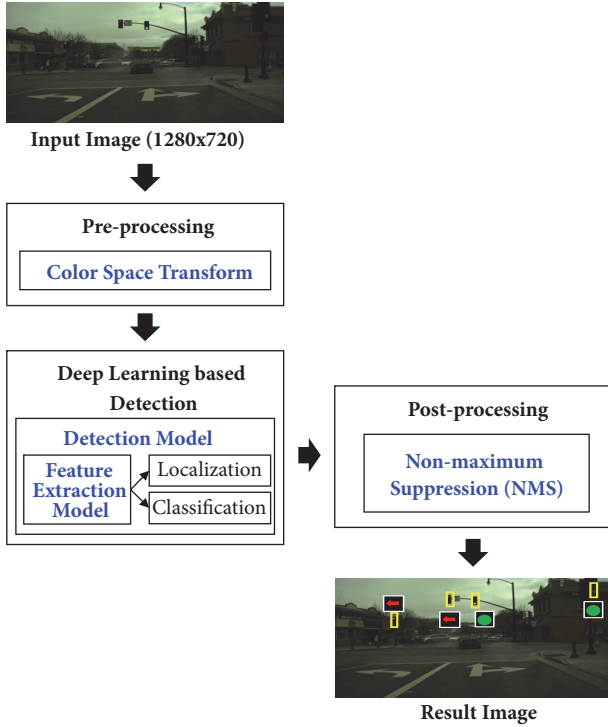


FIGURE 1: Method overview of deep-learning based traffic light detection.

transformed to other color space. Six color spaces are considered. The deep-learning based detection uses ensemble of feature extraction network model and detection one. Here, we consider three kinds of network models based on the Faster R-CNN and R-FCN which can perform localization and classification. In postprocessing, redundant detection is removed by using the nonmaximum suppression (NMS) technique [56, 57].

We focus on the combination of the color spaces and the ensemble networks which can achieve high performance of the traffic light detection. The color spaces and ensemble network models to be considered are described below.

3.1. Color Spaces. In the vision-based object detection and classification, it is necessary to determine the color space in which the characteristic of the object appears well. The RGB color space is defined by the three chromatics, red (R), green (G), and blue (B) [58]. For robustness under changes in the lightning condition, normalized RGB has often been used. The normalized RGB denoted as R_n , G_n , and B_n are obtained by R/S , G/S , and B/S , respectively, where $S = R + G + B$ [59]. At low illumination, it is difficult to distinguish between the normalized RGB colors [60]. To overcome this difficulty, Ruta et al. proposed the new red and blue color transform for traffic sign detection [60]. Since the traffic lights are red, green, and yellow, we modify Ruta's color representation for the same. Ruta's red, green, and yellow, denoted as f_R , f_y , and f_G are obtained as below.

$$f_R = \max(0, \min(R_n - G_n, R_n - B_n)) \quad (1)$$

$$f_Y = \max(0, \min(R_n - B_n, G_n - B_n)) \quad (2)$$

$$f_G = \max(0, \min(G_n - R_n, G_n - B_n)) \quad (3)$$

The YCbCr color space is obtained from the RGB [61]. Y component is luma signal, and Cb and Cr are chroma components. The color space can also be represented in cylindrical coordinates such as HSV color space [62]. The hue component, H , refers to the pure color it resembles. All tints, tones, and shades of red have the same hue. The saturation, S , describes how white the color is. The value component, V , also called lightness, describes how dark the color is. The CIE Lab color space consists of one component for luminance, L , and two color components, a and b [63]. It is known that the CIE Lab space is more suitable to many digital image manipulations than RGB color space.

In this paper, the six kinds of color spaces are considered in preprocessing of the traffic light detection system as shown in Figure 1. Each color representation is applied and its performance is compared.

3.2. Deep-Learning Based Ensemble Networks. It is known that the end-to-end trainable deep-learning models are more efficient than other models in general object detection [35, 36, 44–46], because it allows a sophisticated training by sharing the weights between feature extraction and detection. YOLO [35, 36], Faster R-CNN [44], SSD [45], and R-FCN [46] have been developed for the end-to-end model. In our traffic light detection system, we only consider the end-to-end deep-learning network models that can perform feature extraction and detection.

According to COCO [64], a dataset is divided into three groups depending on the size of the object to be detected; small ($area < 32^2$), medium ($32^2 \leq area \leq 96^2$), and large ($96^2 \leq area$), where $area$ denotes the number of pixels the object occupies. Therefore, the detection performance of a system can be different for different object sizes. Traffic lights are relatively smaller in size than other objects such as vehicle and pedestrian. For example, almost 90 % of traffic lights in our evaluation dataset belong to small-size group ($area < 32^2$) as shown in Table 2. Therefore, it is necessary to determine a deep-learning network model which is suitable for small-size object detection.

Huang et al. applied various network models to general object detection using COCO dataset and their performances are compared [65]. Fourteen kinds of meta-architectures with feature extractors and network models are analyzed. Five feature extractors such as VGGNet [66], MobileNet [67], Inception-v2 [68], Resnet-101 [47], and Inception-Resnet-v2 [69] are compared. Three kinds of network models based on the Faster-RCNN, R-FCN, and SSD are compared. They show that SSD (similar to YOLO) has higher performance for medium and large sized objects, but significantly lower performance than Faster R-CNN and R-FCN for small objects. They show that three ensemble networks such as Faster-RCNN with Inception-Resnet-v2, Faster R-CNN with Resnet-101, and R-FCN with Resnet-101 have higher performances than others for the small-size object detection. This

TABLE 2: The number (%) of small, medium, and large sizes traffic lights dataset.

Types	# of small (%)	# of medium (%)	# of large (%)	Total
green	7,192 (86.83)	1,091 (13.17)	0 (0.00)	8,283
red	4,694 (95.37)	226 (4.59)	2 (0.04)	4,922
yellow	652 (92.22)	55 (7.78)	0 (0.00)	707
red left	1,429 (82.17)	308 (17.71)	2 (0.12)	1,739
green left	225 (75.50)	62 (20.81)	11 (3.69)	298
off	1,031 (89.42)	122 (10.58)	0 (0.00)	1,153
Total	15,223 (89.01)	1,864 (10.90)	15 (0.09)	17,102

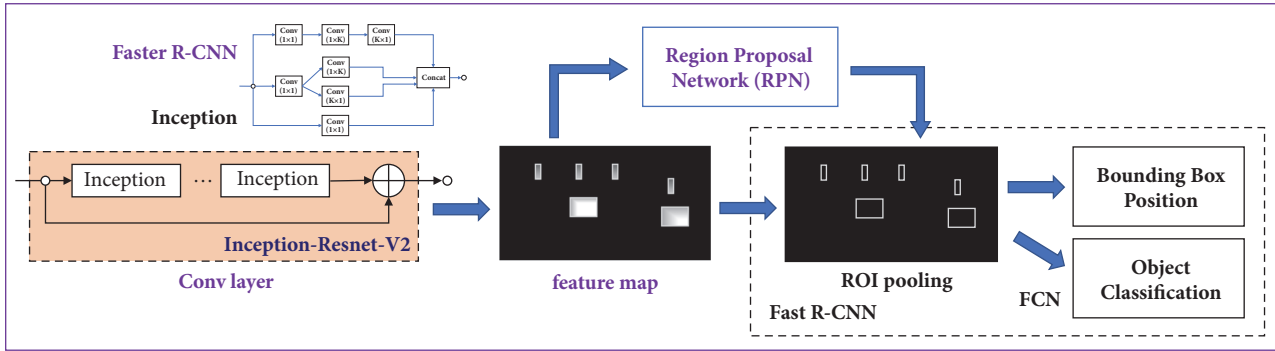


FIGURE 2: Block diagram of Faster R-CNN network model with Inception-Resnet-v2.

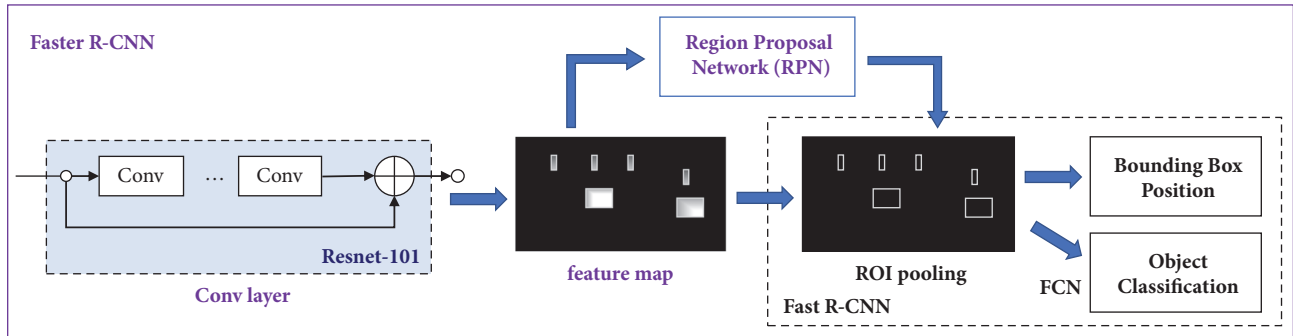


FIGURE 3: Block diagram of Faster R-CNN network model with Resnet-101.

is the reason why these three ensemble networks are applied in our traffic light detection method.

In Faster R-CNN [44], the selective search is replaced by very small convolutional network called RPN to generate regions of interest (RoI). To handle the variations in aspect ratio and scale of objects, Faster R-CNN introduces the idea of anchor boxes. At each location, three kinds of anchor boxes are used for scale 128×128 , 256×256 , and 512×512 . Similarly, three aspect ratios 1:1, 2:1, and 1:2 are used. RPN predicts the probability of being background or foreground for nine anchor boxes at each location. The remaining network is similar to the Fast-RCNN model. It is known that Faster-RCNN is 10 times faster than Fast-RCNN while maintaining a similar accuracy level [44].

R-FCN [46] is a region-based object detection framework leveraging deep fully convolutional networks. In contrast to other region-based detectors such as Fast R-CNN and Faster R-CNN that apply per-region subnetwork hundreds

of times, the region-based detector of R-FCN uses fully convolutional network that applies on the entire image. Instead of RoI pooling at the end layer of Faster R-CNN, R-FCN uses position-sensitive score maps and position-sensitive RoI pooling layer to address a dilemma between translation-invariance in image classification and translation-variance in object detection.

The fully convolutional image classifier backbones, such as Resnet-101 [47] and Inception-Resnet-v2 [69], can be used for object detection. Resnet [47] is a residual learning framework to make the training easy for deeper neural network. It is reported that the residual network with 101 layers (Resnet-101) has the best performance for object classification [47]. Inception-Resnet-v2 [69] is a hybrid inception version which combines residual network and inception network.

In this paper, three kinds of deep-learning based ensemble network models are considered for the traffic light detection (see Figures 2–4). The first network model, Faster-RCNN

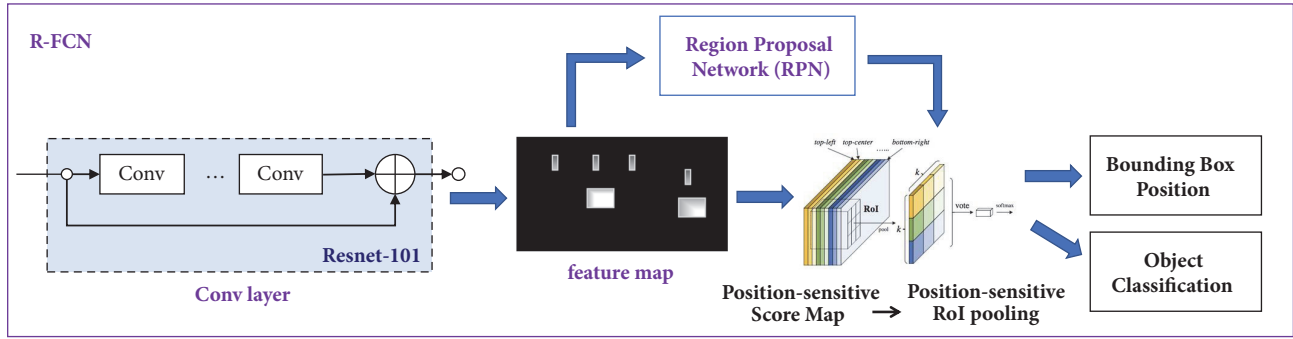


FIGURE 4: Block diagram of R-FCN network model with Resnet-101.

with Inception-Resnet-v2, consists of Inception-Resnetv2 for feature extraction, RPN for candidate extraction, and RoI pooling of Fast R-CNN for classification. The second one, Resnet-101 with Faster R-CNN, consists of Resnet-101 for feature extraction, RPN, and RoI pooling. R-FCN with Resnet-101 consists of Resnet-101, RPN, and position-sensitive score map and position-sensitive RoI pooling for classification. Each network model is applied and its performance is compared.

4. Configuration for Evaluation

In this section, we introduce the dataset and data augmentation method for traffic light detection, parameter tuning, and measurement metrics.

4.1. Dataset and Data Augmentation. For the simulations, we use Bosch Small Traffic Lights Dataset (BSTLD) offered by Behrendt et al. [54]. To use the same types of traffic lights both for training and test, we use only training data set of BSTLD which consists of 5,093 images. Among them, 2,042 images containing 4,306 annotated traffic lights are randomly selected and used as the test data set. The training data set consists of 6,102 images containing 12,796 annotated traffic lights. For testing set, 3,051 images are obtained from BSTLD training set and the others are generated using the following data augmentation techniques.

- (i) **Additional Noise and Blur.** Random addition of Gaussian, speckle, salt and pepper noise, and generation of an image with signal-dependent Poisson noise.
- (ii) **Brightness Changes in the Lab Space.** Addition of random values to luminance (lightness) component.
- (iii) **Saturation and Brightness Changes in the HSV Space.** Additive jitter which is generated at random by means of exponentiation, multiplication and addition of random values to the saturation and value channels.

Both training and testing data sets consist of $1,280 \times 720$ size images with annotations including bounding boxes of traffic lights as well as the current state of each traffic light. An active traffic light is annotated by one of six kinds of traffic

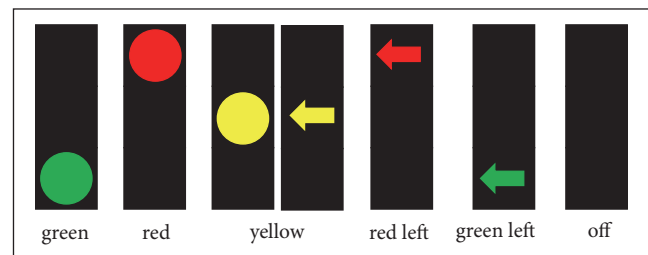


FIGURE 5: Types of traffic lights.

light states (green, red, yellow, red left, green left, and off) as shown in Figure 5. Detail descriptions of training and testing data sets are summarized in Table 3.

4.2. Parameter Tuning for Training. All three ensemble networks are trained until a maximum of 20,000 epochs using the pretrained weights are obtained from the COCO dataset [64]. The Faster R-CNN and R-FCN networks are trained by stochastic gradient descent (SGD) with momentum [70, 71], where the batch size is 1 and the momentum optimizer value is 0.9. We manually tune the learning rate schedules individually for each feature extractor. In our implementation, the tuning parameters of learning rate for SGD with momentum optimizer are set as follows:

- (i) Initial learning rate: 0.0003
- (ii) Learning rate of $0 \leq \text{Step} < 900,000$: 0.0003
- (iii) Learning rate of $900,000 \leq \text{Step} < 1,200,000$: 0.00003
- (iv) Learning rate of $1,200,000 \leq \text{Step}$: 0.000003

As suggested by Huang et al. [65], we limit the number of proposals to 50 in all three networks to attain similar speeds of traffic light detection.

4.3. Measurement Metrics. To evaluate the performances of traffic light detection, we use measurement metrics such as average precision (AP), mean average precision (mAP), overall AP, and overall mAP that have been widely used in VOC challenge [72, 73] and the COCO 2015 detection challenge [74].

TABLE 3: Descriptions of training and testing sets.

Dataset	# of images	# of annotated traffic lights	Ratio
Training set	6,102	12,796 (Total classes: 6 ea) (1) green (6,152) (2) red (3,730) (3) yellow (526) (4) red left (1,294) (5) green left (240) (6) off (854)	75 %
Testing set	2,042	4,306 (Total classes: 6 ea) (1) green (2,131) (2) red (1,192) (3) yellow (181) (4) red left (445) (5) green left (58) (6) off (299)	25 %

TABLE 4: Detection performances (overall mAP and overall AP) of combination methods on test set.

Combination Method	Color Space	Overall mAP (%)					Overall AP (%)				
		total	small	non small	green	red	yellow	red left	green left	off	
Faster R-CNN with Inception-Resnet-v2	RGB	<u>20.40</u>	<u>15.85</u>	36.15	<u>33.46</u>	<u>23.81</u>	4.75	34.69	17.59	<u>8.08</u>	
	Normalized RGB	<u>19.81</u>	<u>15.16</u>	<u>38.10</u>	<u>32.15</u>	<u>22.29</u>	<u>6.06</u>	<u>38.28</u>	11.43	<u>8.65</u>	
	Ruta's RYG	18.07	13.54	33.33	28.58	20.05	2.39	35.30	17.98	4.11	
	YCbCr	16.50	12.71	31.31	29.51	15.25	4.67	31.17	14.33	4.07	
	HSV	<u>19.70</u>	<u>15.41</u>	37.06	29.23	16.91	<u>6.74</u>	<u>36.00</u>	<u>23.54</u>	5.77	
	CIE Lab	17.64	13.31	34.30	26.62	18.27	5.41	34.63	15.82	5.09	
Faster R-CNN with Resnet-101	RGB	19.24	14.67	<u>37.91</u>	<u>31.21</u>	<u>20.73</u>	3.79	<u>36.92</u>	14.34	<u>8.44</u>	
	Normalized RGB	17.57	13.54	32.86	29.70	18.20	4.87	33.67	11.99	6.98	
	Ruta's RYG	14.72	11.21	28.42	26.55	16.62	4.71	26.27	10.14	4.05	
	YCbCr	12.36	9.49	25.02	24.03	10.02	2.83	26.36	8.84	2.05	
	HSV	15.76	11.11	32.24	25.07	14.77	<u>5.64</u>	23.06	<u>17.99</u>	8.01	
	CIE Lab	10.90	7.63	23.73	19.98	13.79	3.67	20.43	5.28	2.28	
R-FCN with Resnet-101	RGB	16.63	11.85	<u>37.27</u>	28.47	13.00	4.92	30.19	<u>18.32</u>	4.85	
	Normalized RGB	14.50	10.95	29.97	23.57	14.41	2.50	27.87	14.59	4.08	
	Ruta's RYG	14.21	10.33	26.66	20.89	9.08	3.01	32.75	13.77	5.72	
	YCbCr	13.06	9.44	25.05	21.43	10.01	2.50	24.49	14.63	5.28	
	HSV	14.66	10.59	29.52	25.40	9.99	3.17	28.39	15.23	5.78	
	CIE Lab	12.24	9.06	23.51	14.58	12.43	1.93	27.87	11.80	4.85	

AP is precision averaged across all values of recall between 0 and 1. Here, AP is calculated by averaging the interpolated precision over eleven equally spaced interval of recall value [0, 0.1, 0.2, . . . 0.9, 1.0] [75]. To evaluate the performance for two or more classes, the average of AP, mAP is calculated by averaging APs over every class. We also use overall AP and overall mAP that are obtained by averaging APs and mAPs, respectively, over the IoU=[0.5, 0.55, 0.60, . . . , 0.90, 0.95], where IoU stands for interval of intersection over union [73].

5. Simulation Results

In this section, we analyze the simulation results and detection examples. For the evaluation, we use measurement

metrics such as overall mAP, overall AP, mAP, and AP. For analysis of the detection examples, we apply NMS.

5.1. Simulation Results. Every eighteen methods combined with six different color spaces and three network models are implemented and compared. Tables 4 and 5 show the detection performances where every combination methods are listed in the left columns. In the tables, bold and underlined numbers indicate the top-ranked method, bold for the second ranked and underlined for the third ranked.

The first two network models, Faster R-CNN model with Inception-Resnet-v2 and Faster R-CNN model with Resnet-101, have roughly better performances than R-FCN model with Resnet-101 in terms of mAP. In all three networks,

TABLE 5: Detection performances (mAP@0.5 and AP@0.5) of combination methods on test set.

Combination Method		mAP@0.5 (%)					AP@0.5 (%)				
Ensemble Network Model	Color Space	total	small	non small	green	red	yellow	red left	green left	off	
Faster R-CNN with Inception-Resnet-v2	<u>RGB</u>	38.48	31.27	57.79	70.56	52.12	8.49	59.11	27.13	13.44	
	Normalized RGB	38.24	31.42	<u>59.87</u>	70.43	52.09	10.98	63.94	17.39	14.60	
	Ruta's RYG	35.94	29.16	52.99	65.02	<u>49.77</u>	06.03	57.87	28.76	8.16	
	YCbCr	35.55	29.32	51.83	<u>68.68</u>	41.30	9.53	58.91	26.07	8.83	
	HSV	35.13	28.82	56.76	58.55	38.50	12.94	57.89	32.88	10.04	
	CIE Lab	32.19	25.45	53.05	54.26	41.84	8.47	55.71	24.00	8.84	
Faster R-CNN with Resnet-101	<u>RGB</u>	<u>37.24</u>	<u>30.25</u>	61.45	65.23	47.68	6.82	63.11	24.37	16.23	
	Normalized RGB	34.24	28.32	51.82	64.11	43.46	8.20	57.30	19.63	12.72	
	Ruta's RYG	31.96	26.14	50.63	61.55	41.21	13.01	50.04	18.11	7.85	
	YCbCr	26.17	21.44	42.64	56.82	27.16	5.52	47.45	15.57	4.48	
	HSV	30.30	22.69	54.00	52.50	34.45	<u>11.02</u>	41.49	27.88	<u>14.44</u>	
	CIE Lab	24.71	18.86	41.38	46.99	33.59	6.56	46.18	9.48	5.48	
R-FCN with Resnet-101	RGB	34.88	27.33	62.19	64.76	36.48	10.07	55.44	30.93	11.57	
	Normalized RGB	32.16	26.18	52.80	58.86	38.17	5.99	54.03	26.46	9.43	
	Ruta's RYG	31.21	24.78	47.20	55.03	30.14	7.13	<u>60.38</u>	23.28	11.29	
	YCbCr	30.42	23.18	50.18	57.18	29.10	5.45	49.49	<u>30.42</u>	10.87	
	HSV	30.05	23.25	51.61	56.33	28.48	7.58	50.58	26.10	11.25	
	CIE Lab	27.33	21.63	44.38	46.86	32.74	4.41	48.95	21.54	9.50	

RGB and normalized RGB have high performance than other colors. There is no method having good performance over every type of traffic light.

In Table 4, from the view point of color space, RGB, normalized RGB, and HSV spaces have higher mAP in Faster-RCNN with Inception-Resnet-v2. RGB and normalized RGB have good performance in Faster R-CNN with Resnet-101. In the case of yellow traffic light, normalized RGB and HSV in Faster R-CNN with Inception-Resnet-v2 and HSV in Faster R-CNN model with Resnet-101 have higher performance than other methods, but most methods have limited overall mAPs depending on sizes of traffic light, small and nonsmall set, because our dataset has very limited number of large size traffic light data. The top-ranked three methods such as RGB based Faster R-CNN with Inception-Resnetv2, normalized RGB based Faster R-CNN with Inception-Resnet-v2, and HSV based Faster R-CNN with Inception-Resnet-v2 retain their good performances in the small-size object.

Table 5 shows the detection performances in terms of AP and mAP when IoU is fixed to 0.5. The top-ranked two methods such as RGB based Faster R-CNN with Inception-Resnet-v2 and normalized RGB based Faster R-CNN with Inception-Resnet-v2 have also better performance than others, even though the ranking order is slightly changed depending on the object size. Ruta's RYG and HSV in Faster-RCNN model with Resnet-101 and HSV in Faster R-CNN with Inception-Resnet-v2 have significantly high performance for yellow traffic light. Similar to Table 4, CIE Lab color space has relatively poor performance regardless of the network models. As shown in Table 5, the performances of mAP depending on the size are similar to Table 4.

5.2. Detection Examples. After the traffic light detection procedure, we use NMS to remove the redundant detections. At final test process, IoU threshold of NMS is fixed to 0.5. The traffic light detection examples of the top-ranked two methods are shown in Figures 6 and 7. Six example images are selected to show detection results for six types of traffic lights. The traffic lights with object score being greater than 0.5 are detected and classified. True positives are indicated by the corresponding traffic light symbol. False positives and false negatives are noted by FP and FN, respectively. As shown in Figure 6, the top-ranked method, RGB color-based Faster R-CNN with Inception-Resnet-v2, has twenty-six true positives, three false positives, and four false negatives in six images. Figure 7 shows that normalized RGB color-based Faster R-CNN with Inception-Resnet-v2 has twenty-four true positives, two false positives, and seven false negatives. Both methods cannot detect the yellow traffic lights well.

5.3. Summary. Based on the performance analysis, the Faster R-CNN model is more suitable to traffic light detection than R-FCN. Inception-Resnet-v2 shows better performance for feature extraction than Resnet-101 in Faster R-FCN framework. From view point of color space, the use of RGB has highest performance in all ensemble networks. The normalized RGB is also a good color space for Inception-Resnet-v2 model.

6. Conclusions

In this paper, we present a deep-learning based traffic light detection system that consists mainly of color space transform and ensemble network model. Through the simulations,

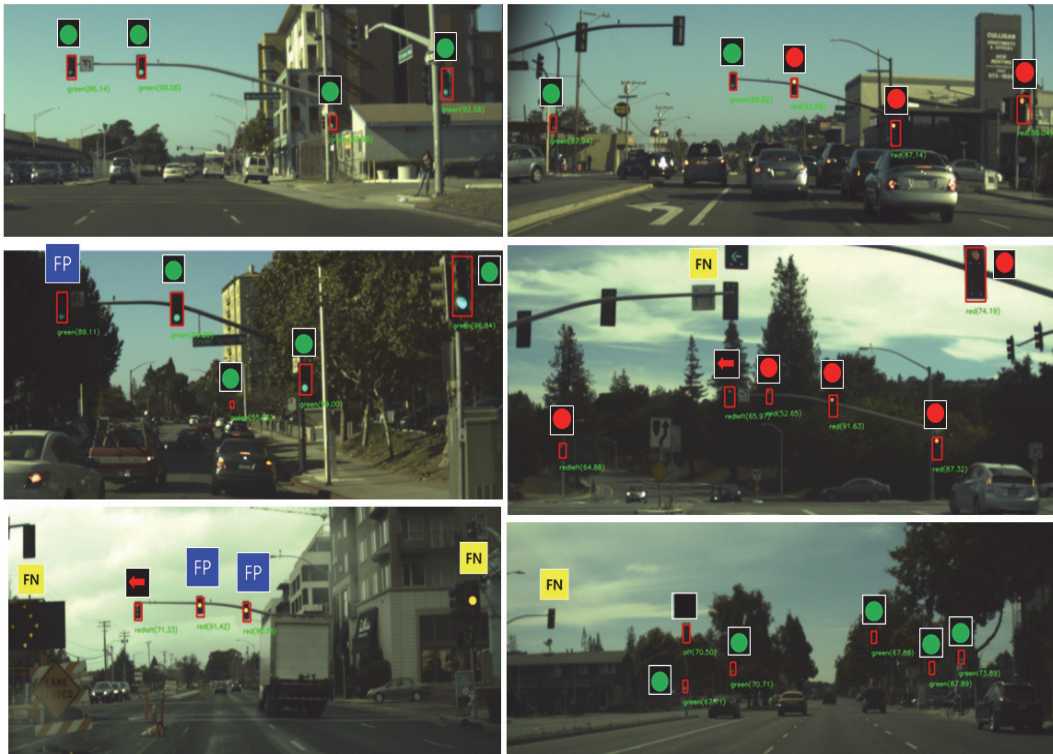


FIGURE 6: Traffic light detection examples of top-ranked RGB based Faster R-CNN model with Inception-Resnet-v2.

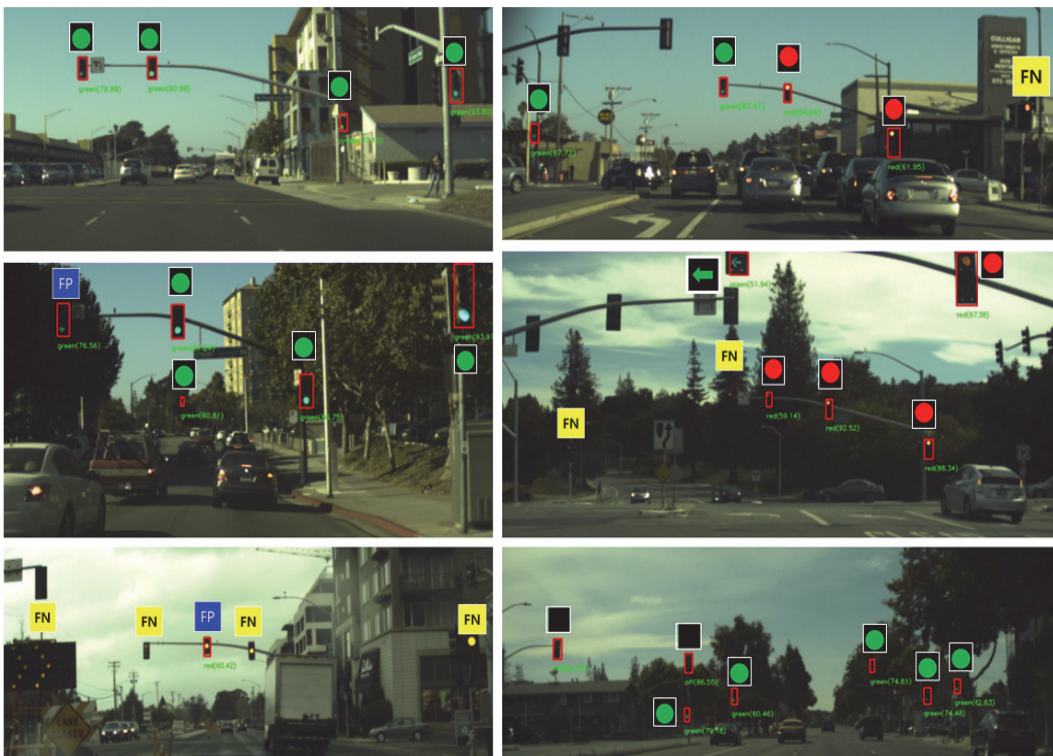


FIGURE 7: Traffic light detection examples of the second-ranked normalized RGB based Faster R-CNN model with Inception-Resnet-v2.

It is shown that Faster R-CNN with Inception-Resnet-v2 model is more suitable to traffic light detection than others. Regardless of the network models, RGB and normalized RGB color spaces have high performance. However, most methods have limited performance to detect yellow traffic lights. It is observed that yellow lights are often misclassified into red lights because the amount of yellow lights is relatively much smaller in training dataset. The performance can be improved, if yellow light training data is large enough as other colors. The results can help developers to choose appropriate color space and network model when deploying deep-learning based traffic light detection.

Data Availability

For the simulations, Bosch Small Traffic Lights Dataset offered by Behrendt et al. is used: <https://hci.iwr.uni-heidelberg.de/node/6132>.

Conflicts of Interest

The authors declare that there are no conflicts of interest regarding the publication of this paper.

Acknowledgments

This work was supported in part by Basic Science Research Programs through the National Research Foundation of Korea (NRF) funded by the Ministry of Education (Grant no. NRF-2018RIA2B6005105), in part by the Brain Korea 21 Plus Program (no. 22A20130012814) funded by National Research Foundation of Korea (NRF), and in part by MSIT (Ministry of Science, ICT), Korea, under the ITRC (Information Technology Research Center) support program (IITP-2018-2016-0-00313) supervised by the IITP (Institute for Information & Communications Technology Promotion).

References

- [1] S. O.-R. A. V. S. Committee et al., "Taxonomy and definitions for terms related to on-road motor vehicle automated driving systems" (Arabic), SAE International, 2014.
- [2] R. De Charette and F. Nashashibi, "Traffic light recognition using image processing compared to learning processes," in *Proceedings of the 2009 IEEE/RSJ International Conference on Intelligent Robots and Systems, IROS 2009*, pp. 333–338, USA, October 2009.
- [3] R. De Charette and F. Nashashibi, "Real time visual traffic lights recognition based on spot light detection and adaptive traffic lights templates," in *Proceedings of the 2009 IEEE Intelligent Vehicles Symposium*, pp. 358–363, China, June 2009.
- [4] J. Park and C. Jeong, "Real-time signal light detection," in *Proceedings of the 2008 Second International Conference on Future Generation Communication and Networking Symposia (FGCNS)*, pp. 139–142, Hainan, China, December 2008.
- [5] C. Yu, C. Huang, and Y. Lang, "Traffic light detection during day and night conditions by a camera," in *Proceedings of the 2010 IEEE 10th International Conference on Signal Processing, ICSP2010*, pp. 821–824, China, October 2010.
- [6] M. Omachi and S. Omachi, "Traffic light detection with color and edge information," in *Proceedings of the 2009 2nd IEEE International Conference on Computer Science and Information Technology, ICCSIT 2009*, pp. 284–287, China, August 2009.
- [7] H.-K. Kim, Y.-N. Shin, S.-g. Kuk, J. H. Park, and H.-Y. Jung, "Night-time traffic light detection based on svm with geometric moment features," *World Academy of Science, Engineering and Technology, International Journal of Computer, Electrical, Automation, Control and Information Engineering*, vol. 7, no. 4, pp. 472–475, 2013.
- [8] H.-K. Kim, K. H. Park, and H.-Y. Jung, "Effective traffic lights recognition method for real time driving assistance system in the daytime, World Academy of Science," *Journal of Engineering and Technology*, vol. 59th, 2011.
- [9] H.-K. Kim, K. H. Park, and H.-Y. Jung, "Vision based Traffic Light Detection and Recognition Methods for Daytime LED Traffic Light," *Journal of IEMEK*, vol. 9, no. 3, pp. 145–150, 2014.
- [10] H. Tae-Hyun, J. In-Hak, and C. Seong-Ik, "Detection of traffic lights for vision-based car navigation system," in *Advances in Image and Video Technology*, vol. 4319 of *Lecture Notes in Computer Science*, pp. 682–691, Springer, Berlin, Germany, 2006.
- [11] J. Levinson, J. Askeland, J. Dolson, and S. Thrun, "Traffic light mapping, localization, and state detection for autonomous vehicles," in *Proceedings of the 2011 IEEE International Conference on Robotics and Automation, ICRA 2011*, pp. 5784–5791, China, May 2011.
- [12] C. Jang, S. Cho, S. Jeong, J. K. Suhr, H. G. Jung, and M. Sunwoo, "Traffic light recognition exploiting map and localization at every stage," *Expert Systems with Applications*, vol. 88, pp. 290–304, 2017.
- [13] D. Barnes, W. Maddern, and I. Posner, "Exploiting 3D semantic scene priors for online traffic light interpretation," in *Proceedings of the IEEE Intelligent Vehicles Symposium, IV 2015*, pp. 573–578, Republic of Korea, July 2015.
- [14] G. Siogkas, E. Skodras, and E. Dermatas, "Traffic lights detection in adverse conditions using color, symmetry and spatiotemporal information," in *Proceedings of the International Conference on Computer Vision Theory and Applications, VIS-APP 2012*, pp. 620–627, Italy, February 2012.
- [15] M. Omachi and S. Omachi, "Detection of traffic light using structural information," in *Proceedings of the 2010 IEEE 10th International Conference on Signal Processing, ICSP2010*, pp. 809–812, China, October 2010.
- [16] M. Diaz-Cabrera, P. Cerri, and P. Medici, "Robust real-time traffic light detection and distance estimation using a single camera," *Expert Systems with Applications*, vol. 42, no. 8, pp. 3911–3923, 2015.
- [17] Z. Cai, M. Gu, and Y. Li, "Real-time arrow traffic light recognition system for intelligent vehicle," in *Proceedings of the International Conference on Image Processing, Computer Vision, and Pattern Recognition (ICCV)*. The Steering Committee of The World Congress in Computer Science, Computer Engineering and Applied Computing (WorldComp), p. 1, 2012.
- [18] M. Michael and M. Schlipfing, "Extending traffic light recognition: Efficient classification of phase and pictogram," in *Proceedings of the 2015 International Joint Conference on Neural Networks (IJCNN)*, pp. 1–8, Killarney, Ireland, July 2015.
- [19] R. M. Haralick, "A measure for circularity of digital figures," *IEEE Transactions on Systems, Man, and Cybernetics*, vol. 4, no. 4, pp. 394–396, 1974.

- [20] N. Kanopoulos, N. Vasanthavada, and R. L. Baker, "Design of an image edge detection filter using the sobel operator," *IEEE Journal of Solid-State Circuits*, vol. 23, no. 2, pp. 358–367, 1988.
- [21] J. Illingworth and J. Kittler, "The adaptive hough transform," *IEEE Transactions on Pattern Analysis and Machine Intelligence*, vol. 9, no. 5, pp. 690–698, 1987.
- [22] T. S. Lee, "Image representation using 2D Gabor wavelets," *IEEE Transactions on Pattern Analysis and Machine Intelligence*, vol. 18, no. 10, pp. 959–971, 1996.
- [23] J. Nishimura and T. Kuroda, "Low cost speech detection using Haar-like filtering for sensor-net," in *Proceedings of the 2008 9th International Conference on Signal Processing, ICSP 2008*, pp. 2608–2611, China, October 2008.
- [24] N. Dalal and B. Triggs, "Histograms of oriented gradients for human detection," in *Proceedings of the IEEE Computer Society Conference on Computer Vision and Pattern Recognition (CVPR '05)*, vol. 1, pp. 886–893, June 2005.
- [25] M. K. Hu, "Visual pattern recognition by moment invariant," *IRE Transactions on Information Theory*, vol. 8, no. 2, pp. 179–187, 1962.
- [26] J. A. Hartigan and M. A. Wong, "Algorithm as 136: A k-means clustering algorithm," *Journal of the Royal Statistical Society. Series C (Applied Statistics)*, vol. 28, no. 1, pp. 100–108, 1979.
- [27] J. Lewis, "Fast template matching," *Vision Interface*, vol. 95, pp. 120–123, 1995.
- [28] C. Liu and H. Wechsler, "Independent component analysis of Gabor features for face recognition," *IEEE Transactions on Neural Networks and Learning Systems*, vol. 14, no. 4, pp. 919–928, 2003.
- [29] T. Li, S. Zhu, and M. Ogihara, "Using discriminant analysis for multi-class classification: An experimental investigation," *Knowledge and Information Systems*, vol. 10, no. 4, pp. 453–472, 2006.
- [30] P. Cunningham and S. J. Delany, "k-nearest neighbour classifiers," *Multiple Classifier Systems*, vol. 34, pp. 1–17, 2007.
- [31] P. Viola and M. J. Jones, "Robust real-time face detection," *International Journal of Computer Vision*, vol. 57, no. 2, pp. 137–154, 2004.
- [32] K.-B. Duan and S. S. Keerthi, "Which is the best multiclass SVM method? An empirical study," in *Multiple Classifier Systems*, vol. 3541 of *Lecture Notes in Computer Science*, pp. 278–285, Springer, Berlin, Germany, 2005.
- [33] Y. LeCun, L. Bottou, Y. Bengio, and P. Haffner, "Gradient-based learning applied to document recognition," *Proceedings of the IEEE*, vol. 86, no. 11, pp. 2278–2323, 1998.
- [34] A. Krizhevsky, I. Sutskever, and G. E. Hinton, "Imagenet classification with deep convolutional neural networks," in *Proceedings of the 26th Annual Conference on Neural Information Processing Systems (NIPS '12)*, pp. 1097–1105, Lake Tahoe, Nev, USA, December 2012.
- [35] J. Redmon, S. Divvala, R. Girshick, and A. Farhadi, "You only look once: Unified, real-time object detection," in *Proceedings of the 2016 IEEE Conference on Computer Vision and Pattern Recognition, CVPR 2016*, pp. 779–788, July 2016.
- [36] J. Redmon and A. Farhadi, "YOLO9000: Better, Faster, Stronger," in *Proceedings of the 2017 IEEE Conference on Computer Vision and Pattern Recognition (CVPR)*, pp. 6517–6525, Honolulu, HI, July 2017.
- [37] A. M. Cailleau, B. Cagneau, L. Chassagne, M. Dimian, and V. Popa, "Novel receiver sensor for visible light communications in automotive applications," *IEEE Sensors Journal*, vol. 15, no. 8, pp. 4632–4639, 2015.
- [38] N. Kumar, N. Lourenço, D. Terra, L. N. Alves, and R. L. Aguiar, "Visible light communications in intelligent transportation systems," in *Proceedings of the 2012 IEEE Intelligent Vehicles Symposium, IV 2012*, pp. 748–753, Spain, June 2012.
- [39] T. Saito, S. Haruyama, and M. Nakagawa, "A new tracking method using image sensor and photo diode for visible light road-to-vehicle communication," in *Proceedings of the 2008 10th International Conference on Advanced Communication Technology*, pp. 673–678, Republic of Korea, February 2008.
- [40] T. Yamazato, I. Takai, H. Okada et al., "Image-sensor-based visible light communication for automotive applications," *IEEE Communications Magazine*, vol. 52, no. 7, pp. 88–97, 2014.
- [41] P. Sermanet, D. Eigen, X. Zhang, M. Mathieu, R. Fergus, and Y. LeCun, "Overfeat: Integrated recognition, localization and detection using convolutional networks," 2013, <https://arxiv.org/abs/1312.6229>.
- [42] R. Girshick, J. Donahue, T. Darrell, and J. Malik, "Rich feature hierarchies for accurate object detection and semantic segmentation," in *Proceedings of the 27th IEEE Conference on Computer Vision and Pattern Recognition (CVPR '14)*, pp. 580–587, Columbus, Ohio, USA, June 2014.
- [43] R. Girshick, "Fast r-cnn," arXiv:1504.080832015.
- [44] S. Ren, K. He, R. Girshick, and J. Sun, "Faster R-CNN: towards real-time object detection with region proposal networks," in *Advances in Neural Information Processing Systems*, pp. 91–99, 2015.
- [45] W. Liu, D. Anguelov, D. Erhan et al., "SSD: single shot multibox detector," *Lecture Notes in Computer Science (including subseries Lecture Notes in Artificial Intelligence and Lecture Notes in Bioinformatics): Preface*, vol. 9905, pp. 21–37, 2016.
- [46] J. Dai, Y. Li, K. He, and J. Sun, "R-FCN: Object detection via region-based fully convolutional networks," in *Proceedings of the 30th Annual Conference on Neural Information Processing Systems, NIPS 2016*, pp. 379–387, Spain, December 2016.
- [47] K. He, X. Zhang, S. Ren, and J. Sun, "Deep residual learning for image recognition," in *Proceedings of the 2016 IEEE Conference on Computer Vision and Pattern Recognition, CVPR 2016*, pp. 770–778, July 2016.
- [48] F. Yang, W. Choi, and Y. Lin, "Exploit all the layers: fast and accurate CNN object detector with scale dependent pooling and cascaded rejection classifiers," in *Proceedings of the 2016 IEEE Conference on Computer Vision and Pattern Recognition, CVPR 2016*, pp. 2129–2137, Las Vegas, Nev, USA, July 2016.
- [49] J. Ren, X. Chen, J. Liu et al., "Accurate single stage detector using recurrent rolling convolution," in *Proceedings of the 30th IEEE Conference on Computer Vision and Pattern Recognition, CVPR 2017*, pp. 752–760, USA, July 2017.
- [50] F. Chabot, M. Chaouch, J. Rabarisoa, C. Teulière, and T. Chateau, "Deep MANTA: A coarse-to-fine many-task network for joint 2D and 3D vehicle analysis from monocular image," in *Proceedings of the 30th IEEE Conference on Computer Vision and Pattern Recognition, CVPR 2017*, pp. 1827–1836, USA, July 2017.
- [51] X. Chen, H. Ma, J. Wan, B. Li, and T. Xia, "Multi-view 3D object detection network for autonomous driving," in *Proceedings of the 2017 IEEE Conference on Computer Vision and Pattern Recognition (CVPR)*, pp. 6526–6534, Honolulu, HI, July 2017.
- [52] S. Saini, S. Nikhil, K. R. Konda, H. S. Bharadwaj, and N. Ganeshan, "An efficient vision-based traffic light detection and state recognition for autonomous vehicles," in *Proceedings of the 28th IEEE Intelligent Vehicles Symposium, IV 2017*, pp. 606–611, USA, June 2017.

- [53] G.-G. Lee and B. K. Park, "Traffic light recognition using deep neural networks," in *Proceedings of the 2017 IEEE International Conference on Consumer Electronics, ICCE 2017*, pp. 277-278, USA, January 2017.
- [54] K. Behrendt, L. Novak, and R. Botros, "A deep learning approach to traffic lights: Detection, tracking, and classification," in *Proceedings of the 2017 IEEE International Conference on Robotics and Automation, ICRA 2017*, pp. 1370-1377, Singapore, June 2017.
- [55] M. B. Jensen, K. Nasrollahi, and T. B. Moeslund, "Evaluating state-of-the-art object detector on challenging traffic light data," in *Proceedings of the 30th IEEE Conference on Computer Vision and Pattern Recognition Workshops, CVPRW 2017*, pp. 882-888, USA, July 2017.
- [56] P. F. Felzenszwalb, R. B. Girshick, D. McAllester, and D. Ramanan, "Object detection with discriminatively trained part-based models," *IEEE Transactions on Pattern Analysis and Machine Intelligence*, vol. 32, no. 9, pp. 1627-1645, 2010.
- [57] R. Rothe, M. Guillaumin, and L. Van Gool, "Non-maximum suppression for object detection by passing messages between windows," in *Computer Vision - ACCV 2014*, vol. 9003 of *Lecture Notes in Computer Science*, pp. 290-306, Springer International Publishing, Cham, 2015.
- [58] S. Süsstrunk, R. Buckley, and S. Swen, "Standard RGB color spaces," in *Proceedings of the Final Program and Proceedings of the 7th IS and T/SID Color Imaging Conference: Color Science, Systems and Applications*, pp. 127-134, USA, November 1999.
- [59] W. Wintringham, "Color television and colorimetry," *Proceedings of the IRE*, vol. 39, no. 10, pp. 1135-1172, 1951.
- [60] A. Ruta, F. Porikli, S. Watanabe, and Y. Li, "In-vehicle camera traffic sign detection and recognition," *Machine Vision and Applications*, vol. 22, no. 2, pp. 359-375, 2011.
- [61] T. Acharya, "Median computation-based integrated color interpolation and color space conversion methodology from 8-bit bayer pattern rgb color space to 12-bit ycrb color space," US Patent 6,356,276, 2002.
- [62] R. G. Kuehni, *Color Space and Its Divisions: Color Order from Antiquity to the Present*, John Wiley Sons, 2003.
- [63] C. Connolly and T. Fleiss, "A study of efficiency and accuracy in the transformation from RGB to CIE Lab color space," *IEEE Transactions on Image Processing*, vol. 6, no. 7, pp. 1046-1048, 1997.
- [64] T.-Y. Lin, M. Maire, S. Belongie et al., "Microsoft COCO: Common objects in context," *Lecture Notes in Computer Science (including subseries Lecture Notes in Artificial Intelligence and Lecture Notes in Bioinformatics): Preface*, vol. 8693, no. 5, pp. 740-755, 2014.
- [65] J. Huang, V. Rathod, C. Sun et al., "Speed/accuracy trade-offs for modern convolutional object detectors," in *Proceedings of the 30th IEEE Conference on Computer Vision and Pattern Recognition, CVPR 2017*, pp. 3296-3305, USA, July 2017.
- [66] T. Sercu, C. Puhersch, B. Kingsbury, and Y. Lecun, "Very deep multilingual convolutional neural networks for LVCSR," in *Proceedings of the 41st IEEE International Conference on Acoustics, Speech and Signal Processing, ICASSP 2016*, pp. 4955-4959, China, March 2016.
- [67] A. G. Howard, M. Zhu, B. Chen et al., "Mobilenets: Efficient convolutional neural networks for mobile vision applications," arXiv:1704.04861, 2017.
- [68] C. Szegedy, V. Vanhoucke, S. Ioffe, J. Shlens, and Z. Wojna, "Rethinking the inception architecture for computer vision," in *Proceedings of the 2016 IEEE Conference on Computer Vision and Pattern Recognition, CVPR 2016*, pp. 2818-2826, July 2016.
- [69] C. Szegedy, S. Ioffe, V. Vanhoucke, and A. A. Alemi, "Inception-v4, inception-ResNet and the impact of residual connections on learning," in *Proceedings of the 31st AAAI Conference on Artificial Intelligence (AAAI '17)*, pp. 4278-4284, February 2017.
- [70] D. E. Rumelhart, G. E. Hinton, and R. J. Williams, "Learning representations by back-propagating errors," *Nature*, vol. 323, no. 6088, pp. 533-536, 1986.
- [71] I. Sutskever, J. Martens, G. Dahl, and G. Hinton, "On the importance of initialization and momentum in deep learning," in *Proceedings of the 30th International Conference on Machine Learning, ICML 2013*, pp. 2176-2184, USA, June 2013.
- [72] M. Everingham, L. van Gool, C. K. I. Williams, J. Winn, and A. Zisserman, "The pascal visual object classes (VOC) challenge," *International Journal of Computer Vision*, vol. 88, no. 2, pp. 303-338, 2010.
- [73] M. Everingham, S. M. A. Eslami, L. Van Gool, C. K. I. Williams, J. Winn, and A. Zisserman, "The pascal visual object classes challenge: a retrospective," *International Journal of Computer Vision*, vol. 111, no. 1, pp. 98-136, 2015.
- [74] O. Russakovsky, J. Deng, H. Su et al., "Imagenet large scale visual recognition challenge," *International Journal of Computer Vision*, vol. 115, no. 3, pp. 211-252, 2015.
- [75] G. G. Chowdhury, *Introduction to Modern Information Retrieval*, Facet publishing, 2010.

Research Article

Video Analytic Based Health Monitoring for Driver in Moving Vehicle by Extracting Effective Heart Rate Inducing Features

Kanghyu Lee,¹ David K. Han,² and Hanseok Ko ^{1,3}

¹Department of Video Information Processing, Korea University, Anam-dong, Sungbuk-gu, 136713 Seoul, Republic of Korea

²Information Science Division, ARL, Adelphi, MD 20783, USA

³School of Electrical Engineering, Korea University, Anam-dong, Sungbuk-gu, 136713 Seoul, Republic of Korea

Correspondence should be addressed to Hanseok Ko; hsko@korea.ac.kr

Received 3 August 2018; Revised 18 October 2018; Accepted 14 November 2018; Published 2 December 2018

Guest Editor: Petru Andrei

Copyright © 2018 Kanghyu Lee et al. This is an open access article distributed under the Creative Commons Attribution License, which permits unrestricted use, distribution, and reproduction in any medium, provided the original work is properly cited.

We propose a novel remote heart rate (HR) estimation method using facial images based on video analytics. Most of previous methods have been demonstrated in well-controlled indoor environments. In contrast, this paper proposes a practical video analytic framework under actual driving conditions by extracting key HR inducing features. In particular, when cars are driven, effective and stable HR estimation becomes challenging as there are many dynamic elements, such as rapid illumination changes, vibrations, and ambient lighting that can exist in the vehicle interior. To overcome those disturbances of HR estimation, the driver face region is first detected and cropped to the region of interest (RoI). Second, the components related to HR are extracted from mixed noisy components using ensemble empirical mode decomposition (EEMD). Finally, the extracted signal is analyzed in frequency domain and smoothed with temporal filtering. To verify our approach, the proposed method is compared with recent prominent methods employing a public HCI dataset. It has been demonstrated that the proposed approach delivers superior performance under driving conditions using Bland-Altman plots.

1. Introduction

Traffic accidents occur due to acute driver heart rate (HR) disease. These accidents can develop into dangerous situations that threaten not only the driver but also the lives of others. If the driver's HR is known in advance, it is possible to prevent the accident by judiciously controlling the vehicle. Methods, such as wired contact sensors, have been proposed to measure the driver's HR. However, due to the invasive nature of the in situ sensors, such methods have not gained much interest. For less intrusive and accurate measurements of driver HR, this research proposes a remote estimation method based on a video analytic framework focused on capturing key HR inducing features.

Nowadays, some systems monitor a driver's condition by placing a camera on the vehicle frame or the windshield of the vehicle. Furthermore, since image based remote HR estimation has been shown possible [1], a series of related studies have been subsequently proposed.

Poh et al. demonstrated the HR estimation technique by separating the observed signal into independent source signals [2, 3]. A bandpass filter is applied to each of the signal and the result was analyzed in frequency domain. Zhao et al. proposed an estimation technique for respiration as well as HR using a delay matrix [4]. Another study estimated the pulse rate by amplifying the frequency of the signal using minute movements of the face associated with vibration associated with human pulses [5]. However, these methods can be successful only if the subject is in a static state and any changes in the environment are limited.

In [6], Li et al. proposed a new approach which made slightly different assumptions compared to the previous studies. By assuming that light change to the face is the same as the light change to the background area, HR can be estimated through the difference between these two areas. Wang et al. demonstrated a pruning architecture using CHROM that removes pixels with values that do not correspond to skin tones and pixels distorted by motion [7, 8]. Also based on

CHROM, Tulyakov et al. improved on previous methods by cropping and warping certain facial regions using a self-adaptive matrix [9]. Similar to the assumption of [6], Xu et al. analyzed the background region as the noise reference to the facial region and then applied blind source separation approach. Even though the result was shown quite impressive, the variation of the result was large, making stable detection difficult in a dynamic environment [10]. Cheng et al. also applied an approach to Poh et al. by extracting unique pulse signals through ensemble empirical mode decomposition (EEMD) for the input signal analyzed by joint blind source separation (JBSS) based on the same assumptions [11, 12]. On the other hand, Huan et al. analyzed the input signal using JBSS in a similar way but exploited correlations between them by dividing the face region into several subregions and applied it to a learning based method [13]. However, in the test data, obstruction caused by wires and tapes in skin region was suggested as a challenging point and there was no significant innovation since the authors did not consider rapidly changing environment. In [14], a deep learning based remote photoplethysmography (rPPG) approach that detects skin regions using convolutional neural network (CNN) was proposed. Although it was a unique method of applying deep learning, there is a disadvantage that data must be learned in a new environment every time in terms of machine learning.

These previous studies have steadily improved the technology, but most estimate pulses from a distance in an indoor environment. In each of these papers, experiments have used well-controlled data and been conducted in controlled environments. Only few studies have addressed extreme illumination changes and vibrations associated with automotive environments. Although, Kuo et al. proposed an HR estimation framework under driving conditions, the approach was conventional and suffered very poor performance [15]. In this paper, the proposed method shows stable HR estimation results in indoors as well as in a wide range of outdoor moving environments.

The structure of this paper is as follows. The framework of the proposed method is shown in detail in Section 2. In Section 3, our proposed algorithm is applied to a public human-computer-interface (HCI) dataset to verify its validity and the results compared with those of previous studies. The experimental results of our driving dataset are presented by a Bland-Altman plot. Finally, the conclusions are discussed in Section 3.

2. Proposed Method

In this section, the proposed method can be divided into three stages: (1) region of interest (RoI) selection, (2) pulse signal extraction, and (3) power spectral density (PSD) analysis and temporal filtering. The overall flow is illustrated in Figure 1.

2.1. Region of Interest Selection. Kumar et al. demonstrated that the color changes due to pulsation are different for each region of the face, and as a result, the forehead and cheek region represent the strongest PPG signal [16]. Based on

this result, the cheek region is selected as the RoI. While the forehead region depends on hair style, the cheek region provides robust features insensitive to facial expressions. In order to extract the RoI, unnecessary background regions are excluded based on the assumption that the driver's facial position is somewhat fixed. A total of 66 facial landmark points are extracted for the remaining facial regions by using discriminative response map fitting (DRMF) to extract both cheek regions as illustrated in Figure 2 [17].

However, in the case of varying driving situations, not only the rotation and movement of the face but also face detection per video frame slows the processing speed, making the camera-based method ineffective for real-time HR estimation. To mitigate such problems, face tracking is applied using a kernelized correlated filter (KCF) [18]. Therefore, facial landmark point extraction is performed only at the first frame, after which the detected cheek region is tracked.

Nevertheless, the tracked RoI may still be incomplete. If the face is rotated or shaken, a background region may be included within the tracked RoI. Furthermore, as the vehicle runs, numerous illumination changes can cause skin region pixel values saturated such that the HR signal disappears. To prevent this, a skin detection scheme is employed using the hue channel in the HSV color model as in

$$p_{ij} = \begin{cases} \text{skin}, & h < \tau \\ \text{non-skin}, & h \geq \tau, \end{cases} \quad (1)$$

where p_{ij} denotes the pixel value in i th row and j th column and h denotes the hue channel value. In our method, we set the threshold of 90 for the hue channel as τ and selected pixels less than 90 as skin regions. The value was determined to be the best choice for the set of facial image data collected and used in this study. According to the work by [19], a value of threshold was used for the similar purpose.

2.2. Feature Extraction and Source Separation. Assuming that the ambient light signal has properties such as white noise of uniform magnitude in all frequency bands, the observed signal S from the RoI can be described as

$$S = S_{HR} + S_{motion} + S_{illumination} + S_{ambient}, \quad (2)$$

where S_{motion} , $S_{illumination}$, and $S_{ambient}$ are motion-induced changes, illumination changes, and changes in the ambient light signal, respectively. As shown in Figure 3, the frequency of illumination changes and vibration in the automotive driving environment appears in a fairly low frequency band compared with HR. Thus, the noise signals caused by illumination change and vibration can be significantly excluded using bandpass filtering. However, given the assumption that ambient light is white noise, it cannot be easily filtered out by the bandpass filter, and so may interfere with the HR signal. Therefore, it is necessary to extract the prominent feature signal of the HR and to separate it into each source signal from a feature that contains various components.

Based on the property that the signal of PPG is different for each channel, the *RoverG* feature that maximizes HR can

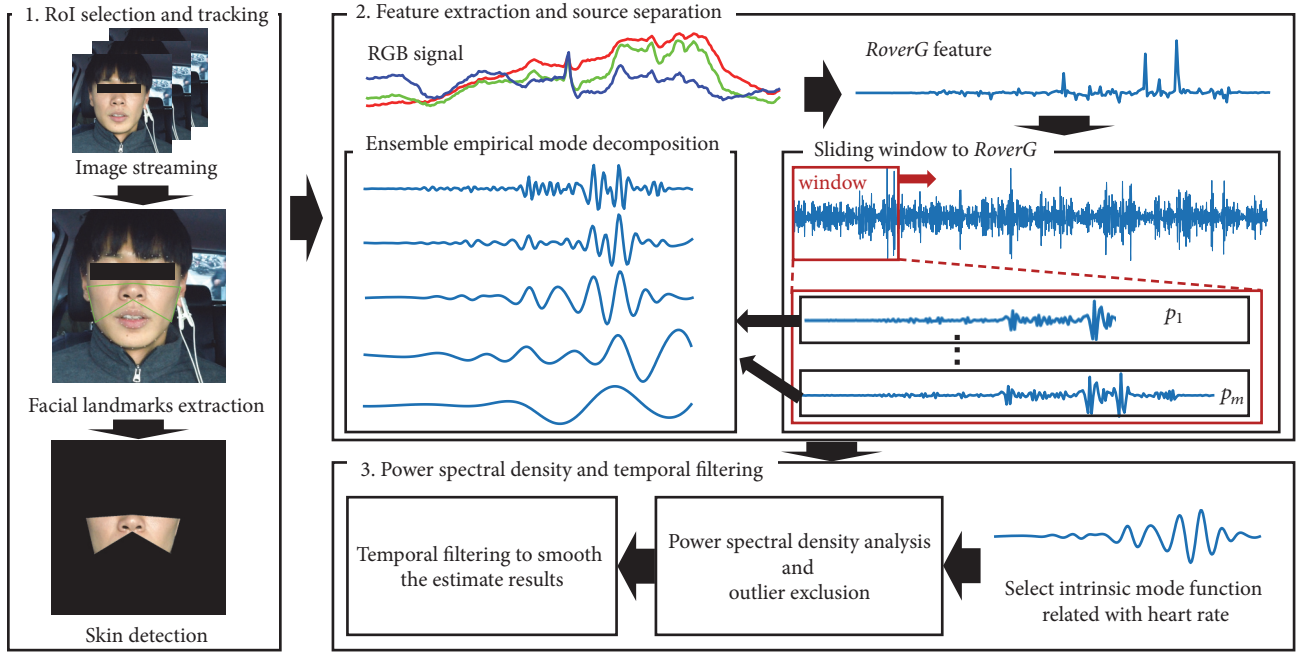


FIGURE 1: Conceptual overview of the proposed heart rate estimation method under driving environment.

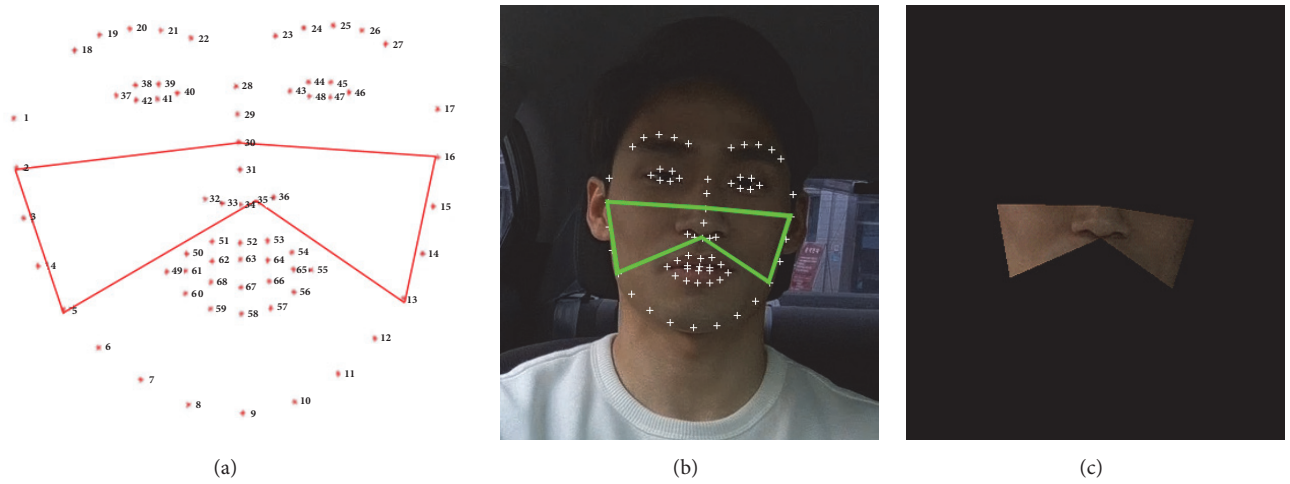


FIGURE 2: Extraction of facial landmark points. (a) The unique number of each of the 66 facial landmark points and the 6 selected points (4 contour points on the cheek and 2 points on the nose). (b) Detected result of the driving dataset. (c) Result of skin detection.

be obtained by taking a ratio from an RGB signal from the ROI as

$$RoverG = \frac{G_n}{R_n}, \quad (3)$$

where G_n and R_n are the normalized green and red signals [20, 21].

However, *RoverG* is an unstable HR feature because it takes a fraction of the purely observed signal without any filtering. Therefore, this feature also includes variations due to illumination change and motion and should be separated into pure HR signals.

Before extracting the HR signal, a detrending method was applied to remove the nonstationary component with the smoothing parameter $\lambda = 10$ [22]. Then ensemble empirical mode decomposition (EEMD) is employed to separate the HR source signal from a number of noisy components in *RoverG* [11]. EEMD is a noise assisted data analysis method that separates the Intrinsic Mode Function (IMF) from the data. The IMF extraction process, called sift, is accomplished by averaging the trials with the signal plus white noise, which is newly generated at every trial. If enough trials are carried out and more white noise is added, the components that make up the observed signal can be separated. In [15], which IMF is close to HR is determined through EEMD, and the fourth IMF is extracted as the HR component.

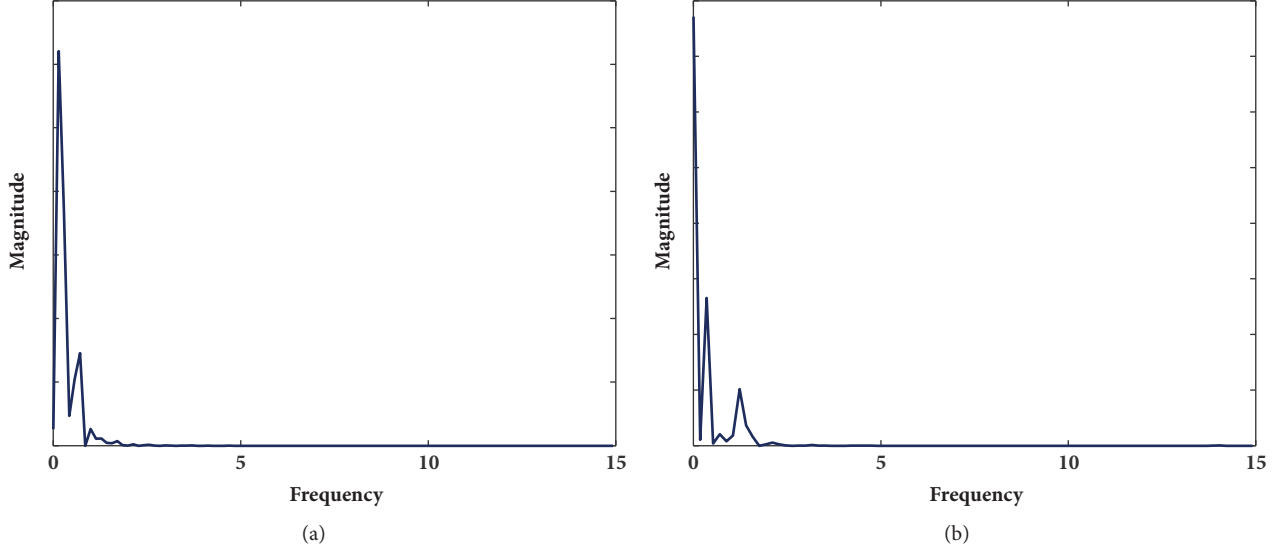


FIGURE 3: Frequency (in Hz) analysis of (a) illumination change and (b) vibration under automotive driving conditions.

However, since the automotive driving environment is very dynamic, several estimated HRs are derived as candidates for one estimation window for a stable HR estimation. Thus, the *RoverG* feature signal conversion and EEMD IMF extraction is iteratively performed in a window. The k th window, denoted as I_k , is divided into m periods by accumulating one second intervals from the first starting point to $p_1, p_2, \dots, p_m (= I_k)$. Then, the HR for each period is estimated, and m estimated HRs are derived from the window. However, since all of the m estimated HRs have different inconsistent results, Mahalanobis distance is employed to exclude the result that is the furthest from most of the m results as

$$d(HR_{cand}, \mu_{cand}) = \left[(HR_{cand} - \mu_{cand})^T S^{-1} (HR_{cand} - \mu_{cand}) \right]^{1/2}, \quad (4)$$

where HR_{cand} and μ_{cand} are $m \times 1$ vectors consisting of m estimated candidate results and the mean of HR_{cand} , respectively, and S^{-1} is the covariance matrix. The candidate estimated HRs left after this exclusion are averaged and adopted as a result at the k second.

2.3. Power Spectral Density Analysis and Temporal Filtering.

In order to calculate the final HR per minute, PSD is analyzed using the Welch method [23]. The cutoff frequency is set as (0.7, 4) HZ, corresponding to (42, 240) beats/min (bpm) and 128-order hamming window is used as the bandpass filter. However, the ambient light of the external noise in the cutoff frequency band may still cause intermittent peaking of the estimate. In order to cope with this problem, temporal filtering is applied to smooth the estimate trend as

$$HR^t = \frac{1}{s} \sum_{r=t-s}^{t-1} HR^r \quad \text{when } HR^t - HR^{t-1} \geq \alpha, \quad (5)$$

where HR^t denotes the HR at time t . Threshold α denotes the allowable maximum value for the difference between the previous HR estimate and the current estimate. The parameter s determines the number of frames used for smoothing. These parameters (α and s) were chosen for optimal performance from the data set collected based on the assumption that HR does not change substantially in one second. The overall algorithm flow is shown in Algorithm 1.

3. Experiments and Results

In this section, we compare the performance of the proposed features against those presented in recent studies with the public HCI dataset.

3.1. Comparative Analysis of Features. As mentioned in Section 2, the green channel has the strongest PPG signal [6, 20]. On the other hand, Haan et al. proposed *XminY* with *RoverG* and proved that *XminY* has the highest performance in terms of experimental results [7]. Thus, it is necessary to determine which of the various feature signals produces the best HR signal.

For stable analysis, the MAHNOB-HCI dataset [24], a public indoor environment dataset, was used to compare the results of the five features, and the results are shown in Table 1.

Several commonly used performance indicators are employed to compare the performance of each feature [6]. M_e and SD_e are the mean and standard deviation, respectively, of the difference between ground truth and the obtained estimate, $HR_{dif} = HR_{est} - HR_{gt}$. Additionally, the root mean square error (RMSE) and M_{eRate} , which is the percentage of $\sum_{n=1}^N (|HR_{dif}(n)|/HR_{gt}(n))$, are employed to measure precision. Finally, r is the Pearson correlation coefficient that can evaluate the correlation between the two values.

```

Input: Image frame consist of RGB channel
Output: Estimated heart rate
Initialization: A video sequence within sliding window
For  $frame = 1, 2, \dots, N$ 
  If  $frame == 1$ 
    Detect a facial landmark points
    Select 6 facial landmark points for cheek and nose
  End
  Track the detected region of interest
  Detect skin region within region of interest
  If  $\text{mod}(frame, \text{frame rate}) == 0$  and  $frame \geq \text{length of window}$ 
    For  $period = p_1, p_2, \dots, p_m$ 
      RGB normalization
      Calculate feature signal,  $RoverG = G_n/R_n$ 
      Extract intrinsic mode function for heart rate from  $RoverG$ 
      Power spectral density analysis
    End
    Filtering outlier using Mahalanobis distance,  $d(HR_{est}, \mu_{est})$ 
    Obtain heart rate result  $HR_{avr}^t$  by averaging remaining estimates
    If  $HR_{avr}^t - HR^{t-1} > \alpha$ 
      Temporal filtering with estimated result
    End
  End
End

```

ALGORITHM 1: Heart rate estimation algorithm.

TABLE 1: Comparison of heart rate estimation using different features (best performance in bold).

Feature	$M_e(SD_e)$ (bpm)	RMSE (bpm)	M_{eRate}	r
<i>Green</i>	-10.6(4.19)	11.3	14.22%	-0.35
<i>Green_mah</i>	-10.33(10.17)	14.45	13.71%	-0.20
<i>Green_mah_TF</i>	-6.63(7.21)	13.68	15.84%	-0.50
<i>XminY</i>	-20.1(6.54)	21.0	27.2%	-0.32
<i>XminY_mah</i>	-11.93(9.91)	15.3	16.11%	0.07
<i>XminY_mah_TF</i>	-12.07(5.15)	13.22	15.11%	0.39
<i>RoverG</i>	-2.43(7.27)	7.27	4.93%	0.59
<i>RoverG_mah</i>	-0.57(5.94)	3.26	5.58%	0.59
<i>RoverG_mah_TF</i>	0.80(3.35)	3.26	3.68%	0.75

Of the features, *Green* and *RoverG* are the signal from the pure green channel value in the RGB image and the feature from (2), respectively. *XminY* is the difference between *X* and *Y*, which is a linear combination feature of the RGB signal as described in (6)

$$\begin{aligned}
 X &= 3R_n - 2G_n \\
 Y &= 1.5R_n + G_n - 1.5B_n.
 \end{aligned}
 \tag{6}$$

RoverG_mah is a method of removing the peak candidate estimation value by applying the Mahalanobis distance to the estimated values of *RoverG*, and *RoverG_mah_TF* is the result of smoothing the outlier through temporal filtering.

As shown in Table 1, of the five metrics, *RoverG_mah_TF* shows the best performance. Although *RoverG* without any postprocessing shows a considerable fluctuation in its the result, the *RoverG_mah* with the statistical exclusion method of candidates has a relatively stable result. On the other hand, *XminY*, which showed the highest performance in [7], shows a lower performance than the other features with the MAHNOB-HCI dataset.

3.2. Validation Using Public Indoor Dataset. To validate the proposed method, its performance was compared with the recently proposed methods using a public dataset. The MAHNOB-HCI dataset is a public HCI dataset captured with several vital signals in the indoor environment. The dataset consists of two experiments containing emotion elicitation and implicit tagging. The subjects consist of 12 males and 15 females, each of whom was synchronized with the image by attaching an electrocardiography (ECG) sensor to their body. The ECG and image are recorded at 256 Hz and a frame rate of 61, respectively, and the resolution of the image is 780 by 580. Since it is of interest to estimate HR change over time, emotion elicitation data is adopted in the experiment. Emotion elicitation data is a data recording the vital signal and the facial image according to the stimulus by showing some videos (e.g., nature documentary or horror movie) to the subject. A comparison of the performance of the related methods on the MAHNOB-HCI dataset is shown in Table 2. For the previous methods, while the MAHNOB-HCI dataset was quite a challenging dataset, Li2014 and Tulyakov2016 achieved substantial accuracy with marginal improvement thereafter. Nevertheless, our algorithm, which is proposed to

TABLE 2: Comparison of the performance of related methods with the MAHNOB-HCI dataset (best performance in bold).

Feature	$M_e(SD_e)$ (bpm)	RMSE (bpm)	M_eRate	r
Poh2010	-8.95(24.3)	25.9	25.0%	0.08
Poh2011	2.04(13.5)	13.6	13.2%	0.36
De Haan2013	4.62(6.50)	6.52	6.39%	0.82
Balakrishman2013	-14.4(15.2)	21.0	20.7%	0.11
Li2014	-3.30(6.88)	7.62	6.87%	0.81
Tulyakov2016	3.19(5.81)	6.23	5.93%	0.83
Ours	0.80(3.35)	3.26	3.68%	0.75

target a dynamic environment (e.g., the automobile driving environment), shows very high accuracy performance in this indoor environment. In terms of the Pearson correlation coefficient, its performance is comparable to the best performing previous method (e.g., Tulyakov2016). Except for this indicator, given the residual performance results related to the error, the estimate result of the proposed method is shown to outperform over all previous methods.

3.3. Demonstration on Dynamic Driving Dataset. To demonstrate the proposed method under a driving scenario, a real driving dataset was collected under driving condition with 19 subjects in their 20s and 30s. The subjects included men and women of different ethnic backgrounds from countries such as Korea, China, and the Middle East. The driving dataset was captured by an action camera, Go-pro HERO 3+, fixed on a windscreen recording at a 30 frames per second rate and a resolution of 1920-by-1080. The ground truth was obtained by attaching a contact based pulse sensor to the earlobe of the subjects and synchronized with the captured dataset (the MP507 model of MEK was used as the earlobe pulse sensor). In order to securely obtain the dataset, the subject in the passenger seat was recorded instead of the actual driver, and they were asked to move their head up and down sometimes during the course of the driving. The subjects were also asked to rush up a hill before boarding the vehicle to check for pulse rate changes. It was recorded as naturally as possible without any additional constraints on the experiment. The driving course included a variety of actual driving road elements such as shade, curved sections, hills, and speed bumps. The ground truth is recorded in synchronization with the dataset using an earlobe attached sensor.

In order to address the stable performance of the proposed method, a Bland-Altman plot is employed. A Bland-Altman plot is a statistical plotting method that represents the agreement between two measurements. Each coordinate of the plot is denoted as in

$$BA(x, y) = \left(\frac{HR_{est} + HR_{gt}}{2}, HR_{est} - HR_{gt} \right). \quad (7)$$

The agreement A at the 95% confidence interval is shown in

$$A = \frac{1}{N} \sum_{i=1}^n a_i \times 100, \quad (8)$$

$$with a_i = \begin{cases} 1, & \text{if } |HR_{est} - HR_{gt}| > 1.96 \times \sigma \\ 0, & \text{if } |HR_{est} - HR_{gt}| < 1.96 \times \sigma, \end{cases}$$

where N is the total number of measurements and σ denotes the standard deviation between the two data sample sets. Figure 4 shows the Bland-Altman plot results of our proposed method with four randomly selected subjects from the driving dataset. The red and green line denotes the mean and standard deviation of the measurements, respectively. Each measurement is a combination of the estimated HR and ground truth per second. Figure 4 shows that although the results are applied to all four driving data sets, the mean of the errors is substantially small and a high agreement is obtained.

In order to visualize the tendency of the estimated HR and ground truth over time, the result is shown in Figure 5. Although the estimated value is slightly fluctuated compared with the ground truth, the difference is maintained within a maximum of 3 beats per minute. Moreover, it maintains similar stability to the normal interval even in the interval of fluctuation caused by speed bump and the rapid illumination change.

3.4. Performance Analysis Based on Execution Speed. Our proposed method is applied to vehicle environment. Therefore, fast performance is required even if some performance degradation occurs using constrained resources. By Huang *et al.* [11], the true IMF can be defined as an ensemble of many trials as shown in

$$EEMD \text{ Components} = \frac{std(x)}{N} \sum_{i=1}^N \{EMD(x + n_i)\}. \quad (9)$$

N is the number of trials and x, n denote the observation signal and noise, respectively. However, this approach requires a very large N resulting a large number of EMD calculations. Our proposed approach here limits the number of EMD calculations by exploiting independent identically distributed (iid) property of the white noise. Self-cancellation of the white noise can be accomplished by

$$EEMD \text{ Components} = \frac{std(x)}{M} \sum_{i=1}^M [EMD \{x + (\text{mod}(i, 2)) \cdot n_i - (\text{mod}(i, 2) - 1) \cdot n_i\}]. \quad (10)$$

mod is a function to obtain the remainder and M denotes the number of limited trials. However, based on the characteristic that noise n is iid like in theoretical EEMD, the process of adding noise in (10) was performed only in $M/2$ trials ($M \approx M/2 \ll N$). This method and (9) are called EEMD_n1 and EEMD, respectively, and 10 and 100 trials are performed, respectively, to compare with EEMD which is commonly used as [12].

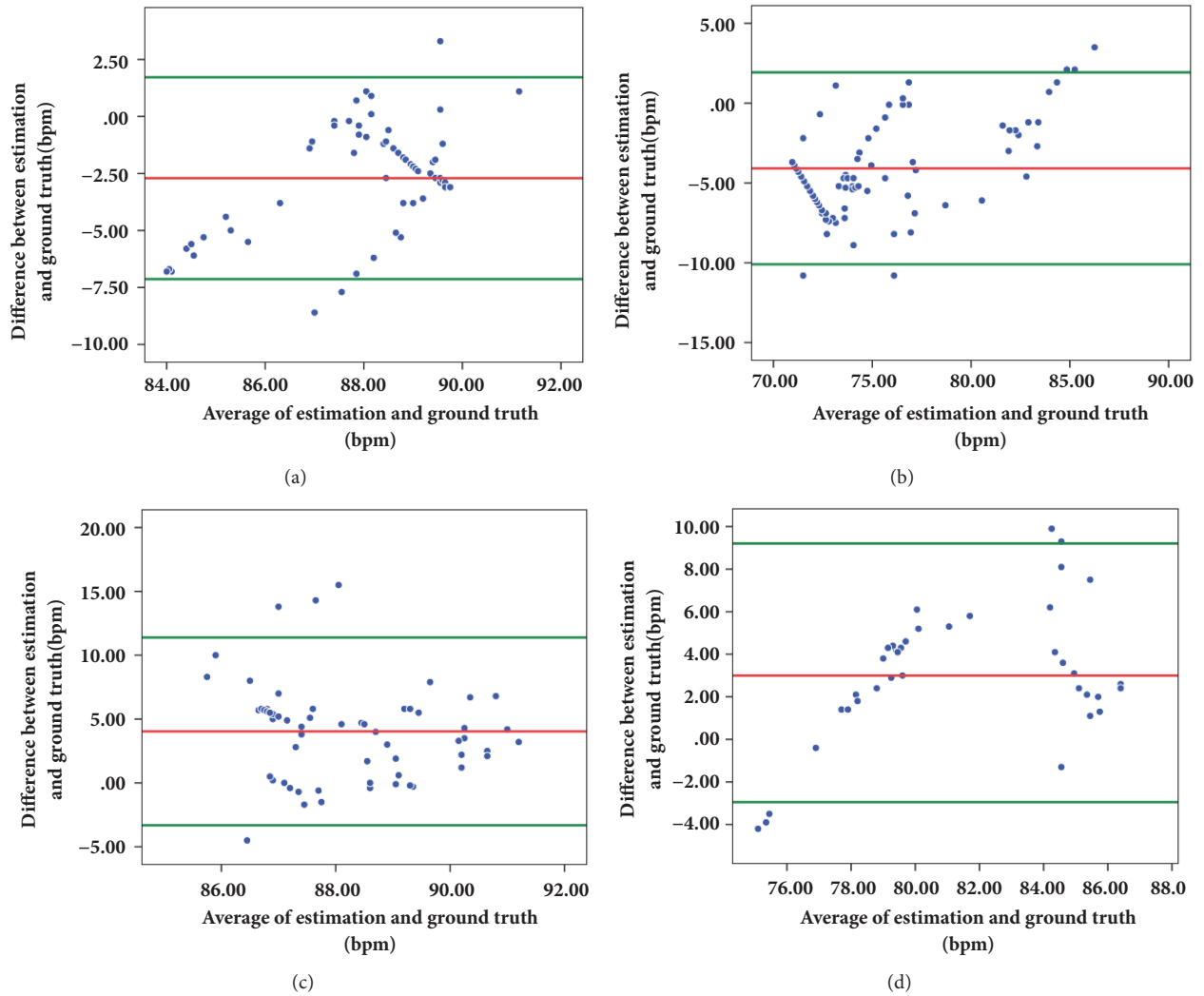


FIGURE 4: Bland-Altman plot analyzed at a 95% confidence interval. Each agreement of plot: (a) 95.9%; (b) 93.2%; (c) 93.5%; (d) 90%.

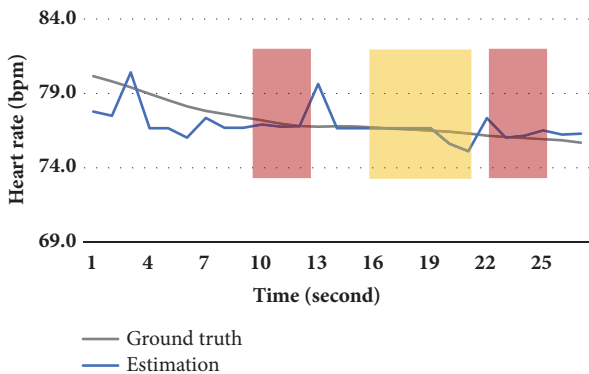


FIGURE 5: Heart rate trend between estimation and ground truth on challenging driving course. Red box: speed bump. Yellow box: rapid illumination change.

On the other hand, in case of RoI selection, the previously proposed method that detects face per frame instead of face

TABLE 3: The time it takes to operate once for each method.

Method	Operation time (second)
DRMF detection	0.86
KCF tracking	0.27
EEMD_n1	0.33
EEMD	4.52

tracking takes a considerable amount of time to process. It also presents a challenge when facial motion takes place. The time taken to operate each module is analyzed and shown in Table 3. While DRMF detection and KCF tracking are performed at every frame, EEMD_n1 and EEMD are performed as many as the number of candidate occurrences when an image frame is presented as input by the sliding window length.

Based on the result, four approaches are constructed as shown in Table 4, and their performance is compared to

TABLE 4: Comparison of heart rate estimations using different features (best performance in bold).

Approach	Absolute mean	Standard deviation	RMSE
DRMF+EEMD	4.35	2.29	4.89
DRMF+EEMD_n1	4.75	1.82	5.08
KCF+EEMD	3.66	2.42	4.37
KCF+EEMD_n1(ours)	3.71	3.07	4.74

determine the most efficient algorithm. Overall, the performance is better when using KCF than when using DRMF. This is because DRMF has difficulty in detecting the correct RoI corresponding to the cheek region when a part of the face is occluded due to shaking or facial motion. In the case of EEMD_n1, although the operation time is greatly reduced, the performance decline is very small.

4. Conclusions

This paper proposed a novel approach to estimating HR remotely in actual driving environments. Most previous studies have been proposed under indoor environments, which often lead to high implied levels of performance based on a well-controlled practical application context. On the other hand, the proposed method showed attaining the highest practical applicability by demonstrating its ability under the most challenging environment, the automotive driving environment. Before testing the proposed method under the automotive driving environment with various obstacles, it was compared to other methods using the same indoor public dataset as previous studies and using the same performance index to validate its effectiveness. The proposed method was then applied to data from an actual driving situation and a fairly stable result was obtained. For automotive driver HR estimation, estimating the HR instantaneously is necessary to prevent accidents. Focusing on this issue, an appropriate approach was sought to maximize performance while reducing operation time. Hence, the performance was also analyzed in terms of processing time by comparing the proposed method with the conventional algorithms and the modified algorithm. The proposed method demonstrated a considerably superior performance and yet had a short processing time.

Data Availability

The experimental data used to support the findings of this study are available from the corresponding author upon request.

Conflicts of Interest

The authors declare that there are no conflicts of interest regarding the publication of this paper.

Acknowledgments

The authors of Korea University were supported by the National Research Foundation (NRF) grant funded by the Korea (no. 2017R1A2B4012720). David Han's contribution was supported by the US Army Research Laboratory.

References

- [1] M. Huelsbusch, A. V. Clough, C. Chen, and V. Blazek, "Contactless mapping of rhythmical phenomena in tissue perfusion using PPGI," in *Proceedings of the Medical Imaging 2002*, vol. 4683, pp. 110–118, San Diego, CA, USA, 2002.
- [2] M.-Z. Poh, D. J. McDuff, and R. W. Picard, "Non-contact, automated cardiac pulse measurements using video imaging and blind source separation," *Optics Express*, vol. 18, no. 10, pp. 10762–10774, 2010.
- [3] M.-Z. Poh, D. J. McDuff, and R. W. Picard, "Advancements in noncontact, multiparameter physiological measurements using a webcam," *IEEE Transactions on Biomedical Engineering*, vol. 58, no. 1, pp. 7–11, 2011.
- [4] F. Zhao, M. Li, Y. Qian, J. Z. Tsien, and I. P. Androulakis, "Remote measurements of heart and respiration rates for telemedicine," *PLoS ONE*, vol. 8, no. 10, p. e71384, 2013.
- [5] H.-Y. Wu, M. Rubinstein, E. Shih, J. Guttag, F. Durand, and W. Freeman, "Eulerian video magnification for revealing subtle changes in the world," *ACM Transactions on Graphics*, vol. 31, no. 4, article 65, 2012.
- [6] X. Li, J. Chen, G. Zhao, and M. Pietikainen, "Remote heart rate measurement from face videos under realistic situations," in *Proceedings of the 2014 IEEE Conference on Computer Vision and Pattern Recognition (CVPR)*, pp. 4264–4271, Columbus, OH, USA, June 2014.
- [7] G. De Haan and V. Jeanne, "Robust pulse rate from chrominance-based rPPG," *IEEE Transactions on Biomedical Engineering*, vol. 60, no. 10, pp. 2878–2886, 2013.
- [8] W. Wang, S. Stuijk, and G. De Haan, "Exploiting spatial redundancy of image sensor for motion robust rPPG," *IEEE Transactions on Biomedical Engineering*, vol. 62, no. 2, pp. 415–425, 2015.
- [9] S. Tulyakov, X. Alameda-Pineda, E. Ricci, L. Yin, J. F. Cohn, and N. Sebe, "Self-adaptive matrix completion for heart rate estimation from face videos under realistic conditions," in *Proceedings of the 2016 IEEE Conference on Computer Vision and Pattern Recognition, CVPR 2016*, pp. 2396–2404, Las Vegas, USA, July 2016.
- [10] L. Xu, J. Cheng, and X. Chen, "Illumination variation interference suppression in remote PPG using PLS and MEMD," *IEEE Electronics Letters*, vol. 53, no. 4, pp. 216–218, 2017.
- [11] Z. H. Wu and N. E. Huang, "Ensemble empirical mode decomposition: a noise-assisted data analysis method," *Advances in Adaptive Data Analysis (AADA)*, vol. 1, no. 1, pp. 1–41, 2009.
- [12] J. Cheng, X. Chen, L. Xu, and Z. J. Wang, "Illumination variation-resistant video-based heart rate measurement using joint blind source separation and ensemble empirical mode decomposition," *IEEE Journal of Biomedical and Health Informatics*, vol. 21, no. 5, pp. 1422–1433, 2017.
- [13] H. Qi, Z. Guo, X. Chen, Z. Shen, and Z. Jane Wang, "Video-based human heart rate measurement using joint blind source separation," *Biomedical Signal Processing and Control*, vol. 31, pp. 309–320, 2017.

- [14] C. Tang, J. Lu, and J. Liu, "Non-contact heart rate monitoring by combining convolutional neural network skin detection and remote photoplethysmography via a low-cost camera," in *Proceedings of the IEEE Conference on Computer Vision and Pattern Recognition Workshops*, pp. 1309–1315, Salt Lake City, USA, June 2018.
- [15] D.-Y. Chen, J.-J. Wang, K.-Y. Lin et al., "Image sensor-based heart rate evaluation from face reflectance using Hilbert-Huang transform," *IEEE Sensors Journal*, vol. 15, no. 1, pp. 618–627, 2015.
- [16] M. Kumar, A. Veeraraghavan, and A. Sabharwal, "DistancePPG: Robust non-contact vital signs monitoring using a camera," *Biomedical Optics Express*, vol. 6, no. 5, pp. 1565–1588, 2015.
- [17] A. Asthana, S. Zafeiriou, S. Cheng, and M. Pantic, "Robust discriminative response map fitting with constrained local models," in *Proceedings of the 26th IEEE Conference on Computer Vision and Pattern Recognition, CVPR 2013*, pp. 3444–3451, USA, June 2013.
- [18] J. F. Henriques, R. Caseiro, P. Martins, and J. Batista, "High-speed tracking with kernelized correlation filters," *IEEE Transactions on Pattern Analysis and Machine Intelligence*, vol. 37, no. 3, pp. 583–596, 2015.
- [19] T. Sawangsri, V. Patanavijit, and S. Jitapunkul, "Face segmentation based on hue-cr components and morphological technique," in *Proceedings of the IEEE International Symposium on Circuits and Systems 2005, ISCAS 2005*, pp. 5401–5404, Japan, May 2005.
- [20] W. Verkruyse, L. O. Svaasand, and J. S. Nelson, "Remote plethysmographic imaging using ambient light," *Optics Express*, vol. 16, no. 26, pp. 21434–21445, 2008.
- [21] J. A. Crowe and D. Damianou, "The Wavelength Dependence Of The Photoplethysmogram And Its Implication To Pulse Oximetry," in *Proceedings of the 1992 14th Annual International Conference of the IEEE Engineering in Medicine and Biology Society*, pp. 2423–2424, Paris, France, Oct 1992.
- [22] M. P. Tarvainen, P. O. Ranta-aho, and P. A. Karjalainen, "An advanced detrending method with application to HRV analysis," *IEEE Transactions on Biomedical Engineering*, vol. 49, no. 2, pp. 172–175, 2002.
- [23] G. Valakrishnan, F. Durand, and J. Guttag, "Detecting pulse from head motions in video," in *Proceedings of the 2013 IEEE Conference on Computer Vision and Pattern Recognition (CVPR)*, pp. 3430–3437, Portland, OR, USA, June 2013.
- [24] J. Kuo, S. Koppel, J. L. Charlton, and C. M. Rudin-Brown, "Evaluation of a video-based measure of driver heart rate," *Journal of Safety Research*, vol. 54, pp. 55–59, 2015.

Research Article

A Comparison Analysis of Surrogate Safety Measures with Car-Following Perspectives for Advanced Driver Assistance System

Sehyun Tak,¹ Sunghoon Kim ,² Donghoun Lee ,² and Hwasoo Yeo ²

¹Department of The Fourth Industrial Revolution and Transport, The Korea Transportation Institute (KOTI), Republic of Korea

²Department of Civil and Environmental Engineering, Korea Advanced Institute of Science and Technology, Republic of Korea

Correspondence should be addressed to Hwasoo Yeo; hwasoo@gmail.com

Received 25 July 2018; Accepted 8 October 2018; Published 1 November 2018

Guest Editor: Luc Chassagne

Copyright © 2018 Sehyun Tak et al. This is an open access article distributed under the Creative Commons Attribution License, which permits unrestricted use, distribution, and reproduction in any medium, provided the original work is properly cited.

Surrogate Safety Measure (SSM) is one of the most widely used methods for identifying future threats, such as rear-end collision. Various SSMs have been proposed for the application of Advanced Driver Assistance Systems (ADAS), including Forward Collision Warning System (FCWS) and Emergency Braking System (EBS). The existing SSMs have been mainly used for assessing criticality of a certain traffic situation or detecting critical actions, such as severe braking maneuvers and jerking before an accident. The ADAS shows different warning signals or movements from drivers' driving behaviours depending on the SSM employed in the system, which may lead to low reliability and low satisfaction. In order to explore the characteristics of existing SSMs in terms of human driving behaviours, this study analyzes collision risks estimated by three different SSMs, including Time-To-Collision (TTC), Stopping Headway Distance (SHD), and Deceleration-based Surrogate Safety Measure (DSSM), based on two different car-following theories, such as action point model and asymmetric driving behaviour model. The results show that the estimated collision risks of the TTC and SHD only partially match the pattern of human driving behaviour. Furthermore, the TTC and SHD overestimate the collision risk in deceleration process, particularly when the subject vehicle is faster than its preceding vehicle. On the other hand, the DSSM shows well-matched results to the pattern of the human driving behaviour. It well represents the collision risk even when the preceding vehicle moves faster than the follower one. Moreover, unlike other SSMs, the DSSM shows a balanced performance to estimate the collision risk in both deceleration and acceleration phase. These research findings suggest that the DSSM has a great potential to enhance the driver's compliance to the ADAS, since it can reflect how the driver perceives the collision risks according to the driving behaviours in the car-following situation.

1. Introduction

Rear-end collision is one of the most frequent traffic accidents on the roads. Common contributing factors for the rear-end crashes include driver's inattention and human misjudgments on the amount of required deceleration in car-following situation. In efforts to prevent the rear-end crash and improve vehicular safety, drivers' judgments must be assisted and guided based on current or upcoming traffic situations. For such matter, various Advanced Driver Assistance Systems (ADAS) such as Forward Collision Warning System (FCWS) and Emergency Braking System (EBS) have been developed based on different data sources, including camera, radar,

LIDAR, GPS, and connected vehicle network. The FCWS and EBS are designed to give warning signals or implement braking autonomously by detecting hazardous situations before a collision ahead of vehicle even occurs. One of major concerns to provide the collision warning or implement the autonomous braking in the ADAS is how the criticality of a certain traffic situation for a vehicle is assessed. To deal with the related problems, various assessment approaches have been proposed. One of the representative methods for identifying the rear-end collision risk is Surrogate Safety Measure (SSM). The SSM calculates the collision risk of a certain traffic situation with microscopic traffic parameters such as vehicle speed, acceleration, time headway, and space

headway. There have been various efforts in developing SSMs for the FCWS or EBS based on the parametric method. The previous studies on the SSMs can be classified into two types. One is the perceptual approach and the other is the kinematic approach [1]. The perceptual approach-based SSM is designed to measure the collision risk based on the thresholds of perception. The representative of such approach is Time-To-Collision (TTC) [2], which estimates the expected time for two successive vehicles to collide. Some modified TTCs have been proposed, such as Inverse TTC [3], Time Exposed TTC [4], Time Integrated TTC [5], and Modified TTC [6]. On the other hand, the kinematic approach-based SSM is to estimate the rear-end collision risk based on the difference between the required stopping distances of two consecutive vehicles. There have been numerous SSMs based on this approach, such as Potential Index for Collision with Urgent Deceleration (PICUD)[7–9], Stopping Distance Index (SDI) [10, 11], Stopping Headway Distance (SHD) [12], Crash Index (CI) [13], and Deceleration Rate to Avoid the Crash (DRAC) [14]. More recently, Deceleration-based Surrogate Measure (DSSM) was proposed by considering a human-centered design [15], and such design significantly affects the performance of the risk evaluation since the human-related parameters are strongly related to the situational awareness measure [16]. Similar to the perceptual approach-based SSMs, the kinematic approach-based SSMs are also used for assessing the safety of a vehicle and giving warning signals to the driver. The previous researches demonstrate that these SSMs show good performances in detecting critical events such as severe braking or jerk maneuvers before a collision.

On the other hand, one of the most critical factors of the SSMs employed in the FCWS and EBS is driver's compliance, which is highly correlated with the system reliability [17]. For example, a conservative SSM designed particularly for passive drivers will give frequent alerts to aggressive drivers in most cases. Then, the driver can become desensitized to the nuisance warnings [18]. On the other hand, imminent threat alerts given by an aggressive SSM may lead to missed alarms, which may not provide enough time to avoid an upcoming collision risk [19]. Therefore, drivers become more intended to ignore such system and they can nullify the effects of potential benefits from the system [20]. However, most of the previous studies on the SSMs applied to the FCWS and EBS have focused on discriminating possible collision situations in a subsequent few seconds, rather than tracking the estimated collision risk according to the drivers' driving behaviours in the entire car-following process. Therefore, there may exist inconsistency between the driver's perception of risk and the actual level of hazard.

Thus, there is a need for exploring the characteristics of existing SSMs particularly in terms of such inconsistency. For such purpose, this study aims to analyse and compare the collision risks estimated by different SSMs based on two different car-following theories, such as action point model and asymmetric driving behaviour model. DSSM is specifically selected as the representative of human-centered design that considers the inconsistency between the driver's perception of risk and the actual level of hazard. TTC

and SHD are selected as the representatives of each of the perceptual approach and kinematic approach, respectively, and they are used as the benchmarking points to be compared with DSSM. In fact, DSSM is basically based on the kinematic approaches like SHD. Compared to the SHD, which calculates the collision risk based on the variables obtained from sensor equipped in the vehicle, DSSM calculates the collision risk with more variables such as jerk rate, acceleration, and transition time for the application in Vehicle-to-Vehicle (V2V) communication environment. By comparing the SHD and DSSM, the characteristics of risk estimation with different technology bases (sensor-based and V2V communication-based) can be shown.

Considering the relationship between the driving behaviours and the collision risk estimated by the SSMs provides a foundation for monitoring the reaction of drivers to the collision risk, which can reflect the different preferences of drivers on the collision risk. The detailed explanation on the analysis method is provided in the following section. Then, Sections 3 and 4 describe the comparison results of the three SSMs according to the action point model and asymmetric driving behaviour model, respectively. Finally, brief concluding remarks are provided in the last section.

2. Analysis Approach

2.1. Car-Following Models for Analysis. To analyze the relationship between driving behaviour and collision risk in car following situation, several traffic variables are considered in this study. The traffic variable includes speed of a subject vehicle, spacing between the subject vehicle and preceding vehicle, and the relative speed between the two consecutive vehicles. There are two types of car-following processes discussed in this paper to examine the different levels of collision risk with the actual driver behaviour.

First one is analyzed in the spacing-relative speed plane, which adopts the perspectives used in action point model [21]. The action point model, which is also known as psychophysiological car-following model, considers drivers' perception thresholds for a certain minimum value of the stimulus based on the spacing and relative speed [22]. This analysis would show how drivers react differently to the collision risk according to the changes in the spacing and relative speed. In the action point model-based analysis, the state of a vehicle is defined by using both the spacing and relative speed. Therefore, the state of a subject vehicle is not defined solely by the speed in a car-following situation of two consecutive vehicles.

Nonetheless, the speed of subject vehicle shows an important aspect of vehicle' state in a car-following process since the driver determines the acceleration depending on not only the relative speed but also the speed of the subject vehicle [23, 24]. Hence, the second method of analyzing car-following process is suggested to show a different aspect of the car-following process by focusing on a speed of subject vehicle and spacing based on the asymmetric driving behaviour [24]. The car-following process of asymmetric driving behaviour can show how a driver differently reacts to the collision risk

when the vehicle is in acceleration phase and deceleration phase.

These two types of car-following processes describe how drivers perceive the collision risk in terms of the spacing, speed of subject vehicle, and relative speed. It is expected that the results of the analysis can explain why drivers show inconsistent choices of headway in car-following situations. However, these two types of car-following processes can describe only some parts of the highly complex human driving behaviours. These two types of car-following processes suit for the human driving behaviours in the stationary traffic state, particularly with the situations that both lead and following vehicles' speed are less than the free flow speed (or speed limit). Since the scope of this study is within such specific cases that have the high possibility of rear-end collision, we extract the car-following cases without any disturbances such as a vehicle cutting in or changing lane for the SSMs analysis.

2.2. Safety Surrogate Measures for Comparison. For analysis on the relationship between driving behaviour and collision risk, investigating different SSMs are necessary to be compared. This study considers three SSMs to estimate the collision risks at a given traffic situation, which includes the TTC, SHD, and DSSM. Since these three SSMs have different perspectives on the collision risk, their performances may be different from each other, even in identical traffic situations.

First introduced by Hayward [2], the TTC is one of the most representative indicators for judging the dangerous situation [25, 26]. It estimates the collision risk between two consecutive vehicles by calculating the remaining time before following vehicle crashes into a front vehicle with the assumption that the path and speed of two consecutive vehicles are maintained. The TTC is defined by

$$TTC = \frac{[x_{n-1}(t) - x_n(t) - s_{n-1}]}{[v_n(t) - v_{n-1}(t)]} \quad (1)$$

where $v_{n-1}(t)$ is the speed of leader vehicle at time t , $v_n(t)$ is the speed of following vehicle at time t , $x_{n-1}(t)$ is the location of leader vehicle at time t , $x_n(t)$ is the location of following vehicle at time t , and s_{n-1} is the length of leader vehicle. For example, a pre-determined TTC threshold value is 2.0 seconds. The current car-following situation is safe when the TTC value is greater than or equal to the threshold value, while the TTC value gets closer to zero as the rear-end collision risk increases.

For evaluating the collision risk, the concept of safe stopping distance has also been used. Methods with this concept calculate the collision risk based on the difference between stopping distances of two consecutive vehicles with full deceleration rate. The methods with such concept calculate the collision risk by assuming that the leader vehicle suddenly brakes with the maximum deceleration rate. The condition that the stopping distance of leader is smaller than sum of stopping distance of the following vehicle and space headway of following vehicle is considered as a dangerous situation. The SHD is a representative safe

stopping distance-based method, which can be formulated as follows:

$$SHD = \max \left[-1.47 \times (v_{n-1}(t) \times h_n(t) - v_n(t) \times \tau) + \left[\frac{v_{n-1}(t)^2 - v_n(t)^2}{30 \times (acc/g \pm Gr)} \right], 0 \right] \quad (2)$$

where $h_n(t)$ is the time headway of the following vehicle at time t , τ is the perception reaction time, acc is the deceleration rate, g is the gravity acceleration, and Gr , the grade expressed as a percentage. For example, a predetermined SHD threshold value is 20. It is risky situation when the SHD value is greater than or equal to the threshold value, while the current situation is safe when the SHD value is less than the threshold value.

The DSSM is also one of the concepts using the safe stopping distance-based method, which can well represent the individual collision risk in both acceleration and deceleration phases compared to other SSMs by adopting the transition time [15]. The DSSM is a ratio of the required deceleration and maximum deceleration performance of a subject vehicle, which is defined as follows:

$$K = [x_n(t) - x_{n-1}(t) + s_{n-1}] + [2 \cdot v_n(t) + a_n(t) \cdot \tau] \cdot \frac{\tau}{2} - M_{n-1,Tran} + M_{n,Tran} \quad (3)$$

$$b_n(t) = b_{max,n-1} \cdot \frac{[v_n(t) + a_n(t) \cdot \tau]^2}{[2 \cdot K \cdot b_{max,n-1} + v_{n-1}(t)^2]} < 0 \quad (4)$$

$$DSSM = \frac{b_n(t)}{b_{max,n}} \quad (5)$$

where $a_n(t)$ is the acceleration rate of following vehicle at time t , $a_{n-1}(t)$ is the acceleration rate of leader vehicle at time t , $b_{max,n-1}$ is the maximum braking rate of leader vehicle, which represents the vehicle's mechanical deceleration performance, $b_n(t)$ is the needed deceleration rate of following vehicle to avoid the accident at time t , $b_{max,n}$ is the maximum braking rate of following vehicle, M_{n-1} is the stopping distance of leader vehicle during transition time, and M_n is the stopping distance of following vehicle during transition time, τ is the perception reaction time. For instance, a predetermined DSSM threshold value is 1. It is an unsafe situation when the DSSM value is greater than or equal to the threshold value, while the DSSM value is less than the threshold value when the current driving situation is safe.

2.3. Data Description. For analysis on the relationship between the driving behaviours and the collision risks estimated by the different SSMs, this research uses one of the Next Generation Simulation (NGSIM) trajectory datasets, which is collected from a segment of U.S. Highway 101 in Los Angeles, California, between 7:50 a.m. and 08:35 a.m. on 15 June 2005 [27]. The length of the study site in the

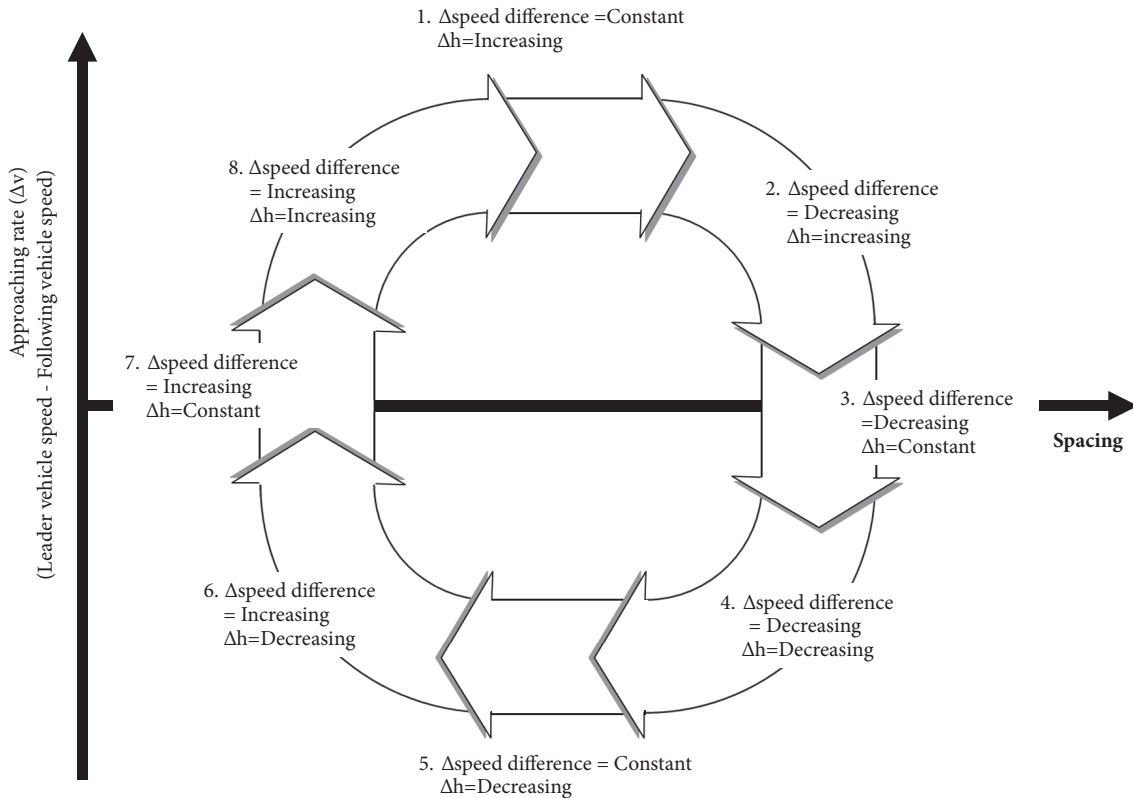


FIGURE 1: The Classification of driving state of subject vehicle.

NGSIM dataset is 640 m with five main lanes. The data contains microscopic traffic information on individual vehicular movements' trajectories, which includes location, speed, space headway, acceleration/deceleration, and vehicle type at 0.1 sec time intervals. Among the car-following cases in the dataset, 143 car-following cases that do not experience any disturbance such as cut-in and cut-out vehicle when passing through the study site are extracted, excluding motorcycles and trucks.

3. Comparison Analysis in Spacing-Relative Speed Plane

3.1. Action Point Model Perspective. As the first step of conducting comparison study, this study compares the SSMs with each other from the perspectives of the action point model. In other words, the collision risks estimated by the three SSMs will be described in the spacing-relative speed plane. As stated earlier, the car-following process of the action point model represents the driving behaviour with the psychophysical basis and shows how the driver of subject vehicle adjusts the differences in the locations and speeds between the leader and subject vehicle. In the action point model, a driver's decision is made upon certain perception threshold values. When the speed of preceding vehicle is much greater than the subject vehicle, the state of subject vehicle exceeds the perception threshold of relative speed. Then, the driver of the subject vehicle decides to accelerate.

On the other hand, when the speed of preceding vehicle is much less than the subject vehicle, the state of subject vehicle exceeds the perception threshold of relative speed in negative direction. Then, the subject vehicle decreases its speed. The spacing adjustment procedure is arranged similarly in the action point model. When the spacing is much greater than the desired spacing, the state of the subject vehicle exceeds the perception threshold of spacing. Then, the subject vehicle increases the speed to reduce the spacing. In contrast, the state of the subject vehicle exceeds the perception threshold of spacing in negative direction when the spacing is much less than the desired spacing. Then, the subject vehicle reduces its current speed. Based on the two kinds of perception thresholds and driving behaviour, the driver in the subject vehicle makes a decision for either accelerating or decelerating.

Hence, in the action point car-following process, the spacing and relative speed are important variables that directly affect the decision on acceleration and deceleration action. By using these two variables, the state of the subject vehicle can be defined as shown in Figure 1.

The state of the subject vehicle can be described by eight states. The states 1, 2, and 8 represent the situations of when the preceding vehicle is faster. And in states 4, 5, and 6, the preceding vehicle is slower than the subject vehicle. The states 1 and 5 are also the points that the driver makes the decision on acceleration and deceleration. After the state 1, which is called as "catch up" action point, the collision risk is increased

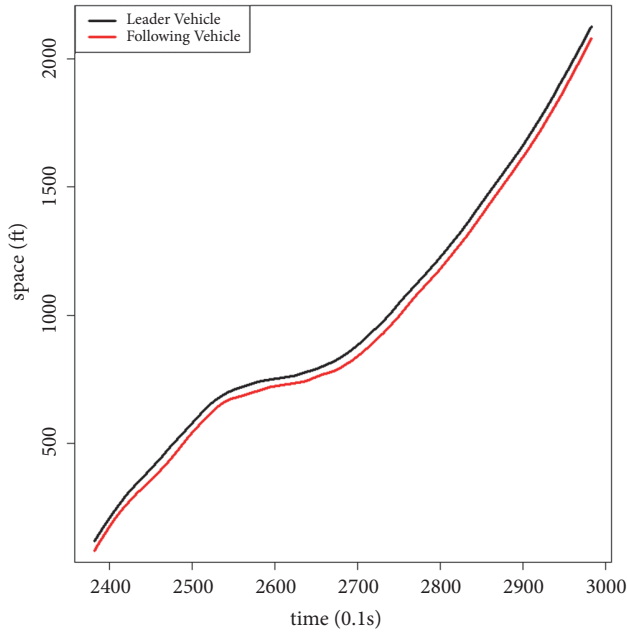


FIGURE 2: The example case for the analysis.

due to the acceleration actions. After the state 5, which is called as “release” action point, the collision risk is decreased due to the deceleration actions. In other states, the driver maintains the decision made in the states 1 and 5.

An example case of car-following for the analysis is depicted in Figure 2. In the figure, the black and red lines are the trajectories of the leader and subject vehicle, respectively. One can easily observe that the car-following case meets a shockwave and shows the both acceleration and deceleration behaviours.

3.2. Car-Following and Collision Risk by TTC. According to the example case shown in Figure 2, the collision risks estimated by the TTC are shown in Figure 3. This figure shows the relationship between the vehicle spacing and the relative speed. The points in the plane represent the temporal measurements of the two properties and the solid lines with arrows connect the sequence of these points. As we can see in the figure, the temporal measurements draw circles recurrently on the plane during the car-following situation, and it is shown that the low relative speed values with the low spacing values tend to have the high collision risk. In this paper, the collision risks are discretionarily classified into four situations for the quantitative analysis. By the concept of TTC, the risk is considered to be high when the TTC value is low. Thus, the four classified situations considered in this paper are High Risk ($TTC \leq 2.5$), Medium Risk ($2.5 < TTC \leq 5.0$), low risk ($5.0 < TTC \leq 7.0$), and Safe ($TTC > 7.0$). Note that since there have not been any previous efforts for defining the exact thresholds of the high or low risk at the current stage, the thresholds classifying the risk levels in this study are defined based on the empirical understandings with the given data. In fact, such thresholds may vary depending on the road characteristics or driving environments. Hence,

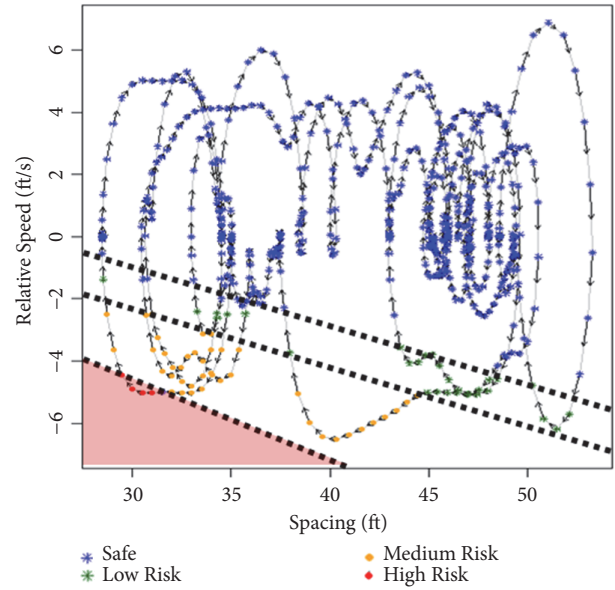


FIGURE 3: Collision risk estimated with the temporal spacing and relative speed (TTC).

some sensitivity analyses are required to investigate the issue further, but they go beyond the scope of this paper.

As shown in Figure 3, the TTC generally considers that it is safe when the preceding vehicle is faster than the subject vehicle. Hence, it only classifies the states 4, 5, and 6 into the dangerous situations. In TTC, at the similar level of spacing, the collision risk consistently increases as the relative speed decreases. At the similar level of relative speed, the collision risk also consistently increases as the spacing decreases. The level of collision risk is also indicated with different colours in the spacing and relative speed plane. Particularly, the red coloured region indicates that the driving situation is dangerous by the TTC estimation.

In terms of the action point car-following perspective, the collision risks estimated by the TTC do not match well to the action points where a driver changes acceleration and deceleration. In the near perception thresholds, which correspond to the states 1, 2, 3, and 7, the changes in the action are rarely observed. Furthermore, the TTC is not a sensitive measure that has a lack of reflecting the dynamic changes of driving situation, and it misses out some parts of the action points.

3.3. Car-Following and Collision Risk by SHD. Similar to the method of using the action point model above, the collision risks estimated by the SHD are shown in Figure 4. Unlike TTC, the risk is considered to be high when the TTC value is also high in SHD. In this paper, the four classified situations based on SHD are High Risk ($SHD > 40$), Medium Risk ($40 \geq SHD > 0$), Low Risk ($0 \geq SHD > -50$), and Safe ($-50 \geq SHD$). The SHD generally considers that it is not safe when the subject vehicle is faster than the preceding vehicle. The situations with high collision risks determined by the SHD are the states 4, 5, and 6. However, unlike the TTC that

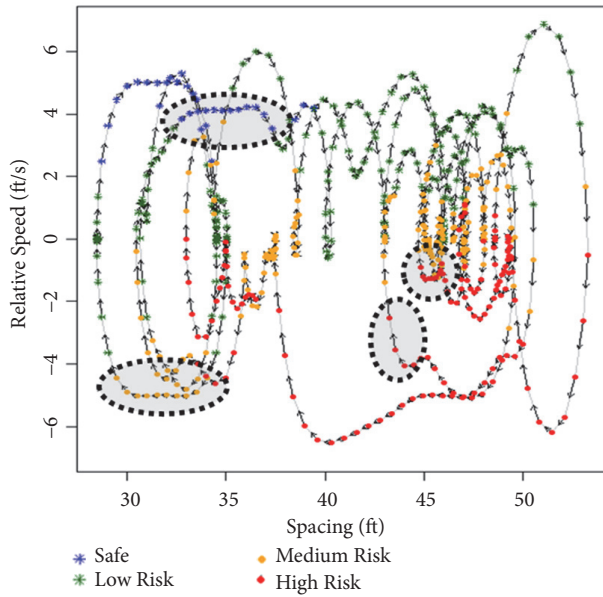


FIGURE 4: Collision risk estimated with the temporal spacing and relative speed (SHD).

considers high risk only when the subject vehicle is faster, the high collision risk is determined by the SHD also when the preceding vehicle is faster than the subject vehicle. In terms of the spacing, there is a significant difference between the SHD and the TTC. The high collision risk in the TTC mainly occurs when the spacing is small, but it is widely distributed over the entire spacing regions in the SHD. As the result, the SHD can evaluate the collision risk in the wider range of vehicle states in the spacing and relative speed plane.

Compared to the TTC, the collision risk in the SHD is more dynamically changed during the car-following process shown in Figure 4. Some corresponding points with the action points are observed, where the driver's driving behaviour is changed due to the excess of perception threshold. The observed action points are marked with the black dotted circles in Figure 4. Before and after the observed action points, the SHD shows approximately one-step difference in terms of collision risk. However, the changing trends of estimated collision risk of the SHD do not match well to the action points of the human driver overall.

3.4. Car-Following and Collision Risk by DSSM. Similar to the TTC and SHD, the DSSM considers also that it is dangerous when the subject vehicle is faster than the preceding vehicle, as shown in Figure 5. For the DSSM cases in this paper, the four classified situations are High Risk ($DSSM \geq 1.1$), Medium Risk ($1.1 > DSSM \geq 0.9$), Low risk ($0.9 > DSSM \geq 0.75$), and Safe ($0.75 > DSSM$). The high collision risk situations are shown in the states 4, 5, and 6. Nonetheless, DSSM shows distinctive differences from other SSMs.

First, the DSSM does not show increasing or decreasing trend only with the relative speed or spacing respectively. In the TTC, the collision risk increases as the relative speed

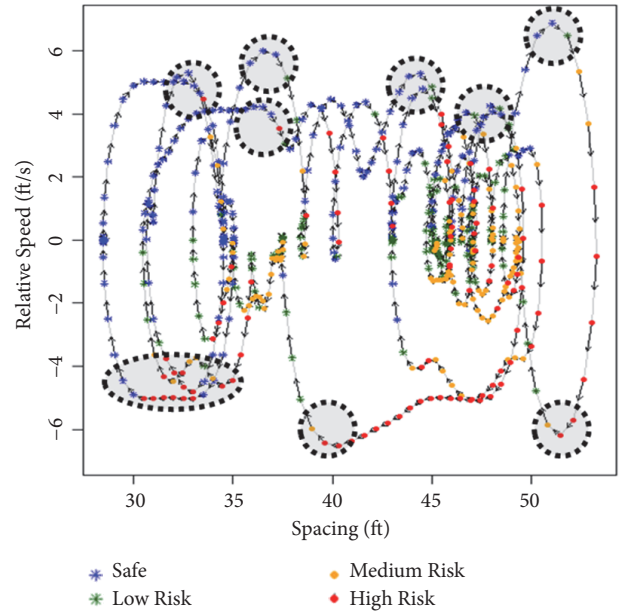


FIGURE 5: Collision risk estimated with the temporal spacing and relative speed (DSSM).

and spacing decrease overall, so that the high collision risk does not occur when there is a large value of the relative speed and spacing. In the SHD, the collision risk generally increases as the relative speed decreases, while it decreases as the spacing decreases overall. Therefore, the high collision risk hardly occurs when there is large relative speed value. On the other hand, the DSSM shows that a high collision risk occurs in all regions, even when the preceding vehicle is faster than the subject vehicle, as shown in Figure 5. Consequently, the DSSM can identify more various dangerous situations than other SSMs in all states of the action point car-following process.

Second, DSSM shows more well-matched results to the human driving behaviour in terms of the action point car-following process. As shown in Figure 5, the collision risk estimated by the DSSM is significantly changed before and after the action points, which are marked with the black dotted circles. After the action points where the preceding vehicle is slower than the subject vehicle, the estimated collision risk is sharply decreased. After the action points, which occur when the preceding vehicle is faster than the subject vehicle, the estimated collision risk of the DSSM shows increasing trend and high collision risk is also observed. This wide perceiving capability of the DSSM beyond the TTC and SHD is from the consideration of vehicles' acceleration in the evaluation of the risk.

3.5. Comparison of Average Collision Risk and High Collision Risk. Based on the classified states described as Figure 1, the trends of the estimated average collision risk and frequency of high collision risks are analyzed. The average collision risks of each SSM are calculated with the four classified situations: safe situation, low risk situation, medium risk situation, and

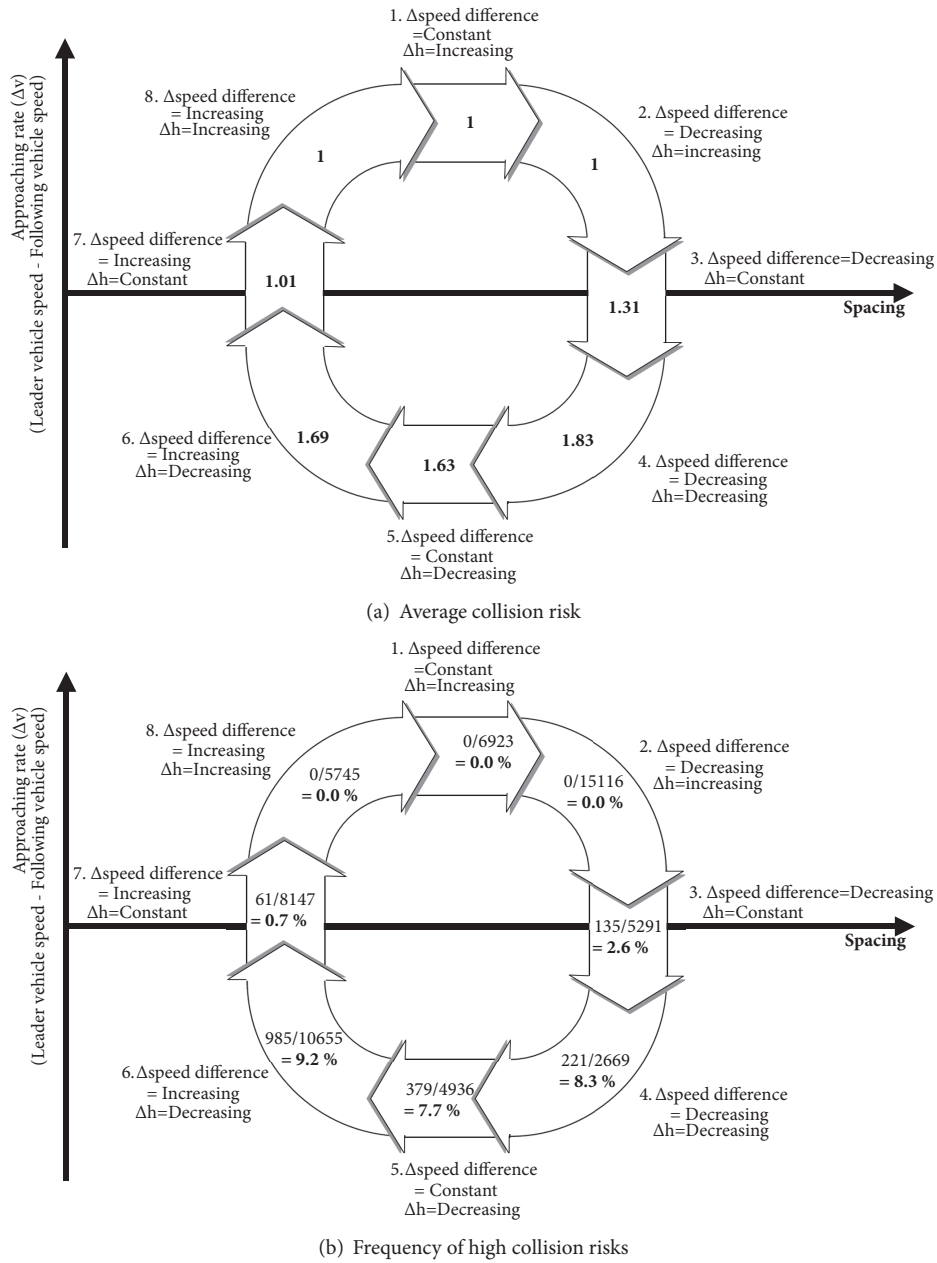


FIGURE 6: The TTC trends on the average collision risk and frequency of high collision risks.

high risk. The four classified situations are graded as 1, 2, 3, and 4, discretionary for the quantitative analysis. The frequency of high collision risks is computed by the same criteria used in average collision risk evaluation, but only the high-risk situations are counted. The number of high-risk situations is divided by the total number of exposure for each classified states.

Figure 6 shows the average collision risk and the frequency of high collision risks of the TTC based on the 143 car-following cases. As depicted in Figures 6(a) and 6(b), it can be seen that the TTCs do not show any common behaviours with the action points of the drivers. The average collision risk estimated by the TTC does not show any variations near the

states 1 and 5, which are the situations when the drivers decide and change the actions of acceleration and deceleration. No specific relationship between the collision risk and driving actions is observed in the trend of collision risk estimated by the TTC.

Similarly, the SHD can evaluate collision risk in more various states compared to the TTC, as shown in Figure 7.

However, the high collision risks estimated by the SHD are concentrated when the subject vehicle is faster than the preceding vehicle. Moreover, the SHD tends to overestimate the collision risk in these situations, such as state 4. In terms of the action point car-following perspective, the estimated collision risk of the SHD is partially matched to the action

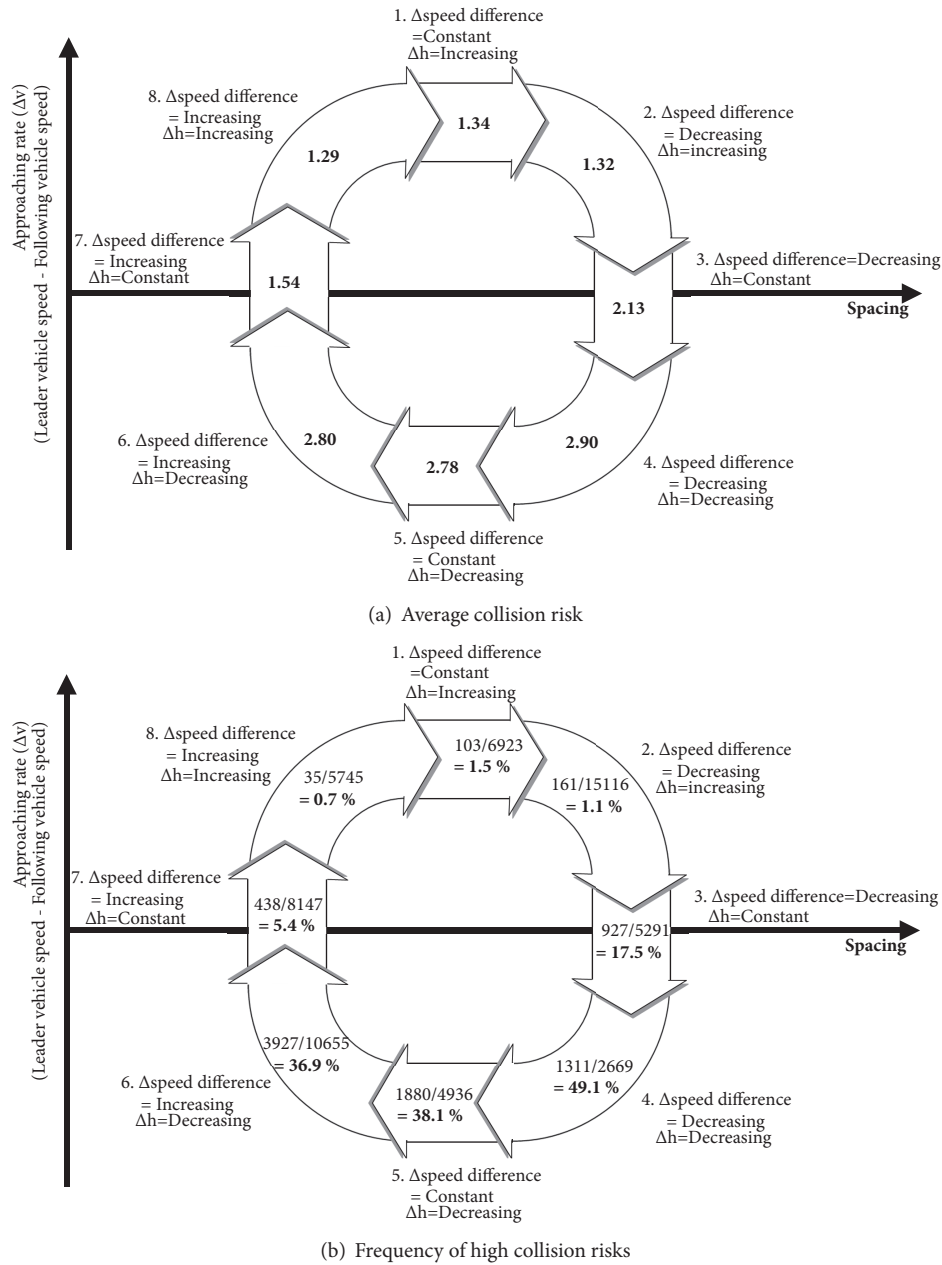


FIGURE 7: The SHD trends on the average collision risk and frequency of high collision risks.

point behaviours of the drivers. In the action point car-following behaviour, the driver decides and changes the actions of acceleration and deceleration near the perception thresholds, which leads to the changes in the collision risks near state 1 and state 5. Near state 5, the SHD shows the similar trend to the driving action of human. When the state is changed from 4 to 5, the SHD value decreases even though the variation is not significantly large. When the state is changed from 5 to 6, the SHD value increases. Near the state 1, SHD shows the dissimilar trend to human behaviour. When the state is changed from 1 to 2, the SHD decreases even though the driver is catching up the speed.

In Figures 8(a) and 8(b), the DSSM can evaluate collision risk from more states compared to TTC and SHD. For both analyses, the maximum values are observed in state 4, while the minimum values are observed in state 8. Near these two states, the average collision risk and frequency of high collision risk show the same increasing and decreasing trends. Given this result, the DSSM is the only SSM, in which the severity grade of the collision risk is divided in balance. Therefore, it can be said that the collision risk by DSSM is well matched to the action point behaviour. Overall, the DSSM continuously increases when the state is changed from 1 to 5. And it continuously decreases when the state is changed from

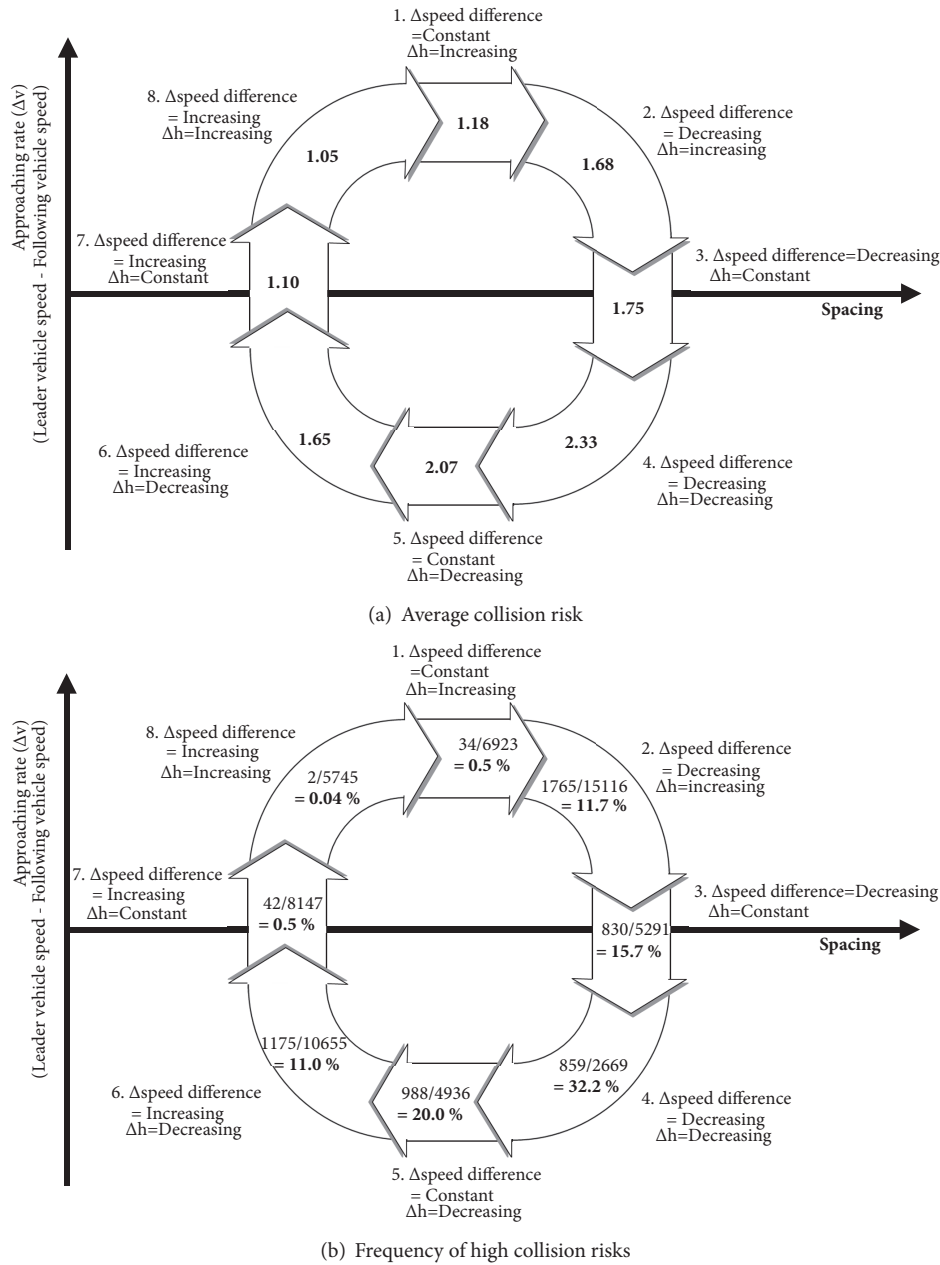


FIGURE 8: The DSSM trends on the average collision risk and frequency of high collision risks.

5 to 1. In detail, near the action points, which are states 1 and 5, the estimated collision risk of DSSM is changed with the similar process of the action point car-following behaviour. After the catch-up action points, which is state 1, the DSSM value rapidly increases. Conversely, near the release action point, which is state 5, the DSSM decreases. Especially, when the state is changed from 5 to 6, more significant decreasing trend of DSSM value is observed compared to that of SHD value due to the release action in state 5. These results coincide with the previous research findings in other car-following models, which is based on the action point driving behaviour [21, 28–32].

4. Comparison Analysis in Speed-Spacing Plane

4.1. Analysis from Asymmetric Behaviour Perspective. The action point model-based analysis shows well how a driver reacts to the external stimuli by focusing on the relationship between the leader and subject vehicle. However, in the spacing and relative speed plane, it still has a limitation to fully describe the human driving behaviour since it does not consider the absolute speed of the subject vehicle. In order to investigate the effect of such property, we analyze the relationship between the collision risk and the asymmetric driving

behaviour. In the asymmetric theory, drivers show different patterns in the acceleration and deceleration phases, and such phenomenon has been observed by several researchers since the 1960's [33–38]. In this theory [24, 39, 40], drivers show two different curves of acceleration curve (A-curve) and deceleration curve (D-curve) with different spacing for the same speed. The A-curve is the boundary curve in the acceleration phase and the D-curve is the boundary curve in the deceleration phase of the car-following situations. In the A-curve, the two consecutive vehicles maintain larger spacing than in the D-curve for the same corresponding speed. The A-curve can be found by connecting the ending points of accelerating actions, and the D-curve can be found by connecting the ending points of decelerating actions. In addition, near the each of the A-curve and D-curve, an acceleration action point line and a deceleration action point line can be observed as well, respectively. The acceleration action point line can be found by connecting the starting points of accelerating actions, and the deceleration action point line can be found by connecting the starting points of decelerating actions.

These accelerating and decelerating actions in the A-curve and D-curve are highly related to the collision risk of the driver. When a driver accelerates to catch up with the leader vehicle's speed during the acceleration process, the driver increases the speed until the collision risk becomes larger than a certain threshold or the desired speed is reached. After that, if the spacing increases and the collision risk drops below certain threshold again, the driver takes acceleration again in order to keep the appropriate spacing. The accelerating actions appear repeatedly to keep the appropriate spacing and collision risk. On the other hand, during deceleration process, the driver reduces the speed until the collision risk is smaller than a certain threshold. After that, if the spacing decreases again and the collision risk is higher than a certain threshold value, the driver decelerates again. The decelerating actions also appear repeatedly in order to keep the appropriate level of collision risk. Based on such logic, a high collision risk would appear near the acceleration and deceleration action point line. Therefore, the estimated collision risk may indicate the timings of the acceleration and deceleration actions.

4.2. TTC in Speed-Spacing Plane. Based on the basic relationship between the collision risk and asymmetric driving behaviour, we analyze the three SSMs in the spacing-speed plane. Figure 9 shows the collision risks estimated by the TTC in the spacing-speed plane. The example case shown in Figure 2 is used in these analyses as well.

In the figure, the blue stars, green stars, yellow circles, and red circles represent the safe situation, low risk situation, medium risk situation, and high risk situation, respectively. The dashed lines represent the virtual deceleration action point line, D-curve, A-curve, and acceleration action point line, respectively, from left to right. The dashed lines shift to right or left depending on the driver's psychology on external stimuli and traffic state.

Figure 9 shows the collision risks estimated by the TTC in the spacing-speed plane. As shown in Figure 9, a variation

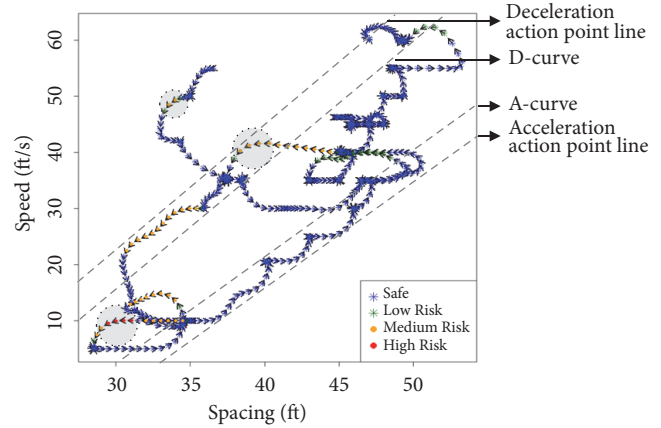


FIGURE 9: Collision risk estimated with the temporal spacing and speed (TTC).

of the collision risks estimated by the TTC is not large as much as the variation of driver's acceleration behaviours. This result shows that TTC is not a sensitive measure to driving actions. Some high and medium collision risk of TTC is only occurred in the deceleration process. Among these high and medium collision risk of TTC, only the three situations, which are marked with black dotted circles in Figure 9, can describe the human driving behaviour in the deceleration process. In these circled areas, it is observed that the collision risk is high until the state of driver reaches deceleration action point line. After that, the risk decreases as the driver reduces the speed overall. In the acceleration process, the high or medium level of collision risks is not observed, and most of the acceleration processes are considered as the safe situation. In the acceleration process, the leader vehicle is generally faster than the subject vehicle since the subject vehicle accelerates after the preceding vehicle accelerates with response-time delay. Therefore, in this process, the TTC does not properly evaluate the collision risk, because the TTC only evaluates the collision risk when the subject vehicle is faster than the preceding vehicle.

4.3. SHD in Speed-Spacing Plane. Figure 10 shows the collision risks estimated by the SHD. Compared to the TTC, the SHD value is more dynamically changed according to the driving action.

The SHD can identify the high collision risk during the acceleration process contrarily to what the TTC can identify only during the deceleration process. The matched results to the driving behaviour during both the acceleration and the deceleration processes are observed and they are marked by the solid and black dotted circles, respectively. In black dotted circled areas, the collision risk is decreased as the driver reduces the speed. After the state of vehicle reaches to D-curve, the driver maintains constant speeds and the SHD value is increased again. In black solid circled areas, the collision risk is increased as the driver increases the speed. After the state of vehicle reaches the A-curve, the driver maintains the constant speed and the collision risk shows the decreasing trend.

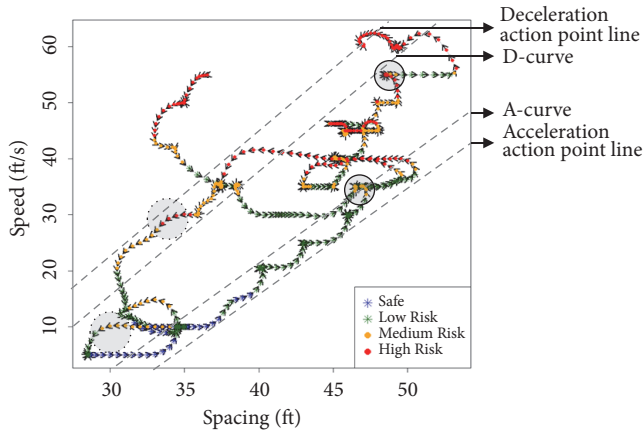


FIGURE 10: Collision risk estimated with the temporal spacing and speed (SHD).

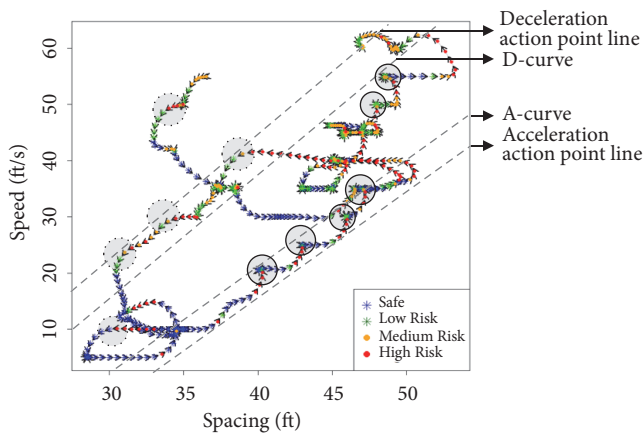


FIGURE 11: Collision risk estimated with the temporal spacing and speed (DSSM).

Even though the collision risks estimated by the SHD show more matched results to the asymmetric driving behaviour, they still show biased results due to several reasons. First, the SHD always considers the deceleration process as more dangerous situation than the acceleration process. The high collision risk is mainly distributed in the deceleration process and the sensitivity of collision risk to driving action is also high in the deceleration process. Second, the SHD is highly affected by the speed of subject vehicle itself. The collision risk estimated by the SHD generally increases as the speed of the subject vehicle increases overall. Due to these influences, the high collision risk is not observed when the speed of the subject vehicle is low, even though the state of the subject vehicle is near the acceleration action point line and deceleration action point line.

4.4. DSSM in Speed-Spacing Plane. Compared to other SSMs, the DSSM shows the most sensitive and well-matched results to the asymmetric driving behaviour, as shown in Figure 11.

The black dotted circles and black solid circles are the representative cases of the matched situations during the

acceleration and the deceleration processes, respectively. In the areas near the black dotted circles in the deceleration process, the high collision risks occur right before the state reaches to the deceleration action point line. The collision risks sharply decrease after the driver starts deceleration action. In the areas near the black solid circles in the acceleration process, the high collision risks occur right before the state of the subject vehicle reaches A-curve. The collision risks decrease right after the state of the subject vehicle reaches the A-curve and as it maintains a constant speed. The collision risks gradually decrease until the state of the subject vehicle reaches to the acceleration action point line.

4.5. Comparison of Average Collision Risk and Frequency of High Collision Risk. Figure 12 compares the average collision risk and the frequency of high collision risk of each SSM. The DSSM well captures the high collision risk particularly in acceleration process compared to other SSMs. Except for the DSSM, the TTC and SHD consider the deceleration process as more dangerous situation than acceleration process. The SHD shows the highest average collision risk in both acceleration process and deceleration process with approximately three or four times higher frequency of high collision risk than the TTC and the DSSM. Considering the slightly low successful alarm ratio of the SHD compared to the DSSM in previous research [15], the SHD has a tendency of overestimating the collision risk.

5. Conclusion

In order to investigate the relationship between collision risk and human driving behaviour, this study analyzes three different SSMs based upon two different car-following theories, including the action point model and asymmetric driving behaviour model. The three SSMs, including the TTC, SHD, and DSSM, show different characteristics and trend in estimating the collision risk. In the analysis with the action-point model, the estimated collision risks of the TTC and SHD only partially match with the pattern of driver's driving behaviour. The high collision risks are concentrated where the subject vehicle is faster than preceding vehicle, so both SSMs overestimate the collision risk particularly in such situations. On the other hand, one could observe that the DSSM shows well-matched results to action point behaviour of the driver. After the catch up action point, the collision risks estimated by the DSSM rapidly increase. Conversely, near the release action point, the DSSM value shows a decreasing trend. In the analysis with asymmetric driving model, the TTC and SHD show biased collision risks in the deceleration process. Especially, the SHD is highly affected by the speed of subject vehicle itself, so the high collision risk is rarely observed when the speed of subject vehicle is low. DSSM equally evaluates the collision risk during acceleration process and deceleration process and it shows well-matched results to acceleration and deceleration actions near acceleration and deceleration action point line.

This study provides ample opportunities to design human-centered services of the FCWS and EBS in two

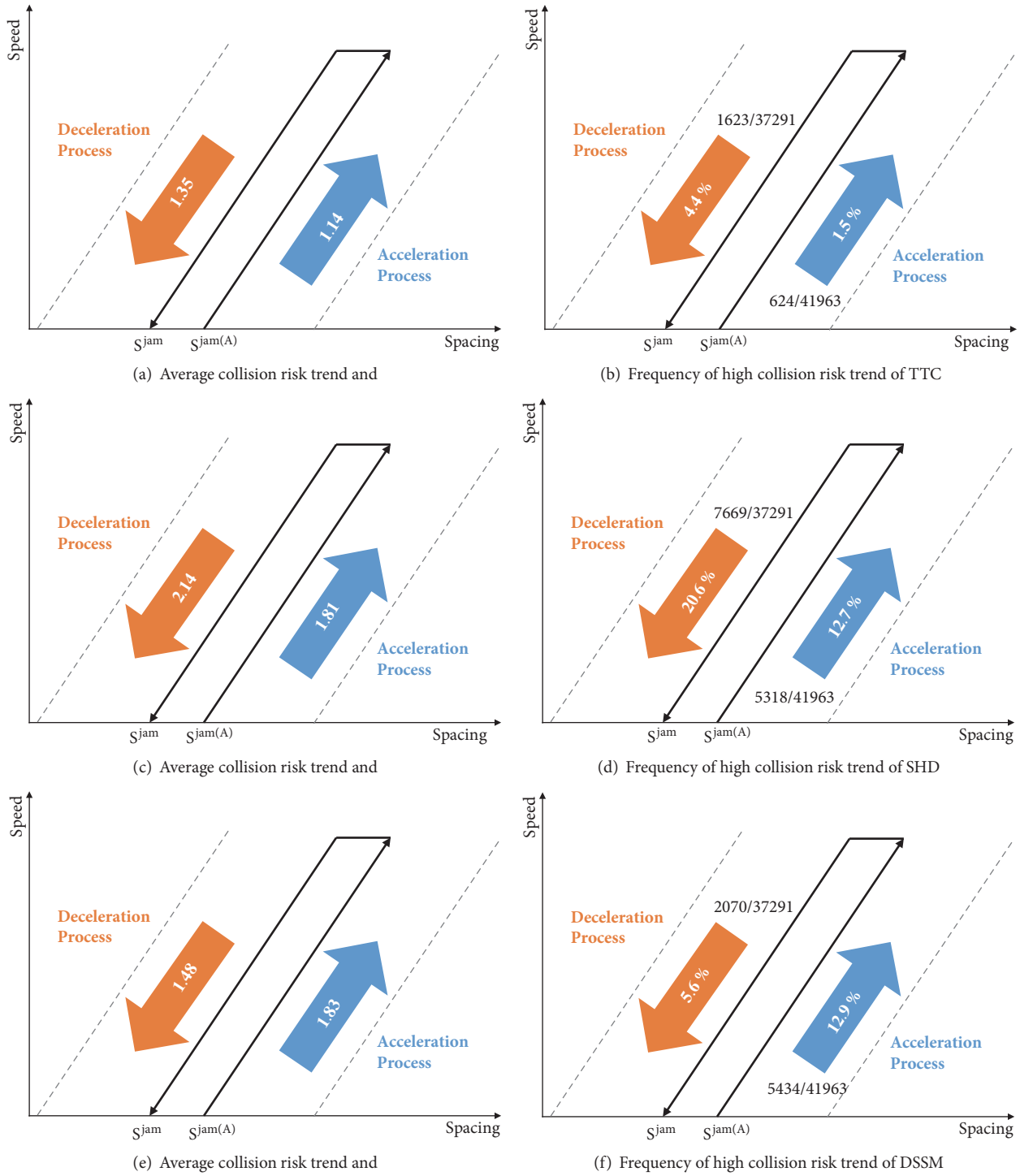


FIGURE 12: Each SSM trends on their average collision risks and frequencies of high collision risks.

aspects. First, it can provide an opportunity for significantly reducing the false-alarm ratio of a collision warning system. The SSMs can estimate a more detailed state of a subject vehicle in terms of the collision risks in various traffic situations. The effect of small changes in the collision risks varied with different driving behaviours can be tracked and analyzed continuously. Based on the research findings of this study,

not only dangerous situations but also the trend of increasing (or decreasing) collision risks can be identified. By providing warnings before collision risk reaches a higher level, safety-related services can significantly improve the accuracy and give enough time for drivers to prepare for a harsh braking. Second, it can render safety-related services more acceptable to drivers. In order to make a collision warning system be

acceptable to human drivers, the judgment on dangerous situations of the system needs to be similar to that of the human drivers. Microscopic analyses on SSMs and driving behaviours would provide the foundation for monitoring the reaction of human drivers to the collision risk. Furthermore, by analyzing the relationship between driving behaviour and collision risk estimated by SSMs, the safety-related services can reflect the different preferences of drivers on the collision risk.

However, this current paper still has a limitation in that the thresholds classifying the risk levels are given based on the empirical understandings with the given data. It is due to that there has not been a previous effort for defining the exact thresholds of the high or low risk so far. In fact, such thresholds for the SSMs may vary depending on the road characteristics like the nature of traffic flow (uninterrupted or interrupted flow) and the free flow speed (or speed limit). The thresholds may vary by different regions or even by different countries. Hence, the results of this current paper shall be revisited later, by considering the variations of the thresholds. Thus, the sensitivity analysis of the thresholds is an essential research topic to be addressed in further studies. Furthermore, the comparative analyses in this paper were done only with the representative SSMs of the perceptual approach (TTC) and kinematic approach (SHD and DSSM). It is suggested also to try other various SSMs while conducting further sensitivity analysis. In addition, the difference among the kinematic approaches like the SHD and DSSM is the selection of the obtainable microscopic variables to be used for the risk calculation, such as the spacing and relative speed, and these variables must be obtainable in real-time. Considering the application of the autonomous vehicles in the near future, in which more detailed information can be obtained in real-time, it is also suggested to develop the existing SSMs further into the more advanced form that can take account into various safety-related variables, such as real-time jerk rate and acceleration.

Data Availability

The data used to support the findings of this study are available from the corresponding author upon request.

Conflicts of Interest

The authors declare that there are no conflicts of interest regarding the publication of this paper.

Acknowledgments

This research was supported by the Ministry of Land, Infrastructure, and Transport (MOLIT, KOREA) [Project ID: 18TLRP-B146748-01-000000, Project Name: Connected and Automated Public Transport Innovation (National R&D Project)] and the Ministry of Trade, Industry, and Energy (MOTIE, KOREA) [Project ID: 10063147, Project Name: Multi-Level Safety System for Intersection Collision Prevention].

References

- [1] D. Lee and H. Yeo, "A study on the rear-end collision warning system by considering different perception-reaction time using multi-layer perceptron neural network," in *Proceedings of the 2015 IEEE Intelligent Vehicles Symposium (IV)*, pp. 24–30, Seoul, South Korea, June 2015.
- [2] J. C. Hayward, "Near-miss determination through use of a scale of danger," *Highway Research Record*, vol. 384, pp. 24–34, 1972.
- [3] R. Kiefer, D. LeBlanc, and C. Flannagan, "Developing an inverse time-to-collision crash alert timing approach based on drivers' last-second braking and steering judgments," *Accident Analysis & Prevention*, vol. 37, no. 2, pp. 295–303, 2005.
- [4] H. C. Chin, S. T. Quek, and R. L. Cheu, "Traffic conflicts in expressway merging," *Journal of Transportation Engineering*, vol. 117, no. 6, pp. 633–643, 1991.
- [5] H.-C. Chin and S.-T. Quek, "Measurement of traffic conflicts," *Safety Science*, vol. 26, no. 3, pp. 169–185, 1997.
- [6] L. Yang, J. H. Yang, E. Feron, and V. Kulkarni, "Development of a performance-based approach for a rear-end collision warning and avoidance system for automobiles," in *Proceedings of the IEEE Intelligent Vehicles Symposium*, pp. 316–321, Columbus, OH, USA, 2003.
- [7] N. Uno, Y. Iida, S. Itsubo, and S. Yasuhara, "A microscopic analysis of traffic conflict caused by lane-changing vehicle at weaving section," in *Proceedings of the 13th Mini-Euro Conference Handling Uncertainty in Transportation Analysis of Traffic and Transportation Systems*, 2002.
- [8] M. Bin, N. Uno, and Y. Iida, "A study of lane-changing behavior model at weaving section considering conflicts," *Journal of the Eastern Asia Society for Transportation Studies*, no. 5, pp. 2039–2052, 2003.
- [9] N. Uno and Y. Iida, "Objective Analysis of Traffic Conflict and Modeling of Vehicular Speed Adjustment at Weaving Section," *Infrastructure Planning Review*, vol. 20, no. 4, pp. 989–996, 2003.
- [10] C. Oh, S. Park, and S. Ritchie, "A method for identifying rear-end collision risks using inductive loop detectors," *Accident Analysis & Prevention*, vol. 38, no. 2, pp. 295–301, 2006.
- [11] C. Oh, J. Oh, and J. Min, "Real-time detection of hazardous traffic events on freeways: Methodology and prototypical implementation," *Transportation Research Record*, no. 2129, pp. 35–44, 2009.
- [12] Y. Kweon, "Development of crash prediction models using real time safety surrogate measures," Tech. Rep. UVACTS-15-0-104, 2008.
- [13] K. Ozbay, H. Yang, B. Bartin, and S. Mudigonda, "Derivation and Validation of New Simulation-Based Surrogate Safety Measure," *Transportation Research Record*, vol. 2083, no. 1, pp. 105–113, 2018.
- [14] F. Saccomanno and F. Cunto, "Comparing safety at signalized intersections and roundabouts using simulated rear-end conflicts," *Transportation Research Record*, vol. 2078, pp. 90–95, 2008.
- [15] S. Tak, S. Kim, and H. Yeo, "Development of a Deceleration-Based Surrogate Safety Measure for Rear-End Collision Risk," *IEEE Transactions on Intelligent Transportation Systems*, vol. 16, no. 5, pp. 2435–2445, 2015.
- [16] F. Muehlfeld, I. Doric, R. Ertlmeier, and T. Brandmeier, "Statistical behavior modeling for driver-adaptive precrash systems," *IEEE Transactions on Intelligent Transportation Systems*, vol. 14, no. 4, pp. 1764–1772, 2013.

- [17] F. Naujoks, A. Kiesel, and A. Neukum, "Cooperative warning systems: The impact of false and unnecessary alarms on drivers compliance," *Accident Analysis Prevention*, vol. 97, Article ID S0001457516303396, pp. 162–175, 2016.
- [18] G. Abe and J. Richardson, "Alarm timing, trust and driver expectation for forward collision warning systems," *Applied Ergonomics*, vol. 37, no. 5, pp. 577–586, 2006.
- [19] D. Lee and H. Yeo, "Real-Time Rear-End Collision-Warning System Using a Multilayer Perceptron Neural Network," *IEEE Transactions on Intelligent Transportation Systems*, vol. 17, no. 11, pp. 3087–3097, 2016.
- [20] A. H. Jamson, F. C. H. Lai, and O. M. J. Carsten, "Potential benefits of an adaptive forward collision warning system," *Transportation Research Part C: Emerging Technologies*, vol. 16, no. 4, pp. 471–484, 2008.
- [21] E. Todorov, *The action point model of the driver-vehicle system*, The Ohio State University, 1963.
- [22] R. M. Michaels, "Perceptual factors in car-following," in *Proceedings of the 2nd ISTTF*, pp. 44–59, London, UK, 1963.
- [23] G. Newell, "A simplified car-following theory: a lower order model," *Transportation Research Part B: Methodological*, vol. 36, no. 3, pp. 195–205, 2002.
- [24] H. Yeo, *Asymmetric microscopic driving behavior theory*, University of California, Berkeley, CA, USA, 2008.
- [25] K. Vogel, "A comparison of headway and time to collision as safety indicators," *Accident Analysis & Prevention*, vol. 35, no. 3, pp. 427–433, 2003.
- [26] Q. Liu, N. Garber, and M. Center, "Identifying the Impact of Truck-Lane Restriction Strategies on Traffic Flow and Safety Using Simulation," Tech. Rep. UVACTS-14-5-103, 2007.
- [27] "NGSIM - Next Generation Simulation," 2006.
- [28] M. Brackstone and M. McDonald, "Car-following: a historical review," *Transportation Research Part F: Traffic Psychology and Behaviour*, vol. 2, no. 4, pp. 181–196, 1999.
- [29] D. Delorme and B. Song, "Human driver model for SmartAHS," *California Partners for Advanced Transit and Highways (PATH)*, 2001.
- [30] S. Panwai and H. Dia, "Comparative evaluation of microscopic car-following behavior," *IEEE Transactions on Intelligent Transportation Systems*, vol. 6, no. 3, pp. 314–325, 2005.
- [31] A. Kesting, M. Treiber, and D. Helbing, "Enhanced intelligent driver model to access the impact of driving strategies on traffic capacity," *Philosophical Transactions of the Royal Society A: Mathematical, Physical & Engineering Sciences*, vol. 368, no. 1928, pp. 4585–4605, 2010.
- [32] M. Treiber and A. Kesting, *Traffic Flow Dynamics: Data, Models and Simulation*, Springer, Berlin, Germany, 2013.
- [33] R. Foote, "Single lane traffic flow control," in *Proceedings of the Proceedings of Second International Symposium on the Theory of Road Traffic Flow*, pp. 84–103, 1965.
- [34] L. Edie, "Discussion of traffic stream measurements and definitions," in *Proceedings of the Proceedings of Second International Symposium on the Theory of Road Traffic Flow*, pp. 139–154, 1965.
- [35] T. Forbes, "Human factor considerations in traffic flow theory," *Highway Research Record*, vol. 15, pp. 60–66, 1963.
- [36] G. F. Newell, "Theories of instability in dense highway traffic," *Journal of the Operations Research Society of Japan*, vol. 5, pp. 9–54, 1965.
- [37] C. F. Daganzo, M. J. Cassidy, and R. L. Bertini, "Possible explanations of phase transitions in highway traffic," *Transportation Research Part A: Policy and Practice*, vol. 33, no. 5, pp. 365–379, 1999.
- [38] H. M. Zhang, "A mathematical theory of traffic hysteresis," *Transportation Research Part B: Methodological*, vol. 33B, no. 1, pp. 1–23, 1999.
- [39] H. Yeo and A. Skabardonis, "Microscopic fundamental relationships between vehicle speed and spacing in view of asymmetric traffic theory," in *Proceedings of the 14th International IEEE Conference on Intelligent Transportation Systems (ITSC)*, pp. 1410–1414, October 2011.
- [40] J. Suh, H. Yeo, and A. Skabardonis, "A Study on the Wave Development and Evolution Characteristics of Stop-and-Go Traffic," in *Proceedings of the Transportation Research Board 91st Annual Meeting*, 2012.

Research Article

An Earlier Predictive Rollover Index Designed for Bus Rollover Detection and Prevention

Shun Tian ¹, Lang Wei ¹, Chris Schwarz,² WenCai Zhou ¹,
Yuan Jiao,³ and YanQin Chen⁴

¹School of Automobile, Chang'an University, Xi'an 710064, China

²National Advanced Driving Simulator, University of Iowa, Iowa City 52242, USA

³School of Construction Machinery, Chang'an University, Xi'an 710064, China

⁴Department of Mechanical Engineering, Inha University, Incheon 2212, Republic of Korea

Correspondence should be addressed to Lang Wei; qch_1@chd.edu.cn

Received 29 July 2018; Accepted 11 October 2018; Published 1 November 2018

Guest Editor: Petru Andrei

Copyright © 2018 Shun Tian et al. This is an open access article distributed under the Creative Commons Attribution License, which permits unrestricted use, distribution, and reproduction in any medium, provided the original work is properly cited.

As vehicle rollovers annually cause a great deal of traffic-related deaths, an increasing number of vehicles are being equipped with rollover prevention systems with the aim of avoiding such accidents. To improve the functionality of active rollover prevention systems, this study provided a potential enhanced method with the intention to predict the tendency of the lateral load transfer ratio (LTR), which is the most common rollover index. This will help provide a certain amount of lead time for the control system to respond more effectively. Before the prediction process, an estimation equation was proposed to better estimate the LTR; the equation was validated using Simulink and TruckSim. Further, to eliminate the influence of drawbacks and make this method practical, a buffer operator was added. Simulation results showed that grey LTR (GLTR) was able to roundly predict the future trend of the LTR based on current and previous data. Under the tests of "Sine with Dwell" (Sindwell) and double lane change (DLC), the GLTR could provide the control system with sufficient time beforehand. Additionally, to further examine the performance of the GLTR, a differential system model was adopted to verify its effectiveness. Through the Sindwell maneuver, it was demonstrated that the GLTR index could improve the performance of the rollover prevention systems by achieving the expected response.

1. Introduction

Among traffic issues, bus rollover is a huge problem for bus manufacturing enterprises and traffic administration. To solve this problem, researchers and engineers have developed many kinds of rollover prevention systems [1]. However, once the phase of the impending rollover begins, there is not enough time left for the actuators to act accurately, especially during extremely dangerous situations [2]. Therefore, being able to predict the rollover tendency beforehand and to produce a suitable compensation time are essential for preventing bus rollover situations.

Currently, the load transfer ratio (LTR) is a widely used reference parameter for rollover detection [3], having been used as the rollover index for antirollover bars [4] and differential braking systems [5]. Commonly, a rollover prevention system initiates the actuators once the LTR exceeds a certain

threshold. If an algorithm could predict the LTR, then the lead time could increase the gap between the predicted LTR and the actual LTR. As a result, there would be enough time for the actuator to initiate an effective countermeasure, therefore increasing its effectiveness.

There are many kinds of prediction methods used for different purposes [6, 7]. Deep learning methods are commonly used prediction tools, which have been used among many fields including car risk prediction [8]. However, LTR prediction is a real-time process; only the newly transitory acquired data can be used. Therefore, since LTR prediction is a real-time process, a potential prediction algorithm should have the following characteristics: a small sample size, fast computation, and small internal storage requirements. One suitable method is the grey model, coined by Deng in the 1980s [9]. This model is good at solving uncertainty problems with small samples and poor information. Vehicle motion is

a rapid course; therefore, old data is not useful for the real prediction and has a side effect on the results because the data is not new enough. Hence, we developed a grey-model-based prediction method to conduct LTR prediction to form an early rollover index. The grey model has achieved great success in many fields and has been used in offline prediction. Using fatal crash data from the United Kingdom, Mao et al. [10] applied the grey model to future risk estimation and found that the predicted value approached the actual value. The grey model was applied to predict the vehicle's wheel slip, and then the predicted slip was transferred to a sliding mode controller, which strengthened the controller's robustness [11]. The grey model has also been used to predict the lateral distance between approaching vehicles to provide drivers with extra time to react to an impending collision [12]. In terms of real-time LTR simulation, Chou et al. [13] combined a grey model and a rollover index to detect the rollover of a 14-degree-of-freedom tractor-trailer. The results showed that the grey rollover index achieved an earlier detection of the rollover threat than the rollover index alone; furthermore, the lead time was sufficient for the actuator to be involved. However, the vehicle model they used was an ideal Simulink model, which is largely different from a real bus, and its LTR estimation did not match well with the TruckSim LTR. In this study, a more accurate estimation model was used, and the outputs from TruckSim were directly adopted. In addition, to mitigate the LTR's shock data, a buffer operator was employed to ensure the effectiveness of the grey LTR (GLTR) throughout a wider speed range. Furthermore, a rollover prevention system model was built to examine the function of the GLTR.

The main contributions of this paper are the following:

- (1) A predictive LTR, which can be regarded as an earlier rollover detection index, was introduced to achieve rollover prediction.
- (2) The GLTR was effective at making predictions during two standard handling tests, "Sine with Dwell" (Sindwell) and double lane change (DLC), proving that GLTR can cope with different kinds of lateral motions.
- (3) A considerable lead time was generated to increase the working time available for initiating a rollover prevention action.
- (4) GLTR index was brought into rollover prevention. The effectiveness in reducing the rollover risks was further verified via TruckSim-Simulink cosimulation by building a differential braking system.

The rest of the paper is organized as follows: Section 2 presents the bus rollover model, tier model, and its LTR estimation. Section 3 introduces the LTR prediction methodology, including the grey model (first-order one variable) known as GM(1, 1), as well as the buffer operator. Section 4 presents the simulation results of the LTR prediction. Section 5 offers a further simulation study, which fused the GLTR with a differential-based braking system. Finally, Section 6 offers our conclusions.

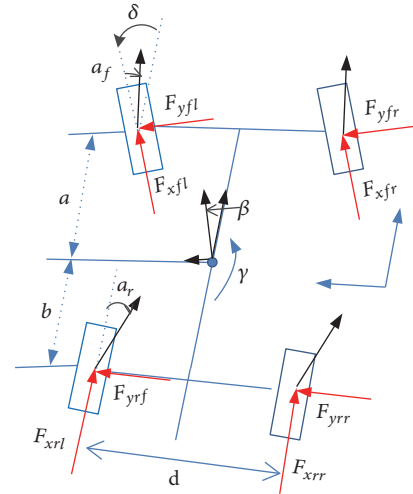


FIGURE 1: Bus rollover dynamic model.

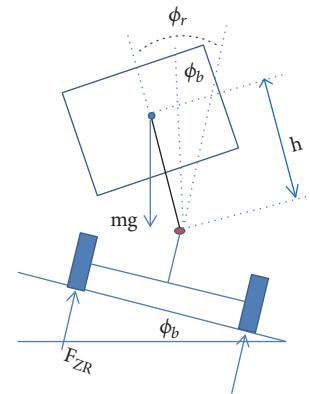


FIGURE 2: Bus roll dynamics.

2. Bus Dynamic Model

2.1. LTR Estimation. It is not easy to detect the real force acting on tires since the necessary sensors are extremely expensive. Therefore, a bus rollover dynamic model was constructed to establish a suitable LTR estimation equation.

Figure 1 illustrates the lateral dynamics of a bus. The diagram includes the bus yaw angle direction and yaw rate, velocity, and slip angle. Figure 2 shows the roll dynamics of the bus. The effect of the bus's unsprung mass on the roll dynamics was neglected. The road bank angle and the bus roll angle and distance associated with the roll center are also indicated in this diagram.

In Figures 1 and 2, d is the bus width; h is the vertical distance from the sprung mass CG to the assumed roll axis; $\dot{\beta}$ is the yaw rate; β is the bus's slip angle; δ is the steering wheel angle; $F_{xfl, xfr}$ are the front left and the front right longitudinal forces; $F_{yfl, yfr}$ are the front left and the front right lateral forces; a_f and a_r are the front tire's slip angle and rear tire's angle; and finally, ϕ_b and ϕ_r are the road bank angle and the vehicle roll angle, respectively.

The bus lateral dynamics can be written as

$$\begin{aligned} \sum F_y &= mA_y \\ &= F_{yrl} + F_{yrr} + (F_{yfl} + F_{yfr}) \cdot \cos \delta \\ &\quad + (F_{xfl} + F_{xfr}) \cdot \sin \delta \end{aligned} \quad (1)$$

and

$$\begin{aligned} (I_{xx} + mh^2) \cdot (\ddot{\phi}_r - \ddot{\phi}_b) &= (F_{zL} - F_{zR}) \cdot \frac{d}{2} \\ &+ \sum F_y \cdot h \cdot \cos \phi_r + mgh \cdot \sin \phi_r \cdot \cos \phi_b \\ &- mgh \cdot \cos \phi_r \cdot \sin \phi_b \\ &+ [(I_{yy} - I_{zz}) - mh^2] \cdot \gamma^2 \cdot \sin(\phi_r - \phi_b) \cdot \cos(\phi_r - \phi_b) \end{aligned} \quad (2)$$

where $A_y = \dot{v} + ru - g \cdot \sin \phi_b + h\dot{\phi}_r^2 \cdot \sin \phi_r + h\gamma^2 \cdot \sin \phi_r - h\ddot{\phi}_r \cdot \cos \phi_r$; A_y is the lateral acceleration; $I_{xx,yy,zz}$ are the moments of inertia about the respective axes; u is the bus's longitudinal velocity; v is bus's lateral velocity.

The vertical dynamics of the sprung mass can be shown as

$$\begin{aligned} m\ddot{z} &= m \cdot (\dot{\phi}_r^2 h \cdot \cos \phi_r + \ddot{\phi}_r h \sin \phi_r) \\ &= (F_{zL} + F_{zR}) - mg \cdot \cos \phi_r \end{aligned} \quad (3)$$

where m is the sprung mass; A_y is the lateral acceleration.

If the road bank angle is zero, (1)–(3) can be expressed as follows:

$$\sum F_y = m \cdot (\dot{v} + ru + h\gamma^2 \cdot \sin \phi_r + h\dot{\phi}_r^2 \cdot \sin \phi_r - h\ddot{\phi}_r \cdot \cos \phi_r) \quad (4)$$

$$\begin{aligned} (I_{xx} + mh^2) \cdot \ddot{\phi}_r &= (F_{zL} - F_{zR}) \cdot \frac{d}{2} + \dots \sum F_y \cdot h \cdot \cos \phi_r \\ &+ mgh \cdot \sin \phi_r + [(I_{yy} - I_{zz}) - mh^2] \cdot \gamma^2 \cdot \sin \phi_r \cdot \cos \phi_r \end{aligned} \quad (5)$$

$$m\ddot{z} = m \cdot (\dot{\phi}_r^2 h \cdot \cos \phi_r + \ddot{\phi}_r h \sin \phi_r) = (F_{zL} + F_{zR}) - mg \quad (6)$$

The LTR, which estimates the difference in the tire's normal forces acting on each side of the bus, is a commonly used load transfer metric [14]. Equation (7) gives the expression of the LTR:

$$LTR = \left| \frac{F_{zR} - F_{zL}}{F_{zR} + F_{zL}} \right| \quad (7)$$

where F_{zR} and F_{zL} represent the vertical force of the right tire and the left tire, respectively, and $F_{zR} + F_{zL} = mg$. The LTR varies from 0 to 1, where 1 represents one side of bus tires losing contact with the ground.

Solving the simultaneous equations, assuming that $\ddot{\phi}_r$ and $\dot{\phi}_r$ are zero and substituting them into (7), the following LTR expression is obtained, as shown below:

$$\begin{aligned} LTR &= \left| \frac{2}{d} \cdot \frac{h \cdot (\cos \phi_r \cdot (\dot{v} + \gamma u) + h\gamma^2 \cdot \sin \phi_r + g \cdot \sin \phi_r)}{g} \right| \end{aligned} \quad (8)$$

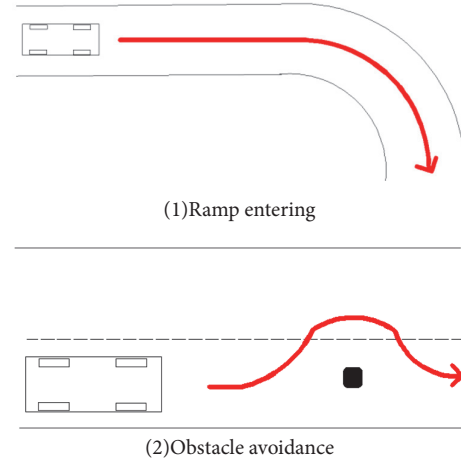


FIGURE 3: Bus rollover conditions.

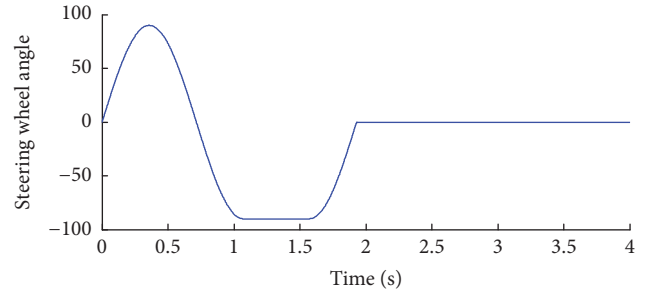


FIGURE 4: Steering wheel angle with 89 km/h Sindwell at 90° steering amplitude.

Further assumptions were adopted as follows: $\cos^2 \phi_r \approx 1$, $h\gamma^2 \approx 0$, and $\dot{v} + \gamma u = A_y \cdot \cos \phi_r$. Therefore, the final expression of the estimated LTR is

$$LTR_e = \left| \frac{2h}{dg} [A_y + g \cdot \sin \phi_r] \right|. \quad (9)$$

The results using (9) were abbreviated as Est-LTR. A built-in bus model provided by TruckSim can output each tire's vertical force; thus, the real LTR value can be calculated by (7) with these tire forces. The calculated result of (7) was referred to as the actual LTR, abbreviated as Act-LTR.

Some parameters of the bus are listed in Table 1.

To verify the effectiveness of (9), simulation works were carried out by comparing the estimated LTR (Est-LTR) and the actual LTR (Act-LTR) models. The road adhesion coefficient was set as 0.85, ensuring the lateral risk of rollover, but not of lateral slip. Figure 3 shows the common situations in which the rollover happens easily. In order to simulate these two conditions, we used the more complex maneuvers of Sindwell and DLC, which are often utilized for vehicles' lateral performance tests, to reproduce the rollover situations.

Figure 4 shows the steering angle of the 89-km/h Sindwell test where the steering amplitude was 90°. Results of the comparison under this test are demonstrated in Figure 5, which indicate that the trends of the two curves matched well. Figure 6 illustrates the steering wheel angle of the DLC

TABLE I: Some parameters of the bus in TruckSim.

Sprung mass (m/kg)	7690
Bus width (d/m)	1.93
Distance from the sprung mass CG to the assumed roll axis (h/Vertical/m)	0.563

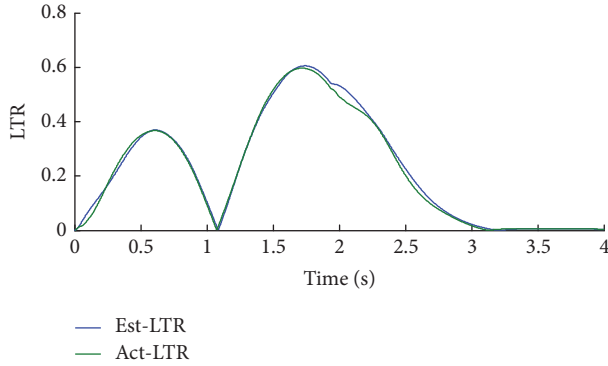


FIGURE 5: Estimated versus TruckSim load transfer ratio (LTR) with 89 km/h Sindwell at 90° steering amplitude.

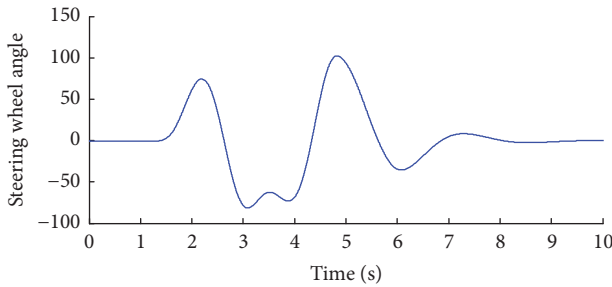


FIGURE 6: Steering wheel angle with 105 km/h double lane change (DLC).

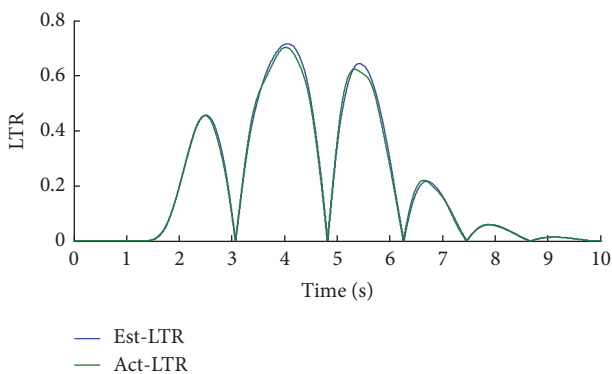


FIGURE 7: Estimated versus TruckSim LTR with 105 km/h DLC.

test, which was conducted according to ISO 3888-2:2002 [15]. Figure 7 demonstrates the comparison of the Est-LTR and Act-LTR under a test of a 105-km/h DLC; the figure indicates a slight lead time, with the Est-LTR reaching 0.7 at 3.841 s and Act-LTR reaching at 3.852 s. Hence, the estimation equation was valid as the reference formulation for a rollover

prevention system. As a result, in the following sections, we considered the Est-LTR as the actual LTR.

2.2. Tire Model. To calculate the tire forces, this study utilized the Dugoff tire model, which is a nonlinear tire model. Compared with some empirical tire models, such as the “magic formula” (MF) model, which require a large number of tire-specific parameters that are probably unknown, the Dugoff model, by simple equations, can acquire the longitudinal and lateral tire-road forces under different wheel slip conditions [16].

Lateral and longitudinal tire-road forces can be defined as

$$\begin{aligned}
 F_{yi} &= \frac{C_{yi} \tan \alpha_i}{1 - \lambda_i} f(S) \\
 F_{xi} &= \frac{C_{xi} \lambda_i}{1 - \lambda_i} f(S) \\
 S &= \frac{\mu F_{zi}}{2 \sqrt{C_{xi}^2 \lambda_i^2 + C_{yi}^2 \tan^2 \alpha_i}} (1 - \lambda_i^2) \\
 f(S) &= \begin{cases} 1 & S > 1 \\ S(2 - S) & S < 1. \end{cases}
 \end{aligned} \tag{10}$$

C_{xi} and C_{yi} are the longitudinal and lateral corner stiffness of the tire, μ is the road adhesion coefficient maximum friction coefficient, λ_i is the slip ratio, and α_i is the slip angle of the wheels. In this study, the value of μ is 0.85; therefore, the bus lateral motion risk is the rollover rather than sideslip. The longitudinal wheel slip ratio λ_i can be obtained from TruckSim.

3. LTR Prediction Methodology

3.1. Grey Model. Among the grey model types, the one suitable for LTR prediction is the GM(1, 1) type, meaning “first-order one variable” [9]. This model is a time series forecasting model. The differential equations of the GM(1, 1) model are renewed as data becomes available to the prediction.

The grey prediction model’s advantage is that just a few discrete data are necessary to characterize an unknown system. The GM(1, 1) steps are as follows [17]:

(1) Sort the initial series of $X(0)$ as $X^{(0)} = (X^{(0)}(1), X^{(0)}(2), X^{(0)}(3), \dots, X^{(0)}(n))$. $X(0)$ is the series of LTR values that can be obtained by the tapped delay block in Simulink. In this study, we set n as equal to 10.

(2) Generate the first-order accumulated generating operation (1-AGO) sequence. The general form of $X^{(1)}$ is

$X^{(1)}(1), X^{(1)}(2), X^{(1)}(3), \dots, X^{(1)}(n)$ and the definition of 1-AGO of $X^{(0)}$ is

$$X^{(1)}(k) = \sum_{i=1}^k X^{(0)}(i) = X^{(1)}(k-1) + X^{(0)}(k). \quad (11)$$

(3) Set the first-order original differential equation of $X(1)$. Suppose $X(1)$ meets the equation below:

$$\frac{dX^{(1)}}{dt} + aX^{(1)} = b \quad (12)$$

This is the basic form of GM(1, 1), where variable a and variable b are coefficients. Define variable $\hat{a} = [a, b]^T$.

Its difference equation is

$$X^{(0)}(k) + aZ^{(1)}(k) = b \quad k = 2, 3, \dots, n. \quad (13)$$

$Z^{(1)}(k)$ is called the background value, and its equation is $Z^1(k) = \alpha X^1(k-1) + (1-\alpha)X^1(k)$. α is often set to 0.5. Therefore, according to the roots of this differential equation, the particular solution of (10) can be described as

$$\widehat{X}^{(0)}(k) = \left(X^{(0)}(1) - \frac{b}{a} \right) e^{-ak} + \frac{b}{a} \quad (14)$$

where $\widehat{X}^{(0)}(k)$ is the predictive value of the series.

(4) Use the least square to obtain parameters a and b . Equation (15) can be written as

$$X^{(0)}(k+1) = a \left[-\frac{1}{2(X^{(1)}(k+1) + X^{(1)}(k))} \right] + b, \quad k \geq n \quad (15)$$

$$\begin{bmatrix} a \\ b \end{bmatrix} = (B^T B)^{-1} B^T Y_n,$$

where

$$B = \begin{bmatrix} -(X^{(1)}(1) + X^{(1)}(2)) \\ -(X^{(1)}(2) + X^{(1)}(3)) \\ \dots \\ -(X^{(1)}(n-1) + X^{(1)}(n)) \end{bmatrix} \quad (16)$$

and

$$Y_n = (X^{(0)}(2), X^{(0)}(3), \dots, X^{(0)}(n)) \quad (17)$$

(5) Estimate the AGO value $X^1(1)$ and insert a and b into (8) in order to obtain the particular solution of the differential equation.

As a result, the recovery of the predictive value can be acquired by the following equation:

$$\widehat{X}^{(0)}(k) = \widehat{X}^{(1)}(k) - \sum_{i=1}^{k-1} \widehat{X}^{(0)}(i) \quad (18)$$

3.2. Buffer Operator. During some severe handling tests, the LTR value changes rapidly. This results in the predictive values growing fast and causing unintended local peaks in the prediction curve. For this reason, it is necessary to mitigate the growth trend among the time sequence to obtain smooth predictive curves.

$X(0)$ is the delayed LTR data series, D is the grey buffer operator applied to $X(0)$, and $XD = (X(1)d_1, X(2)d_2, \dots, X(n)d_n)$ is the sequence after the function of the operator D on X . D is called the sequence operator and XD is the first-order operator acting sequences $D = (d_1, d_2, \dots, d_n)$.

Basic knowledge about the weakening buffer operator: when D meets the three conditions below, D can be called a weakening buffer operator [18]; otherwise, it cannot be:

(a) If X is a monotonic increasing series:

$$B \text{ is a weakening buffer operator} \iff X(k) \leq X(k)d_k$$

(b) If X is a monotonic decreasing series:

$$D \text{ is a weakening buffer operator} \iff X(k) \geq X(k)d_k$$

(c) If X is a vibrational series:

$$\min_{1 \leq k \leq n} \{x(k)\} \leq \min_{1 \leq k \leq n} \{x(k)d_k\}$$

$$\text{and } \max_{1 \leq k \leq n} \{x(k)\} \geq \max_{1 \leq k \leq n} \{x(k)d_k\} \quad (19)$$

D is a weakening buffer operator.

In this study, a buffer operator was utilized as below:

$X(k)D = (X(n))\rho(X(k))(1-\rho), k = 1, 2, 3, \dots, n$; D is a buffer operator and ρ is the weight of $X(n)$. In this paper, the prediction results could reach a balance between the ideal lead time and the smoothness of the prediction curve when the value of the weight variable ρ was 0.8.

3.3. Real-Time LTR Prediction. The simulation works of LTR prediction were implemented in the TruckSim and Simulink co-atmosphere. The TruckSim software can provide a built-in bus model with dynamic outputs that are very close to the filtered data acquired from a real running bus. Figure 8 shows the LTR prediction process using the grey model, which is an open loop. The lateral acceleration and roll angles $-A_y$ and ϕ_r were exported in real time from TruckSim and then utilized by the LTR equation to obtain an estimated LTR. The tapped delay block was utilized to delay and save the LTR values of a continuous time period, and the LTR series was sent to the next process. At first, 10 continuous data were acquired in real time. To avoid the results being infinity or not being a number, we set the initial LTR data as 0.01. We used a heuristic method to find that 10 was a suitable number. If n is over 10, the series contains too much old information which will have a side effect on the prediction result; if n is less than 10, the number is not enough to give a reasonable prediction result. Before the grey model process, the buffer operator was used on $(X^{(0)}(1), X^{(0)}(2), \dots, X^{(0)}(n))$

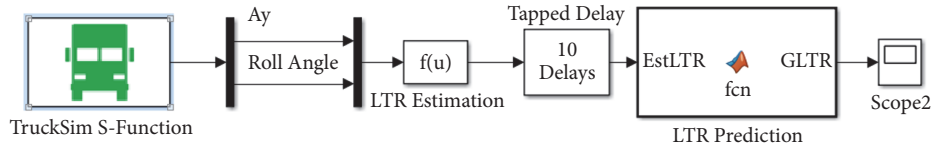


FIGURE 8: LTR prediction process.

and the buffered sequence $D*(X^{(0)}(1), X^{(0)}(2), \dots, X^{(0)}(n))$ was generated. On the basis of the new sequence, the five steps of GM(1,1) were implemented to get the predicted series $(\hat{X}^{(0)}(1), \hat{X}^{(0)}(2), \dots, \hat{X}^{(0)}(n), \dots, \hat{X}^{(0)}(n+f))$, and $\hat{X}^{(0)}(n+f)$ is the predicted LTR value. During the predicted sequence, the preferred lead time is $f*Ts$, where f and Ts represent the forward steps and the sample interval separately. Hence, if it is assumed that Ts is 0.02 s and f is 10, then the preferred lead time is 0.2 s. After the grey model process, the future LTR was obtained and stood as the reference value of earlier rollover detection. When a processing cycle ends, the old data are released, and a new cycle begins. The predicted LTR value produced by the grey model is called the GLTR.

4. LTR Prediction Results

To examine how long the lead time can be generated by the GLTR index, some comparison simulations are reported in this section. Under the cosimulation atmosphere, high-risk rollover maneuvers were carried out to examine the different performances between the GLTR and LTR. The chosen tests were the Sindwell and DLC maneuvers. Sindwell is a typical maneuver for testing a vehicle's lateral performance, which was established by the National Highway Traffic Safety Administration (NHTSA). Concurrently, the double lane change maneuver has been adopted by many vehicle companies as another typical lateral procedure.

In this part, the forward prediction steps were all 10, and the interval time was 0.02 s. As a result, the corresponding preferred lead time was 0.2 s.

4.1. Limiting Factor of GM(1,1). This part discusses the LTR prediction results without the buffer operator process. The prediction results for more complex handling tests such as the DLC and Sindwell tests proved that GM(1,1) had a severe limitation. The drawback was that if the predicted LTR was saturated by the physical threshold, the algorithm may generate a wrong warning or activate the control system, even at a safe driving speed.

To demonstrate this issue, a typical example of the 85-km/h DLC test is presented in Figure 9. During this maneuver, the LTR threshold we set for rollover prevention was 0.7. Nevertheless, the actual LTR was about 0.6, meaning that there was no actual rollover risk. Under this practical circumstance, there is no need to initiate the rollover prevention systems at this relatively safe driving speed. However, the peak points of the prediction curves were (3.82, 0.985) and (5.86, 1.031), which were all above the threshold. Due to the peak point being over 0.7, the prediction curve will lead to the unnecessary initiation of the prevention system.

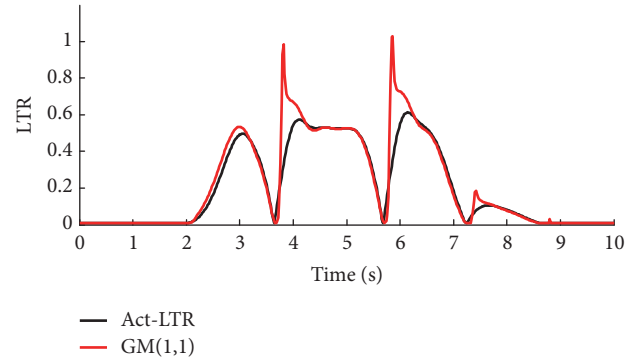


FIGURE 9: Prediction results in 85-km/h DLC using GM(1,1).

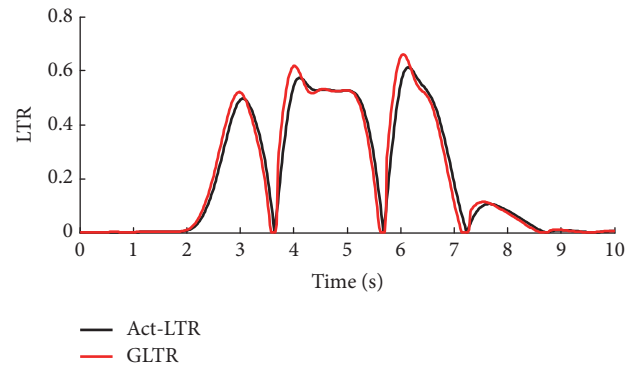


FIGURE 10: Prediction result for 85-km/h DLC using the grey LTR (GLTR).

As a result, particularly at a lesser high speed, the use of basic GM(1,1) in the LTR prediction has limiting factors in serious rollover risk conditions where these prediction mutations will cause the unintended initiation of the rollover prevention system. This limiting factor prevents the grey model from extending its application to the entire speed range.

To overcome this issue, first, the trend development in the old data series needed to be reduced. As shown in Figure 10, we used a buffer to shrink the data tendency before we applied GM(1,1) to the real-time data series. Therefore, after combining GM(1,1) with the proposed buffer, the GLTR algorithm was formed.

Figure 10 displays the effectiveness of the GLTR in the 85-km/h DLC test. Compared with Figure 9, the weakening effect was obvious, causing the peak position to reduce from (5.86, 1.031) to (6.04, 0.661), which was very close to the peak position (6.14, 0.623) of the Est-LTR. As a result, after the

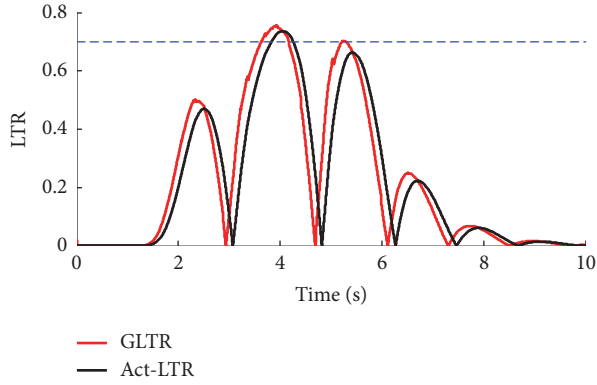


FIGURE 11: Prediction results for the 105-km/h DLC test.

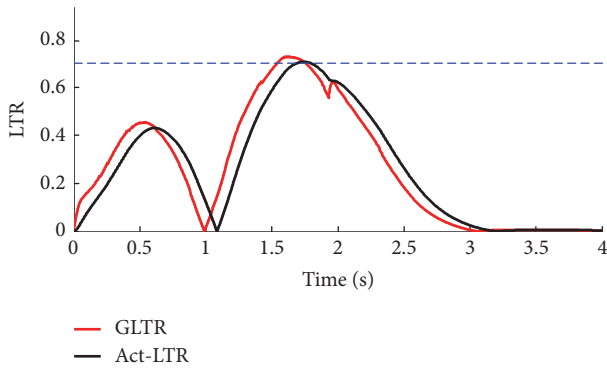


FIGURE 12: Prediction results for the 89-km/h Sindwell test.

TABLE 2: Prediction of GLTR efficacy.

Tests	T1	T1'	$\Delta T1$
A. 105 km/h DLC	3.841 s	3.634 s	0.207 s
B. 89 km/h Sindwell	1.698 s	1.521 s	0.177 s

addition of a buffer operator, the GLTR can overcome the limiting factor of GM(1, 1) by giving a reasonable prediction performance at a secondary high speed for rollover-risk maneuvers.

4.2. Prediction Results of the GLTR. In order to verify the effectiveness of the GLTR for the target lead time, 105-km/h DLC and 89-km/h Sindwell simulation tests were conducted using the GLTR index. The prediction results of these two maneuvers are shown in Figures 11 and 12. T1 and T1' are the time points at which the Est-LTR and the GLTR reach the threshold. Table 2 provides a detailed description of the prediction results for these two maneuvers where the lead times were substantial. During the 105-km/h DLC, with the rollover threshold set as 0.7, the lead time was 0.207 s. Concurrently, during the 89-km/h Sindwell, the lead time was 0.177 s.

Therefore, after applying the GLTR index, with the sufficient lead time, the activation command could be triggered in advance about 0.2 s. GLTR performed better than GM(1, 1) in LTR prediction by acquiring enough lead time and reducing the prediction crests. Furthermore, the new threshold signal

can be useful for additional warning systems or differential-based systems, which will highly reduce the rollover risks.

To further illustrate the efficacy of the GLTR, the results were compared with other works. We still use a 89-km/h Sindwell maneuver as an example. In [19], a predictive LTR index PLTR was introduced. Equation (20) is the basic expression for the PLTR. In the test, future time Δt is 0.2 s, corresponding to the preferred lead time in this study.

$$PLTR_{t_0}(\Delta t) = LTR(t_0) + \dot{LTR}(t_0) \cdot \Delta t \quad (20)$$

The lead time of PLTR was 0.163s, which is less than 0.177s (using GLTR), proving GLTR's efficacy.

5. Further Verification

In addition, to further examine the actual effectiveness of this new rollover index, a Simulink model (an active differential braking system) was added to function as the rollover prevention system. GLTR works as the threshold of the rollover prevention action. Figure 13 shows the control structure of the differential braking system. Once the system detects that the GLTR has exceeded the threshold, the actuator will begin to provide differential braking forces as the yawing moment intervention. F_{flb} , F_{frb} are the front left and front right braking forces. F_{rlb} , F_{rrb} are the rear left and rear right braking forces. Once GLTR is over 0.7, the antirollover countermeasure begins by adding an additional yawing moment.

A 2-DOF vehicle model, which is the so-called "bicycle model", was used as the reference model.

Based on the 2-DOF model and Formula (10), the reference yawing moment can be calculated as below:

$$\sum M_{zr} = aF_{y1} - bF_{y2} = aC_{y1}\alpha_1 - bC_{y2}\alpha_2 \quad (21)$$

Therefore, the additional moment can be obtained by the equation as below:

$$\Delta M_z = M_z - M_{zr} \quad (22)$$

The differential braking is achieved by establishing a PID controller. A proportional-integral-derivative controller (PID controller) is a control loop feedback mechanism widely used in industrial control systems and a variety of other applications requiring continuously modulated control [20]. The distinguishing feature of the PID controller is the ability to use the three control terms of the proportional, integral, and derivative influence on the controller output to apply accurate and optimal control.

The overall control function can be expressed mathematically as

$$U(s) = K_p \left(1 + \frac{1}{k_i \cdot s} + K_d \cdot s \right) \cdot E(s) \quad (23)$$

where

K_p is the proportional gain, a tuning parameter,

K_i is the integral gain, a tuning parameter,

K_d is the derivative gain, a tuning parameter.

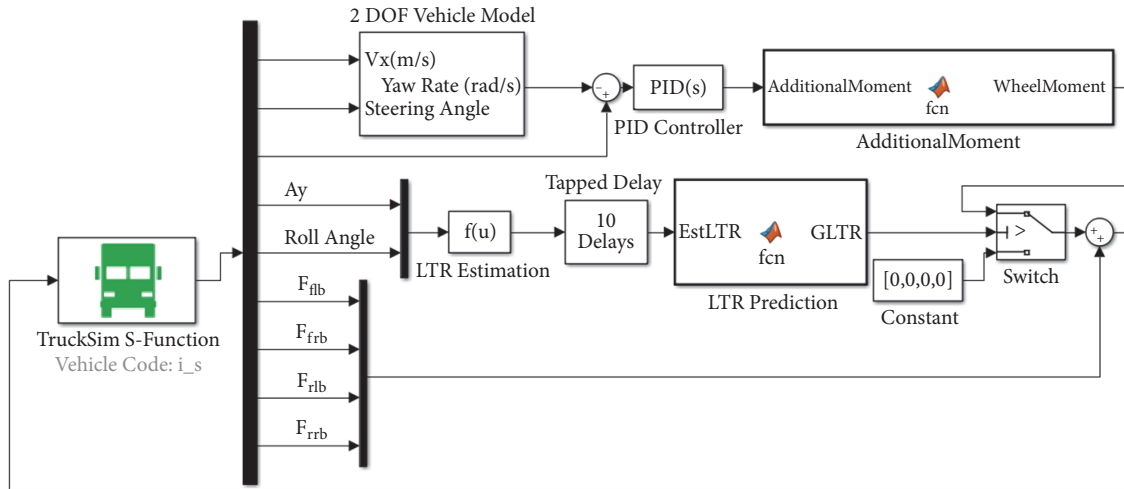


FIGURE 13: GLTR control system using PID controller.

$E(s) = \gamma_e - \gamma_r$ is the error of yaw rate, where γ_e and γ_r are the measured raw rate and reference yaw rate.

We used the yaw rate error as the control goal to calculate the target yawing moment. In (23), $K_p = 290$, $K_i = 120$, and $K_d = 2.4$.

According to steering characteristic of a bus, Table 3 is listed for the selection of the braking wheel to achieve the required yawing moment.

To better understand the effectiveness of GLTR, estimated LTR was also used as the threshold in the comparison simulation tests. This simulation tested the performances of the prevention system after the application of the GLTR and LTR.

This part demonstrates the simulation results acquired from the closed-loop cosimulation utilizing the GLTR index studied in this paper. The cosimulation model included the bus model in TruckSim, an active differential braking system built in Simulink. The active differentials obtained opposite moment by adding extra braking torque on a certain wheel, so that the vehicle was able to effectively control the roll and yaw motions.

We used LTR and GTR as the threshold in the controllers separately. To validate the GLTR, comparison simulation tests were carried out with TruckSim to find the impact of the new controller. The comparison was conducted among a bus with the control system off, a bus with the LTR active, and a bus with the GLTR active. The simulation test was for the 100-km/h “Sindwell” maneuver with a 90° amplitude. First, Figure 14 shows the LTR prediction result using LTR. The peak points of LTR and GLTR curves are (1.608, 0.775) and (1.802, 0.758), where there are 0.2 s between the two peak points.

From Figure 15, the buses with the LTR and the GLTR matched well until the midpoint of the second turn when the GLTR systems activated prior to the LTR. The peak points of GLTR control and LTR control were reduced to (1.639, 0.671) and (1.727, 0.691) separately. We could see that the GLTR control could help the bus reach a steady state prior to the bus under LTR control. The two curves reached zero at 2.55

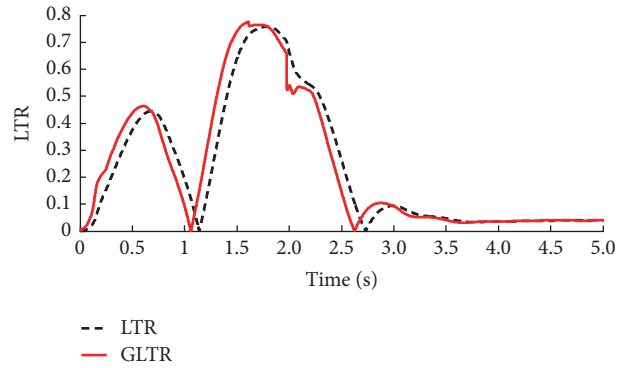


FIGURE 14: Prediction results for the 100-km/h Sindwell test.

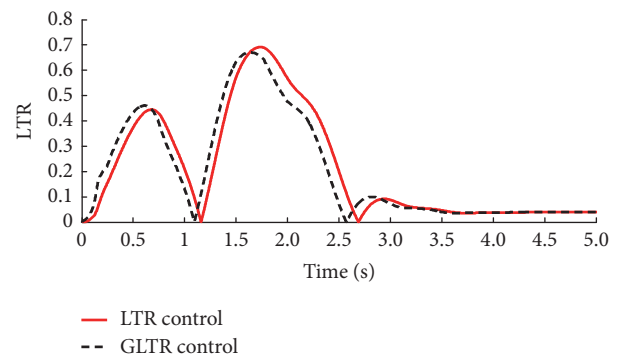


FIGURE 15: Comparison result in the 100-km/h Sindwell test using differential controllers.

s and 2.72 s, showing that the GLTR control could make the bus steady 0.17 s in advance.

Figure 16 shows the comparison result of the roll angles between the LTR control and GLTR control. The GLTR could help the bus reduce the yawing rate about 0.035 rad/s, remarkably reducing the possibilities of rollover.

TABLE 3: Braking strategy of a bus.

Steering angle	$\Delta\gamma$	Steering property	Braking wheel
> 0	> 0	oversteer	Right front
	< 0	understeer	Left rear
< 0	> 0	understeer	Right rear
	< 0	oversteer	Left front

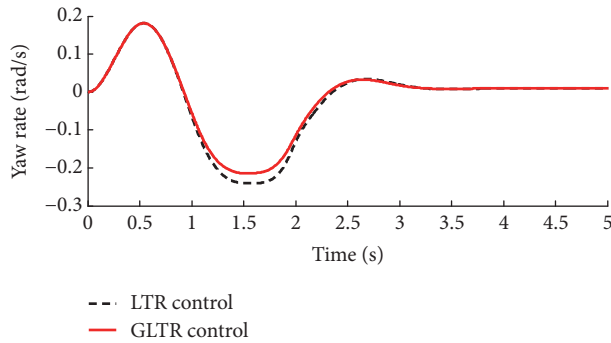


FIGURE 16: Comparison result of the yaw rate in the 100-km/h Sindwell test.

6. Conclusions

This study demonstrated an LTR prediction algorithm for bus rollover systems. Unlike existing methods that are based on estimation algorithms, the proposed algorithm could generate a considerable lead time for rollover prevention systems or warning systems. This rollover index was the fusion of the grey model and a buffer operator that was introduced for bus rollover detection. The simulation study aimed at examining the prediction effectiveness of the GLTR and its application possibility. Some conclusions regarding this approach can be made as follows.

- (1) An LTR estimation equation was developed and then verified to have a rather suitable agreement with the LTR definition formula that directly makes use of the vertical tire forces from TruckSim.
- (2) Lead times produced by the GLTR help the warning systems activate in advance, which will reduce the possible risks of bus rollover.
- (3) Further simulation verification was carried out by applying the GLTR in a differential-based system. Compared with the traditional LTR index, the GLTR could help the differential-based system have better performance and efficacy.
- (4) In the future, for further promotion, this new rollover index should be applied to a real rollover prevention system to conduct hardware in loop tests or road assessments.

Data Availability

The data used to support the findings of this study are available from the corresponding author upon request.

Conflicts of Interest

The authors declare that there are no conflicts of interest regarding the publication of this paper.

Acknowledgments

This work is supported by National Natural Science Foundation of China (Grant No. 51278062).

References

- [1] V. Eyges, J. Padmanaban, and G. Stadter, "A comparative study of rollover crashes involving passenger cars with and without electronic stability control (ESC)," *SAE Technical Papers*, 2011.
- [2] M. E. Greene and V. S. Trent, "A predictive rollover sensor," *SAE Technical Papers*, 2002.
- [3] R. D. Ervin, "The influence of size and weight variables on the roll stability of heavy duty trucks," *SAE Technical Papers*, 1983.
- [4] H. Yu, L. Güvenç, and Ü. Özgüner, "Heavy duty vehicle rollover detection and active roll control," *Vehicle System Dynamics*, vol. 46, no. 6, pp. 451–470, 2008.
- [5] S. Solmaz, M. Akar, and R. Shorten, "Adaptive rollover prevention for automotive vehicles with differential braking," *IFAC Proceedings Volumes*, vol. 41, no. 2, pp. 4695–4700, 2008.
- [6] A. Mayr, G. Klambauer, T. Unterthiner et al., "Large-scale comparison of machine learning methods for drug target prediction on ChEMBL," *Chemical Science*, vol. 9, no. 24, pp. 5441–5451, 2018.
- [7] Z. Liu, H. Li, K. Liu, H. Yu, and K. Cheng, "Design of high-performance water-in-glass evacuated tube solar water heaters by a high-throughput screening based on machine learning: A combined modeling and experimental study," *Solar Energy*, vol. 142, pp. 61–67, 2017.
- [8] Y. Cheng, F. Wang, P. Zhang, and J. Hu, "Risk Prediction with Electronic Health Records: A Deep Learning Approach," in *Proceedings of the 2016 SIAM International Conference on Data Mining*, pp. 432–440, 2016.
- [9] J. L. Deng, "Introduction to grey system theory," *The Journal of Grey System*, vol. 1, no. 1, pp. 1–24, 1989.
- [10] M. Mao and E. C. Chirwa, "Application of grey model GM(1,1) to vehicle fatality risk estimation," *Journal of Technological Forecasting & Social Change*, vol. 73, no. 5, pp. 588–605, 2006.
- [11] A. Manivanna Boopathi and A. Abudhahir, "Design of grey-verhulst sliding mode controller for antilock braking system," *International Journal of Control, Automation, and Systems*, vol. 14, no. 3, pp. 763–772, 2016.
- [12] S.-J. Huang and S.-T. Chao, "A new lateral impact warning system with grey prediction," *Proceedings of the Institution of Mechanical Engineers, Part D: Journal of Automobile Engineering*, vol. 224, no. 3, pp. 285–297, 2010.

- [13] T. Chou and T.-W. Chu, "An improvement in rollover detection of articulated vehicles using the grey system theory," *Vehicle System Dynamics*, vol. 52, no. 5, pp. 679–703, 2014.
- [14] J. Preston-Thomas and J. H. F. Woodrooffe, "Feasibility Study of a Rollover Warning Device for Heavy Trucks," *Transport Canada*, 1990.
- [15] S. Wood, *Passenger Cars—Test Track for a Severe Lane-Change Maneuver—Part 2: Obstacle avoidance*, The international organization for standardization, 2011.
- [16] T. Hsiao, "Robust estimation and control of tire traction forces," *IEEE Transactions on Vehicular Technology*, vol. 62, no. 3, pp. 1378–1383, 2013.
- [17] S. F. Liu and Y. Lin, *Grey Systems: Theory and Applications*, Springer, Berlin, Germany, 2010.
- [18] L. F. Wu, S. F. Liu, Y. J. Yang, L. Ma, and H. Liu, "Multi-variable weakening buffer operator and its application," *Information Sciences*, vol. 339, pp. 98–107, 2016.
- [19] C. Larish, D. Piyabongkarn, V. Tsourapas, and R. Rajamani, "A new predictive lateral load transfer ratio for rollover prevention systems," *IEEE Transactions on Vehicular Technology*, vol. 62, no. 7, pp. 2928–2936, 2013.
- [20] K. H. Ang, G. Chong, and Y. Li, "PID control system analysis, design, and technology," *IEEE Transactions on Control Systems Technology*, vol. 13, no. 4, pp. 559–576, 2005.

Research Article

Characterization of Road Condition with Data Mining Based on Measured Kinematic Vehicle Parameters

Johannes Masino ¹, Jakob Thumm,¹ Guillaume Levasseur,² Michael Frey,¹ Frank Gauterin,¹ Ralf Mikut,³ and Markus Reischl³

¹Institute of Vehicle System Technology, Karlsruhe Institute of Technology, Germany

²Artificial Intelligence Research Laboratory, Université Libre de Bruxelles, Belgium

³Institute for Automation and Applied Informatics, Karlsruhe Institute of Technology, Germany

Correspondence should be addressed to Johannes Masino; johannes.masino@kit.edu

Received 31 July 2018; Accepted 30 September 2018; Published 22 October 2018

Guest Editor: Petru Andrei

Copyright © 2018 Johannes Masino et al. This is an open access article distributed under the Creative Commons Attribution License, which permits unrestricted use, distribution, and reproduction in any medium, provided the original work is properly cited.

This work aims at classifying the road condition with data mining methods using simple acceleration sensors and gyroscopes installed in vehicles. Two classifiers are developed with a support vector machine (SVM) to distinguish between different types of road surfaces, such as asphalt and concrete, and obstacles, such as potholes or railway crossings. From the sensor signals, frequency-based features are extracted, evaluated automatically with MANOVA. The selected features and their meaning to predict the classes are discussed. The best features are used for designing the classifiers. Finally, the methods, which are developed and applied in this work, are implemented in a MATLAB toolbox with a graphical user interface. The toolbox visualizes the classification results on maps, thus enabling manual verification of the results. The accuracy of the cross-validation of classifying obstacles yields 81.0% on average and of classifying road material 96.1% on average. The results are discussed on a comprehensive exemplary data set.

1. Motivation

In 2006, bad conditions of road infrastructure were one of the causes of 50% of fatal accidents in France [1]. In 2016, four accidents in Germany were caused exclusively by road surface damage [2]. Road traffic authorities are aimed to improve and automate monitoring the road state to detect and repair road damages to enhance the safety of road traffic. Based on the detection results, specific and cost-optimized maintenance of roads can be ensured. Furthermore, suppliers of navigation systems can profit from the available information of the road state, because roads in bad condition may be neglected in route planning [3]. Automotive manufacturers can use the collected data to control adaptive vehicle suspensions and to display warnings in real time [4].

Contrary to physical modeling, data-based estimation of the road state does not require any comprehensive system characterization, such as vehicle, road, sensor, and environment. Moreover, modeling of a full vehicle requires five acceleration sensors or gyroscopes to measure vertical

accelerations of unsprung masses and accelerations and rotations of the vehicle body [5]. To monitor road sections, a vehicle can be used as a mobile sensor platform that records both vehicle dynamics and the environment, such as the road state. The road state can be estimated using cameras or inertial measurement units to record rotation speeds and accelerations of the vehicle. Such sensors are already integrated into modern vehicles having an active or adaptive body control or new lighting systems. Inertial sensors are even part of the standard equipment of new vehicles and data can be fused with GPS data for more accurate positioning, an example being the new Audi A7. Previous studies revealed that measurements made by these sensors allow for the derivation of road features, such as potholes or mends of asphalt roads [6–8].

The inertial sensor is inexpensive and part of the standard equipment of many vehicles. Its data include information of minor unevenness of road surfaces that causes the vehicle to vibrate. Inertial sensors, however, only provide data on the road section just crossed. Cameras, by contrast, record

the complete road section in front of the vehicle, including the neighboring lane. However, they are integrated into high-class vehicles only. Cameras currently used in vehicles are of limited accuracy and can detect potholes with a minimum depth of about 3 cm only.

Presently, the state of motorways is measured automatically using expensive and complex measurement vehicles, while that of roads in urban and rural areas is determined manually [9]. These methods are associated with a high expenditure. Due to manual evaluation, it takes a long time until the road network quality is updated. Safety-relevant damage may be detected too late. This may have severe consequences, such as traffic accidents or cost-intensive and complete renewal of the road.

For road maintenance, some countries determine the stochastic road profile depth or international roughness index (IRI), as outlined in [10]. However, the latter is often calculated for 100 m intervals only. As a result, certain obstacles, such as potholes, are not detected. In countries pursuing a systematic road maintenance scheme, not only the IRI but also individual obstacles are measured. This also is the objective of the present study.

Approaches to automatic road state monitoring using inertial sensors exist, e.g., [6, 11–13]. They only concentrate on single road features (such as potholes), do not have any representative dataset, or are based on data measured under restricted conditions, e.g., in speed limit areas or on certain sections only. Moreover, the validation phase only covers checks as to whether the road damage detected actually is damage or not (true or false positives), but not whether road damage was overseen (false negatives).

Road construction offices also need to know the material (road surface), as repairs on different surfaces produce different results and may cause different types of damage [14]. It is also important to distinguish between safety-relevant damage that has to be repaired within 24 hours and damage that is not relevant to safety and the repair of which can be planned and postponed.

The main contribution of this paper is to evaluate the principle feasibility of automatic road surface and road damage measurement with an inertial sensor in the vehicle body. Therefore, this work is aimed at

- (i) designing a processing chain to evaluate road data based on measurements of inertial sensors,
- (ii) automatically recording an adequate dataset,
- (iii) developing and evaluating a method to estimate road surfaces and damage, and at
- (iv) integrating the algorithms developed into a graphic user interface for evaluation of datasets with alternative parameterizations by nonexperts as well.

The methodology will be presented in Section 2. Section 3 will outline the implementation derived, while Section 4 will explain the results based on a first dataset. The result, its applicability, and open problems will be discussed in Section 5.

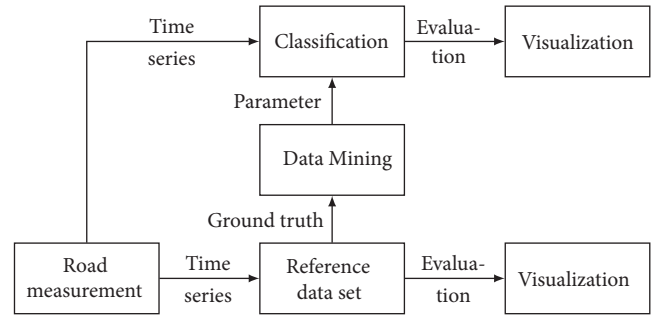


FIGURE 1: Overview of method.

2. Methods

2.1. Design. Figure 1 presents an overview of the method to evaluate the road state [15]. In a first step, the road state is to be measured by suitable sensors. For measurement, acoustic sensors, such as the sensors described in [16], acceleration sensors and gyroscopes, cameras, and similar devices, can be used. As a result, several synchronized time series will be obtained. To obtain a representative reference data set, sensor data have to cover a maximum of framework conditions, e.g., variations of external temperature, driver, and speed. Every point of time/road section has to be assigned a label, e.g. type of road surface, simultaneously or afterwards. In this way, a data set with correct allocations of sensor data to labels is obtained (ground truth). By means of data mining, models can be designed (offline) for retrospective evaluation (offline) or classification during driving operation (online). The results of the classification models then have to be visualized and evaluated on the basis of map material. To estimate the information on the road surface and event or damage that is of relevance to road construction offices, two separate classification routines have to be developed.

2.2. Data Acquisition. The data measured by the sensors installed in the vehicle, e.g., GPS and inertial sensors, are encoded on the CAN bus and cannot be read without the communication matrix that is available to the control system developer and automotive manufacturer only. Hence, an inexpensive measurement system similar to the inertial sensor incorporated in the vehicle is proposed for the easy measurement and readout of data. Measurements cover the position and dynamics of the vehicle, in particular vertical dynamics caused by unevenness [17]. In addition, the data may be assigned labels during measurement already. The measurement system (Figure 2) mainly consists of a GPS receiver (Adafruit ultimate GPS Hat) and a MEMS inertial sensor (LSM9DS1) measuring accelerations and rotation rates of the vehicle along all three axes. The sensor data are acquired using a Raspberry Pi and stored as a csv-table in fused form. As soon as the engine of the vehicle is turned off, the UPS is activated and data can be transmitted via WiFi to a central data base, if the Raspberry Pi is connected to a known WiFi network.

The GPS receiver has a sample rate of 10 Hz, a position resolution of 3 m, and a speed resolution of 0.1 m/s. As the

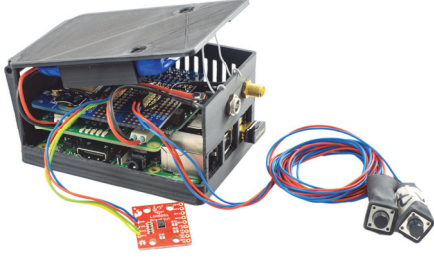


FIGURE 2: Measurement unit, consisting of Raspberry Pi, inertial sensor, Adafruit ultimate GPS Hat, UPS Hat, and two buttons for labeling the data. In service, the inertial sensor is fixed under the Raspberry Pi on the bottom of the case. The case is cut open for visualization purposes.

TABLE 1: Code and corresponding name of the classes for material and event.

<i>m</i> -Material	<i>e</i> -Event
0- Unknown	0- Unknown
1- Smooth surface	1- Good
2- Damaged asphalt	2- Light damages
3- Damaged concrete	3- Pothole
4- Cobblestone	4- Manhole cover
	5- Railway crossing
	6- Speed bump

inertial sensor is a low-cost MEMS sensor, the sample rate is not uniform. This has to be compensated by a filter in data processing. The sample rate is about 220 Hz. The accuracy of the acceleration sensor is 0.05 m/s^2 and of the gyroscope 0.003 degree/s . Without data transfer, a 32 GB memory card can record data for up to 1000 h.

For allocating labels to data, different approaches are presented in literature. For example, a microphone records the (road) damage report of the passenger [13]. This method, however, is subject to several deficiencies. Among others, the labels are recorded much later than the actual road damage and the soundtrack is not synchronized with the sensor data. Reference [6] uses “loosely labeled” training data. Here, only the number of classes but not the exact position is recorded for large road segments.

The measurement system developed for this study is based on two buttons. A pressed button annotates the damage class (event) or the change of road surface (material). For every measurement drive, data with a certain material (e.g., if asphalt 1, otherwise 0) and an event (e.g., if pothole 1, otherwise 0) are recorded. After the measurement drives, binary coding of the data of the respective files is transformed into the coding given in Table 1.

The unix time t , ID for the sensor, speed v , position and time stamp of the GPS lat , lon , and t_{GPS} , accelerations a and rotation rates ω along all three axes, and the two labels for the event e and material m are recorded and stored in a csv-table on the measurement system (Figure 2). The

measurement system is installed near the static center of mass of a BMW 116d in the console between the driver’s seat and passenger’s seat. Orientation of the sensor axes corresponds to the vehicle axes according to ISO 8855:2011. For the method to be generally applicable, measurement data are recorded on randomly selected roads in the region of Karlsruhe, Germany. The speed, road condition, and environmental conditions (e.g., measurement drives in good and rainy weather) are varied strongly. In total, reference data are recorded for a period of three months on a distance of more than 200 km. The data are recorded on eight days (three times a whole day) by three different drivers. Acquisition of reference data is a time-consuming process, as the materials and events have to be crossed under variable environmental conditions and at variable speeds. In particular, individual events, such as potholes, of various types have to be found in the road network and crossed several times with variable approach angles and vehicle tracks.

Lacking GPS data due to variable scanning rates are reconstructed by linear interpolation. As the measurement series are not recorded at a constant sample rate, resampling is required. By resampling, the data are converted from the time domain (s^{-1}) to the space domain (m^{-1}). In [18, 19], it was shown that the response of the vehicle to the excitation of the road depends on speed and that presentation in the space domain reduces this effect. All-time series are resampled with a (spatial) frequency of 100 m^{-1} . The section driven is calculated from the time stamp and speed with the help of the implicit Euler method. Calculation via GPS would also be possible but lacks precision.

The classes of materials m and events e are encoded by natural numbers (Table 1). Light damages are general types of unevenness, which are not safety-relevant and include minor faults and repairs. Manhole cover, railway crossing, and speed bump are construction obstacles. A speed bump is defined as an elevated construction transverse to the driving direction. The pothole represents a fault of at least 2 cm in depth. The latter event is safety-relevant and should be repaired within a maximum of 24 h. For every sample point k of the reference data set, two labels are annotated for the material $m[k]$ and event $e[k]$.

2.3. Signal Processing

2.3.1. Overview. To derive information on the road surface or material and event/damage from the sensor data recorded, the data streams first have to be transferred to a feature space. Feature extraction calculates representative and useful individual features from complete or partial measurement series. Without knowing the physical model of effects of asphalt changes or road damage on the sensor, it is recommended to calculate a large set of features and to check their suitability for the classification problem based on data with the corresponding labels (ground truth). Efficient feature calculation is needed for calculation on mobile devices (e.g., microcontrollers).

2.3.2. Generation of New Time Series. To describe the road state, acceleration in vertical direction (a_z) and rotation

speeds in longitudinal and transverse direction (ω_x and ω_y) are very important [6]. Furthermore, the roll and pitch acceleration ($\dot{\omega}_x$ and $\dot{\omega}_y$) as well as the jerk (\dot{a}_z) of the vehicle are done using the derivation of the vertical acceleration in time domain. The space series data of the vertical roll and pitch acceleration is transformed into frequency domain with the short-time Fourier transform, which contains the short-term distance-localized frequency content of the signal. Hereby, features based on specific frequency bands can be investigated. Hence, the three distance series data are extended by the following data streams, which lead us to 7 data streams in total:

- (i) vertical acceleration,
- (ii) roll acceleration,
- (iii) pitch acceleration,
- (iv) deviation of vertical acceleration,
- (v) short-time Fourier transformed vertical acceleration,
- (vi) short-time Fourier transformed pitch acceleration and
- (vii) short-time Fourier transformed roll acceleration.

2.3.3. Feature Extraction. The features are calculated for windows with a specific length in distance domain and a specific overlap. A window U_i denotes all indexes $[n_i - L/2, n_i + L/2 - 1]$ with the running index n , window index i , and window length L . The window overlap r corresponds to those values from the window U_i that are contained in the previous window U_{i-1} , i.e., $n_{i+1} = n_i + L(1 - r)$. If a longer distance is chosen, short amplitudes, for example, due to potholes, have a weaker impact on the value of features, which incorporate the overall signal, such as the standard deviation. These short amplitudes can be captured by shortening the window size or using features, which calculate extrema.

For the feature extraction for material and events we use window sized of 50 m or 5 m, respectively, and an overlap of 20%.

From the distance series data, we calculate the standard deviation as well as peak-to-peak. The root mean square value or effective value for specific frequencies and the spectral centroid is extracted from the short-time Fourier transformed data streams for the following spatial frequency bands (1 m^{-1}):

$$[0.1, 0.5] [0.5, 15] [15, 20] [0.1, 25] [0.1, 50] \quad (1)$$

The vehicle velocity has a strong sensitivity on the vehicle vibration. Previous research suggests performing a linear regression with each feature as the dependent variable and the velocity as the independent variable [12]. The velocity dependency is then removed by subtracting the estimated linear equation from the corresponding feature. However, the vehicle vibration and the extracted features are not linear dependent on the velocity. The dependent parameters are incorporated and the mean velocity is calculated for each window as additional feature. To allow nonlinear relationships a kernel function of higher order can be applied for the classification.

Of the GPS latitude *lat* and longitude *lon* time series, the medians in every window are used for later visualization.

2.3.4. Classification. Based on the extracted individual features and the corresponding labels, two classifiers are designed for material and event. For the design and application of classification, a combination of feature selection, feature aggregation, and classifier is chosen.

For the surface classification, the five best individual features each are determined using the multivariate analysis of variances (MANOVA) method, for event classification the ten best features are selected. For visualization purposes, the selected individual features are then aggregated to two features using linear discriminant analysis (DA), which can also minimize the calculation expenditure. A support vector machine (SVM) classifier with polynomial kernel function with order 2 is used. Validation is carried out with the help of cross-validation with 5-folds.

2.3.5. Performance Measures. From the correct and false predicted instances, we can calculate a confusion matrix $M = (m_{ij}) \in \mathbb{N}^{k \times k}$ for classes K_i , $i = 1, \dots, k$. In the confusion matrix, m_{ii} presents the *true positives* for class i . The other elements in column j are called *false negatives*, in row i *false positives* and in the diagonal *true negatives*.

From the confusion matrix, one can calculate multiple performance measures to evaluate the model, such as recall with $m_{ii} / \sum_{j=1}^n m_{ji}$ for class K_i , the overall accuracy of the classifier with $\sum_{i=1}^n m_{ii} / \sum_{i=1}^n \sum_{j=1}^n m_{ij}$, or the precision $m_{ij} / \sum_{j=1}^n m_{ij} = \pi_{ij}$. The precision presents the fraction of retrieved instances that are relevant and can be seen as the probability π_{ij} of the classifier to predict class i as class j for $i, j = 1, \dots, l$. An overview for performance measures for different calculation problems can be found in [20].

3. Implementation

To facilitate operation by non-experts, the methods are implemented in a graphical user interface called *Vehicle Learner Toolbox*, which is available in [21]. It is based on MATLAB and implements several machine learning operations of the freely available toolbox SciXMiner [22] (formerly, Gait-CAD [23]). The *Vehicle Learner Toolbox* provides the possibility to

- (i) import vehicle sensor data in different file formats,
- (ii) compress the imported data and automatically extract various features,
- (iii) train a classifier model with a wide-ranging set of options,
- (iv) test the trained classifier with a test set,
- (v) visualize the results with the help of plots and maps.

A project folder can be selected and sensor data can be imported in the corresponding frame *Data* (Figure 3). There is the option to assign the sensor data to specific vehicles, since they vary in suspensions, damping, and other

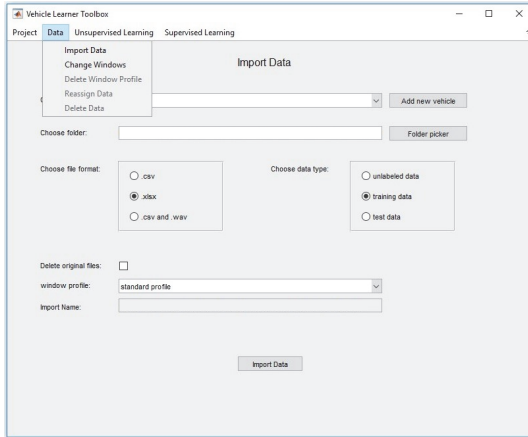


FIGURE 3: The import data frame of the *Vehicle Learner Toolbox*. Different vehicles can be chosen and the data type can be set.

parameters, which have an impact on the vibration behaviour. Therefore, in the following data processing, feature selection and classification can be performed for data from specific vehicles. The import allows .csv and .xlsx file format with the following column headers:

- (i) timestamp (unix timestamp)
- (ii) x-, y-, z-accel (the acceleration values in each direction)
- (iii) x-, y-, z-gyro (the gyroscope values in each direction)
- (iv) gps-timestamp (format: YYYY-MM-DDThh:mm:ss,000Z)
- (v) lat, lon (position in latitude and longitude)
- (vi) speed (in m/s)
- (vii) m, e (material m and event e labeling, if the data is not labeled, these columns should only contain zeros).

Since the GPS data is acquired with a lower sample rate compared to the inertial sensor, these data are automatic interpolated. Furthermore, the sensor signals are subject to noise [24] and are automatic smoothed during the import process with the following filters. Despite the noise of a MEMS gyroscope visible as spikes in the signal, it is well known for its good accuracy in short term [25]. A suitable filter for this purpose is the median filter, which is robust against outliers and removes noise while preserving high frequency content. Since the data from the MEMS accelerometer do not show such spikes but contains more noise in the short term [25], a Savitzky-Golay FIR smoothing filter is applied. It fits a polynomial of a specified degree to frames of noisy data and minimizes the least-squares error [26]. Therefore, the filter outperforms standard averaging FIR filters, which might remove high frequency content with the noise.

There is also the possibility to import tire cavity sound data along the inertial sensor data for road roughness estimation, as presented in [16, 27], but is not substance in this paper. Moreover, the imported data set can be categorized as training, testing or unlabeled data.

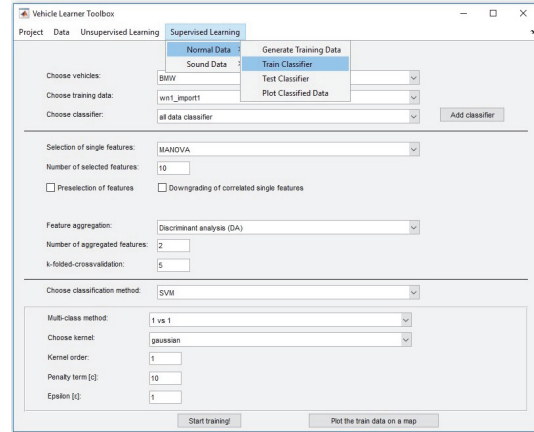


FIGURE 4: The train classifier frame of the *Vehicle Learner Toolbox*. Multiple classifiers can be trained with a wide range of options.

Furthermore, the parameters for the window profile, such as length of road segments and overlapping factor of these windows, can be determined, as well as the resampling frequency. The standard window profiles are *material* with a window length of 50 m and *event* with a window length of 5 m.

After the import and preprocess of the data, new time series data are calculated and features are automatically extracted, as proposed in Sections 2.3.2 and 2.3.3. The code to calculate new data series or features can be easily added in the corresponding MATLAB function.

The proposed data mining methods (Section 2.3.4) can be applied in the toolbox under the menu *Supervised Learning* (Figure 4). In the first step, a training data set must be generated. There are two different ways to accomplish this. Either an external data set containing features can be imported or the imported data within the toolbox can be used and modified by choosing the time interval of the data acquisitions or the area. Furthermore, data annotated with specific labels can be excluded from the classification. For our example, all data with labels *0-unknown* were deleted (Table 1). Another option is to thin out classes with significant more data points than other classes to allow an approximately uniform distribution of data points among the classes to prevent over-fitting of specific classes. Furthermore, systematic errors during labeling the data can be removed; e.g., if the trigger to annotate the data was activated too early or too late the annotation can be moved or data points with the wrong annotation can be excluded. After the generation of the data set to be processed, the settings for the classifier can be determined under the tab *Train Classifier* (Figure 4).

In the first step the vehicle and the training data set must be set. Afterwards a new classifier model can be created or an existing model can be selected. The next section contains the settings of feature selection (e.g., MANOVA) and aggregation (e.g., discriminant analysis), as proposed in Section 2.3.4. Reducing the amount of features highly influences the classification result by reducing the chances for overfitting. It is possible to cross-validate the training process

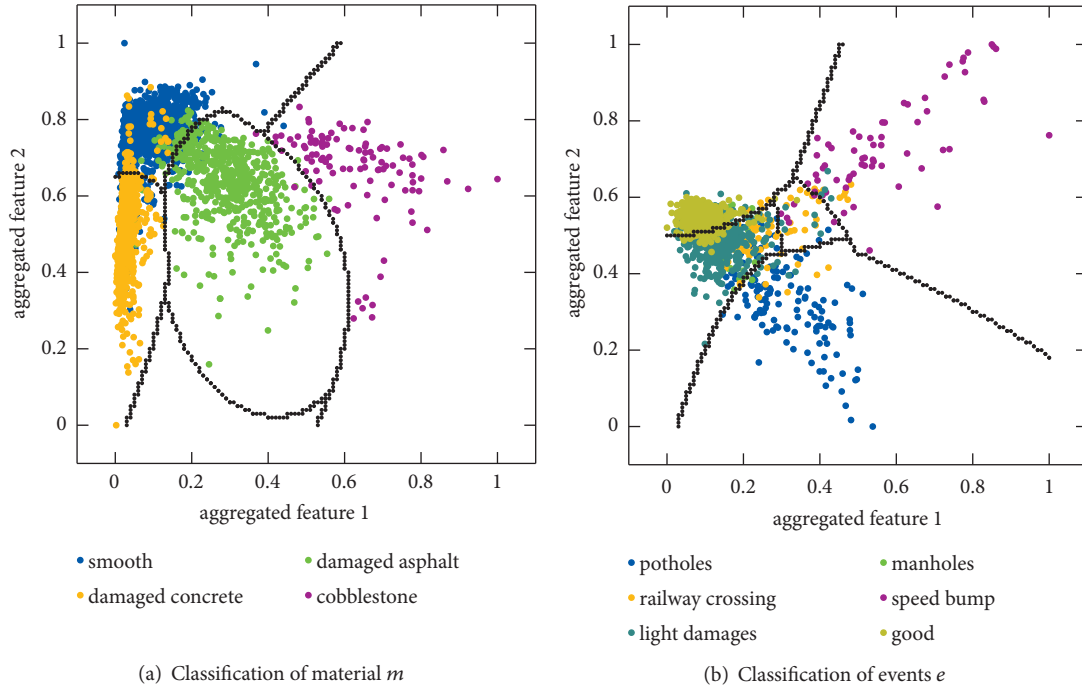


FIGURE 5: Classification results with two aggregated features and borders of the classifier in black.

by setting the k-folded-cross-validation value to higher than 1. The last section offers a variety of settings for the classifier, e.g. for a SVM, including the kernel function and penalty term. Afterwards, the classifier can be trained and data can be plotted on open street maps. Furthermore, the confusion matrix and the total loss is shown in the MATLAB console.

For testing new data, a data set with modifications in time range and area to be analyzed can be generated as described for training, and a trained classifier must be selected. If the test data set is labeled, the output of the prediction is again a confusion matrix and the classification error. Moreover, the results can be visualized and plotted on open street maps, as it will be presented in Section 4. The trajectories will be cut into segments of different color referring to the corresponding classes, which are predicted.

4. Results

4.1. Event Classification. The accuracy of the cross-validation of classifying events yields 81% on average without feature aggregation. The aggregated feature space and the lines of the function to classify the events is shown in Figure 5(b).

The illustration of the classification shows that road segments in *good condition*, with *light damages*, *speed bumps*, and *potholes*, can be separated well. This indication is proofed by the quantitative results, listed in Table 2.

The precision and recall for the mentioned classes is above 70%, whereas the performance measures for *manhole cover* and *railway crossing* is below 62% on average.

The most important features, determined with MANOVA, are

- (i) peak-to-peak of pitch acceleration
- (ii) peak-to-peak of roll acceleration
- (iii) maximum of jerk in vertical direction
- (iv) root mean square (RMS) of the vertical acceleration
- (v) speed

By comparing each class with each other, it emerges that the peak-to-peak value of pitch and roll acceleration are mainly responsible to separate events, which occur on

- (i) both vehicle lanes (railway crossing, speed bump),
- (ii) on only one side of the vehicle (manhole cover, pothole),
- (iii) or have only little impact on the vehicle vibration (light damages, road segments in good condition).

In addition, the average RMS of the vertical acceleration is important to separate light damages and road segments in good condition. Furthermore, *potholes* and *manhole covers* are dividable through the maximum RMS of the roll acceleration for the frequency range 15 to 25 m^{-1} . However, latter events are often misclassified as segments in *good condition* or *light damages*. *Speed bumps* and *railways crossings* are separable by the value of the peek-to-peek of the pitch rate, whereas *railways crossings* are also often misclassified as light damages.

To test the classifier, a data set of more than 200 km of street data is classified and plotted on open street maps. The results are promising and represent the actual street condition in many occasions. A few examples of classified areas are shown below.

TABLE 2: Results of single features classification.

Material	Precision (% ± SD)	Recall (% ± SD)	Events	Precision (% ± SD)	Recall (% ± SD)
smooth surf.	95.8 ± 0.7	97.6 ± 0.7	good	83.9 ± 1.5	92.4 ± 2.7
damaged asph.	97.3 ± 2.0	94.9 ± 1.4	light dam.	78.5 ± 3.8	70.8 ± 3.3
damaged con.	95.6 ± 0.8	92.9 ± 1.1	pothole	85.3 ± 6.6	77.4 ± 7.2
cobblestones	99.1 ± 1.8	100.0 ± 0.0	manhole	40.9 ± 13.6	29.1 ± 15.7
			railway cro.	61.6 ± 4.9	57.0 ± 7.9
			speed bump	94.9 ± 7.1	91.0 ± 12.2
Average	96.4 ± 0.8	96.4 ± 0.8		74.2 ± 6.3	69.6 ± 8.1
Accuracy	96.1 ± 0.4			81.0 ± 1.7	

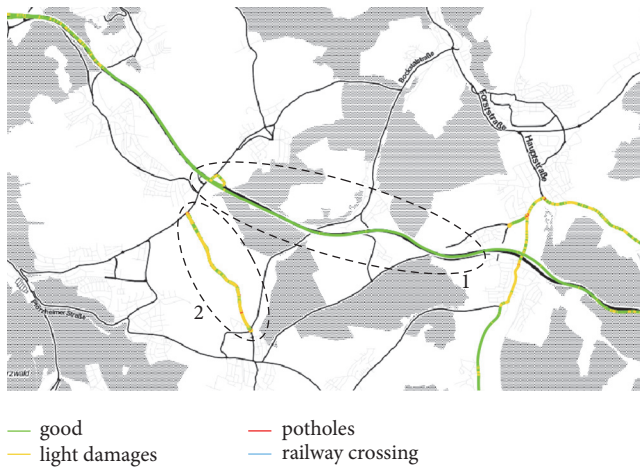


FIGURE 6: Event classification results of two high speed roads in the south west of Karlsruhe, Germany.

The first example shows the event classification results on two different high speed roads (Figure 6). The upper one with Label 1 is a freshly renovated asphalt highway with close to no damages and the lower one with Label 2 is a poorly patched asphalt road with a lot of medium and severe damages. The classification successfully predicted the upper roadway as *good street*. Most parts of the lower street were predicted as *light damage* and some points even as *potholes*. The results represent the road condition very accurate. The only noticeable misclassification is *railway crossing* that was predicted once (Label 3).

The second example presents data acquired in an urban area in Karlsruhe, the predictions are shown in Figure 7. The roads in this area are poorly preserved and there is a *speed bump* at a pedestrian crossing (Label 1). The classification model correctly predicts the *speed bump* (Label 1) for all overdrives and a *pothole* (Label 2) on both driving directions.

The third interesting sector is shown in Figure 8. Potholes (Labels 2 and 3), which were at the edge of the driving line, were overdriven multiple times and the classifier predicts the severe damage accordingly. Sometimes the output at the road segments is not *pothole* but *light damages* or even *good road condition*. The reason might be that the pothole was avoided by the driver.



FIGURE 7: Event classification results for road segments in the city of Karlsruhe, Germany.

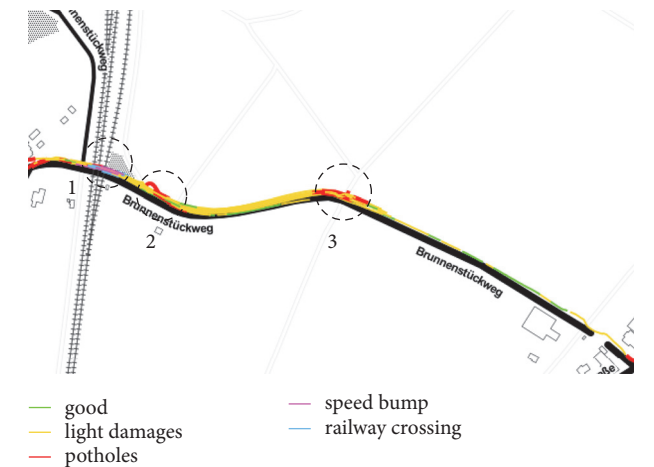


FIGURE 8: Event classification results of road segments outside of Karlsruhe, Germany, for the events *potholes* and *railways crossing*.

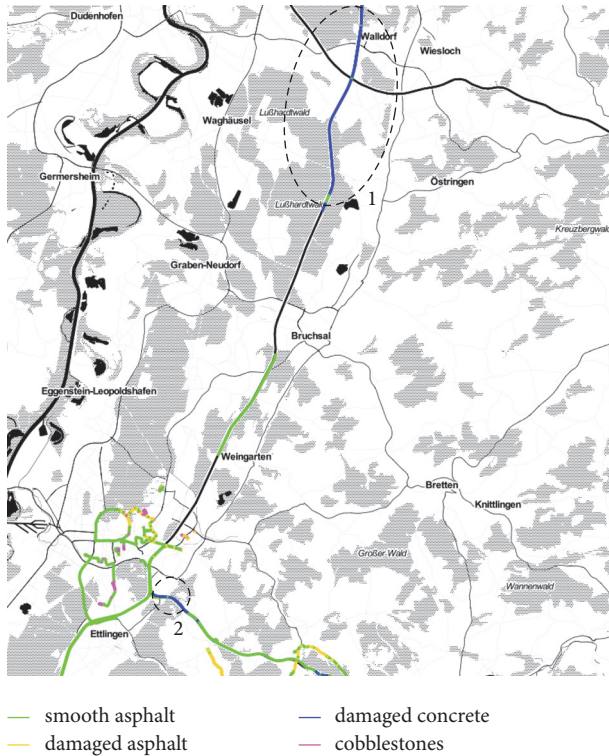


FIGURE 9: Material classification of an aged concrete highway.

The *railway crossing* (Label 1) is more elevated than other crossings and miss-classified as *speed bump* in few cases.

4.2. Road Surface Classification. When classifying road surfaces, cross-validation yields 96.1% accuracy on average without aggregation of features. The aggregated feature space is shown in Figure 5(a). The figure indicates, that the misclassifications are asphalt classified as *damaged asphalt* or *damaged concrete* and vice versa. The illustrated results are underlined by Table 2, where the precision and recall for *cobblestone* is above 99.0%, whereas the performance measures for *asphalt*, *damaged asphalt*, and *damaged concrete* are between 92.0 and 97.6 percent.

The three best individual features for the classification of road surface according to MANOVA are

- (i) RMS of the roll acceleration for frequency range from 5 to 15 m^{-1} on average
- (ii) standard deviation of the pitch rate
- (iii) stand deviation of the RMS of the vertical acceleration for frequency range 15 to 25 m^{-1}

The values of RMS of the roll acceleration and vertical acceleration separate the classes *smooth surfaces*, *damaged asphalt* and *cobbled stone*. The values are greatest for *cobbled stone* and low for *smooth surface*.

Standard deviation of pitch rate separates the classes *damaged concrete* from all other classes. The reason are probably poor and aged concrete joints.

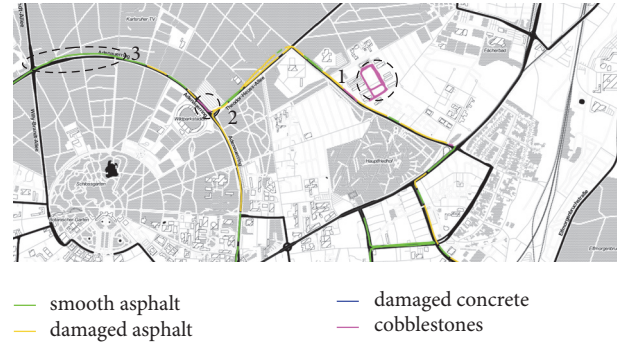


FIGURE 10: Material classification of cobblestone and road segments in urban area.

The material classifier was applied to the same data set described for event classification. The classifier was able to reflect the road surface very precisely. The following figures display the performance on different surfaces. Analog to the event classification shown in Figure 6, the material classifier could distinguish between both roads and correctly classified them as *smooth surface* and *damaged asphalt*, respectively.

In contrast, Figure 9 shows a long highway segment with aged concrete and distinctive concrete joints, which have to be maintained shortly. Except for one short segment, which was classified as *smooth surface*, the road state was correctly predicted.

The classification results of data acquired in the urban area of Karlsruhe (Figure 10) show two correctly predicted areas of cobblestone (Label 1 and 2). The remaining road segments are correctly classified as segments with *light damages* or in *good condition*. Especially latter class was correctly predicted for a road segment, which was recently renewed (Label 3). One miss-classification of *cobblestone* can be found close to Label 1. However, this road segment is highly damaged with multiple potholes, which have a high impact on the vehicle vibration similar to cobblestones.

5. Conclusions and Outlook

The results show that the system presented in this paper can classify both road materials and events. The features selected by MANOVA are in agreement with the theory of vehicle excitation. Material classification performs well according to the results of the cross-validation and the test data.

There are multiple miss-classifications of the prediction of events, especially for structural obstacles, such as *manhole covers* and *railway crossing*. However, these events might be marked on a map and excluded from classification and investigation, as the main objective is to detect road damage.

One reason for misclassifications of the events *good condition*, *light damages*, and *pothole* might be false manual annotating, since there is sometimes only a fine line between the degree of damages, or the events were not fully over-driven, especially for *potholes*.

As the system is of modular design, the number and type of sensors and sensor modality can be varied. When adapting feature extraction, also camera recordings might be

useful. Transferability to other vehicles with different chassis and dimensions has not been examined so far. Presumably, the algorithms of parameters are adapted to the vehicle with which the learning data set was recorded. Here, fusion of learning data sets from several vehicles and an accordingly adapted classification routine might help. It can be assumed that the results will be slightly worse.

Generally, the inertial sensor represents a very good option to collect information on the tire/road contact at low costs and over wide areas. Use of information of several vehicles can compensate the drawback of some drivers passing by safety-relevant damage that, hence, is not measured by the sensor. Moreover, obstacles at the roadside are not crossed and, hence, cannot be detected.

Fusion of camera and inertial sensor data probably would be the optimum solution for a mobile determination of the state of road traffic infrastructure. For road construction offices, use of a low-cost and computationally efficient system, consisting of an inertial sensor, Raspberry Pi, and simple signal processing, is sufficient and can be recommended.

Data Availability

The raw data used to support the findings of this study have been deposited in <http://doi.org/10.5281/zenodo.1461243> [28]. The data can be processed with the presented toolbox available in <http://doi.org/10.5281/zenodo.1216187> [21].

Conflicts of Interest

The authors declare that they have no conflicts of interest.

Acknowledgments

This work was funded by the Federal Ministry for the Environment, Nature Conservation, Building and Nuclear Safety, Germany, within the Environmental Research Plan 2014 (Project no. 3714541000).

References

- [1] P. De Gonneville and G. Martin, "Le mécanisme d'accident," in *Sétra: Service d'études techniques des routes et autoroutes*, Bagnex, 2006.
- [2] "Destatis. Verkehrsunfälle. Destatis, Mar. 2017. Artikelnummer: 2080700161124".
- [3] P. Mohan, V. N. Padmanabhan, and R. Ramachandran, "Nericell: Rich monitoring of road and traffic conditions using mobile smartphones," in *Proceedings of the The ACM Conference on Embedded Networked Sensor Systems*, 2008.
- [4] M. Schade, "Der intelligente Löcher-Sucher," *Auto Bild*, 2016.
- [5] E. Esmailzadeh and F. Fahimi, "Optimal adaptive active suspensions for a full car model," *Vehicle System Dynamics*, vol. 27, no. 2, pp. 89–107, 1997.
- [6] J. Eriksson, L. Girod, B. Hull, R. Newton, S. Madden, and H. Balakrishnan, "The pothole patrol: using a mobile sensor network for road surface monitoring," in *Proceedings of the 6th International Conference on Mobile Systems, Applications, and Services (MobiSys '08)*, pp. 29–39, Breckenridge, CO, USA, June 2008.
- [7] C. Koch and I. Brilakis, "Pothole detection in asphalt pavement images," *Advanced Engineering Informatics*, vol. 25, no. 3, pp. 507–515, 2011.
- [8] S. C. Radopoulou and I. Brilakis, "Patch detection for pavement assessment," *Automation in Construction*, vol. 53, pp. 95–104, 2015.
- [9] S. C. Radopoulou and I. Brilakis, "Improving Road Asset Condition Monitoring," pp. 3004–3012.
- [10] ISO, *ISO 8608: Mechanical Vibration - Road Surface Profiles - Reporting of Measured Data*, International Organization for Standardization, 2016.
- [11] K. Chen, G. Tan, M. Lu, and J. Wu, "CRSM: a practical crowdsourcing-based road surface monitoring system," *Wireless Networks*, vol. 22, no. 3, pp. 765–779, 2016.
- [12] M. Perttunen, O. Mazhelis, F. Cong et al., "Distributed road surface condition monitoring using mobile phones," in *Proceedings of the International Conference on Ubiquitous Intelligence and Computing*, pp. 64–78, Springer, 2011.
- [13] F. Seraj, A. Dilo, T. Luarasi et al., "RoADS: A Road Pavement Monitoring System for Anomaly Detection Using Smart Phones," in *Big data analytics in the social and ubiquitous context*, pp. 128–146, 2016.
- [14] I. Tekin, *Economic investigations of the current state of the road system in order to determine the advantages and areas of application of a road monitoring system [Bachelors Thesis]*, Karlsruhe Institute of Technology, Institute of Vehicle Systems Technology.
- [15] J. Masino, G. Levasseur, M. Frey, F. Gauterin, R. Mikut, and M. Reischl, "Charakterisierung der Fahrbahnbeschaffenheit durch Data Mining von gemessenen kinematischen Fahrzeuggrößen," *Automatisierungstechnik*, vol. 65, no. 12, 2017.
- [16] J. Masino, J. Pinay, M. Reischl, and F. Gauterin, "Road surface prediction from acoustical measurements in the tire cavity using support vector machine," *Applied Acoustics*, vol. 125, pp. 41–48, 2017.
- [17] J. Masino, M. Frey, F. Gauterin, and R. Sharma, "Development of a highly accurate and low cost measurement device for Field Operational Tests," in *Proceedings of the 3rd IEEE International Symposium on Inertial Sensors and Systems, ISS 2016*, pp. 74–77, USA, February 2016.
- [18] M. Sayers, T. Gillespie, and C. Queiroz, "The international road roughness experiment: Establishing correlation and a calibration standard for measurements," *World Bank Technical Paper*, 1986.
- [19] C. C. Ward and K. Iagnemma, "Speed-independent vibration-based terrain classification for passenger vehicles," *Taylor & Francis, Vehicle System Dynamics*, vol. 47, no. 9, 2009.
- [20] M. Sokolova and G. Lapalme, "A systematic analysis of performance measures for classification tasks," *Information Processing & Management*, vol. 45, no. 4, pp. 427–437, 2009.
- [21] J. Thumm and J. Masino, *Vehicle Learner Toolbox for Road Condition Estimation, Matlab files*, 2018.
- [22] R. Mikut, A. Bartschat, and W. Doneit, "The MATLAB toolbox SciXMiner: User's manual and programmer's guide," 2017, <https://arxiv.org/abs/1704.03298>.
- [23] R. Mikut, O. Burmeister, S. Braun, and M. Reischl, "The open source MATLAB toolbox Gait-CAD and its application to bioelectric signal processing," in *Proceedings of the DGBMT-Workshop Biosignalverarbeitung*, pp. 109–111, Potsdam, Germany, 2008.

- [24] C. Halfmann and H. Holzmann, *Adaptive Modelle für die Kraftfahrzeugdynamik*, Springer, Berlin, Germany, 2003.
- [25] O. J. Woodman, "An introduction to inertial navigation," Tech. Rep., University of Cambridge, Computer Laboratory, 2007.
- [26] S. J. Orfanidis, *Introduction to signal processing*, Prentice-Hall, Inc, 1995.
- [27] J. Masino, M.-J. Foitzik, M. Frey, and F. Gauterin, "Pavement type and wear condition classification from tire cavity acoustic measurements with artificial neural networks," *The Journal of the Acoustical Society of America*, vol. 141, no. 6, pp. 4220–4229, 2017.
- [28] J. Masino, "Characterization of Road Condition with Data Mining Based on Measured Kinematic Vehicle Parameters, Data," 2018.

Research Article

Blind Corner Propagation Model for IEEE 802.11p Communication in Network Simulators

Sanchai Jaktheerangkoon , Kulit Na Nakorn, and Kultida Rojviboonchai 

Chulalongkorn University Big Data Analytics and IoT Center (CUBIC), Department of Computer Engineering, Faculty of Engineering, Chulalongkorn University, Bangkok, Thailand

Correspondence should be addressed to Kultida Rojviboonchai; kultida.r@chula.ac.th

Received 27 March 2018; Accepted 11 June 2018; Published 18 July 2018

Academic Editor: Mihai Dimian

Copyright © 2018 Sanchai Jaktheerangkoon et al. This is an open access article distributed under the Creative Commons Attribution License, which permits unrestricted use, distribution, and reproduction in any medium, provided the original work is properly cited.

Vehicular Ad Hoc Network (VANET) has been developed to enhance quality of road transportation. The development of safety applications could reduce number of road accidents. IEEE 802.11p is a promising standard for intervehicular communication, which would enable the connected-vehicle applications. However, in the well-known network simulators such as NS3 and Omnet, there is no propagation model that can simulate the IEEE 802.11p communication at blind corner realistically. Thus, in this paper, we conducted the real-world experiments of IEEE 802.11p in order to construct the model to describe the characteristics of the IEEE 802.11p communication at the blind corners. According to the experimental results, we observe that the minimum distance between the vehicle and the corner can effectively be represented as the key parameter in the model. Moreover, we have a variable parameter for adjusting the impact of the obstruction which could be different at each type of blind corners. The simulation results using our proposed model are compared with those using the existing obstacle model. The results showed that our proposed model is much more closely aligned with the real experimental results.

1. Introduction

World Health Organization (WHO) reported that 1.2 million people from all over the world die and 20 to 50 million people suffer from injuries because of road accidents each year [1]. According to [2], a lot of accidents occurred at the intersections. Blind corner is one type of the intersections where the accidents occur easily. This is because one vehicle from one side of the corner cannot see the other vehicles from the other side of the corner. We consider the blind corners as the corners with obstacles and they rarely have space for sidewalk. The blind corners can be generally found in many locations, for example, in the cities of Asian countries, in small alley, in local way, and inside the organization area. These locations are surrounded by buildings that obstruct the driver's line of sight as shown in Figure 1. Not only can the buildings cause the blind corner, but also walls, trees, and construction sites can also cause the blind corner. Furthermore, the traffic lights are rarely found in such locations. That is why the accidents could occur easily at the blind corners.

Even though the line of sight of the driver at the blind corners is blocked by the obstacles, wireless communication can partially pass through the obstacles. As a result, the vehicles can sense other vehicles around. The wireless communication network among vehicles is introduced as Vehicular Ad Hoc Network (VANET). VANET has been developed to enhance the quality of road transportation and Intelligent Transportation System (ITS). VANET consists of 2 types of communications: vehicle-to-vehicle (V2V) and vehicle-to-infrastructure (V2I). One of the major ITS applications is the safety application, in which some warning signals can be sent to other vehicles in case there are vehicles or pedestrians nearby. By receiving the signals, the intelligent vehicle can decide if it can move on or it needs to brake. This could reduce the number of accidents.

The IEEE developed the 802.11p Wireless Access for Vehicular Environment (WAVE) standard as a support for VANET applications [3]. The IEEE 802.11p has the communication range up to 1,000 m if the vehicle speed is less than 200 km/h. As the blind corner is one of the critical locations where the accidents can occur easily, the VANET



FIGURE 1: Sample building that causes blind corner.

communication could help notify the driver. Nevertheless, the obstacles at the blind corner not only obstruct the sight of the driver but also obstruct the wave propagation signal. Consequently, the communication could fail easily. In other words, the performance of IEEE 802.11p can be degraded when the communication occurs at the blind corner. This is one of the vulnerabilities of IEEE 802.11p communications for safety applications [4].

The effect of the obstruction leads to the decreased communication range of IEEE 802.11p and the performance degradation of the protocols and applications that rely on VANET. To consider this issue, researchers and developers evaluate their work using both real-world experiment and simulation. The real-world experiment is the evaluation method that uses real equipment running in real scenarios. Although this method provides the testing performance accurately, it is time-consuming, expensive, and difficult to reproduce the test cases and it is difficult to scale to large scenarios. Thus, the simulation is an alternative method for performance evaluation.

To enable realistic simulation, the propagation models are applied to the nodes in the simulation. Recently, there have been researches about the propagation models for each kind of obstructions such as vehicle obstruction [5, 6] and building obstruction [7–12]. These models have been evaluated by comparison to the results from the real experiments. As the models are applied, the simulation results can become more realistic in each specific scenario. However, to the best of our knowledge, the existing models are not suitable for applying in blind corner scenario.

In our previous works, we conducted the real-world experiment to study the performance of IEEE 802.11p in blind corner scenario [12]. The experiment was conducted using Denso Wireless Safety Unit (WSU), which is IEEE 802.11p communication module. Each vehicle was equipped with the WSU module. The results showed that two vehicles at different sides of the corner can communicate with each other when the minimum distance between the vehicle and the corner is less than 60 m. The results emphasized that the performance at the blind corner should be taken into a serious consideration when developing any safety applications.

In this paper, our contribution is twofold. The first contribution is that we extend our previous work to cover more blind corners in order to investigate and generalize the characteristics of the blind corners regardless of the specific corners. The second contribution is that we propose a novel blind corner model, which is implemented as an extension of the well-known models in the network simulators. This model can represent the characteristics of IEEE 802.11p communication at blind corners realistically.

There are two methods to construct a new model which are ray tracing method and flat propagation method [10]. The ray tracing method has a complex computation, consumes a lot of resources and time, and is difficult to parameterize the parameters. On the other hand, the flat propagation method normally calculates some values and uses some probabilistic functions to represent signal propagation loss. Our design concern is that the model has to be simple in order to consume less time when it is applied in the simulation. Therefore, we use the flat propagation method. Our model can be implemented as an extension of the two-ray ground model and the Nakagami model, the well-known propagation models in the network simulators, so it is easily applied to any network simulators. The network simulator that we use in this work is NS-3 [13], which is open source software for network simulation and is very popular as a network platform in research and education. For performance evaluation, we conduct extensive real-world experiments and compare the results from the experiments to the results from our proposed model.

The following of this paper is organized as follows: the background knowledge and related works about propagation models are described in Section 2. Then, our field experiment settings and results are shown in Section 3. In Section 4, our model is elaborated. The discussion and comparison with other related works are shown in Section 5. Finally, Section 6 concludes our work.

2. Background Knowledge and Related Works

The blind corner is a critical scenario for the safety applications, so the performance of the safety application should be considered. Although we can install the infrastructure such as Roadside Unit (RSU) at the corner to improve the communication performance, it consumes a lot of cost for deployment. Moreover, it is not cost-effective to deploy the RSUs at all corners in the city because there are too many blind corners in most of the countries, especially the countries in Asia. Therefore, the scenario where the communication occurs at the blind corners without any additional infrastructures should be taken into consideration. Such scenario can be considered as beneficial to the safety applications because it can help reduce the accidents at any corners.

One method that can help simulate the communication effectively is to add the propagation loss models or signal attenuation models. There are two methods to construct propagation models, which are ray tracing method [14, 15] and flat propagation method [8–11]. The ray tracing method traces the signal from source to destination using the characteristics of signals like reflection, diffraction, and interference. Then, the loss of the signal is calculated. Although this

TABLE 1: Comparison of the models.

Issue	Obstacle model [8, 9]	CORNER model [10, 11]	Blind corner model (our model)
(i) Signal attenuation	✓	✓	✓
(ii) Simulator used	NS-3, Omnet	QualNet	NS-3
(iii) Communication module used in the real experiments	IEEE 802.11p	IEEE 802.11b/g	IEEE 802.11p
(iv) Characteristics of the corner used in the experiment	Not blind corner	Not blind corner	Blind corner (the corner with no space for side walk or the side walk less than 1 m)
(v) Parameters used in path loss calculation approach	Number of walls penetrated	Wave characteristics parameter	Minimum distance

method can give an accurate signal strength at the destination as an output of the model, it is not widely used because the obstacle topologies and the signal attenuation characteristics for each obstacle have to be collected and set in advance. Moreover, it consumes a lot of resource and simulation time.

Researchers mostly use the flat propagation method instead of the ray tracing method. The flat propagation method utilizes values that can be obtained from the topology easily as inputs for the formula. The formula will give a result as attenuated signal strength. The most common value that is used as an input is distance. This method consumes less resource and simulation time. The examples of the models using this method are two-ray ground model and Nakagami model. These two models are embedded into most of the network simulators. However, many researchers still introduce new models based on the flat propagation method for more realistic simulation in some specific scenarios.

The obstacle model [8, 9] uses number of walls where the signal has to penetrate as a main variable for formula calculation. As a result, the obstruction amount of the signal depends on number of walls the signal is passing through. This model focuses mainly on building obstacles, while the CORNER model [10, 11] uses the wave characteristics such as reflection and diffraction as a main variable for formula calculation. The CORNER model classifies the scenarios into 3 categories: line of sight (LOS), non-line of sight with 1 corner (NLOS1), and non-line of sight with 2 corners (NLOS2).

Our work focuses on blind corners, which are the corners that have no space for sidewalk, which are the corners with the sidewalk less than 1 meter. At the corner with no space for sidewalk, the signal from the transmission node will penetrate to the wall, leading to more signal obstruction. Our model is different from the obstacle model and the CORNER model in that we use the minimum distance between the vehicles to the corner as the main parameter to calculate in our formula. We explain the rationale behind our design in Section 4.

Our model, the obstacle model, and the CORNER model are compared as shown in Table 1. All of the models perform signal attenuation when the transmitted signal travels through the obstacles. In order to calculate the path loss, the obstacle model uses number of walls penetrated, the CORNER model uses wave characteristics such as reflection and diffraction effects, and our model uses the minimum

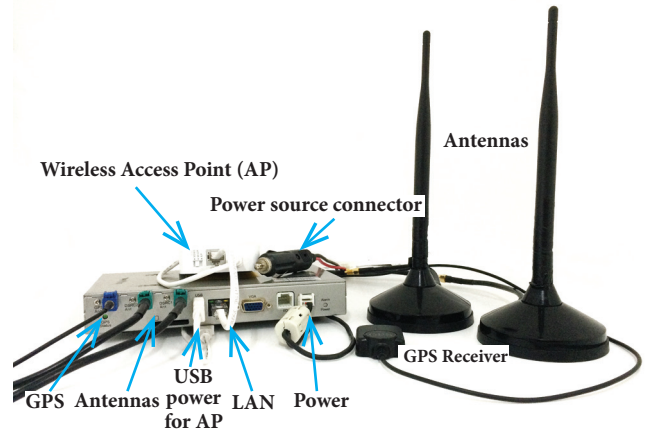


FIGURE 2: Denso WSU experiment set.

distance as the main parameter. The obstacle model and our model are implemented in the NS-3 simulator, whereas the CORNER model is implemented in the QualNet simulator. The obstacle model is also embedded in Veins framework based on Omnet simulator [16]. For the communication module used in the real experiments, IEEE 802.11p is used in our model and the obstacle model, whereas IEEE 802.11b/g is used for the CORNER model.

3. Field Experiment

We set up field experiment to study the characteristics of real IEEE 802.11p communication devices in blind corner scenario [12]. Our previous work reveals the performance of IEEE 802.11p where the communication range among 2 vehicles in blind corner scenario is less than 6% of full specification of IEEE 802.11p, which is 1,000 m. In order to investigate the performance in more details, we extend the experiment to cover more samples of blind corners and propose the model for using in the simulators.

3.1. Field Experiment Settings. We set up the experiment scenario using 2 vehicles on different side of the blind corner. Each vehicle is equipped with Denso Wireless Safety Unit (WSU), which is connected to 2 external antennas (see Figure 2). The antennas are placed at 1.2 m from ground. IEEE



FIGURE 3: The experiment scenario: (a) bird view and (b) perspective view.

TABLE 2: The experiment settings.

Settings	Values
(i) Data transmission device	Denso WSU 5001-T
(ii) Antennas	2 external antennas at 1.2 m from ground
(iii) Transmission power	20 dBm
(iv) Beacon interval	10 Hz
(v) Total number of packets sent each experiment case	Approximately 100 beacons
(vi) Number of experiments	4 blind corners

802.11p is used as a communication module in Denso WSU. Because GPS does not provide accurate position information, we have measured and recorded the location manually with a standard measuring wheel. As a result, we can obtain an accurate position of the vehicle which leads to more accurate result.

The network traffic generated in the experiment is 10 Hz beacon, which is the minimum transmission frequency required for safety applications [17]. The attached antennas transmit the signal with 20 dBm power. In each experiment case, one vehicle is fixed at distance d_1 on one side of the blind corner. The other vehicle is moving between $d_2 - 1$ m and $d_2 + 1$ m on the other side of the blind corner. Then, we calculate the average value of the results for that point. We send approximately 100 beacons for each case and calculate the packet delivery ratio and average RSSI. The experiment scenario is depicted in Figure 3 and the settings are summarized in Table 2.

We did experiments at 4 blind corners: Electrical Engineering Lab (see Figure 4), Mechanical Engineering Lab (see Figure 5), Civil Engineering Lab (see Figure 6), and Centennial Building (see Figure 7) in Faculty of Engineering, Chulalongkorn University. These 4 blind corners represent different types of blind corners. We divide the blind corners into 2 types, which are the corner with large obstruction (Electrical Engineering Lab and Mechanical Engineering



FIGURE 4: Electrical Engineering Lab.



FIGURE 5: Mechanical Engineering Lab.

Lab) and the corner with small obstruction (Civil Engineering Lab and Centennial Building). The corner with large obstructions is the corner with concrete building, which has a lot of large machines made of metal inside. The corner with small obstruction is the corner with concrete building which has a wide free space inside and mostly contains tables and chairs. The locations of all blind corners in our experiment are shown in bird's eye view in Figure 8. Because the range of each corner is different, the maximum distance between the vehicles and the corner is differently set for each blind corner. The range for each experiment is shown in Table 3. We conducted extensive experiments and found out that the results have the same trend regardless of the day of the experiment and distance step. In order to conduct the experiment with less time, we increase the distance step in our later experiments.

TABLE 3: Experiment distance for each blind corner.

Location	Vehicle 1 distance (d_1)	Vehicle 2 distance (d_2)
Electrical Engineering Lab	0, 5, 10, 15, 20, 30, 40 m	1 – 55 m (step every 2 m)
Mechanical Engineering Lab	0, 5, 10, 15, 20, 30, 40 m	1 – 30 m (step every 3 m) 30 – 58 m (step every 4 m)
Civil Engineering Lab	0, 5, 10, 15, 20, 30, 40 m	1 – 15 m (step every 2 m) 15 – 39 m (step every 3 m) 39 – 55 (step every 4 m)
Centennial Building	0, 5, 10, 20, 30 m	1 – 30 m (step every 3 m) 30 – 42 m (step every 4 m)



FIGURE 6: Civil Engineering Lab.



FIGURE 8: The bird's eye view of the blind corners in our experiment. (1) Electrical Engineering lab. (2) Mechanical Engineering Lab. (3) Civil Engineering Lab. (4) Centennial Building.



FIGURE 7: Centennial Building.

3.2. Field Experimental Results. Packet delivery ratio (PDR) and average Received Signal Strength Indicator (RSSI) are our evaluation metrics. The PDR is calculated from the ratio between number of packets received at the destination node and number of packets sent by the source node. The average RSSI is calculated by averaging RSSI of all the received packets at the destination node. The results for each blind corner are shown in 3-dimensional graph. For the PDR, the 3 dimensions are the distance between the first vehicle and the corner, the distance between the second vehicle and the corner, and PDR. For the average RSSI, the 3 dimensions are the distance between the first vehicle and the corner, the distance between the second vehicle and the corner, and the average RSSI.

Figure 9 shows the real experimental results for all blind corners. Figures 9(a) and 9(b) show PDR and RSSI results of the first blind corner (Electrical Engineering Lab). Figures 9(c) and 9(d) show PDR and RSSI results of the second blind corner (Mechanical Engineering Lab). Figures 9(e) and 9(f) show PDR and RSSI results of the third blind corner (Civil Engineering Lab). Figures 9(g) and 9(h) show PDR and RSSI

results of the fourth blind corner (Centennial Building). As can be seen from the results, both PDR and RSSI are an inverse variation to the distance from the corner.

According to the results from 4 blind corners, we can divide the blind corners into 2 types which are the corner with large obstruction (the first and the second blind corners) and the corner with small obstruction (the third and the fourth blind corners). The first and the second blind corners are concrete buildings with a lot of large machines inside, leading to a lot of signal attenuations, while the third and the fourth blind corners are concrete buildings with a wide free space inside, leading to less signal attenuation.

Moreover, it can be noticed that all the results shown in the graphs are quite symmetric. Therefore, PDR and the average RSSI are associated with the minimum distance between the vehicles and the corner. This is because the closer the vehicle to the corner is, the smaller effect of blind corner the communication experiences. More discussion can be found in our previous work [12].

From the experimental results, we also observe the latency of the transmission between 2 nodes. The latency is around 89-95 ms for all distances at all blind corners. This latency value can be considered as a parameter in the simulation setup.

4. Blind Corner Propagation Loss Model

4.1. Study of NS-3 Propagation Model. Network simulator is a tool that is very popular in education and research field. The network simulator allows researchers to simulate various kinds of networks and various kinds of scenarios

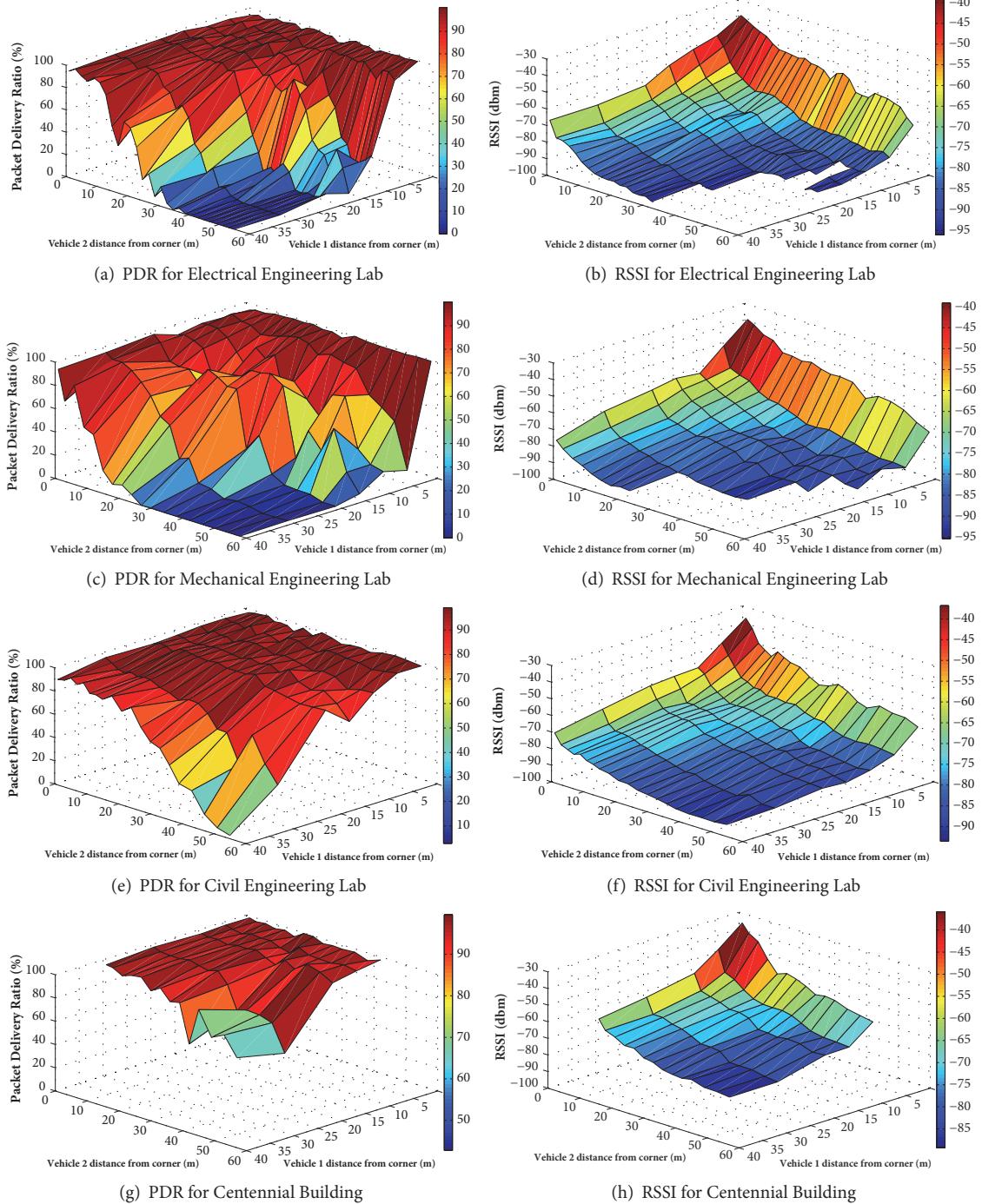


FIGURE 9: Results from real experiments. (a) PDR for Electrical Engineering Lab. (b) RSSI for Electrical Engineering Lab. (c) PDR for Mechanical Engineering Lab. (d) RSSI for Mechanical Engineering Lab. (e) PDR for Civil Engineering Lab. (f) RSSI for Civil Engineering Lab. (g) PDR for Centennial Building. (h) RSSI for Centennial Building.

which are convenient for simulating a large-scale network. One of the most popular network simulators is NS-3, which is open-sourced software. Moreover, NS-3 also supports simulation over vehicular network that uses IEEE 802.11p as wireless interface. Using the simulator, we have to consider which propagation model is suitable to simulate packet loss.

Normally, for vehicular network, the well-known propagation model setting is to use two-ray ground model coupled with Nakagami model. These two models result from the Euclidean distance between transmission node and receive node. By using NS-3, the results of PDR and the average RSSI when applying these models are shown in Figure 10. We observe that the graph characteristics of the simulation results

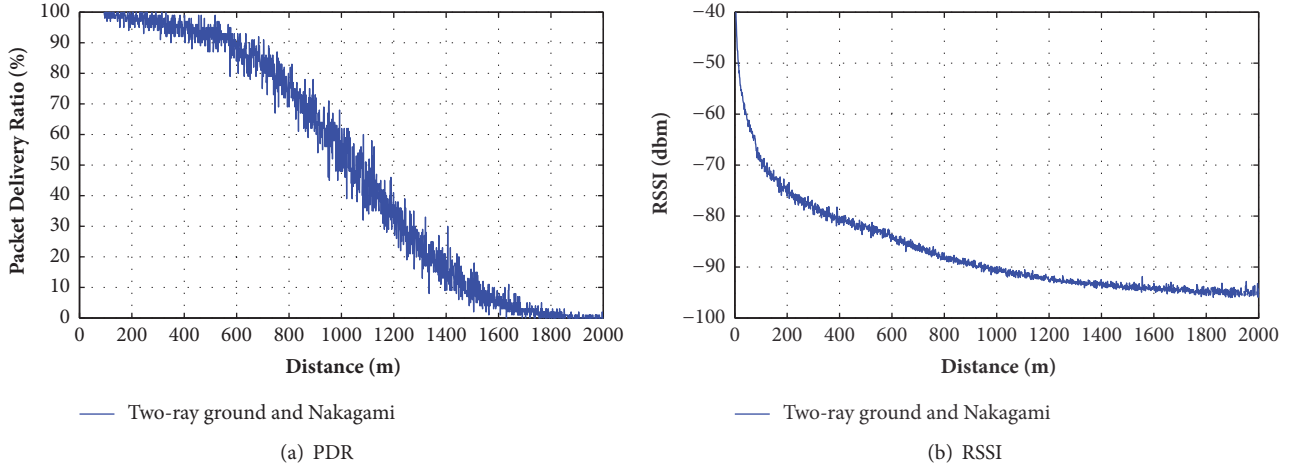


FIGURE 10: Simulation results when applying two-ray ground model coupled with Nakagami model. (a) PDR. (b) RSSI.

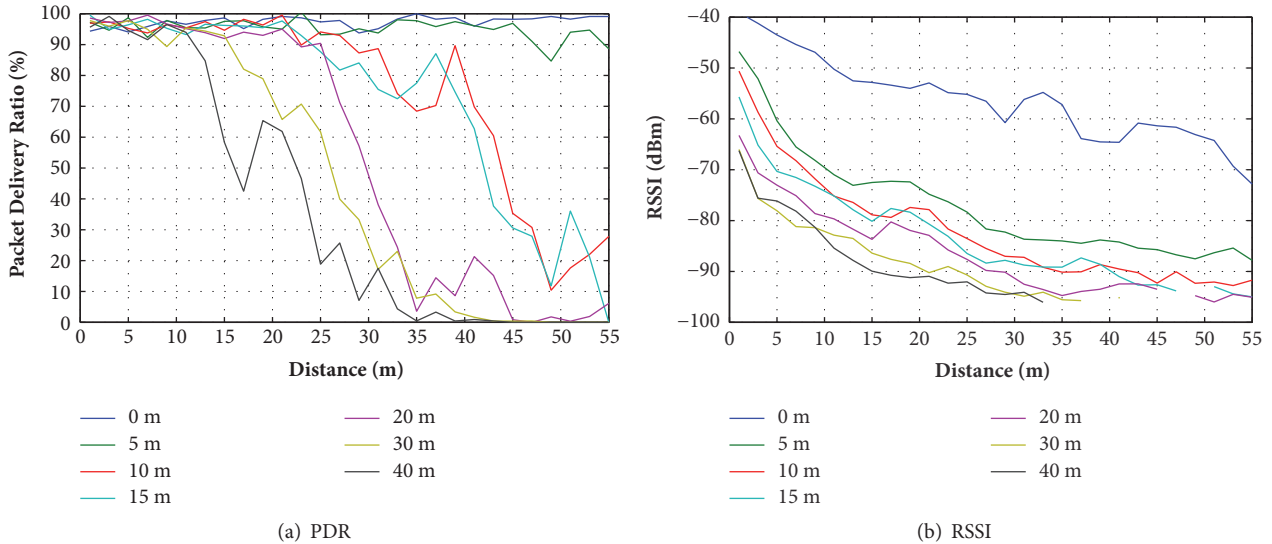


FIGURE 11: Results from real experiments for Electrical Engineering Lab. (a) PDR. (b) RSSI.

are similar to the results from real blind corner experiments. For more clarification, we simplify the result from real experiments in Figures 9(a) and 9(b) to 2-dimensional graph as shown in Figures 11(a) and 11(b). Each graph shows the result for different distances of vehicle 1. As can be seen, all the graphs have the same trend, similarly to S-shaped curve. Each point in the real experiment result in Figure 11 can be mapped to the result in Figure 10 by increasing the distance. On the other words, the signal characteristics when travelling through the blind corner behave the same as the signal when the vehicles are in line of sight at longer distance. As a result, we modify the distance calculation when the signals travel through blind corner. Since distance is the most important factor for calculation in the propagation models, modifying distance calculation is like modifying the characteristics of the models applied. This can represent characteristics of the communication at blind corners.

Referring to the variables depicted in Figure 3, we modify the distance calculation and use the summation of distances

between the vehicles and the corner ($d_1 + d_2$) instead of using the Euclidean distance (d). This is because in the case of the blind corner this summation represents the distance the signal really travels. Moreover, as we discussed that the minimum distance is associated with the result, we add the minimum distance factor to the distance calculation. This factor represents that the closer the vehicle to the corner is, the smaller effect of blind corner the communication experiences. This leads to the higher PDR. As a result, the estimated distance is formulated as shown in the following equation:

$$\text{Estimated Distance} = (d_1 + d_2) \times \min(d_1, d_2) \quad (1)$$

In order to investigate the PDR and RSSI results when applying our estimated distance equation, we set up the simulation scenario the same as the real experiment scenario which is shown in Table 2. There are 2 vehicles on different side of blind corners. The 2 vehicles are transmitting and

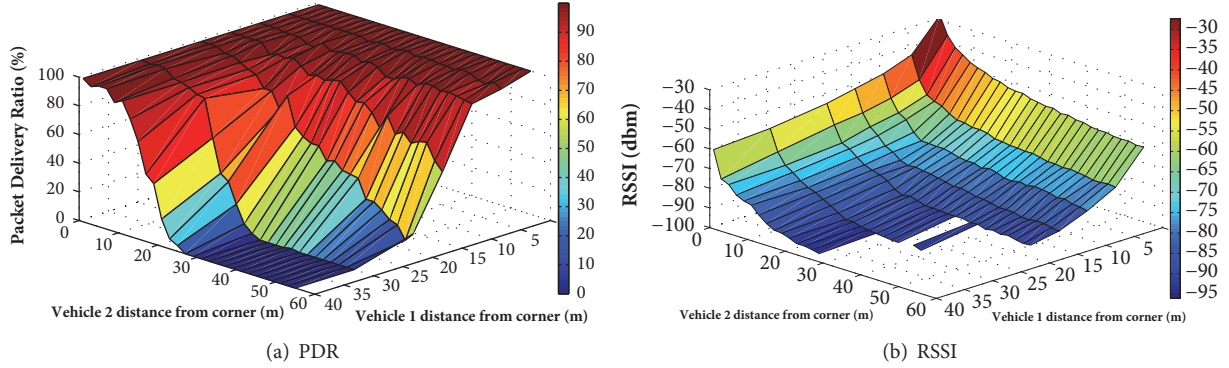


FIGURE 12: Results for preliminary simulation. (a) PDR. (b) RSSI.

Input: Location of vehicle V_1 and V_2 , Obstacles list, α
Output: Distance
(1) Distance = UNKNOWN
(2) if there are obstacles between V_1 and V_2 then
(3) d_1 = Distance of V_1 from corner
(4) d_2 = Distance of V_2 from corner
(5) Distance = $(d_1 + d_2) \times \min(d_1, d_2) \times \alpha$
(6) else do
(7) Distance = Distance between V_1 and V_2
(8) end if
(9) return Distance

ALGORITHM 1: Blind corner model.

receiving IEEE 802.11p signal. The transmitted signal strength is 20 dBm. The traffic generated is 10 Hz beacon.

The result from the preliminary simulation is shown in Figure 12. As can be seen, the graph characteristics in Figure 12 are similar to the results from real experiments shown in Figure 9. The packet delivery ratio and the average RSSI have inverse variation to the distance. So we consider this method to be used in our model.

4.2. Proposed Blind Corner Model. From the experimental results in Figure 9, each type of blind corners does not obstruct the transmitted signal equally. The PDR ratio and the average RSSI are not the same for all blind corners. According to this reason, it can be seen that only the minimum distance is not enough for the model. Therefore, we add a parameter α in order to adjust the degree of the obstruction. Equation (2) formulates the modified version of the estimated distance from (1).

$$\text{Estimated Distance} = (d_1 + d_2) \times \min(d_1, d_2) \times \alpha \quad (2)$$

The parameter α is used to adjust the degree of the obstruction, which represents low obstruction to high obstruction. α must be greater than or equal to 0.4. If α is less than 0.4, it cannot be used because it makes the estimated distance lower than the real Euclidean distance. This will lead to nonrealistic simulation result.

The distance calculation can be divided into 2 cases: (1) line of sight and (2) non-line of sight. If the vehicles are in line of sight, it is not necessary to use our distance calculation

model. The real Euclidean distance can be used as an input in Nakagami or two-ray ground models. However, if the vehicles are in non-line of sight, our distance calculation model is useful. The estimated distance calculated according to (2) can be used as an input in Nakagami or two-ray ground models instead. The algorithm that describes our distance calculation is shown in Algorithm 1.

5. Results and Discussion

In this section, we show the results from the simulation using our model and suggest the appropriate range of the parameter α . We simulate the scenarios using the simulation setting as shown in Table 2, so that all the settings will be the same as the real experiments. Then, we vary the value of α . We compare the results from the simulation and those from the real experiments for each blind corner. We calculate the root-mean-square error (RMSE) between the results from the simulation and those from the real experiments using (3). Equation (3) shows RMSE calculation, where i is the distance between the first vehicle and the corner, j is the distance between the second vehicle and the corner, $x_{i,j}$ is the PDR of the distance pair i, j from the real experiment, $s_{i,j}$ is the PDR from the simulation, and n is number of distance pairs. The RMSE for each α and each blind corner are shown in Figure 13.

$$\text{RMSE} = \sqrt{\frac{\sum_{\text{Each pair of distance } i,j} (x_{i,j} - s_{i,j})^2}{n}} \quad (3)$$

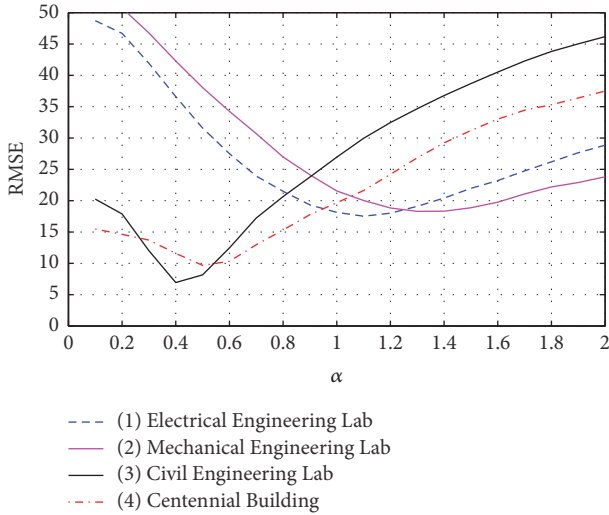


FIGURE 13: RMSE between simulation result and real experiment result.

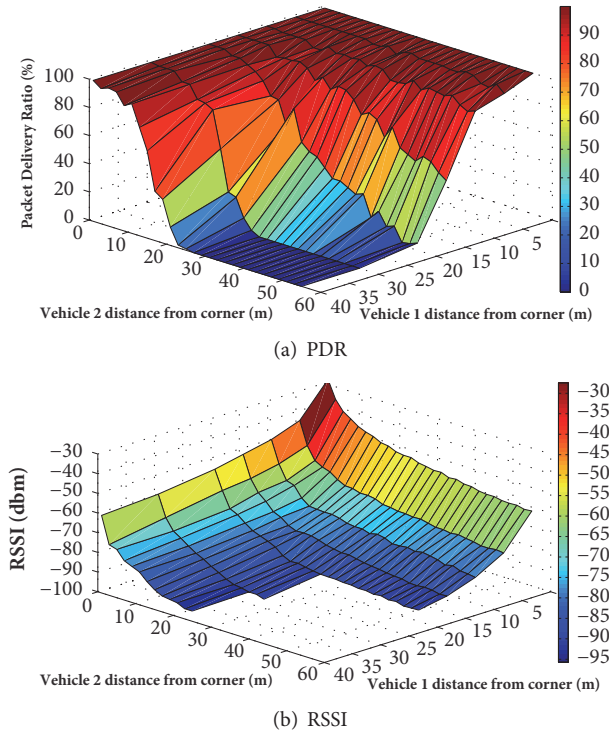


FIGURE 14: Results from the simulation with $\alpha = 1.1$ for blind corner with large obstruction. (a) PDR. (b) RSSI.

According to Figure 13, we suggest the weight factor α for each type of blind corners as follows.

For the first and the second blind corners of the building with large obstruction, we use α between 1.1 and 1.3. The simulation results using the recommended values 1.1 and 1.3 are shown in Figures 14 and 15, respectively. As can be seen, Figure 14 provides similar results to Figures 9(a) and 9(b). Figure 15 provides similar results to Figures 9(c) and 9(d).

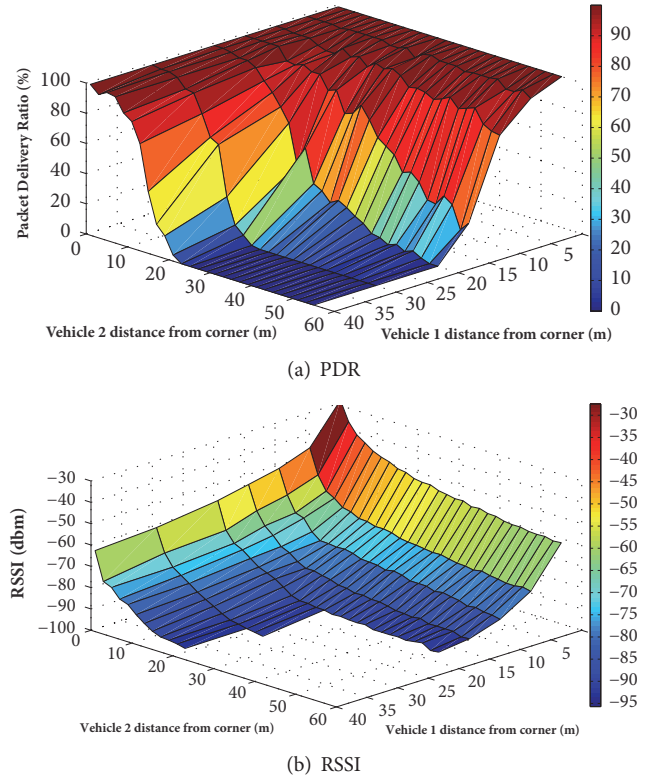


FIGURE 15: Results from the simulation with $\alpha = 1.3$ for blind corner with large obstruction. (a) PDR. (b) RSSI.

For the third and the fourth blind corners of the building with small obstruction, we use α between 0.4 and 0.5. The simulation results using the recommended values 0.4 and 0.5 are shown in Figures 16 and 17, respectively. As can be seen, Figure 16 provides similar results to Figures 9(e) and 9(f). Figure 17 provides similar results to Figures 9(g) and 9(h).

The results from the simulation are close to the results from real experiments. However, the results from the simulation have a higher PDR and average RSSI, and the graph trends are smoother than the graph for real experiments. This is because in real experiments there might be some other factors that we cannot detect or some factors that are difficult to produce in simulations such as environmental interferences.

We also compare our work with the obstacle model [8, 9] which is implemented in NS-3. The obstacle model is also embedded in Veins framework based on Omnet simulator, which is another popular network simulator. Therefore, we use the obstacle model as our baseline. The simulation scenario is set the same as the real experiment scenario, which is shown in Table 2. The results using the obstacle model are shown in Figure 18. As can be seen, the graph characteristics of PDR reduce rapidly at a specific range. The result does not reflect communication in real world, where PDR gradually reduces. Compared to our results shown in Figures 14–17, it can be seen that our model can provide much more similar results to the real world and better represents the real characteristics of IEEE 802.11p at blind corners.

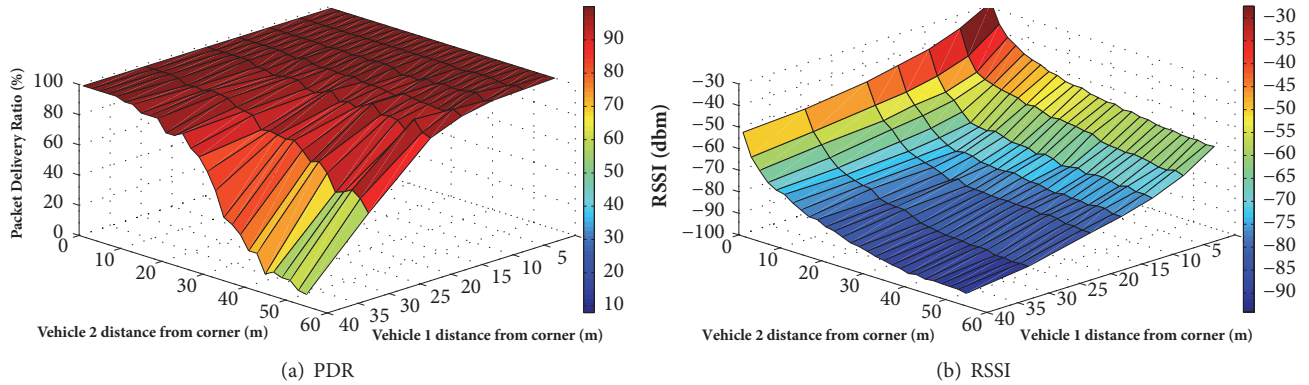


FIGURE 16: Results from the simulation with $\alpha = 0.4$ for blind corner with small obstruction. (a) PDR. (b) RSSI.

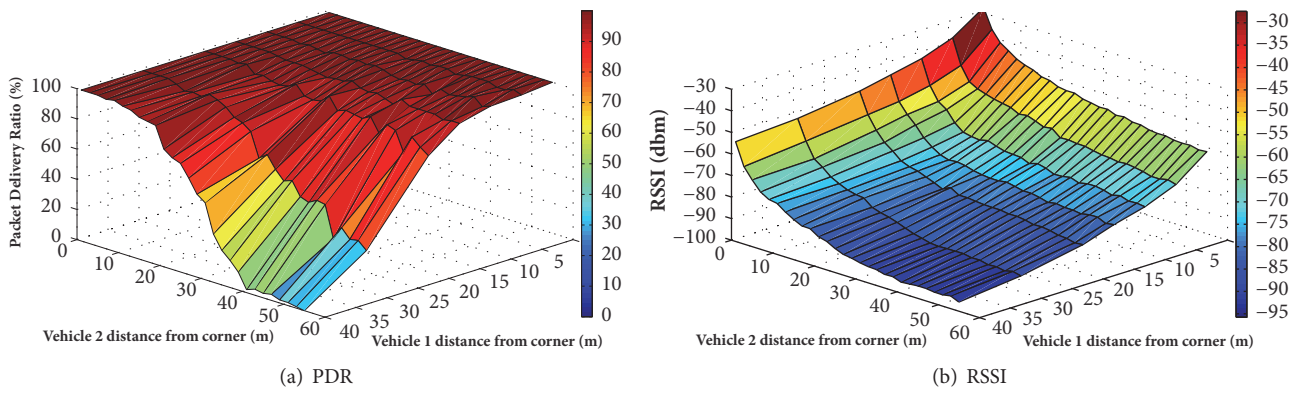


FIGURE 17: Results from the simulation with $\alpha = 0.5$ for blind corner with small obstruction. (a) PDR. (b) RSSI.

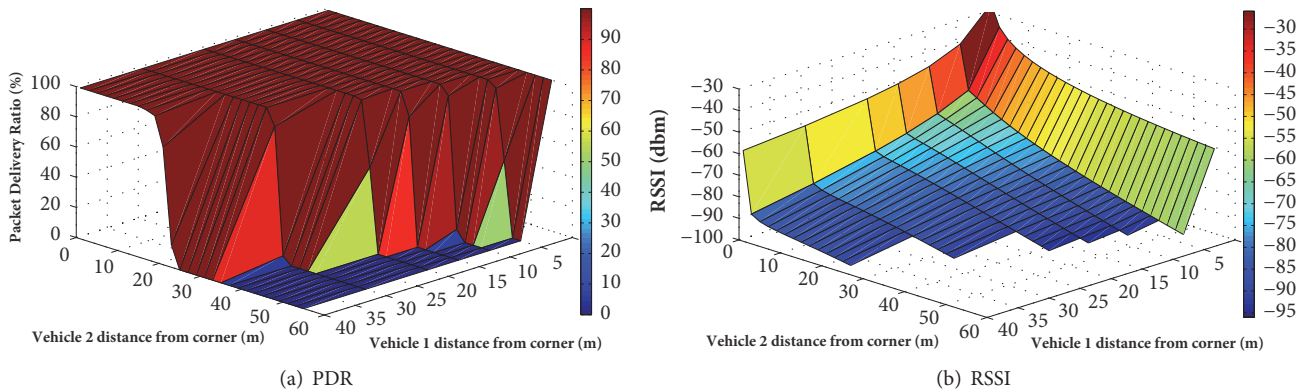


FIGURE 18: Results from the simulation when simulating with obstacle model. (a) PDR. (b) RSSI.

6. Conclusion

In this paper, we propose the blind corner model that represents the characteristics of IEEE 802.11p communication at blind corners. We modify the distance calculation when the signals travel through blind corner. Our model utilizes the minimum distance between the vehicles to the corner, which is the most important variable for propagation model calculation. Moreover, our model has a parameter to adjust the degree of the obstruction. We also conduct extensive real experiments with IEEE 802.11p communication devices and

do comparison to the simulation result. According to the experimental results and the simulation results, we suggest that the parameter should be set between 1.1 and 1.3 for the buildings with large obstruction and between 0.4 and 0.5 for the buildings with small obstruction. The comparison result shows that our proposed model can represent the characteristics of IEEE 802.11p communication at blind corners better than the obstacle model. Therefore, our research is useful in research field. The protocols and applications can be tested realistically in blind corner scenarios by using our model.

Data Availability

The experimental data used to support the findings of this study are available from the corresponding author upon request.

Conflicts of Interest

The authors declare that there are no conflicts of interest regarding the publication of this paper.

Acknowledgments

This research was supported by Chula Computer Engineering Graduate Scholarship for CP Alumni and the Wireless Network and Future Internet Research Unit, Ratchadaphiseksomphot Endowment Fund, Chulalongkorn University. The authors would like to acknowledge ITS Thailand and DENSO for the support of the wireless safety units and National Broadcasting and Telecommunications Commission (NBTC) for partial support and thank Mr. Pawissakan Chirupphapa, Mr. Chanthawat Rattanapongphan, Mr. Teerapat Vongsuteera, Mr. Adsadawut Chanakitkarnchok, and members of ISEL Lab for their help in the experiments.

References

- [1] World Health Organization, *Global status report on road safety 2017*, World Health Organization, 2017.
- [2] New South Wales Government, *Road traffic casualty crashes in New South Wales 2016*, New South Wales Government, 2016.
- [3] *IEEE Standard for Information technology—Local and metropolitan area networks—Specific requirements*, Specifications Amendment 6: Wireless Access in Vehicular Environments, Part II edition, 2010, Wireless LAN Medium Access Control (MAC) and Physical Layer (PHY), pp. 1 - 51.
- [4] A.-M. Cailean, B. Cagneau, L. Chassagne, V. Popa, and M. Dimian, "A survey on the usage of DSRC and VLC in communication-based vehicle safety applications," in *Proceedings of the 2014 21st IEEE Symposium on Communications and Vehicular Technology in the BeNeLux, IEEE SCVT 2014*, pp. 69–74, Netherlands.
- [5] R. Meireles, M. Boban, P. Steenkiste, O. Tonguz, and J. Barros, "Experimental study on the impact of vehicular obstructions in VANETs," in *Proceedings of the IEEE Vehicular Networking Conference (VNC '10)*, pp. 338–345, December 2010.
- [6] R. He, A. F. Molisch, F. Tufvesson, Z. Zhong, B. Ai, and T. Zhang, "Vehicle-to-vehicle propagation models with large vehicle obstructions," *IEEE Transactions on Intelligent Transportation Systems*, vol. 15, no. 5, pp. 2237–2248, 2014.
- [7] H. Tchouankem, T. Zinchenko, and H. Schumacher, "Impact of buildings on vehicle-to-vehicle communication at urban intersections," in *Proceedings of the 2015 12th Annual IEEE Consumer Communications and Networking Conference, CCNC 2015*, pp. 206–212, USA, January 2015.
- [8] S. E. Carpenter and M. L. Sichitiu, "An obstacle model implementation for evaluating radio shadowing with ns-3," in *Proceedings of the the 2015 Workshop*, pp. 17–24, Barcelona, Spain, May 2015.
- [9] C. Sommer, D. Eckhoff, R. German, and F. Dressler, "A computationally inexpensive empirical model of IEEE 802.11p radio shadowing in urban environments," in *Proceedings of the 8th International Conference on Wireless On-Demand Network Systems and Services (WONS '11)*, pp. 84–90, January 2011.
- [10] E. Giordano, R. Frank, G. Pau, and M. Gerla, "CORNER: A radio propagation model for VANETs in Urban scenarios," *Proceedings of the IEEE*, vol. 99, no. 7, pp. 1280–1294, 2011.
- [11] Q. Sun, S. Y. Tan, and K. C. Teh, "Analytical formulae for path loss prediction in urban street grid microcellular environments," *IEEE Transactions on Vehicular Technology*, vol. 54, no. 4, pp. 1251–1258, 2005.
- [12] S. Jaktheerangkoon, K. N. Nakorn, and K. Rojviboonchai, "Performance study of IEEE 802.11p in blind corner scenario," in *Proceedings of the 2016 International Symposium on Intelligent Signal Processing and Communication Systems, ISPACS 2016*, Thailand, October 2016.
- [13] "Network Simulator 3," <https://www.nsnam.org/>.
- [14] S. A. Hosseini Tabatabaei, M. Fleury, N. N. Qadri, and M. Ghanbari, "Improving propagation modeling in urban environments for vehicular ad hoc networks," *IEEE Transactions on Intelligent Transportation Systems*, vol. 12, no. 3, pp. 705–716, 2011.
- [15] J. Maurer, T. Fügen, and W. Wiesbeck, "Physical layer simulations of IEEE802.11a for vehicle-to-vehicle communications," in *Proceedings of the 62nd Vehicular Technology*, pp. 1849–1853, 2005.
- [16] "Vehicles in Network Simulation," <http://veins.car2x.org/>.
- [17] Z. Hameed Mir and F. Filali, "LTE and IEEE 802.11p for vehicular networking: a performance evaluation," *Eurasip Journal on Wireless Communications and Networking*, vol. 1, pp. 1–15, 2014.